MODELLING AND CONTROL OF LASER SURFACE TREATMENT

CIP-GEGEVENS KONINKLIJKE BIBLIOTHEEK, DEN HAAG

Römer, Gerardus Richardus Benardus Engelina

Modelling and control of laser surface treatment /
Gerardus, Richardus, Benardus, Engelina, Römer. - [S.l. : s.n.]. - Ill.
Thesis Enschede. - With ref.
ISBN 90-365-1304-9
Subject headings: laser surface treatment / control applications.

Printed by Print Partners Ipskamp, Enschede, the Netherlands.

MODELLING AND CONTROL OF LASER SURFACE TREATMENT

PROEFSCHRIFT

ter verkrijging van
de graad van doctor aan de Universiteit Twente,
op gezag van de rector magnificus,
prof. dr. F.A. van Vught,
volgens het besluit van het College voor Promoties
in het openbaar te verdedigen
op donderdag 3 juni 1999 te 13.15 uur.

door

Gerardus Richardus Benardus Engelina Römer

geboren op 11 oktober 1969
te 's-Heerenberg

Dit proefschrift is goedgekeurd door
prof. dr. ir. J.B. Jonker, promotor,
prof. dr. ir. J. Meijer, promotor.

PREFACE

The work presented in this thesis has been performed within the framework of the project *Laser Alloying* as part of the *Innovatiegericht Onderzoeksprogramma* (IOP) *Metalen* (Innovation aimed Research Program-Metals), which was initiated by the Dutch Department of Social and Economic Affairs. Goal of this project was to develop the relative new technology of laser surface alloying for the Dutch industry. In the project three Dutch research institutes co-operated:

(*i*) the University of Groningen, Department of Applied Physics, Research Group Materials Science and Engineering,
(*ii*) the University of Twente, department of Mechanical Engineering, Laboratory of Mechanical Automation,
(*iii*) the *Nederlandse Organisatie voor Toegepast Natuurwetenschappelijk Onderzoek* (TNO), (Netherlands Organization for Applied Scientific Research).

The tasks of the University of Twente in this project consisted of three parts. The first part covered the achievement and enhancement of insight in the phenomena that occur during laser alloying. The second part involved the development of tools and methods that facilitate the use of laser alloying. The third part covered the development of feedback control for laser alloying to cope with process disturbances. The results of this latter part are discussed extensively in this thesis. Results on parts, which are not covered by this thesis, are discussed in the final report of the project (Römer, 1998).

List of publications

Parts of the work presented in this thesis has been published in:

- G.R.B.E. Römer and J. Meijer (1995) Metal surface temperature induced by moving laser beams. *Optical and quantum electronics*, **27**, 1397-1406.

- G.R.B.E. Römer (1997) Controlled laser surface alloying of Ti6Al4V with nitrogen, *Poster presentation on the 10th symposium on plasma physics and radiation technology*. March 11 & 12, Lunteren, The Netherlands.
- G.R.B.E. Römer (1997) Vision-system controls laser alloying process. (in Dutch) *Elektronica Markt + Techniek*, **7**(8), 33-35.
- G.R.B.E. Römer, M. Hoeksma and J. Meijer (1997) Industrial imaging controls laser surface treatment. *Photonics Spectra*, **11**, 104-109.
- G.R.B.E. Römer and J. Meijer (1997) Analytical model describing the relationship between laser power, beam velocity and melt pool depth in the case of laser (re)melting, -alloying and -dispersing, *Proceedings of the conference on lasers in material processing* EUROPTO/SPIE, **3097**, 507-515.
- G.R.B.E. Römer, H. Zwart, K.A.J. de Graaff and J. Meijer (1998) Modelling of the temperature field induced by laser surface irradiation in the view of feedback control theory. *Lasers in Engineering*. Special issue: *Proceedings of the 13th meeting on mathematical modelling of materials processing with lasers*, **7**(3-4), 179-197.
- G.R.B.E. Römer, J. OldeBenneker and J. Meijer (1998) Control of laser surface alloying, *Surface Engineering*, **14**(4), 295-298.
- G.R.B.E. Römer, R.G.K.M. Aarts and J. Meijer (1999) Dynamic models of laser surface alloying. *Lasers in Engineering*. Special issue: *Proceedings of the 14th meeting on mathematical modelling of materials processing with lasers*, **8**(4), 251-266.

Acknowledgements

Producing a thesis is not a one-man job, but a ”team sport”. Therefore, I am indebted to a lot of team players, who have been contributing to the ”game”.

First of all, I would like to thank prof. Jonker, prof. Meijer and prof. Beckmann. The many discussions with them were very valuable to me. As were the discussions with prof. De Hosson and Arjen Kloosterman from the University of Groningen.

Special thanks are in place for my (old) colleagues and room mates: Chris, Erwin, Jeroen, Jindřich, Johannes, Marcel, Paul, Roelof, Ronald, and Sjoerd. They created a nice atmosphere to work in, and frequently had to put up with my abundant reflections on laser surface treatment in the view of control theory.

None of the experiments would have been carried out, if it weren't for the people with the ”golden hands”, Gert, Gerrit, Gerard, Michel, Tyrone and Wim. In particular, I would like to mention Bertus van Drogen, Jilles Eindhoven and Jan Wes for their share in realizing the experimental set-up. I am especially indebted to dr. Pathiraj for his effort and suggestions during the preparation and microstructural analysis of the numerous samples.

Over 17 students have contributed to the work described in this thesis. Of them I owe much to the ”fabulous four”: Arnout, Ger, Koen and Marten.

And last, but not least, I would like to thank my parents and Miranda, who supported me in my study and in writing this thesis.

Gert-Willem

NOMENCLATURE

Symbol	Description	Units
A	Absorptivity	$-$
A	System matrix in state space representation	
B	Input matrix in state space representation	
C	Output matrix in state space representation	
c	Speed of light in vacuum ($2.9979246 \cdot 10^8$)	$\mathrm{m \cdot s^{-1}}$
c_p	Thermal capacity at constant pressure	$\mathrm{J \cdot kg^{-1} \cdot K^{-1}}$
D_λ	Relative spectral sensitivity of a detector	$-$
d	Diameter of laser spot	m
$d_x,\ d_y$	Length (width) of laser spot in x (y) -direction	m
f	Focal distance lens	m
f_s	Sample frequency	Hz
GL	Gray level $\in [0,255]$	$-$
GL_m	Gray level corresponding to solid-liquid interface	$-$
$H(\cdot)$	Heaviside function (unit step function)	
H_r	Reaction energy	$\mathrm{J \cdot kg^{-1}}$
h	Plank's constant ($6.62176 \cdot 10^{-34}$)	$\mathrm{W \cdot s^2}$
h_c	Heat exchange coefficient of convection with atmosphere	$\mathrm{W \cdot m^{-2} \cdot K^{-1}}$
$I(x,y)$	Laser beam intensity profile	$\mathrm{W \cdot m^{-2}}$
I_0	Laser beam intensity scale factor	$\mathrm{W \cdot m^{-2}}$
J	Cost function in LQG controller design	
K	Kalman matrix in LQG controller design	
K	Thermal conductivity	$\mathrm{W \cdot m^{-1} \cdot K^{-1}}$
K_{DC}	Low frequency or DC gain of process	
K_P	Proportional controller gain	

K_I	Integral controller gain	
K_D	Derivative controller gain	
k	Boltzmann's constant ($1.38066 \cdot 10^{-23}$)	$\mathrm{W \cdot s \cdot K^{-1}}$
L	State feedback matrix in LQG control	
L_f	Latent heat of fusion	$\mathrm{J \cdot kg^{-1}}$
l	Distance between radiating body and detector	m
M^2	Times-diffraction-limited-factor, or beam quality $\in [1, \infty\rangle$	–
m	Mass	kg
N_λ^b	Spectral radiance of a black body	$\mathrm{W \cdot m^{-3} \cdot sr^{-1}}$
$\mathbf{n}$	Normal to a surface	
n	Index of refraction	–
n	Memory horizon, during recursive process identification	–
n_a, n_b	ARX model orders	–
n_k	Delay in ARX model	–
Pe	Peclet number ($\mathrm{Pe} = d_x v / \kappa$)	–
P_A	Absorbed laser power	W
P_L	Laser power incident on the work piece	W
P_R	Reflected laser power	W
Q	Weighting matrix in LQG controller design	
q_0	Tuning parameter of LQG controller	
R	Reflectivity	–
R	Weighting matrice in LQG controller design	
S_b	Area of body emitting thermal radiation	$\mathrm{m^2}$
S_d	Active area of optical detector	$\mathrm{m^2}$
S_m	Melt pool surface area	$\mathrm{m^2}$
$S_{m,T}$	Melt pool surface "area" measured by spectral pyrometer	°C
S_{sl}	Area of solid-liquid interface	$\mathrm{m^2}$
T	Transmittance	–
T	Temperature	K
T_i	Temperature behind the melt pool	°C
T_m	Melting temperature	K
s	Frequency (or Laplace) variable	$\mathrm{rad \cdot s^{-1}}$
t	Time	s
t_i	Laser-material interaction time	s
t_r	Rise time	s
$\mathbf{U}$	Fluid velocity in coordinate system fixed to laser beam	$\mathrm{m \cdot s^{-1}}$
$\mathbf{v}$	Commanded beam velocity	$\mathrm{m \cdot s^{-1}}$
v^*	Measured beam velocity	$\mathrm{m \cdot s^{-1}}$
w	Noise in ARX model	
$\mathbf{w}_d$	White process noise in LQG controller design	
$\mathbf{w}_n$	White measurement noise in LQG controller design	
X	Solution to the algebraic Riccati equation	
x	Coordinate (in direction of beam translation)	m
$\mathbf{x}$	State vector	
y	Coordinate (perpendicular to direction of beam translation)	m
$\mathbf{y}$	Output vector	

z	Coordinate (in direction of laser beam, depth)	m
$\mathbf{z}$	Vector of observed outputs	
z_d	Thickness of a plate	m
z_m	Melt pool depth	m

β	Fraction of reaction product in melt pool	–
Γ	Surface area irradiated by the laser beam	–
$\delta(\cdot)$	Dirac delta function	–
δ_o	Optical penetration depth	m
δ_h	Thermal penetration depth	m
ε	Emissivity	–
ε_t	Hemispherical total emissivity	–
ζ	Dimensionless coordinate ($\zeta = 2z/d_x$)	–
η	Dimensionless coordinate ($\eta = 2y/d_x$)	–
Θ	Angle of incidence	rad
θ	Angle of detection relative to normal on surface	rad
$\theta(\chi,\eta)$	Dimensionless temperature ($\theta = T(\chi,\eta)K\pi\sqrt{d_x d_y}/2P$)	–
κ	Thermal diffusivity ($\kappa = \lambda/\rho c_p$)	$\mathrm{m^2 \cdot s^{-1}}$
λ	Wavelength	m
λ	Forgetting factor $\in [0,\,1\rangle$ in recursive system identification	–
λ_0	Wavelength in vacuum	m
ρ	Density	$\mathrm{kg \cdot m^{-3}}$
σ	Stefan-Boltzmann constant $(5.67051 \cdot 10^{-8})$	$\mathrm{W \cdot m^{-2} \cdot K^{-4}}$
σ_s	Fluid surface tension	$\mathrm{N \cdot m^{-1}}$
τ	Time constant	s
τ_i	Integration time of integral action in PID-controller	s
τ_d	Carbon diffusion time	s
τ_λ	Spectral transmittance	$\mathrm{m^{-1}}$
$\Phi(\chi,\eta)$	Dimensionless laser beam intensity profile ($\Phi = I\,\frac{d_x d_y}{4P}$)	–
χ	Dimensionless coordinate ($\chi = 2x/d_x$)	–
Ω	Space $(x,y,z) \in$ taken by the work piece	
ω_{BW}	Bandwidth	$\mathrm{rad \cdot s^{-1}}$
$\partial\Omega$	Surface(s) of work piece	
$\partial\Omega_{sl}$	Solidification front	

CONTENTS

Chapter 1
INTRODUCTION

1.1 Laser surface treatment

Laser surface treatments, such as transformation hardening, remelting, alloying and cladding, are techniques for improving the mechanical, tribological or chemical properties, such as wear, fatigue and erosion resistance, of metal parts (Heuvelman *et al.*, 1992; Gasser *et al.*, 1996). The surface improvement is based on a rapid thermal cycle of a thin surface layer (typically 1 mm), induced by absorbed laser energy, resulting in microstructural refinement, phase transformation or the formation of alloyed or clad layers (Steen, 1994). The processing results are determined by the laser beam parameters, such as power density, the beam velocity, and the thermo-physical properties of the component. These technologies allow the selection of the bulk material of the component to be determined by strength or low cost, whereas the properties of the surface may be selected for wear, corrosion resistance or other properties desirable for its service use (Oakley, 1981).

An example is the laser cladding of the rim of a diesel outlet valve, see figure 1.1. By cladding with a cobalt-based material locally a wear resistant clad is fused on top of the surface, where it is really needed (Bloehs *et al.*, 1996a; Lubbers, 1994). Another example is laser nitriding of titanium turbine blades of steam turbines (Robinson and Reed, 1995; Gerdes *et al.*, 1995). By melting the surface in a nitrogen atmosphere, a top layer of titanium-nitride is formed showing high wear and friction resistance (Savvides and Window, 1988; Zambon *et al.*, 1994; Fischer and Lensch, 1996).

The main advantages of laser surface treatments over conventional surface treatment techniques, such as flame spraying and plasma spraying are (Scheller, 1995; Oakley, 1981; Steen, 1993; Schneider, 1998):

- The power supplied to the surface of the product can be well mastered due to the well defined geometry and energy distribution of the laser beam. For this reason,

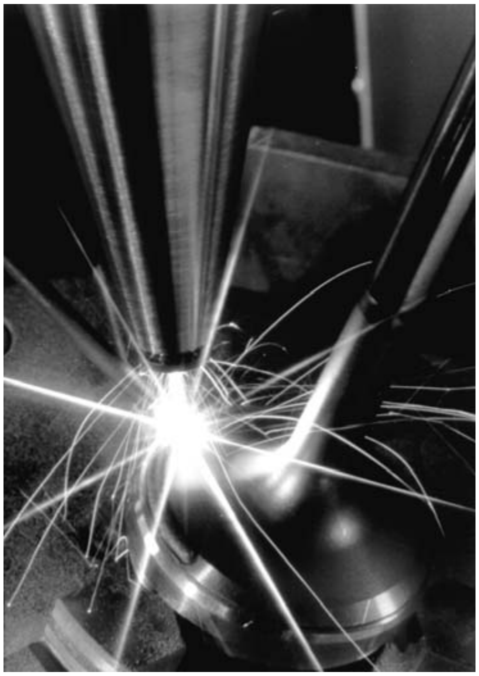

Figure 1.1: Injection of a cobalt-based material into a laser-generated melt pool at the rim of a diesel outlet valve improves the valve's wear resistance.

the treatment is precise and can be restricted to localized areas, even to reach areas of a product which are otherwise difficult to access (Funk and Müller, 1990; Arlt and Müller, 1994),

- Due to high heating and cooling rates, the gross heat input is low, resulting in minimal thermal distortion of the component. Moreover, high heating and cooling rates allow high production rates,
- Laser processing is a non-contact treatment. Therefore, no special product mounting or support tools are necessary,
- Higher quality surface layers with little contamination and strong bonding to the base material are obtained,
- The optical energy is delivered to the surface with minimal environmental disturbance. Hence, except for the electro-magnetic laser radiation, any detected signal is related to the process itself, rather than the energy delivery system. This facilitates process monitoring.

1.2 The need for process control and modelling

It is well known that the obtained processing quality may vary significantly during laser surface processing (Lim and Chatwin, 1994; Bergmann and Geissler, 1988). Variations of the quality may be observed between processing cycle performed with the same laser equipment, with (apparently) maintained constant operating and material properties. Even within a single processing sequence, without any adjustment of operating parameters, the quality of the results may change (Jørgensen, 1990). This poor reproducibility arises from the high sensitivity of laser surface treatment to small changes in the operating parameters (such as laser power and beam velocity), as well as to process disturbances (such as varying absorptivity). As a result, the desired temperature distribution of the work piece is perturbed, which in turn may induce large and unacceptable process errors (Kechemair *et al.*, 1990; Beyer and Abels, 1992; Li *et al.*, 1990a). E.g. a change of 10% in absorbed laser power at constant beam velocity, during laser transformation hardening, may cause a change of 50% in hardening depth (Geissler and Bergmann, 1990).

The current practice to establish an acceptable quality of the laser treatment consists of two steps:

(*i*) The operating parameters, which yield an acceptable quality, are established by modelling, simulation and experiments. Although extensive modelling and simulation has been conducted to predict the required machining parameters for specific materials (Tosto, 1994), the repeatability is relatively poor (Lim and Chatwin, 1994). Therefore, usually time-consuming *trial and error* experiments are performed to find the optimal operating parameters. This approach implicitly assumes perfect correlation between operating parameters and final processing quality (Kechemair *et al.*, 1990),

(*ii*) The optimal operating parameters, as obtained in the previous step, are monitored during laser processing. As soon as one or more of the operating parameters exceed a pre-determined tolerance band, the product being treated is rejected. Then some randomly selected parts are inspected for processing faults, to verify the processing quality of a batch of completed components.

Unfortunately, processing faults caused by disturbances, which are *not* related to varying operating parameters (e.g. varying absorptivity), can not be detected nor be compensated for by this two-step method. Moreover, the expenses due to defective products caused by processing failures are usually high (Tönshoff and Overmeyer, 1995; Müller *et al.*, 1996). Or as Seidel *et al.* (1994) expressed it: *Quality can not be inspected into a product— it has to be designed or built in*. Therefore, monitoring and control of the laser treatment itself is required to reduce the negative effects of varying operating parameter values and of process disturbances (Lim and Chatwin, 1994; Herziger and Loosen, 1993; Funk and Müller, 1990; Deinzer *et al.*, 1994; Tönshoff and Overmeyer, 1995).This can be achieved by feedback control, in which the product quality is measured in real-time, and subsequent intervention of the process over the operating parameters in the case process quality is (about to be) jeopardized.

Unfortunately, not all the desired process results, such as melt pool depth, can be measured on-line. The quantities which can be measured relatively easily are temperature related, such as the melt pool surface temperature and the melt pool surface area. Therefore, it is important to know the relations between the desired product properties and these measurable quantities. As a consequence, process models are to be developed,which relate the processing quality to the measurable quantities. On the basis of these models an efficient feedback controller for laser surface treatment can be designed.

1.3 Problem definition

The problem statement for this thesis is formulated as follows:

> *Develop process models of laser surface treatment, which relate the processing results (thickness of the treated surface layer) to the measurable quantities. Based on these models, develop a feedback control system to reduce the negative effects of process disturbances as well as of varying operating parameters.*

The development of the control system includes the following iterative stages (Nava-Rüdiger and Houlot, 1997):

(*i*) Characterization of the laser-material interaction and the physical phenomena created by this interaction,
(*ii*) Specification of the process of laser surface treatment in the view of control theory. This includes the definition of the quantities to be controlled (outputs) and the selection (or development) appropriate sensors to measure these outputs. In addition, the input signals and corresponding actuators, which allow the manipulation of the outputs, are selected,
(*iii*) The development of process models which relate the input signals (command signals) to the output (measured signals) of the process, by theoretic modelling or system identification,
(*iv*) Analysis of the correlation between measured signals and disturbances,
(*v*) Establishment and design of a control law, based on the process model(s).

As a test case, the alloying of titanium with nitrogen using a continuous wave CO_2 laser is considered. However, general concepts will be developed in order to be able to apply the control strategies to other laser surface treatments.

1.4 Outline of this thesis

Chapter 2 discusses the operating procedure of laser surface treatment, and a qualitative description of the physical phenomena created by the laser-material interaction is presented. In addition, the characteristics of a number of laser surface treatments are discussed in more detail.

Chapter 3 discusses laser surface treatment in the view of control theory. It includes an overview of the current status of on-line control for laser surface treatment.

Process models are derived and discussed in chapter 4. It will be shown that the conservation law of energy (heat conduction equation) plays a central role in the physical modelling of the process. The models, which follow from this mathematical description, relate the processing results to the measurable quantities and are used to analyze the effects of the operating parameters and disturbances on the outputs. The conclusions drawn from these models are used for system identification of the process and for the design of control algorithms.

In chapter 5 the experimental set-up is presented and some of the models derived in chapter 4 are verified experimentally. Moreover, the steady state as well as the dynamic behavior of laser alloying of titanium is identified by experiments. This chapter includes the design and implementation of a CCD-camera to be used as a real-time two-dimensional thermal detector.

Chapter 6 is addressed to the design and implementation of control algorithms for laser surface alloying, based on results obtained from chapter 5. Next, the performance of the controlled process is evaluated by analyzing its response to typical disturbances.

Finally, in chapter 7 a review, conclusions and suggestions for future research are presented.

Chapter 2

LASER SURFACE TREATMENT

In this chapter the technology of laser surface treatment is discussed and the characteristics of the different treatments are discussed in more detail.

2.1 Operating procedure

The typical set-up of laser surface processing is shown in figure 2.1. In this set-up the laser beam irradiates the surface of the work piece, which is manipulated by a product manipulator. The relative velocity of the laser beam to the work piece induces a thermal cycle in the surface layer. The relative velocity can also be realized by a stationary work piece and a moving laser beam. In the mathematical description of the process (chapter 4) this latter configuration is considered. The relative velocity of the laser beam to the work piece will be referred to as the *beam velocity*.

The laser-material interaction zone is usually shrouded with an inert gas (argon or helium), to prevent oxidation of the surface at the high processing temperatures. In the case of laser alloying, dispersing and cladding, additional material is supplied to melt pool (e.g. through a pipe) to improve the surface properties. To cover larger areas, overlapping tracks are applied.

As a laser source mainly a continuous wave CO_2 laser (wavelength $\lambda = 10.6\,\mu$m) is applied, with power levels ranging from 2 kW up to 25 kW. The intensity profile, as generated by a practical laser source is a superposition of several *Transverse Electromagnetic Modes* (TEM), see appendix A.1. The raw laser beam is generally not suitable for surface treatment and some beam forming optics are applied to transform the intensity profile of the raw beam into a desired profile of appropriate dimensions.

A number of physical phenomena determines the results of laser surface treatment. Figure 2.2 shows the physical phenomena during laser surface treatment. First, the laser

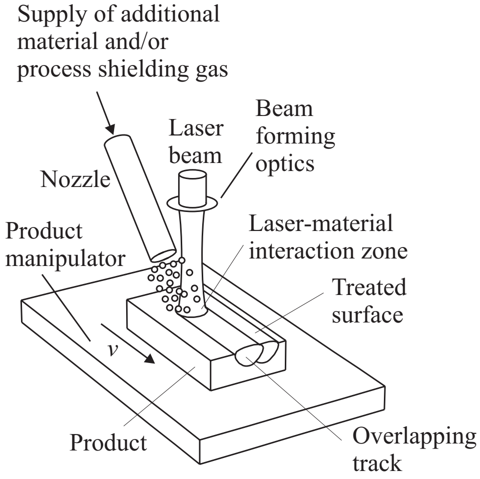

Figure 2.1: Typical set-up of a laser surface treatment system.

energy is absorbed in a thin surface layer and is subsequently transformed into heat (a). Deeper layers are heated by thermal conduction (b). At high power levels the surface is melted. Convective fluid flows may be observed in the molten pool (c). In the case of alloying, dispersing and cladding external material is supplied to the melt pool (d).

Temperature cycle

The temperature cycle of the surface layer is characterized by high heating rates, due to the localized heat input of concentrated laser radiation and the thermal conductivity of the metal. High cooling rates are achieved, due to conduction of heat from the interaction zone to the relatively cold bulk material (self-quenching). The heating and cooling rates may range from 10^2 up to $10^8\,\mathrm{K\cdot s^{-1}}$. These high values imply that the metallurgical processes take place far from the thermo-dynamic equilibrium. This in turn, results in microstructural refinement, phase transformation or formation of super-saturated solid solutions (Steen, 1994). The heating and cooling rates are much higher than the rates of conventional heat treatments, such as induction hardening and thermal spraying (Steen, 1993; Oakley, 1981). Figure 2.3(a) shows a typical thermal cycle induced during laser transformation hardening. Figure 2.3(b) shows a measured temperature cycle of the surface during alloying of titanium with nitrogen. The thermal cycle, for a given laser surface treatment, is determined by the absorbed laser power, the laser beam intensity profile, the beam velocity, the thermo-physical properties of the bulk material as well as its chemical composition. In the case of surface melting the processing results are also influenced by temperature induced melt flows and the thermo-physical and chemical properties of the added material (if any).

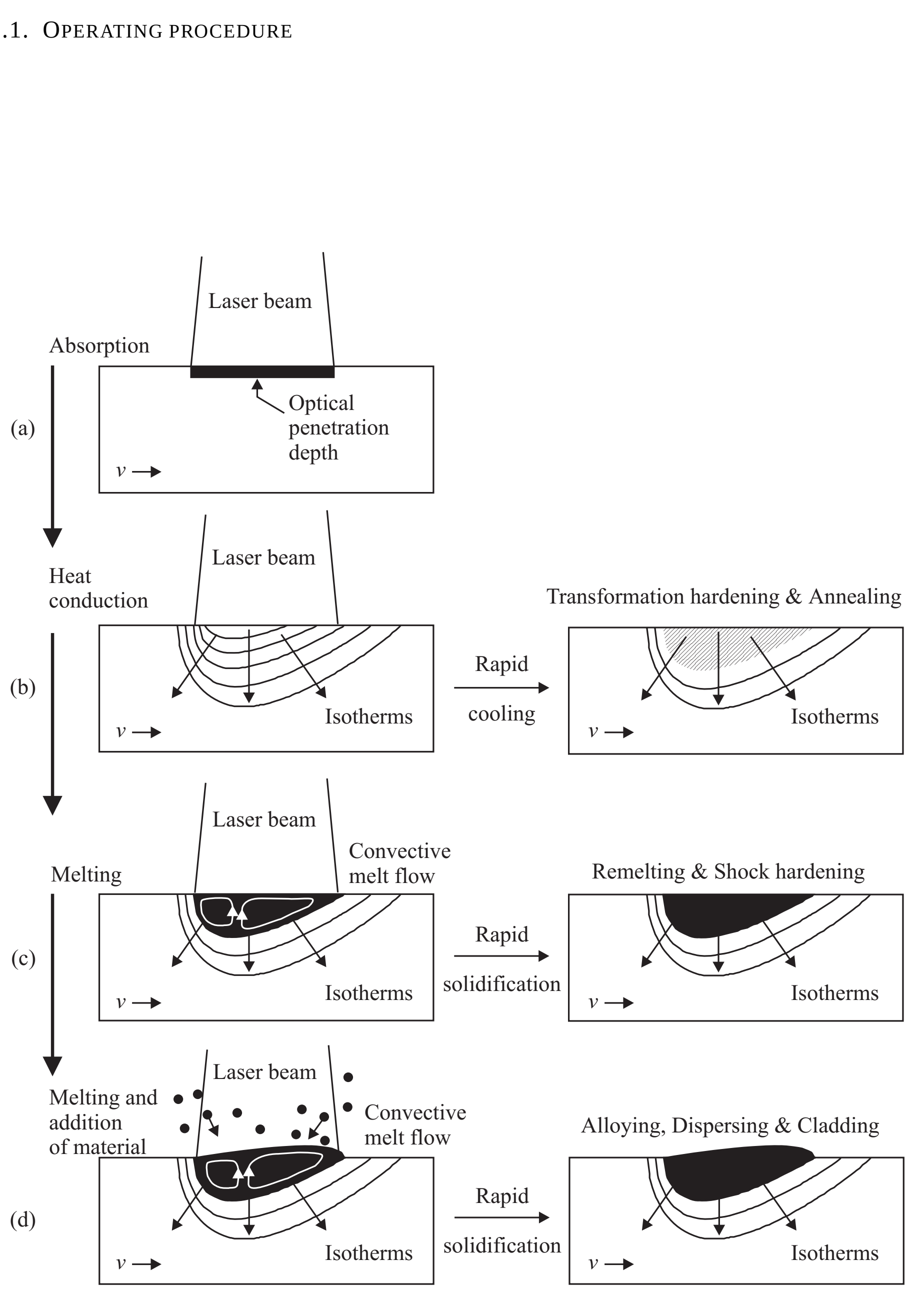

Figure 2.2: Schematic representation of physical phenomena during laser surface treatment.

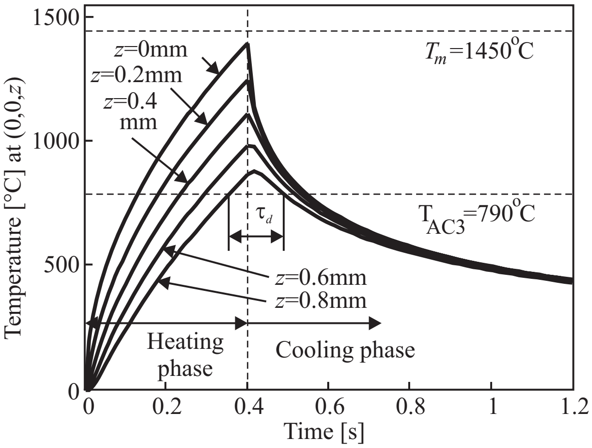

(a) Typical calculated (see chapter 4) temperature history, at several depths z, during laser transformation hardening of low carbon steel C45, absorbed laser power 300 W, beam velocity $v = 7.5\,\text{mm}\cdot\text{s}^{-1}$, beam diameter $d = 3\,\text{mm}$. Carbon diffusion time: τ_d.

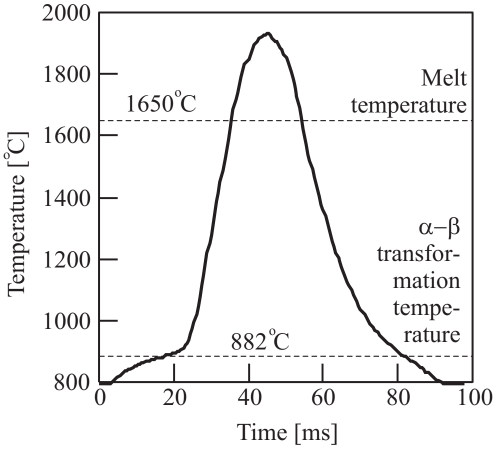

(b) Measured temperature history at the work piece surface during laser alloying of titanium with nitrogen. Laser power 1000 W, beam diameter 1.1 mm, beam velocity $v = 50\,\text{mm}\cdot\text{s}^{-1}$. Measured with a KLEIBER 270A spectral pyrometer, rise time 0.3 ms, size measurement spot 1.1 mm.

Figure 2.3: Thermal cycles occurring during laser surface treatments

Thermal processes and thermo-chemical processes

Generally two classes of laser surface treatments are distinguished: (*i*) *thermal processes* and (*ii*) *thermo-chemical processes*, in which additional material is supplied to the laser generated melt pool (Oakley, 1981). The thermal processes involve the modification of surface properties by changing only the metallurgical structure of the surface layer induced by the thermal cycle, such as transformation hardening, annealing, remelting, glazing and shock hardening (figure 2.2(b) and 2.2(c)). The class of thermo-chemical processes includes all processes which change not only the metallurgical structure, but also its composition by the addition or redistribution of new materials in the laser-generated melt pool, such as alloying, dispersing. The fusion of a material on top of the surface is referred to as cladding (figure 2.2(d)). This wide range of processes can be performed using essentially the same equipment (Steen, 1988).

Methods to add additional material to the melt pool

Two methods, to add the additional material to the melt pool, are distinguished:

(*i*) the additional material is pre-placed as a coating prior to laser processing, and is melted with the base material by the laser beam in a second stage. This method is referred to as the *two-stage method*, see figure 2.4(a). Pre-placed coatings may be applied in the form of a powder paste, a thin foil, or by electroplating, ion implantation or by solid-state diffusion,

(*ii*) by injection of the material into the melt pool simultaneously with the displacement of the laser beam. This method is referred to as the *one-stage method*, see figure 2.4(b). The additional material may be supplied in the form of powder, wire, or as a reactive gas.

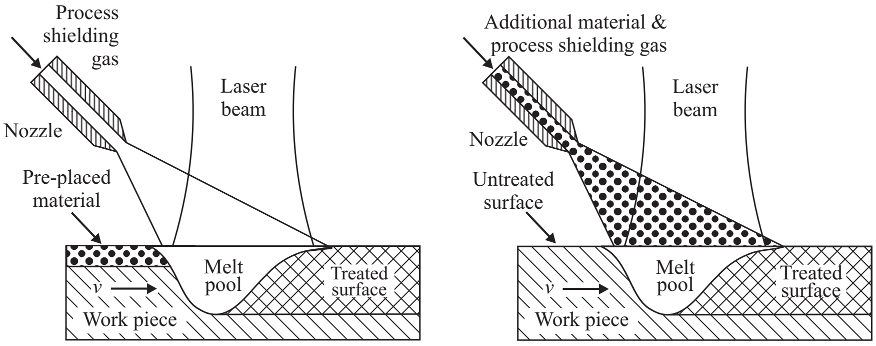

(a) Two-stage method

(b) One-stage method

Figure 2.4: Methods to supply additional material to the melt pool

Schneider (1998) showed experimentally that more uniform surface layers are obtained by applying the one-stage method.

Plasma

Vaporization of the metal surface may occur at high power densities above $10^{11}\,\mathrm{W{\cdot}m^{-2}}$. Then, the laser beam may ionize some of the metallic vapor and may create a plasma over the irradiated region. The plasma prevents the laser radiation from reaching the work piece. The plasma, in turn transfers the absorbed energy to the work piece. The plasma dynamics are unstable and may cause a high surface roughness as well as porosities in the surface layer. Therefore, plasma should be avoided. This is achieved by applying a laser power which is less than the threshold of plasma formation. Moreover, plasma may be suppressed and blown away by an inert gas flow over the laser-material interaction zone. The characteristics of plasma during laser material processing is discussed in more detail by Beyer (1985).

2.2 Characteristics of laser treatment processes

In the following, the characteristics of laser surface treatments are discussed in more detail.

Transformation hardening

In laser transformation hardening, hard martensitic surface layers are produced, which show improved corrosion resistance, fatigue strength and a low friction coefficient, compared to the initial microstructure of the steel (Steen, 1994; Bergman and Geissler, 1990; Kuilboer *et al.*, 1994). It is applied to steels with 0.5 to 1.5 wt% carbon (Van Sprang, 1992). In transformation hardening the work piece is heated above the austenite transformation temperature T_{AC3} [°C], where the initial microstructures of the steel transform into austenite, see figure 2.3(a). To obtain homogeneous austenite the T_{AC3} temperature has to be maintained for a period exceeding the minimum carbon diffusion time τ_d (Willerscheid, 1990). After the heating phase, the austenite transforms into hard martensite, due to the high cooling rates caused by self-quenching. Typical hardened depths are of the order of 1 mm.

Annealing

The aim of annealing is to repair (re-crystallization) or to increase the homogeneity of a metallurgical structure by slowly heating and cooling of the surface layer (Meijer, 1988; Steen, 1994). As opposed to other laser surface treatments, annealing relies on the thermodynamic equilibrium to be reached.

Remelting and glazing

The aim of laser remelting is the transformation of a surface layer into a fine and homogeneous structure, which is formed when the melt cools quickly (Steen, 1994). As a result, over-saturated solutions, metastable phases and fine crystalline structures can be formed, which may show greater hardness and improved corrosion resistance compared to the initial structure (Draper and Ewing, 1984; Yilbaş, 1997; Bergmann *et al.*, 1988).

The improvement may also be based on solution or evaporation of contaminates such as non-metallic enclosures (oxides, nitrides, sulfides or phosphates). Laser remelting is mainly applied to improve the surface properties of cast iron (Lepski *et al.*, 1999).

At extremely high cooling rates (typically over $10^5\,\mathrm{K\cdot s^{-1}}$), diffusion processes or nucleus initiation are impeded. As a result, amorphous glass-like structures (metallic glasses) are formed. This process is referred to as *glazing* (Oakley, 1981).

Shock hardening

Laser shock hardening results in residual compressive stresses, which are introduced by shock waves (Meijer *et al.*, 1987; Steen, 1994). By irradiation with short laser pulses (1 to 50 ns) at high energy densities (typically over $10^{13}\,\mathrm{W\cdot m^{-2}}$) surface atoms are being explosively evaporated, with hardly any surface melting. The rapidly expanding vapor exerts a pressure (typically 10^{10} Pa) on the surface of the work piece, which then propagates through the bulk material as a stress wave. As a result compressive stresses are introduced, which improve the wear resistance of the surface.

Alloying

During laser alloying, additional material is melted together with the base material to obtain a desired composition (Draper and Poate, 1985; Draper and Ewing, 1984; Van der Staay, 1994). Due to thermally induced fluid flows, the additional material is distributed homogeneously in the melt pool. This homogeneous distribution results in a uniform hardness with depth. After solidification a fine grained structure in the surface layer is obtained in which the base material content predominates (figure 2.5(a)).

Typical materials used for alloying low carbon and low alloy steels are Ni, Cr, W, B, C, WC, Cr_3C_2, Mo, VC, Mn and TiC (Klocke *et al.*, 1996; Chande and Mazumder, 1983a; Chande and Mazumder, 1983b; Vasilev *et al.*, 1990; Holleck, 1986; Tomie *et al.*, 1991; Abboud *et al.*, 1994). Materials used for alloying of aluminum and aluminum-alloys are B, Ni, Fe, Mn, Cr, Ti, Co, V, Mo, Ta, Cu, Zr, SiC, B_4C and Si_3N_4 (Smurov and Ignatiev, 1994; Fischer and Lensch, 1996; Schneider, 1994; Duverneix *et al.*, 1990).

Dispersing

Laser dispersing is based on the insertion of hard particles in the melt pool, and ensuring that these particles are not dissolved or molten, but distributed homogeneously in the metal matrix (figure 2.5(b)). For this purpose hard particles with high melting points (typically over 3000 °C), such as SiC, WC, VC, TiB_2, TiO_2, $TiSi_2$, BN, B_4C, are applied to substrates with low melting points, such as aluminum and titanium (Schneider, 1994; Meyer *et al.*, 1995). The two-stage method (figure 2.4(a)) should not be applied to introduce the particles to the melt pool, because the pre-placed particles may (partly) melt due to the absorbed laser energy.

Cladding

The goal of laser cladding is the fusion of a coating of the clad material on top of the base material, with minimal dilution of the clad layer by the base material (Schneider, 1998).

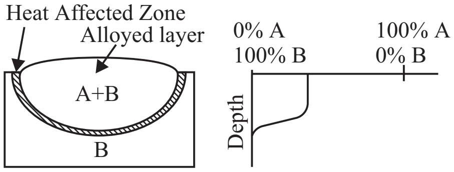

(a) Alloying: The additional material is homogeneously distributed.

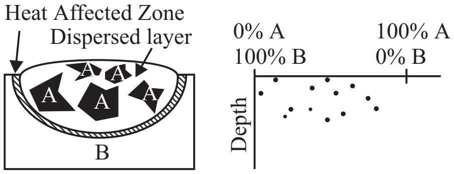

(b) Dispersing: hard particles are homogeneously scattered.

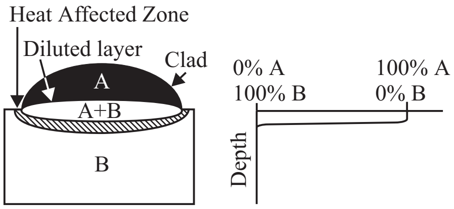

(c) Cladding: additional material on top of surface and minimal dilution with the bulk material

Figure 2.5: Cross section of surface layers generated by thermo-chemical laser surface treatment (left) and dilution of the additional material with the base material (right) A*: additional material,* B*: base material.*

Then the properties of the surface solely depend on the clad material used. A small degree of dilution in the transition zone (typically $100\,\mu$m) is unavoidable, and even beneficial as it ensures good metallurgical bonding between the clad layer and the base material (figure 2.5(c)). Supplying the additional material by means of the one-stage method to can be best applied to minimize dilution (Vetter *et al.*, 1994; Schneider, 1998). For the same reason, the materials for laser cladding should have a lower melting point than that of the base material. Suitable clad materials to be applied on steels are cobalt and nickel based alloys. Examples of clad materials for aluminium and titanium are SiC, Cr_3C_2 (Ellis *et al.*, 1994; Folkes and Shibata, 1994). Schneider (1998) presented an extensive and detailed survey on the state of the art of laser surface cladding.

Review

It can be concluded that a large variety of operating parameters and physical phenomena determines the results of laser surface treatment. Figure 2.6 summarizes these parameters grouped as *inputs*, *process*, and *outputs*. The inputs, or operating parameters are the laser beam properties, work piece properties, properties of the operating procedure (machining properties), and the supply of additional material. The outputs of the process are the geometry and the metallurgical microstructure of the produced layer, its defects (cracks, porosity, surface roughness) and its quality (residual stress, reproducibility, functional properties).

In the next chapter the process of laser surface treatment is discussed in the view of control theory.

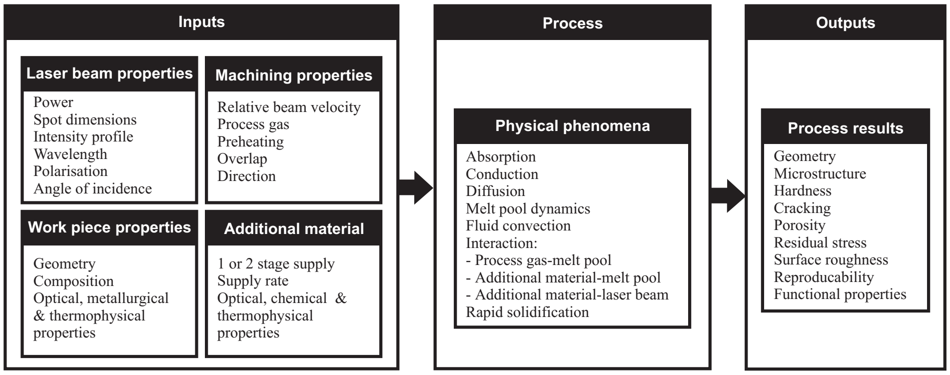

Figure 2.6: Overview of operating parameters and physical phenomena during laser surface treatment

Chapter 3

SURFACE TREATMENT IN THE VIEW OF CONTROL THEORY

This chapter discusses laser surface treatment in the view of control theory. In addition, the current status in the field of on-line control for laser surface treatment is discussed.

3.1 The objective of the control system

The objective of the control system for laser surface treatment is to obtain well defined process results, such as the surface layer thickness, despite disturbances and varying operating parameters. The process results can be any of the quantities in the ”output box” of figure 2.6 on page 15.

Unfortunately, it is often impossible to measure the processing results on-line. Moreover, these output quantities can only be measured after the laser treatment is completed, whereas the manipulation of the process output has to take place during processing at the laser-material interaction zone. Quantities, which can be readily measured on-line, are temperature related. Moreover, the processing results are known to be related to the induced temperature cycle of the surface layer. The desired temperature cycle is usually derived from metallurgical considerations and micro-structure selection maps (Gilgien and Kurz, 1994; Bamberger *et al.*, 1998). For laser surface treatments including a liquid phase, the resulting microstructure not only depends on the temperature cycle, but also depends on the shape and dimensions of the melt pool (Kurz and Trivedi, 1988; Gilgien and Kurz, 1994), see also section 4.1. Hence, the objective of the control system can be reformulated as ensuring that all locations in the surface layer of the work piece undergo a predefined temperature cycle.

The temperature cycle is defined in a coordinate system fixed to the work piece, whereas process sensing and actuation takes place at the laser-material interaction zone. Hence, the requirements on the temperature cycle have to be translated to a coordinate system fixed to the laser beam. When it is assumed that the beam velocity is constant, it is easy to understand that a constant processing results is obtained if the temperature distribution is constant. Hence, the objective of the control system for laser surface treatment is to obtain a constant temperature distribution in the surface layer, despite disturbances. For surface treatments including a liquid phase, an additional requirement is to obtain constant melt pool dimensions.

Three longitudinal stages can be distinguished during a single pass of the laser beam over the surface of the work piece, see figure 3.1. In the first stage (A), the laser material interaction commences—i.e. the work piece is solid and ”cold”, it is accelerated and irradiation by the laser beam starts. In the second stage (B), a *steady-state* or *quasi-stationary* situation is established— i.e. when observed from the coordinate system fixed to the laser beam, the temperature field and the geometry of the melt pool no longer change with time, as long as the process is not perturbed by disturbances. In the final stage (C), the process terminates—i.e. the work piece is decelerated and irradiation of the laser beam stops. One objective of the control system is to reduce the duration of the first and last stage to a minimum. Another objective is to maintain the steady-state situation during the second stage, despite process disturbances. This type of control system is referred to as a *regulator system*. If, in addition to ensuring a steady-state situation, the task of the control system is to change the temperature field according to a commanded reference signal (e.g. to increase the melt pool depth over some length in the work piece), the control system is referred to as a *servo system*. In this thesis only regulator systems are considered.

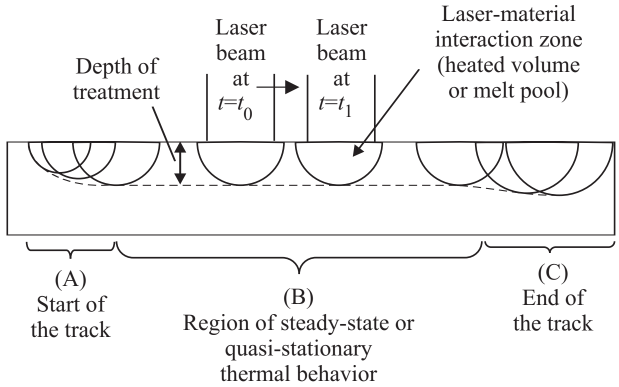

Figure 3.1: The three longitudinal stages during the processing of one track on the work piece.

3.2 The control loop

During feedback control the processing quality is measured in real-time, and subsequent intervention of the process over the operating parameters takes place, in the case process quality is (about to be) jeopardized. Figure 3.2 shows the structure of the corresponding control loop for laser surface treatment. This control loop consists of five components:

(*i*) the process to be controlled, (*ii*) a sensor, which measures the output of the process, a (*iii*) comparator, (*iv*) a controller and (*v*) an actuator. The purpose of the control system is to keep the process output $y(t)$ as close as possible to a desired constant value $r(t)$.

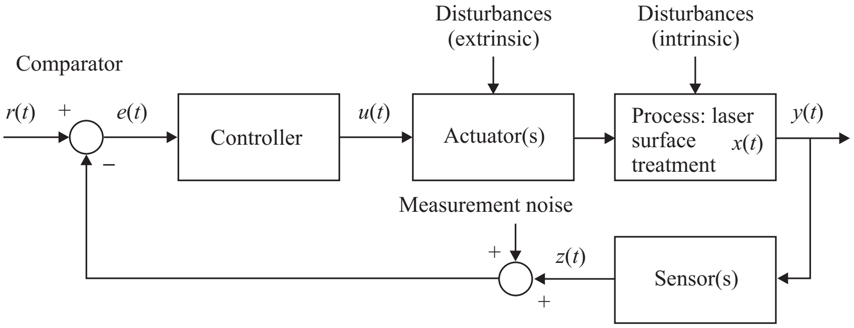

Figure 3.2: Block diagram of control loop for laser surface treatment.

To design a controller which satisfies the conditions, as described in the previous section, first the *process*, the process *state vector*, the *state equation*, *inputs* & *outputs* of the process, and *disturbances* have to be defined. The *process* under consideration is the transfer of heat in a work piece of appropriate geometry and dimensions. In the simplest case (no surface melting), the *state vector*, denoted by $\mathbf{x}(t)$, is the temperature distribution in the work piece. In the case of melting the state vector is composed of the temperature distribution and the geometry of the melt pool. The concept behind the state vector is that the dynamic state of a process is completely described by it. Knowledge of the state vector together with the inputs allows the future state of the process to be calculated. The state equation relates the state vector to the inputs $u(t)$ and outputs $y(t)$

$$\begin{aligned} \dot{\mathbf{x}} &= f(\mathbf{x},\mathbf{u}) \\ \mathbf{y} &= g(\mathbf{x},\mathbf{u}) \end{aligned} \tag{3.1}$$

where $f(\cdot)$ and $g(\cdot)$ are functions. For laser surface treatment the state vector is a set of partial differential equations, which describe the heat transport in the work piece, the internal fluid flows of the melt pool, as well as concentration of the additional material in the melt pool. These equations will be discussed in more detail in chapter 4. In chapter 5, the process dynamics will be determined experimentally.

Input commands $u(t)$ are the quantities which allow the manipulation of the state vector. All quantities listed in the ”input box” of figure 2.6 on page 15, are in principle suitable as a process input. However, input quantities, which can be commanded relatively easily with todays CNC operated laser-material-processing systems are laser power and beam velocity. Then the laser source and the work piece handling system are referred to as the corresponding *actuators*.

The output of the process $y(t)$ can be a set of quantities listed in the ”output box” of figure 2.6. As was mentioned before, it is difficult to measure the output quantities y on-line. The relevant quantities, which are measured instead, are referred to as the *observed* *outputs* and are denoted by $z(t)$. In the general case, the observed signals $z(t)$ may be any combination of elements of the state vector and input signals.

The input commands $u(t)$, the output signals $y(t)$ and the observed outputs may each be composed of more than one signal each. Therefore, laser surface treatment is a *Multiple-Input-Multiple-Output* (MIMO) process. Hence, each arrow in figure 3.2 may represent multiple signals. In the case only one input signal (e.g. laser power) and one output signal (e.g. surface layer thickness) are considered, the process is referred to as a *Single-Input-Single-Output* (SISO) process. In any case, the selected measured signals $z(t)$ and the command inputs $u(t)$ must result in a system which is *controllable* and *observable* (Åström and Wittenmark, 1997). A process is said to be controllable when it is possible to steer the process, using $u(t)$, from one arbitrary state to another. A process is said to be observable when it is possible to calculate the state vector from the observed outputs and command inputs.

3.3 Process disturbances

The process quantities, which perturb the desired temperature cycle in the work piece are called disturbances. These disturbances can be categorized as either being *extrinsic* or *intrinsic*, with respect to the work piece. Intrinsic disturbances of the temperature field arise from fluctuations of the properties of the work piece itself. Extrinsic disturbances arise from fluctuations of the properties of the devices, composing the laser surface treatment system.

3.3.1 Extrinsic disturbances

The major extrinsic disturbances are varying laser beam properties and varying beam velocity.

Varying laser beam properties

For CO_2 laser sources, fluctuation of the laser power, its intensity profile and beam diameter, at frequencies ranging from a few Hertz up to a few megaherz, have been reported (Deinzer *et al.*, 1994; Jørgensen, 1990; Li *et al.*, 1987). Figure 3.3 shows the high and low frequency fluctuations of a ROFIN SINAR 1700RF axial fast flow CO_2 laser source. When the laser is switched on, a power drift over several minutes can be observed, see figure 3.3(a). This power drift can be attributed to the increase of the gas temperature in the laser resonator with time (Deinzer *et al.*, 1994). At low temperatures the efficiency of the gaseous laser medium is high, resulting in high laser power. Within a few minutes, the temperature of the gaseous medium increases to its stationary value, resulting in a somewhat lower laser power.

Figure 3.3(b) shows the high frequency fluctuation of the laser power. High frequency fluctuations in laser power, in the range of 50 kHz up to 5 Mhz, arise from non-linear amplification of the radiation due to non-homogeneous gas distribution in the resonator, as well as the thermal instabilities of optical elements in the resonator and gas circulation system (Jørgensen, 1990).

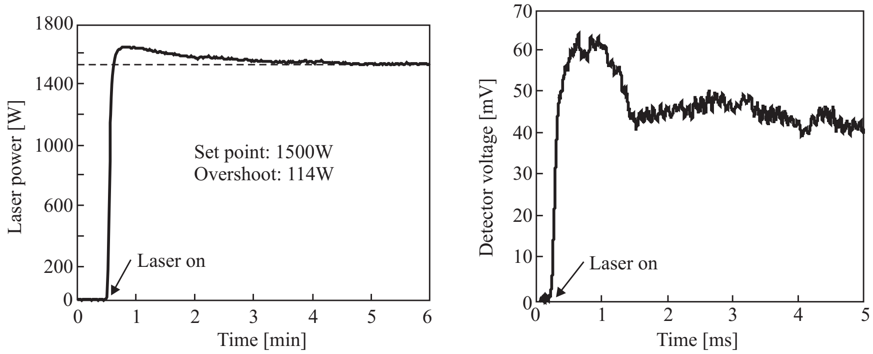

(a) Low frequency fluctuations (drift). Laser power variations as a function of time, as measured by a PROMETEC LMETER with a sample frequency of 1 Hz.

(b) High frequency fluctuations. Voltage as generated by a pyroelectric detector (bandwidth 1 to $7 \cdot 10^6$ Hz).

Figure 3.3: Fluctuation of laser output power of a axial fast flow, RF-excited, ROFIN SINAR CO_2 laser source as a function of time.

Laser radiation, which is reflected by the work piece, may reenter the laser resonator, where it disturbs the stimulated emission of radiation and therefore laser power and beam quality M^2 (appendix A.2). These disturbances are significant at frequencies over 1 kHz (Pöhler, 1998; Hoffmann and Geiger, 1995; Deinzer *et al.*, 1994; Olsen *et al.*, 1992).

In addition to the laser power also the dimensions of the laser spot at the work piece surface, may vary with time. These variations can be attributed to variations in the beam guidance system and beam shaping optics. In particular, transmissive optics (lenses) are the main cause of these variations (Biermann and Geiger, 1991; Bea *et al.*, 1990). Figure 3.4 shows the diameter $d\,[\mathrm{m}]$ as a function of time, of a laser beam, generated by the aforementioned ROFIN SINAR laser source, when focused by a zinc-selenium (ZnSe) lens. As can be observed, the beam diameter varies significantly during the first 30 to 50 seconds, after the laser beam has been switched on. This time interval is of the same order as the duration of a typical processing cycle and can therefore not be neglected. The variation of the beam diameter is caused by non-uniform heating of the lens. Because the lens is cooled at its rim, the absorbed laser energy (typically up to 0.5%, (Bea *et al.*, 1990)) causes a radial temperature gradient in the lens. As the refractive index of the lens material depends on temperature, a radial gradient of the refractive index is introduced. As a result of this gradient, the propagation of the beam through the lens varies, resulting in a decrease of the focal length of the lens (Beckmann and Ehrlichmann, 1995; Penz *et al.*, 1994). This effect is referred to as *thermal lensing* (Tangelder *et al.*, 1992).

Besides the dimensions of the laser spot, also the intensity profile may vary with time and laser power (figure 3.4). A varying intensity profile strongly influences the thermal cycle of the surface layer. Therefore, *integrating optics*, which transform an arbitrary intensity profile to a desired profile, are frequently applied to reduce the effect of a varying

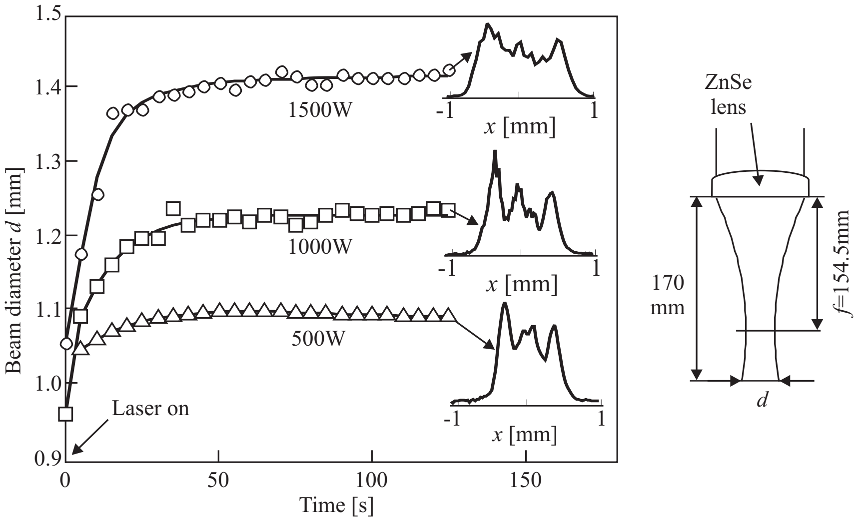

Figure 3.4: Laser beam intensity profile at 500, 1000 and $1500\,W$ *and beam diameter as a function of time at a distance of* $170\,mm$ *to a ZnSe lens with focal length* $154.5\,mm\,(6")$. *Laser source:* ROFIN SINAR *1700RF.*

intensity profile.

Varying beam velocity

When applying constant laser power, reduced beam velocity will in increase the temperature of the work piece, and vice versa. As a result, the temperature cycle of the surface layer changes. Significant variations of the velocity occur when a product manipulator with finite acceleration is tracking an complex geometry (Meijer and Bakker, 1997). E.g. when an XY-table is tracking a complex trajectory, including a sharp angle, the product velocity changes over the sharp angle, due to the finite deceleration and acceleration of the X and Y axis.

Fluctuations of other subsystems

Fluctuations of the properties of other subsystems, such as the device supplying additional material and the device supplying process shielding gas, may also perturb the desired temperature field. E.g. increased feed rate of additional material during laser cladding reduces the temperature of the work piece, due to the energy absorbed by the injected powder (Bloehs *et al.*, 1996b).

3.3.2 Intrinsic disturbances

The major intrinsic disturbances are varying absorptivity and a complex work piece geometry.

Varying absorptivity

The absorptivity of metals, irradiated by a CO_2 laser, is small (typically 10%) and may vary considerably during processing. Variations up to 100% have been reported (Stern, 1990).

Quantitatively, the absorptivity $A \in [0, 1]$ is the ratio of the energy P_A [W] absorbed by the material and the incident laser energy P_L [W]

$$A = \frac{P_A}{P_L} \tag{3.2}$$

Similarly, the *reflectivity*, which is denoted by $R \in [0, 1]$, and the *transmittance*, which is denoted by $T \in [0, 1]$, of the material are defined as

$$R = \frac{P_R}{P_L} \text{ and } T = \frac{P_T}{P_L} \tag{3.3}$$

where P_R [W] denotes the reflected laser energy and P_T [W] the transmitted laser energy. As $P_L = P_A + P_R + P_T$, it follows from equation (3.2) and (3.3),

$$A + R + T = 1 \tag{3.4}$$

In metals the transmission is virtually zero, so equation (3.4) reduces to

$$A = 1 - R \tag{3.5}$$

In principle the absorptivity A can be calculated from the optical properties of the material at the wavelength of the laser radiation (Charschan, 1972). However, the absorptivity* may vary during processing for a number of reasons:

- The optical properties of the material depend on temperature. As the temperature varies significantly during processing, also the absorptivity varies with temperature, see e.g. figure 3.5,
- Unless the laser beam impinges perpendicularly on the work piece surface, the absorptivity differs for parallel and perpendicular polarized laser radiation. For metals irradiated by a CO_2-laser, the absorptivity of parallel polarized radiation increases gradually with the angle of incidence* Θ [rad] to a maximum, after which it decreases rapidly. The angle at which maximum absorptivity occurs is referred to as the *Brewster angle*. For perpendicularly polarized radiation the absorptivity decreases with increasing Θ.
- The absorptivity depends on the surface morphology (roughness) of the work piece. Stern (1990) as well as Scheller (1995) showed that with increasing surface roughness the absorptivity increases,
- In the case of a phase change (solid-liquid) the absorptivity changes (Zwikker, 1968; Dekumbis and Frenk, 1988; Hüttner, 1996),

---

[*] Theoretically, the term absorptivity is defined for optically smooth and clean surfaces. When, in addition to the optical properties, other mechanisms (e.g. the surface morphology) contribute to the absorption of laser radiation, it is appropriate to use the term *coupling rate* or *coupling* instead (Bloehs *et al.*, 1996b). However, in this thesis absorptivity and coupling (rate) are considered as equivalent terms.

[*] The angle of incidence is defined relative to the normal on the surface.

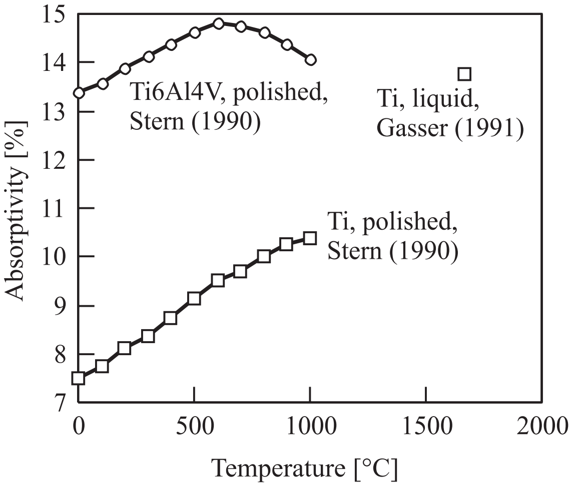

Figure 3.5: Absorptivity of titanium (squares) and its alloy Ti6Al4V (circles) at $\lambda = 10.6\,\mu m$*, as a function of temperature at perpendicular incidence (Stern, 1990; Gasser, 1991).*

- The chemical composition of the surface may alter during processing, and in turn also the optical properties of the work piece vary. E.g. the formation of oxides on the surface affect the absorptivity. In the case additional material is supplied to the melt pool, the absorptivity is affected by the optical properties of the supplied material and its (possible) reaction product with the base material (Dausinger *et al.*, 1990). E.g. Schneider (1998) measured an increase in absorptivity from a few percent to 40%, during laser cladding of steel with a cobalt based powder.
- When the additional material is supplied by means of the one-stage method, it may absorb, scatter and transmit laser radiation while traveling through the laser beam. This affects the absorption of laser radiation by the work piece (Gasser, 1991; Kaplan *et al.*, 1997; Schneider, 1998).

The influence of these effects on the absorptivity are hard to predict prior to processing. To reduce the influence of absorptivity variations, usually methods are applied to increase the absorptivity of the work piece significantly. E.g. in the case of transformation hardening, the work piece is usually coated with a thin ($50\,\mu$m) graphite or MoS_2 layer (Geissler and Bergmann, 1990; Drenker *et al.*, 1991). In the case of surface melting, these coatings can not always be applied, as undesirable as mixing with the base material may occur. Therefore, the work piece is usually roughend (e.g. by sandblasting) to increase absorptivity. The application of the Brewster angle to increase absorptivity is may introduce alignment problems, because for metals this angle is larger than 80°. These methods to increase absorptivity either require additional processing steps (coating, sandblasting), reduce the aesthetic quality of the surface (sandblasting) or are impractical (Brewster angle).

Therefore, in this thesis the absorptivity is assumed to be constant and absorptivity variations are considered as process disturbances.

Complex work piece geometry

When a work piece with small dimensions is processed, the number of dimensions in which the heat can be transported into the bulk material, is reduced. As a result the desired temperature cycle in the work piece is perturbed. This not only results in an overall increase of the work piece temperature, but also in a change of the temperature gradients. These perturbations are significant in the case the dimensions of the work piece are of the same order as the heat penetration depth. The heat penetration depth is defined as the depth at which the temperature is decreased by a factor *e* compared to the temperature at the surface, see equation (4.4).

Figure 3.6 shows the calculated temperature field in a semi-infinite work piece and in a plate (thickness 0.4 mm), when processed with constant laser power and constant beam velocity. For the operating parameters and material properties considered in these calculations, the heat penetration depth is of the same order as the thickness of the plate. As can be observed from this figure the temperature distribution in the semi-infinite work piece and in the plate differ considerably. The increased temperature may even destroy the work piece due to melting of the work piece boundaries, see e.g. figure 3.7.

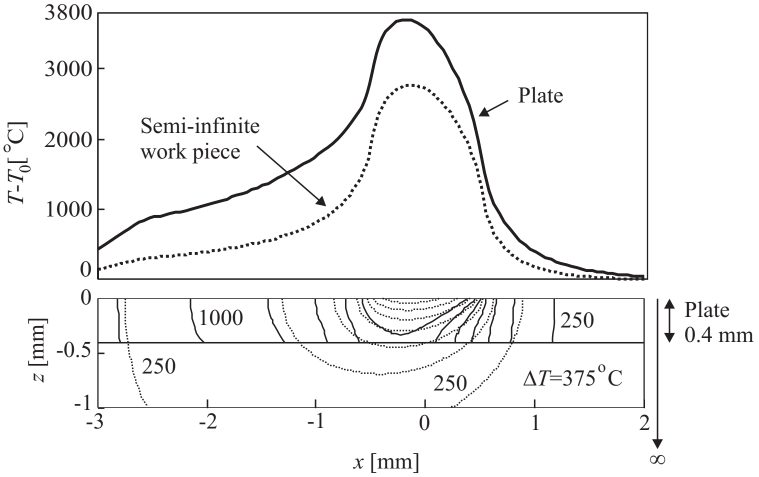

Figure 3.6: Longitudinal-section of the calculated surface temperature distribution $T - T_0$ at the surface (top graph) of Ti6Al4V and the corresponding isotherms (bottom graph) in semi-infinite work piece (dotted) and a plate (solid curve). Beam diameter $d = 1\,mm$, beam velocity $v = 5\,mm{\cdot}s^{-1}$, intensity profile Top Hat with absorbed power $AP_L = 35\,W$.

Because the effects of the geometrically small dimensions on the temperature distribution are measurable (see chapter 5), the geometry of the work piece is not taken into account in this thesis. The work piece is assumed to be of semi-infinite dimensions, and the perturbations of the temperature distribution, due to small dimensions of the work piece, are considered as process disturbances.

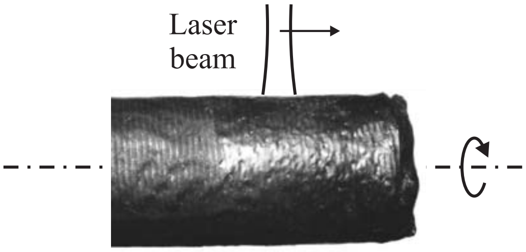

Figure 3.7: An rod which was cladded by moving the laser beam in a helix over the surface towards the end of the rod. Due to the accumulated heat at the end of the rod the temperature increased to an unacceptable level. This resulted in excessive melting of the end of the rod.

3.4 Supervisory control

A typical laser surface treatment system consist of several subsystems (or devices), see figure 3.8. The total set of adjustable parameters of these subsystems form the *operating parameters* of the laser surface treatment.

Each subsystem must operate steadily to obtain constant processing results when applying constant operating parameters. Because a subsystem may be perturbed by disturbances (extrinsic disturbances), this may require real-time feedback control of the subsystem, see figure 3.8. E.g. laser sources are equipped with a feedback controller, which regulates the laser power (Tönshoff and Overmeyer, 1995).

The subsystems are coupled. For example, when the laser power increases, not only the temperature of the work piece will increase, but it may also affect the performance of the beam guidance system, the beam shaping optics, as well as the temperature of additional material traveling through the laser beam. Therefore, Li *et al.* (1987) as well as Parthasarathia *et al.* (1991) suggested *supervisory control* to supervise all control loops of the subsystems (figure 3.8). In this hierarchy, the supervisory controller monitors the performance (status) of all subsystems. It diagnoses the possible causes for processing faults, and may then start a correction procedure by adjusting the settings of one or more subsystems. The diagnostics may be supported by a database or an expert system and the operator.

However, it should be noted that every extrinsic disturbance (device instability), which results in a reduced processing quality, will be detected by the sensors monitoring the laser-material interaction zone (Griebsch *et al.*, 1996). Then, the process controller (bold in figure 3.8) can counteract this deviation by proper steering of the chosen actuator. For example, if the laser source is chosen as the actuator, the laser power can be increased to compensate for reduced power density introduced by thermal lensing. In this approach, the control loop (enclosed by the dashed box in figure 3.8), consisting of the laser-material interaction process and the corresponding controller, suffices to control the laser surface treatment. Hence, the implementation of multiple control loops and a supervisory controller may not be necessary after all. Therefore, only the single control loop (enclosed by the dashed box in figure 3.8) is discussed in this thesis.

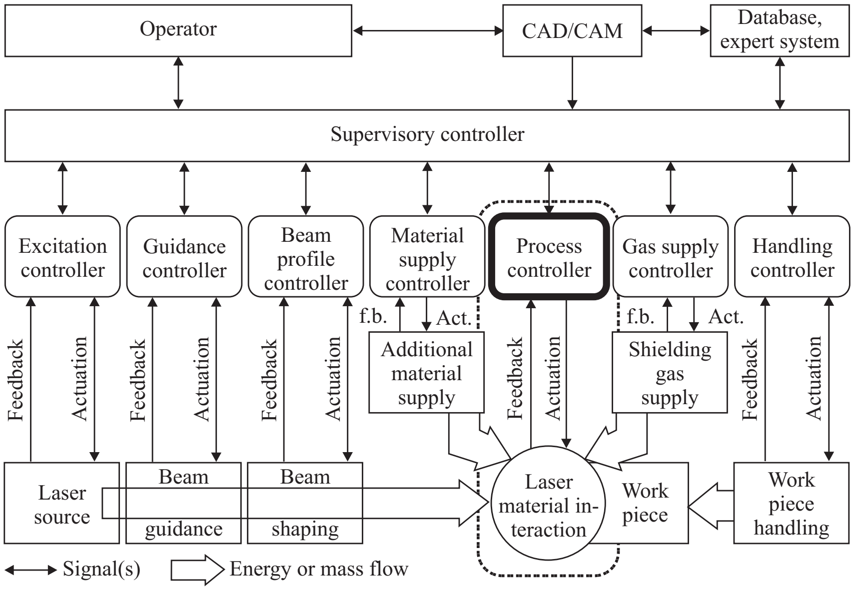

Figure 3.8: Supervisory control of laser surface treatment. The hierarchy of distributed control and centralized supervision stabilizes the output of each subsystem separately and compensates for the coupling between the subsystems.

3.5 Current status of controlled laser treatment

This section presents an overview of the current status of controlled laser surface treatment by discussing the elements of the control loop (figure 3.2). Also aspects of the control of laser cutting and welding are discussed, in the case these aspects may be relevant for the control of laser surface treatment.

3.5.1 Sensors

Process automation by closed loop control necessarily starts by a sensor detecting an output signal which is known to be related to the processing quality. A sensor for laser surface treatment has to meet the following requirements:

- The sensor should be non-destructive— i.e. the sensor should not negatively influence the processing result,
- The sensor reaction has to be faster than the speed of variation of the process,
- The sensor should be configured such that the laser beam path is not obstructed and an unrestricted accessibility for the observation of the laser-material interaction zone is guaranteed, even if clamping devices or the contours of the work piece may cause problems (Beyer, 1995; Beyer and Abels, 1992),
- The sensor must be able to withstand the high temperatures and contamination from the laser-material interaction zone (Beyer, 1995).

Sensors applied for laser surface treatment generally fall into two classes, see figure 3.9:

(*i*) Sensors measuring a signal, which is spontaneously emitted from the laser-material interaction zone, see figure 3.9(a). Various physical phenomena occur during processing, which are potential sources of diagnostic signals. These phenomena include thermal, electro-magnetical, optical, mechanical and acoustic events,

(*ii*) Sensors measuring the response of the laser-material interaction zone to an external stimulus generated by a transmitter, see figure 3.9(b).

In the following, frequently applied sensors for laser material processing are discussed, grouped by the physical domain of the detected signal.

Optical sensors

The most applied sensors for laser surface treatment operate in the optical domain. For example, such sensors are used to measure the radiance of the plasma, the thermal radiation of the melt pool and the reflectivity of the surface.

Two configurations of optical sensors can be distinguished (figure 3.10), based on the alignment of the optical axis of the laser beam to the optical axis of detection: *off-axis* detection and *collinear* detection.

Optical detectors in the off-axis configuration (figure 3.10(a)) are aligned under arbitrary inclination θ, on a cone around the laser beam (Bieler *et al.*, 1988). A detector equipped with an optical fiber may be used to reduce the angle θ, because of the small dimensions of an optical fiber. Then the fiber transports the optical signal from the laser-material interaction zone to a distant detector (Backes *et al.*, 1994; Seidel *et al.*, 1994; Hoffmann *et al.*, 1996). The implementation of the off-axis alignment of the detector is simple, but its optical arrangement varies relative to the interaction zone if the direction of processing changes.

The configuration in which the laser beam axis coincides with the axis of detection (figure 3.10(b)) is referred to as *collinear optical detection* (Beyer and Abels, 1992). In this configuration the optics, which are used to focus the laser beam, are used in the reverse direction to capture the radiation from the interaction zone. This allows to ”look into” the material-interaction zone, e.g. the key hole during welding, without blocking the laser beam by external diagnostic devices. When reflective optics are used, the point of the optimum focus of detection coincides with the focus of the laser beam. When transmissive optics are applied the focus of the laser beam may differ from the focus of detection, due to the wavelength dependence of the transmittive optics.

To selectively guide the laser radiation and radiation originating from the process, a *scraper* mirror, a *grating* mirror, a *dichroic* mirror, or a *pinhole* mirror can be applied (figure 3.10(b)).

A scraper mirror is a mirror with a central hole, through which the laser beam passes unrestrictly, whereas the mirror reflects radiation from the interaction zone onto the optical detector (Beyer, 1995; Seidel *et al.*, 1994).

A grating mirror is covered with grooves (e.g. $0.3\,\mu$m deep, repeated every μm), but is optically flat for laser radiation. The laser beam is reflected towards the work piece, whereas visible light originating from the work piece, is diffracted onto an optical detector (Beyer and Abels, 1992).

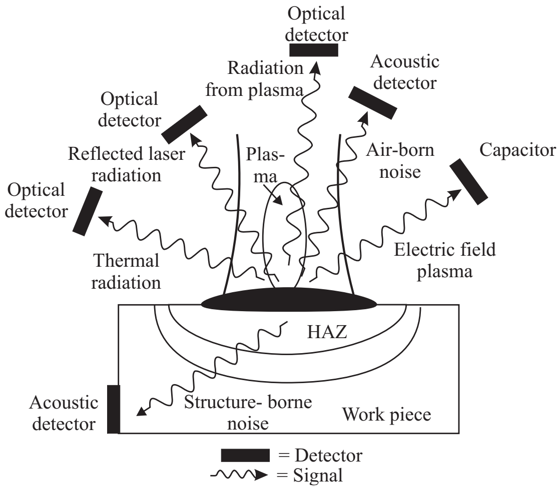

(a) Sensors measuring a signal, which is spontaneously emitted from the laser-material interaction zone.

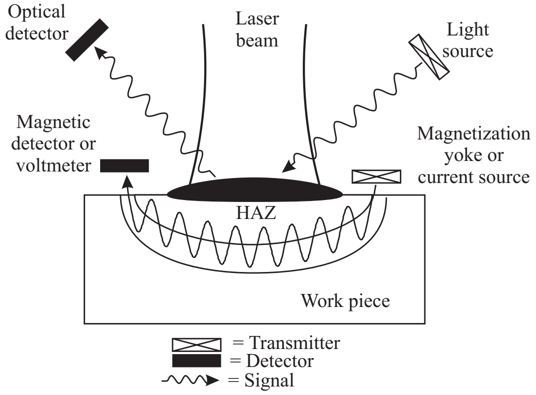

(b) Sensors measuring the response of the laser-material interaction zone to some probing signal generated by a transmitter.

Figure 3.9: Overview of possible sensors for on-line control of laser surface treatment.

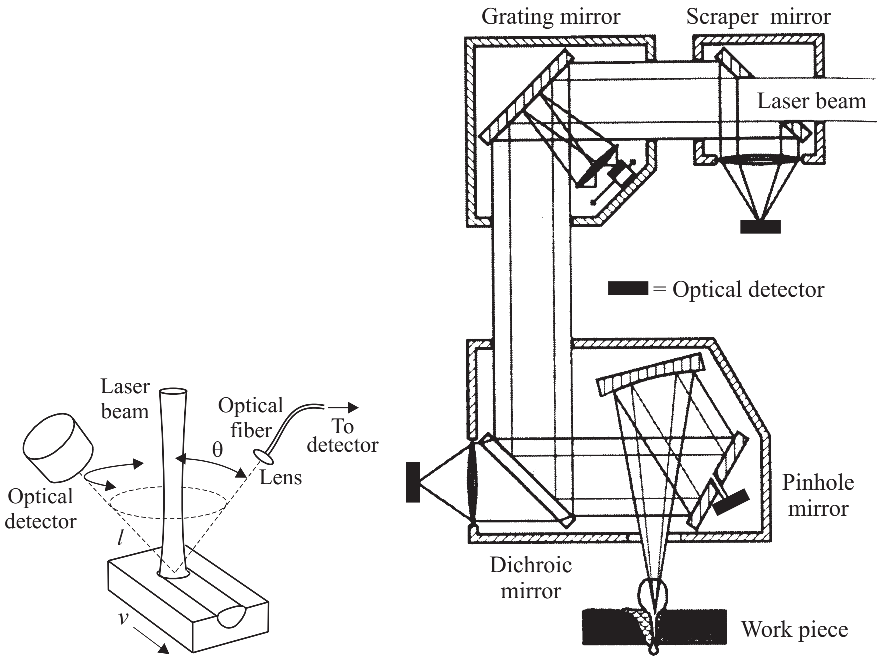

(a) Off-axis detection: the optical detector is positioned on a cone around the laser beam. The axis of laser beam axis and the axis of detection do not coincide.

(b) Collinear optical detection in which the laser beam axis and the axis of optical detection coincide (Beyer and Abels, 1992).

Figure 3.10: Configurations of optical detectors.

A dichroic mirror reflects the laser radiation, but is transparent for radiation with wavelengths in the visible range (Griebsch *et al.*, 1996; Olsen *et al.*, 1992; Jørgensen, 1990; Funk and Müller, 1990).

A pinhole mirror is equipped with a hole, which is small (1 to 2 mm) compared to the diameter of the (unfocussed) laser beam (Müller *et al.*, 1996; Chen *et al.*, 1991; Steen, 1992). Radiation originating from the laser-material interaction zone passes through the hole onto the optical detector.

Thermal radiation

A body above absolute zero temperature is continuously emitting electromagnetic radiation (thermal radiation). The spectrum and intensity (radiance) of this radiation depends on temperature. Hence, the radiation emitted by the laser-material zone can be used as a measure for its temperature.

The spectral radiance of a blackbody $N_\lambda^b\,[\mathrm{W \cdot m^{-2} \cdot sr^{-1} \cdot m^{-1}}]$ at temperature T per unit solid angle and per unit area is described by Planck's law (Smith, 1990)

$$N_\lambda^b = \frac{2hc^2}{\lambda^5}\left(e^{hc/k\lambda T} - 1\right)^{-1} \tag{3.6}$$

where $h\,[\mathrm{W\cdot s^2}]$ denotes Planck's constant, $c\,[\mathrm{m}]$ the speed of light, $k\,[\mathrm{W\cdot s\cdot K^{-1}}]$ Boltzmann's constant, and $\lambda\,[\mathrm{m}]$ the wavelength of the emitted radiation. Figure 3.11(a) shows N_λ^b as a function of wavelength and temperature. The spectral radiance increases with increasing temperature. The wavelength $\lambda_m\,[\mathrm{m}]$, at which the maximum spectral radiance occurs, shifts towards shorter wavelengths with increasing temperature. This is described by Wien's displacement law (Smith, 1990),

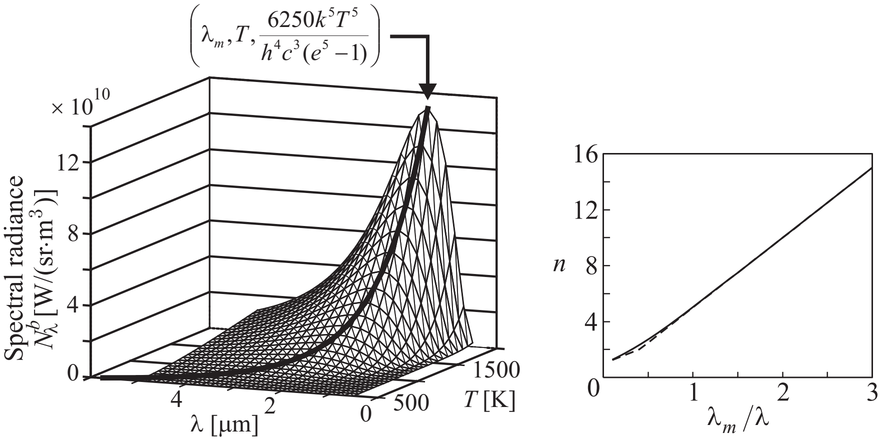

(a) Spectral radiance N_λ^b of a blackbody as a function of temperature and wavelength, and the curve of maximum radiance (bold).

(b) Sensitivity n (3.8) and its approximation (dashed).

Figure 3.11: Spectral radiance and its sensitivity to a temperature change.

$$\lambda_m = \frac{hc}{5kT} \approx \frac{2.867\cdot 10^{-3}}{T} \tag{3.7}$$

For example, laser heated metals reach temperatures of the order of 2500 K. Hence, the maximum radiance is at $\lambda_m \approx 1\mu$m, which is in the near infrared (NIR) range.

The sensitivity $n\,[-]$ of the radiance to temperature variations is high and varies with wavelength. This sensitivity n equals

$$n = \frac{dN_\lambda^b}{N_\lambda^b}\Bigg/\frac{dT}{T} = \frac{hc}{\lambda kT}e^{hc/k\lambda T}\left(e^{hc/k\lambda T}-1\right)^{-1} \approx \begin{cases} 5\frac{\lambda_m}{\lambda} & \text{for } \frac{\lambda_m}{\lambda} \geq \frac{2}{5} \\ 1+\frac{5\lambda_m}{2\lambda} & \text{for } \frac{\lambda_m}{\lambda} < \frac{2}{5} \end{cases} \tag{3.8}$$

where the approximation was suggested by Dreyfus (1963). Then, the spectral radiance (3.6) can be approximated by

$$N_\lambda^b \approx CT^n \tag{3.9}$$

where C is a constant. The sensitivity n increases with increasing ratio λ_m/λ (figure 3.11(b)). Hence, a highly sensitive temperature sensor is obtained by selecting an optical detector, which spectral sensitivity $D_\lambda(\lambda)$ includes wavelengths smaller than λ_m (Kanstad and Nordal, 1986). Usually Si photodiodes ($0.4-1.8\mu$m) are applied as detectors. The detectors may be equipped with optical filters, which cut off the longer wavelengths, to increase their temperature sensitivity, at the expense of signal loss.

The spectral radiance N_λ of a real body— i.e. a non black body, can be approximated by a black body radiator of reduced emissivity

$$N_\lambda = \varepsilon N_\lambda^b \tag{3.10}$$

where $\varepsilon \in [0, 1]$ denotes the emissivity of the real body. According to Kirchhoff's law, the emissivity $\varepsilon(\lambda)$ of a body is equal to its spectral absorptivity $A(\lambda)$ (Smurov and Ignatiev, 1996). The emissivity typically depends on wavelength, temperature, etc. If the emissivity is wavelength independent, the body is referred to as a *gray body*.

Usually optics are applied to image (part of) the radiating body onto the detector. Then, the response V of the optical detector depends on the radiance, the area $S_b\,[\mathrm{m}^2]$ of the emitting body, the area of the detector $S_d\,[\mathrm{m}^2]$, the properties of the focusing optics, and their spectral transmittance $\tau_\lambda(\lambda)$, the distance $l\,[\mathrm{m}]$ of the radiating body to the detector, the angle of detection $\theta\,[\mathrm{rad}]$(figure 3.10(a)), and is proportional to (Li *et al.*, 1990b; Ueda *et al.*, 1995)

$$V \propto \int_{S_d}\int_{S_b}\int_{\lambda} \varepsilon(\lambda,T)N_\lambda^b(\lambda,T)D_\lambda(\lambda)\tau_\lambda(\lambda)\frac{\cos\theta}{l^2}\,d\lambda\, d_{S_b}\, d_{S_d} \tag{3.11}$$

For most applications this expression can be simplified significantly. First, the distance l is usually large compared to the dimensions of the radiating body and detector. Then the dependence of angle θ and the distance l on the location on both the detector and the radiating body can be neglected. Secondly, when the range of wavelengths $[\lambda_1, \lambda_2]$ for which the detector is sensitive is small, i.e. $\lambda_2 - \lambda_1 = \Delta\lambda \ll 1$, the emissivity ε, the spectral sensitivity D_λ and the transmittance τ_λ may assumed to be wavelength independent—i.e. $\varepsilon = \varepsilon_0$, $D_\lambda = D_0$ and $\tau_\lambda = \tau_0$ respectively. Hence, by defining $\lambda_d = (\lambda_1+\lambda_2)/2$, and using equation (3.9), the response of the detector V (3.11) can be approximated by

$$V \propto K_s S_b S_d \frac{\cos\theta}{l^2}\varepsilon_0 D_0 \tau_0 C \lambda_d T^n = K_s' S_b S_d T^n \tag{3.12}$$

where K_s and $K_s' = K_s \varepsilon_0 D_0 \tau_0 C \lambda_d \cos\theta/l^2$ are constants.

These detectors were successfully applied by several authors to capture the dynamics of the melt pool, during laser surface treatment, e.g. by Backes *et al.* (1994) and Li *et al.* (1990b).

Relation (3.12) will be used in chapter 5 to show that the signal variations of a spectral pyrometer (see next paragraph), during laser alloying of titanium, are mainly determined by the melt pool area, and to a lesser extend by the melt pool temperature.

Pyrometry

The temperature of the work piece can be calculated from the measured radiance. This approach is referred to as *radiation pyrometry* (Smurov and Ignatiev, 1996; Cielo *et al.*, 1992). Two frequently applied methods of pyrometry are *monochromatic pyrometry* and *ratio-pyrometry*.

A monochromatic pyrometer is a device which measures the radiation from the body at over a small range of wavelengths and calculates the actual temperature according to

$$T = \frac{hc}{\lambda k} \Big/ \ln\left[1+\varepsilon\left(e^{hc/k\lambda T_b}-1\right)\right] \approx \frac{hcT_b}{hc+k\lambda T_b\ln(\varepsilon)} \quad \text{for } \lambda T \leq \frac{hc}{5k} \tag{3.13}$$

where T_b denotes the temperature of a blackbody with the same radiance as the body under consideration. Lack of reliable emissivity data (especially for high temperatures) is the major drawback of monochromatic pyrometry. When the emissivity varies during processing, it introduces an error in the calculated temperature (3.13). However, the sensitivity of the monochromatic pyrometer to a change in temperature is much larger than to a change in emissivity. E.g. a change in emissivity from 0.3 to 0.6 (100%!) at $T_b = 2000\,\mathrm{K}$ and $\lambda = 1\,\mu\mathrm{m}$ results in an error of only 10% in the calculated temperature (3.13). This error decreases with decreasing wavelength λ. E.g. at $\lambda = 0.8\,\mu\mathrm{m}$, the error in the calculated temperature is only 8%.

Moreover, exact knowledge of the emissivity, and knowledge of the exact temperature is not necessary for feedback control. A signal, which is monotonously increasing with the actual temperature is sufficient for temperature control. The signal as described by equation (3.13) meets this requirement.

If an absolute temperature measurement is required, ratio-pyrometry can be applied. Ratio-pyrometers measure the radiance N_{λ_1} and N_{λ_2} at two distinct wavelengths λ_1 and λ_2. When applying Wien's law these radiances read

$$N_{\lambda_1} = \varepsilon_1 \frac{2hc^2}{\lambda_1^5} e^{-hc/k\lambda_1 T} \text{ and } N_{\lambda_2} = \varepsilon_2 \frac{2hc^2}{\lambda_2^5} e^{-hc/k\lambda_2 T} \tag{3.14}$$

where ε_1 and ε_2 denote the emissivity at the selected wavelengths respectively. Combining both equations, and solving for T yields

$$T = \frac{hc(\lambda_2-\lambda_1)}{k\lambda_1\lambda_2} \Big/ \ln\left(\frac{\varepsilon_1}{\varepsilon_2}\frac{N_{\lambda_1}}{N_{\lambda_2}}\left(\frac{\lambda_2}{\lambda_1}\right)^5\right) \tag{3.15}$$

If the emissivities at the two wavelengths are equal (gray body), which is a reasonable assumption when λ_1 and λ_2 are close, the emissivity dependence of equation (3.15) disappears. Hence, a ratio-pyrometer is less sensitive to varying emissivity than a spectral pyrometer. Because of the ratio $N_{\lambda_1}/N_{\lambda_2}$ in the denominator (3.15) this method is referred to as *ratio-pyrometry*.

Temperature measurement by monochromatic pyrometry, for feedback control, is most frequently applied during transformation hardening to measure the (maximum) temperature of the coated (graphite, MoS_2) or uncoated work piece (Brookfield and Sharkey, 1992; Rudlaff and Dausinger, 1990; Funk and Müller, 1990; Bataille *et al.*, 1991; Bergman and Geissler, 1990). Grünenwald *et al.* (1993) applied monochromatic pyrometry during

---

Monochromatic pyrometry is also referred to as *spectral pyrometry*, *brightness pyrometry*, *single wavelength pyrometry* or *single-color pyrometry*.

Ratio-pyrometry is also referred to as *two-color pyrometry* or *quotient pyrometry*.

laser cladding. They showed that the melt pool temperature is correlated to the melt pool depth, and to the concentration of the additional material in the base material.

Pyrometers provide valuable information on the temperature cycle during laser surface treatment. Therefore, a spectral pyrometer and a ratio-pyrometer will be applied in chapter 5 to measure the temperature during laser nitriding of titanium.

Thermography

Pyrometers yield the temperature of only one point on the work piece surface. Knowledge of the entire surface temperature distribution provides valuable information on the process state. Therefore, several authors applied a thermal camera to measure the temperature distribution of the laser-material interaction zone (Backes *et al.*, 1994; Willerscheid, 1990; Bataille *et al.*, 1990; Kußmaul *et al.*, 1996; Meriaudeau and Truchetet, 1996; Renier *et al.*, 1996; Derouet, 1996; Rosenthal, 1990).

The data from a thermal camera can be evaluated in terms of the maximum temperature, the location of this peak temperature, temperature gradients, and statistics like first and second moment. In the case of surface melting, the shape and area of the melt pool can be determined. It will be shown in chapter 5 that the melt pool area is a measure for the melt pool depth. In turn, the melt pool depth determines the thickness of the resulting surface layer.

Typical frames rates of thermographic camera's for on-line process control are of the order of 50 frames per second. This is slow compared to the response time of a pyrometer. In chapter 5, the implementation of a fast (419 frames per second) thermographic camera is discussed, which will be used to monitor the melt pool, during laser alloying of titanium.

Measurement of reflected laser radiation

Varying absorptivity is a severe disturbance. Therefore, several authors applied optical detectors to measure the reflected laser power P_R during processing (Beyer, 1995; Olsen *et al.*, 1992; Jørgensen, 1990; Müller *et al.*, 1996; Griebsch *et al.*, 1995; Alavi *et al.*, 1989). Then with equations (3.3) and (3.5) the absorptivity can be calculated (Coutouly and Merlin, 1993). Usually pyroelectric detectors, equipped with band pass filters, which are transparent at the laser wavelength, are applied for this purpose.

Gasser (1991) applied a probing sensor (figure 3.9(b)), during laser surface treatments. This sensor consists of a HeNe probing laser, which irradiates the laser-material interaction zone and an optical detector. The detector is sensitive to the reflected HeNe laser radiation. From the reflected HeNe radiation, the absorptivity of CO_2 radiation was estimated. Bieler *et al.* (1988) showed, with a similar configuration, that the reflected laser power from the pilot laser is correlated to the composition of the produced surface laser during alloying of Ti with N_2.

This probing sensor suffers some practical difficulties. First, in general the reflected light not only consists of a direct component, but also of a diffuse (or scattered) component, requiring signal collection over the half space of the irradiated surface. Secondly, for metals the reflectivity is large (typically $R > 0.7$). Consequently a small relative measurement error in R results in a large relative error in $A = 1 - R$. Therefore, this method will not be applied in this thesis.

Sensor operating in the electrical domain

Rubruck *et al.* (1990) developed a method to measure the hardened depth during laser transformation hardening, by applying a DC-current through the work piece and measuring the induced voltage over the track. The method is based on the larger specific electrical resistivity of the hard martensitic layer compared to the initial microstructure. It was shown experimentally that the measured voltage varies nearly linearly with the hardened depth.

However, as this method relies on sliding electrical contacts with the sample, erroneous measurements are obtained due to surface contaminations (e.g. oxides) and thermal voltages in the electrodes, which are induced by the high processing temperatures. Moreover, the method is limited to materials, which show different electrical resistivity in the treated state in comparison to the untreated state of the material. For these reasons this sensor will not be applied in this thesis.

Electro-magnetic sensors

When the magnetic material properties of the processed surface layer differ from those of the original (untreated) surface, magnetic probing methods can be applied to measure processing results, such as dilution and hardened depth (Li, 1989; Kern and Theiner, 1986; Kern and Theiner, 1987; Kern *et al.*, 1995).

In this approach the work piece is magnetized dynamically by an electro-magnet. The magnetic field is perturbed by the conducting work piece. These perturbations are measured by a coil or a Hall sensor, which allow the determination of several magnetic properties (coercive magnetic field intensity, incremental permeability, Barkhausen noise) of the magnetic hysteresis curve. These characteristics are related to the results of the laser treatment.

A magnetic probing sensor suffers some practical difficulties, which impedes its use as an on-line sensor for feedback control:

- The magnetic sensor must be positioned at 1 to 10 cm behind the laser beam, to ensure that the temperature of the measured surface is smaller than the Curie temperature. This introduces an unacceptable delay in the control loop,
- Magnetic testing is limited to ferromagnetic materials, which show different magnetic properties in the treated state in comparison to the untreated state of the material,
- The sample frequency of the sensor (typically 1 Hz) is too low compared to the dynamics of laser surface treatment (Kern *et al.*, 1995),
- The dimensions of the electro-magnet are usually large and therefore impractical.

Therefore, electro-magnetic sensors are not considered for the use in on-line feedback control of laser surface treatment.

Acoustic sensors

Pressure waves (or shock waves) are emitted from the laser-material interaction zone, during laser processing. These waves are referred to as *acoustic emission* and can be classified as *air-borne* or *structure-borne*, based on the mechanism initiating the acoustic emission.

Air-borne acoustic signals, originate from pressure variations in the atmosphere over the laser-material interaction zone. These pressure variations may be caused by events such as the expulsion of melt drops from the melt pool and the vaporization of the metal surface (Farson *et al.*, 1996; Jon, 1985). Structure-borne acoustic signals, originate from sudden relaxation of mechanical or thermal stresses in the work piece, e.g. due to plastic deformation of the material and crack growth (Deimann *et al.*, 1988; Farson and Kern, 1995).

The acoustic signals are measured by a microphone (frequently in the form of a piezo-electric crystal). The time-domain acoustic signals are usually processed, using the *Fast Fourier Transform* (FFT) algorithm, to obtain a corresponding frequency-domain (power) signature of the signal. Then, ”good” processing results can be discriminated from ”bad” results by analyzing specific frequency ranges of the spectrum (Nava-Rüdiger and Houlot, 1997; Steen, 1992; Chang, 1995; Farson *et al.*, 1991; Grad and Monžina, 1995).

An acoustic sensor suffers some practical difficulties, which impedes its use as an on-line sensor for feedback control:

- Acoustic sensing is slow compared to optical sensing, due to the difference in speed of propagation. Moreover, the characteristics of the signals generated by the acoustic and optical sensors are comparable for a given quantity of the laser treatment (Biermann and Geiger, 1991),
- The speed of propagation of acoustic waves in the work piece strongly depend on temperature. Therefore elaborate calculations are required to predict the processing quality from acoustic signals (Müller *et al.*, 1996),
- Acoustic measurements suffer from interference of other disturbances, e.g. machine vibrations (Chang, 1995; Müller *et al.*, 1996).

For these reasons sensors operating in the acoustic domain will not be applied for controlled laser alloying of titanium.

3.5.2 Actuators

All quantities (see ”input box” of figure 2.6 on page 15), which allow the manipulation of the state vector $\mathbf{x}$, are suitable as a command signal to control the process. However, the only input commands, which can be commanded readily with todays CNC operated laser-material-processing systems, are laser power and beam velocity. For successful suppression of disturbances, the bandwidth of the chosen actuator should be large compared to the dynamics of the disturbances. The laser power can be modulated relatively fast (typically $\leq 1\,\mathrm{ms}$). Therefore, most authors referred to in the previous section apply laser power as the command signal to control the process. Beyer (1995) applied the beam velocity as a command signal. Bataille *et al.* (1990; 1991; 1992) applied laser power and the beam velocity simultaneously.

In this thesis, the laser power and the beam velocity are considered (separately as well as simultaneously) as command signals. It will be verified theoretically (chapter 4), as well as experimentally (chapter 5), which combination of command signals yields the best processing results.

3.5.3 Process models

Process models of laser surface treatment are applied for two purposes:

(*i*) To gain detailed physical insight in the process behavior. E.g. to analyze the dependency of the process outputs on the operating parameters. Or, to relate the process results to the measurable quantities,
(*ii*) For the design of model based controllers.

Table 3.1 lists a (non-comprehensive) overview of publications on process models for laser surface treatment. Tosto (1994), as well as Prokhorov *et al.* (1990) and Schuöcker and Kaplan (1994), present a more elaborate overview of the current status in theoretical modelling of laser surface treatments.

For the design of controllers, models are required, which accurately describe the *temporal* relation between the command signals $u(t)$ and the measured signals $z(t)$. For this purpose, linear time-invariant parametric models are preferred, because for this type of model extensive mathematical analysis and mathematical tools for controller design are available. The basic idea of parametric modelling is to approximate the (possibly) nonlinear dynamic behavior of a process with many variables by a simple model with a small number of time-invariant parameters. The model should be sufficiently accurate such that the negative effects of unmodelled process dynamics on the performance of the controlled process can be eliminated by the feedback controller (Bosgra and Kwakernaak, 1995).

A linear parametric model can be obtained from theoretical or experimental process analysis.

Derivation of the model from theoretical analysis

The theoretical model follows from the solution of the set of equations, which describe the physical phenomena of laser surface treatment. These equations are presented and discussed in detail in chapter 4.

The solution of the equations may be obtained by numerical methods, but for computational reasons, analytical solutions are preferred for feedback control. Moreover, analytical models provide better insight in the fundamental relations between the process inputs (laser power, beam velocity) and outputs (temperature, melt pool dimensions), than numerical models.

In spite of the large number of publications on modelling of laser surface treatment, no explicit analytical solution of the complete set of equations is available. After appropriate simplification of the problem under consideration and linearization of the equations, the analytical solution may be approximated by a linear parametric model, which then can be used for the design of a controller. Only in simple cases this approach leads to a model of sufficient accuracy (Drenker *et al.*, 1990; Drenker *et al.*, 1991).

Derivation of the model from experimental analysis

A parametric process model for the design of a controller can be obtained experimentally by analyzing the measured temporal behavior of the input and output signals. This approach is referred to as *system identification* (Ljung, 1987) or *process identification*. This

Table 3.1: Non-comprehensive overview of publications on process models for laser surface treatment.

Author(s)	Model
	No surface melting
Rosenthal (1946)	Implicit analytical transient temperature model of 3D heat flow in (in)finite work pieces induced by moving heat sources.
Cline and Anthony (1977)	Implicit analytical 3D heat flow model using Green's functions.
Pietro *et al.* (1994)	Implicit analytical transient models of laser heating of 1-, 2-, and 3-dimensional heat flow.
Prokhorov *et al.* (1990)	Several implicit and explicit temperature models.
Li *et al.* (1997)	Numerical transient temperature model of 3D heat flow using, the two-dimensional Fast Fourier Transform algorithm.
Yilbaş and Sami (1997), (1994)	Explicit analytical transient temperature model of 1D heat flow including evaporation.
Hassan *et al.* (1997), (1993)	Explicit analytical transient temperature model of 1D heat flow in infinite slab.
El-Adawi *et al.* (1994), (1996)	Explicit analytical transient temperature model of 1D heat flow in infinite slab having temperature dependent absorptivity.
Shercliff and Ashby (1991)	Explicit stationary 2D heat flow model and prediction of hardened depth.
	Including surface melting
Hoadley *et al.* (1991)	Numerical transient model of 3D heat flow (neglecting fluid flow) of melting.
Kreutz and Pirch (1990), (1992)	Numerical stationary model of 2D and 3D heat and fluid flow during melting.
Basu and Date (1990a), (1990b)	Numerical stationary and transient model of 2D heat and fluid flow during laser melting.
Basu and Date (1992a), (1992b)	Numerical stationary and transient model of 2D heat and fluid flow during rapid solidification following laser melting.
Yilbaş and Sami (1997), (1994)	Explicit analytical transient temperature model of 1D heat flow including evaporation.
	Alloying and cladding
He *et al.* (1995)	Numerical stationary model of 2D heat, fluid and mass flow during alloying.
Ollier *et al.* (1995)	Numerical stationary model of 2D heat, fluid and mass flow during cladding using the one-stage method.
Bamberger *et al.* (1998)	Explicit analytical transient model of 1D heat flow during cladding including power attenuation due to injected powder.
Picasso *et al.* (1994)	Implicit analytical stationary model of 3D heat flow during cladding including power attenuation and melt pool calculations.

method is usually applied when theoretical modelling is too complex, or does not provide a sufficiently accurate dynamic model.

Basically, process identification consists of adjusting the parameters of the model (e.g. a transfer function) such that the output of the model coincides well with the measured series of inputs and outputs. The structure of the model and the number of parameters (order) depend on the dynamics of the process and the required accuracy.

Process identification was successfully applied by Brookfield and Sharkey (1992), as well as Bataille *et al.* (1992) and Derouet (1996), to obtain accurate dynamic models of laser transformation hardening and laser alloying. These models were used in a subsequent stage for the design of a controller.

In chapter 4 process models are developed to gain physical insight in the behavior of the temperature and melt pool, and their response to the operating parameters and disturbances. These models are also used to estimate the structure and the number of parameters of a parametric model, on the basis of which an efficient controller can be designed. Process identification of these models will be applied in chapter 5 to obtain an accurate dynamic model, which relates the laser power and the beam velocity to the melt pool surface area.

3.5.4 Controllers

Proportional-Integral-Differential (PID) controllers are most frequently applied to control laser processing (Beyer, 1995; Kechemair *et al.*, 1990; Bataille *et al.*, 1990; Rudlaff and Dausinger, 1990; Backes *et al.*, 1994; Geissler and Bergmann, 1990; Deinzer *et al.*, 1994; Derouet, 1996). A PID controller is described by

$$u(t) = K_P e(t) + K_I \int_0^t e(t)dt + K_D \frac{de(t)}{dt} \tag{3.16}$$

where K_P, K_I and K_D are the proportional, integral and derivative gain respectively. Also simpler versions (P, PI and PD) are applied (Tal *et al.*, 1982; Brookfield and Sharkey, 1992).

A more sophisticated controller was tested by Bataille *et al.* (1992), who applied a multivariable *Linear Quadratic Gaussian* (LQG) controller for laser transformation hardening. LQG control is discussed in more detail in section 6.5.1.

When the process parameters vary with time, an *adaptive controller* may be required to control the process (Åström and Wittenmark, 1995). An adaptive control system is composed of two sub-control loops (figure 3.12):

(*i*) an on-line (recursive) process identification algorithm, combined with an adaptation algorithm, which adapts the controller parameters (at a low rate), and
(*ii*) a regular controller, which acts on disturbances (at a high rate).

Drenker *et al.* (1990; 1991) applied this approach, during transformation hardening, to cope with the varying process dynamics introduced by a varying coating thickness.

When the process is insufficiently understood, but general process knowledge is available, *fuzzy control* may be applied. Fuzzy control is also referred to as *Rule-based control* or *Decision-based control* and is similar to human decision-making, which is based

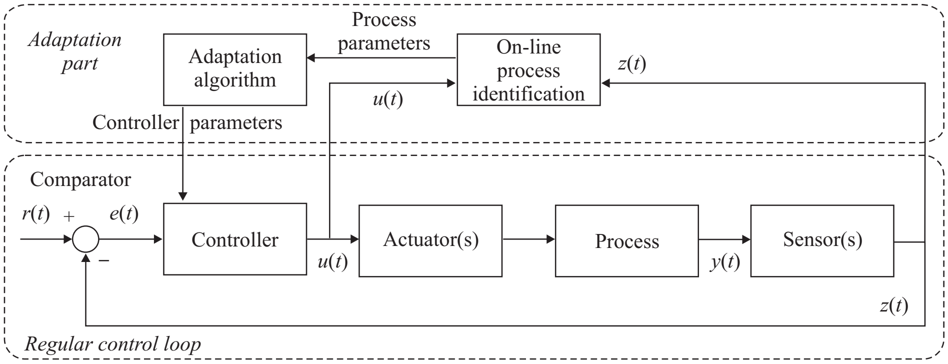

Figure 3.12: Block diagram of an adaptively controlled process.

on ”rules” rather than on algorithms. Fuzzy control was applied by Bullema (1994) and Farson *et al.* (1991) for control of laser welding. Lim and Chatwin (1994) and Kechemair *et al.* (1993) applied fuzzy control for laser cutting.

In chapter 6 several PI-controllers and a LQG controller, to control the laser alloying of titanium, will be implemented and tested.

3.6 Conclusions

The objective of the control system for laser surface treatment is to obtain well defined process results, such as the surface layer thickness, despite disturbances and varying operating parameters. It is difficult to measure these output quantities on-line. Quantities, which can be easily measured on-line, are temperature related. Hence, the objective of the control system, when defined in a coordinate system fixed to the laser beam, can be reformulated as to obtain a constant temperature distribution in the surface layer, despite disturbances. For surface treatments including a liquid phase, an additional requirement is to obtain constant melt pool dimensions. The objective of the control system for laser alloying of titanium is defined as to obtain a well defined layer thickness (which is determined by the melt pool depth during processing), despite disturbances.

Two intrinsic disturbances are the varying absorptivity and the small dimensions of the work piece. The laser power and the beam velocity are the only input quantities, which can be commanded readily with todays CNC operated laser-material-processing systems. In the following a control system is developed, which reduces the influence of the intrinsic disturbances by actuation of the laser power or beam velocity (or both).

An overview of the current status in laser surface treatment was presented. A wide variation of sensors was discussed. For the observation of the temperature field or the melt pool dimensions during laser alloying, optical sensors, which measure thermal radiation (pyrometers, thermal camera’s) can be best applied.

In the next chapter models are developed, which provide insight in the process behavior, and which provide an estimate of the structure and the number of parameters of a parametric model. On the basis of these results a controller can be designed.

Chapter 4

PHYSICAL MODELLING OF LASER SURFACE TREATMENT

In this chapter the relevant physical phenomena, which occur during laser surface treatment, are discussed in detail. It will be shown that the conservation law of energy (heat conduction equation) plays a central role in the physical modelling of the process. The models resulting from this equation are used to analyze the effects of the laser power, the beam velocity and the disturbances on the temperature distribution and the melt pool dimensions. The results from this analysis are used in subsequent chapters for process identification and controller design.

4.1 The description of phenomena

In this section, the heat conduction in the work piece, the melt pool dynamics including thermally induced fluid flows and the additional material in the melt pool are discussed.

Heat conduction

As laser surface treatment is a thermal process, the well known heat conduction equation plays a central role in the physical modelling of the process. Moreover, the quantities which can be measured readily on-line are temperature related.

The heat conduction equation follows from the energy balance of an appropriately chosen volume and consists of diffusive heat flows, convective heat flows and possible sources of heat (Carslaw and Jaeger, 1959). When, defined in a cartesian coordinate system (x, y, z), fixed to the laser beam (figure 4.1), the heat conduction equation reads

$$\rho c_p \frac{\partial T}{\partial t} - \nabla \bullet (K \nabla T) + \nabla \bullet (\mathbf{U} \rho c_p T) = Q \qquad (4.1)$$

where T [K] denotes the temperature at (x,y,z,t) relative to the ambient temperature T_0 [K], t [s] denotes time, ρ [kg$\cdot$m^{-3}] the density of the material, c_p [J$\cdot$kg$^{-1}\cdot$K^{-1}] its thermal capacity, and K [W$\cdot$m$^{-1}\cdot$K^{-1}] its thermal conductivity. In general, all material parameters depend on temperature. Q [W$\cdot$m^{-3}] represents heat sources and heat sinks in the work piece, e.g. due to latent heat of fusion and solidification in the case of a melt pool, or due to an exothermic or endothermic chemical reaction of the additional material with the base material. Finally, **U** denotes the fluid flow, with respect to the coordinate system (x,y,z) fixed to the laser beam. The temperature in equation (4.1) is defined relative to the coordinate system fixed to the laser beam, because it will be measured by sensors fixed to this coordinate system. Note that the local time derivative $\partial T/\partial t$ is calculated by varying t only and therefore refers to a fixed point in the moving coordinate system.

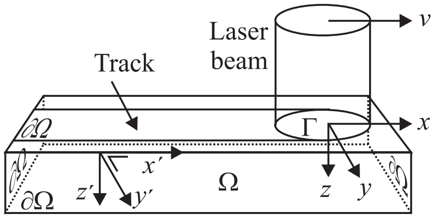

Figure 4.1: Configuration of the laser beam and the work piece. (x,y,z) *is the cartesian coordinate system fixed to the laser beam, with the origin at the surface of the work piece, the x-axis in the direction of translation and z in the direction of the laser beam (depth).* (x',y',z') *is the coordinate system fixed to the work piece.* Ω *denotes the region determined by the dimensions of the work piece, and* $\partial\Omega$ *its surfaces.* Γ *represents the surface area irradiated by the laser beam.*

The fluid velocity **U** in the (x,y,z) coordinate system, is related to the fluid velocity $\mathbf{U}'$ and the beam velocity $\mathbf{v}'$, both defined in the coordinate system (x',y',z') fixed to the work piece, as (Tosto, 1993)

$$\mathbf{U} = \mathbf{U}' - \mathbf{v}' \tag{4.2}$$

In the solid region of the work piece, there are no fluid flows, hence $\mathbf{U}' = 0$, and therefore $\mathbf{U} = -\mathbf{v}'$. Then, if the prime is omitted for convenience, the heat conduction equation in the solid regions of the work piece, simplifies to

$$\rho c_p \frac{\partial T}{\partial t} - \nabla \bullet (K \nabla T) - \nabla \bullet (\mathbf{v} \rho c_p T) = Q \tag{4.3}$$

The absorbed laser energy is described as a boundary condition for the heat conduction equation. This can be understood by comparison of the *optical penetration depth* of the laser radiation to the *heat penetration depth*. The heat penetration depth δ_h [m] is defined as the depth at which the temperature is decreased by a factor e compared to the temperature at the surface (Bass, 1987)

$$\delta_h = 2\sqrt{\frac{K t_i}{\rho c_p}} = 2\sqrt{\kappa t_i} \tag{4.4}$$

where the thermal diffusivity $\kappa = K/\rho c_p\,[\mathrm{m}^2\cdot\mathrm{s}^{-1}]$ was introduced, and where t_i [s] denotes the *interaction time* of the laser beam with a point on the surface. In the case of laser surface treatment, the interaction time is typically in the range of 10^{-2} to 10 s (Oakley, 1981). Then, the heat penetration depth for metals is in the range of 0.5 to 15 mm.

The optical penetration depth δ_o [m] of laser radiation is defined as the depth at which the intensity of the laser radiation is attenuated by a factor e^2 compared to the intensity at the surface (Bass, 1987). Over this optical penetration depth 86% of the laser energy is transformed into heat. The optical penetration depth of CO_2 laser radiation in metals ranges from 10 to 100 nm, and is thus much smaller than the heat penetration depth ($\delta_o \ll \delta_h$). Consequently, the effect of the laser beam can be modelled as a surface heat source, defined by the boundary condition

$$-K\,(\nabla T \bullet \mathbf{n})\,|_{\partial\Omega} = \begin{cases} AI(x,y,t) - h_c T - \varepsilon_t \sigma (T+T_0)^4 & \text{for} \quad \partial\Omega \in \Gamma \\ -h_c T - \varepsilon_t \sigma (T+T_0)^4 & \text{for} \quad \partial\Omega \notin \Gamma \end{cases} \tag{4.5}$$

where $\partial\Omega$ denote the surfaces of the work piece (figure 4.1), $\mathbf{n}$ their corresponding outward normals, A the absorptivity, $I(x,y,t)$ the laser beam intensity profile, and Γ the irradiated surface. The laser power P_L is related to the laser beam intensity profile as

$$P_L = \int_\Gamma I(x,y)\,d\Gamma \tag{4.6}$$

Heat losses at the surfaces $\partial\Omega$ are due to convection with the surrounding atmosphere (e.g. due to convective cooling of the process gas), and radiative emission. The convective losses with the surrounding atmosphere are characterized by the heat exchange coefficient $h_c\,[\mathrm{W}\cdot\mathrm{m}^{-2}\cdot\mathrm{K}^{-1}]$. Radiative emission is characterized by the hemispherical total emissivity $\varepsilon_t \in [0,1]$ of the material and the Stefan-Boltzmann constant $\sigma\,[\mathrm{W}\cdot\mathrm{m}^{-2}\cdot\mathrm{K}^{-4}]$. Both heat losses are small compared to the absorbed laser energy and heat losses due to conduction in the metallic work piece itself (Pietro *et al.*, 1994). For example, the cooling capacity of the shielding gas is typically in the range of 10 to 20 W (Shuja *et al.*, 1998), which is negligible compared to the absorbed laser energy. Therefore, the heat losses at the surface can be neglected, by setting $h_c = 0$ and $\varepsilon_t\sigma(T+T_0)^4 = 0$ in equation (4.5) respectively (Rosenthal, 1941).

A second boundary condition for the heat conduction equation follows from the fact that the temperature, at a distance far from the melt pool, for a finite time t is limited. Mathematically this boundary condition, for a semi-infinite work piece, reads

$$T(\infty,\infty,\infty,t) < \infty, \text{ for } t < \infty \tag{4.7}$$

The mathematical description of heat conduction is completed by the initial condition

$$T(x,y,z,0) = 0 \tag{4.8}$$

Melt pool

The molten pool, which forms on the work piece surface if the laser power density and the interaction time are sufficiently high, shows internal fluid flows. These flows are mainly initiated by surface forces resulting from the temperature dependence of the surface tension and are referred to as *thermocapillary flow* or *Marangoni flow* (Pirch *et al.*, 1990; Tosto, 1993; Peidao *et al.*, 1993).

Figure 4.2 illustrates the thermocapillary flow induced by a Gaussian temperature distribution. Due to the temperature gradient over the melt pool, and the temperature dependence of the surface tension, the surface tension $\sigma_s\,[\mathrm{N\cdot m^{-1}}]$ varies over the melt pool. These variations induce surface melt flows, which in turn induce shear forces in the fluid, propagating thereby into deeper regions of the melt pool in combination with a back flow because of mass conservation. Because for most metals the surface tension coefficient is negative, the surface tension increases from the center of the melt pool to its rim. This induces a surface melt flow from locations of high temperature in the center to lower temperatures at the rim. Gasser (1991) showed that the shear stresses imposed by the process gas (typically 0.2 to $1\,\mathrm{N\cdot m^{-2}}$) are negligible compared to surface stresses induced by the thermocapillary flow (typically 100 to $200\,\mathrm{N\cdot m^{-2}}$).

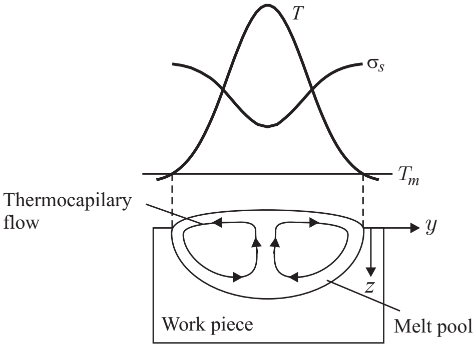

Figure 4.2: Thermocapillary flow, induced by a Gaussian temperature distribution, in a metal with a negative surface tension coefficient. $T_m\,[K]$ *denotes the melting temperature of the material.*

As can be observed from figure 4.2, a pair of counter rotating vortices is formed in the fluid. More than one pair of vortices may form depending on the dimensions of the melt pool and the material properties. These additional pairs of vortices may form and disappear periodically. This explains the periodicity found in the microstructure upon solidification of the melt pool (Basu and Date, 1990a; Jianglong, 1990; Derouet, 1996; Pirch *et al.*, 1990). The melt pool dynamics are described by the momentum conservation law for a Newtonian incompressible fluid and is referred to as the *incompressible Navier-Stokes equation* (He, 1994; Tosto, 1993). Computation of the fluid flow in the melt pool by means of this equation is very complicated due to the non-linear nature of the Navier-Stokes equation and the complex boundary conditions at the free self-adjusting surface of the melt pool, as well as at the moving solid-liquid interface (Stefan problem). Fortunately, the problem can be simplified while leaving the essentials of the heat transport intact. That is, compared to laser processing of a solid work piece, the heat transport from the melt pool surface to the bottom is increased by the fluid flows.

This effect of convective heat transport on the temperature distribution can be modelled by considering a solid work piece with increased thermal conductivity $\bar{K}$ (Lampa, 1997). The effect of the latent heat of fusion L_f [$\mathrm{J{\cdot}kg^{-1}}$] on the temperature distribution can be approximated by an increased thermal capacity of the solid (Gasser, 1991)

$$\bar{c}_p = \frac{1}{T_m - T_0}\left(L_f + \int\limits_{T_0}^{T_m} c_p(T)\,dT\right) \tag{4.9}$$

in which $c_p(T)$ denotes the temperature dependence of the thermal capacity. However, for most metals, the energy required to heat up the volume under consideration to the processing temperature, is larger than the energy required to melt it. For example, during laser nitriding of titanium the processing temperature ranges from 1650 °C (melting temperature of titanium) to 2500 °C, see section 5.3.1. Then, the energy c_pT required per unit of mass to heat up the material to its processing temperature ranges from 863 to 1307 $\mathrm{kJ{\cdot}kg^{-1}}$ (see appendix D for thermo-physical properties of titanium). Whereas the energy per unit of mass required to melt it is only $L_f = 292\,\mathrm{kJ{\cdot}kg^{-1}}$. Hence, the energy required to create a melt pool comprises less than 20% of the total energy required for processing. This implies that the contribution of the latent heat of fusion and solidification to the term Q in equation (4.1), which represents heat sources and heat sinks in the work piece, can be neglected.

For a first approximation of the temperature distribution, temperature independent material properties may be considered (Bergman and Geissler, 1990)—e.g. by considering averaged values over the temperature range $T \in [T_0, T_1]$ of interest, such as for the density

$$\bar{\rho} = \frac{1}{T_1 - T_0}\int_{T_0}^{T_1} \rho(T)\,dT \tag{4.10}$$

where $\rho(T)$ denotes the temperature dependence of the density.

These observations support the fact that for a first approximation of the temperature distribution, the melt pool and its direct surroundings may be modelled as a solid with increased heat conductivity $\bar{K}$, modified thermal capacity $\bar{c}_p$ and constant material parameters.

Additional material

Laser alloying, dispersing and cladding rely on the supply of external material to the laser generated melt pool. The additional material is usually supplied to the melt pool in the form of powder or as a reactive gas. Once immersed in the melt, powder particles are melted (except for dispersing) and distributed over the melt pool by convection (He *et al.*, 1995). The time required for powder particles to completely dissolve in the melt pool is of the order of 10 μs (Kaplan *et al.*, 1997). Due to the relatively long laser-material interaction times (typically 10^{-2} to 10 s) and due to the internal fluid flows in the melt pool, the additional material will circulate in the melt pool several times before ”freezing” at its location upon solidification (Chen, 1994). This results in a homogeneous microstructure. The same applies for the case where additional material is supplied as a reactive gas. Then, the reaction product between the gas and the molten bulk material is also distributed over the melt pool by convection.

In the case of laser alloying, the base material content predominates in the melt pool, and the effect of the additional material on the thermo-physical properties of the melt pool may be neglected.

The reaction energy, due to a chemical reaction of the additional material with the base material, is accounted for by the term Q in equation (4.1) and may have a considerable effect on the temperature distribution. In the case of laser nitriding of titanium, the exothermic reaction of nitrogen with the liquid titanium takes place at the surface of the melt pool. Hence, the reaction energy is mainly released at the surface of the melt pool, which can be represented as a surface heat source in addition to the absorbed laser energy. Therefore, the energy released by the exothermic reaction can be modelled as part of the absorbed laser energy, by considering a material with increased absorptivity $\bar{A}$. Then, the contribution of the reaction energy to the term Q in equation (4.1) can be disregarded.

Simplified heat conduction equation

From the above analysis of the physical phenomena, occurring during laser surface treatment, it follows that:

(*i*) the heat losses from the surface of the work piece, as a result of radiant emission and heat loss through convection with the atmosphere, can be neglected—i.e. $\varepsilon_t \sigma (T + T_0)^4 = 0$ and $h_c = 0$ respectively,
(*ii*) the effect of fluid flows on the temperature distribution of the melt pool and its direct surroundings can be compensated for by considering a solid work piece with increased thermal conductivity $\bar{K}$,
(*iii*) the effect of latent heat of fusion on the temperature distribution can be accounted for by considering a solid material with modified thermal capacity $\bar{c}_p$, and the contribution of the latent heat of fusion to the term Q is disregarded,
(*iv*) the material properties are assumed to be constant,
(*v*) the effect of the additional material on the thermo-physical properties of the melt pool can be neglected,
(*vi*) the energy released by the exothermic reaction of the base material with the additional material can modelled as part of the absorbed laser energy, by considering a material with increased absorptivity $\bar{A}$, and disregarding the contribution of the reaction energy to the term Q.

By combining (*iii*) and (*vi*) it follows that the term representing heat sources and heat sinks in the work piece can be set to zero, $Q = 0$.

Without loss of generality, it may be assumed that the laser beam moves in the positive x-direction, $\mathbf{v} = v\mathbf{e}_x$. Then, by applying all the simplifications mentioned above, and omitting the bars over the symbols of the material properties for convenience, the temperature distribution in a semi-infinite work piece during laser surface treatment is described by the equations

$$\rho c_p \frac{\partial T}{\partial t} - K\nabla^2 T - \rho c_p v \frac{\partial T}{\partial x} = 0 \tag{4.11}$$

$$-K \left.\frac{\partial T}{\partial z}\right|_{z=0} = \begin{cases} AI(x,y,t) & \text{for} \quad \partial\Omega \in \Gamma \\ 0 & \text{for} \quad \partial\Omega \notin \Gamma \end{cases} \tag{4.12}$$

with boundary condition (4.7) and initial condition (4.8). The heat loss per unit of volume, as described by equation (4.11), consists of an accumulation term (first term on the left hand side), a diffusion term (second term on the left hand side) and a convective term (third term on the left hand side). The latter accounts for the heat transport caused by the relative translation between the work piece and the laser beam. The beam velocity is multiplied by a temperature gradient in equation (4.11). Hence, the temperature will depend non-linearly on the beam velocity. Increasing the beam velocity will reduce the temperature of the work piece, due to the increased convective heat loss from the laser-material interaction zone. Hence, when observed from the coordinate system fixed to the laser beam, the beam velocity can be considered as a process input allowing the withdrawal of energy from the laser-material interaction zone. This is important as this allows the asymmetry of the laser power to be compensated for, because the laser source can obviously not remove energy from the work piece ($P_L \geq 0$).

The heating and cooling mechanisms are different and therefore have different time constants (see for example figure 2.3 on page 10). This asymmetry can be attributed to the asymmetry of the boundary condition (4.12). This can be understood by analyzing the energy balance of the dominant energy contributions describing the heating phase and the cooling phase. The heating phase of an appropriately chosen volume in the work piece surface layer is characterized by the energy balance

$$\begin{aligned} \textit{absorbed laser energy} = {} & \textit{conduction of heat into work piece} + \\ & \textit{convection of heat due to beam velocity} + \\ & \textit{(chemical) reaction energy} \end{aligned} \tag{4.13}$$

whereas the cooling phase is characterized by the energy balance

$$\begin{aligned} & \textit{energy absorbed during heating phase} = \\ & \qquad \textit{conduction of heat into work piece} + \\ & \qquad \textit{convection of heat due to beam velocity} \end{aligned} \tag{4.14}$$

To cope with these non-linearities in a control loop, an operating point will be chosen (see chapter 5). Then, only small variations of the temperature around the operating point are considered. In the following, the solution of the heat equation (4.11) is calculated. The response of the temperature distribution to laser power, the beam velocity and the disturbances, is analyzed. The dependency of the melt pool geometry on the operating parameters is discussed in section 4.3.3.

4.2 Solution of heat conduction equation

4.2.1 The use of Green's function

A well known approach to solve the simplified heat conduction equation (4.11), given its boundary and initial condition, is by the use of Green's functions (Carslaw and Jaeger, 1959).

Green's function, for the problem under consideration, is the analytical solution of (4.11) and (4.12) with $I(x,y,t) = \delta(x)\delta(y)H(t)$, where $\delta(\cdot)$ is the Dirac delta function and $H(\cdot)$ the unit step function or Heaviside function. That is, the Green's function $G(x,y,z,t,x',y',z',t',v,K,\kappa)$ represents the temperature at (x,y,z) at time t due to a point source of unit strength generated at (x',y',z') at time t', which is moving with velocity v. Then by integrating the product of the Green's function G with the actual absorbed power density $AI(x,y,t)$, over the dimensions of the laser spot and time, the temperature $T(x,y,z,t)$, induced by a the laser beam moving over the surface ($z'=0$), is obtained

$$T(x,y,z,t) = T_0 + \int_0^t \int_{-\infty}^{\infty} \int_{-\infty}^{\infty} G(x,y,z,t,x',y',0,t',v) AI(x',y',t') dx'\, dy'\, dt' \tag{4.15}$$

For the problem under consideration the Green's function equals (Carslaw and Jaeger, 1959)

$$G(x,y,z,t,x',y',0,t') = \frac{1}{4\sqrt{\kappa}[\pi(t-t')]^{\frac{3}{2}} K} \exp\left[\frac{[(x-x')+v(t-t')]^2+(y-y')^2+z^2}{-4\kappa(t-t')}\right] \tag{4.16}$$

For the design of a controller the transient behavior, as well as the steady state behavior of the temperature field is of interest. Therefore, the Green's function is rewritten as the product of a steady state term W and a time dependent term U (Li *et al.*, 1997)

$$G(x,y,z,t,x',y',0,t',v) = W(x,y,z,x',y',v)U(x,y,z,t,x',y',t',v) \tag{4.17}$$

with

$$W(x,y,z,x',y',v) = \frac{1}{2\pi K\vartheta} \exp\left[-\frac{v}{2\kappa}\left(x-x'+\vartheta\right)\right] \tag{4.18}$$

$$U(x,y,z,t,x',y',t',v) = \frac{\vartheta}{2\sqrt{\pi\kappa}(t-t')^{\frac{3}{2}}} \exp\left[-\frac{(\vartheta - v(t-t'))^2}{4\kappa(t-t')}\right] \tag{4.19}$$

where $\vartheta = \sqrt{(x-x')^2+(y-y')^2+z^2}$. Then, after reversing the order of integration, the temperature distribution (4.15) can be written as

$$T(x,y,z,t) = \int_{-\infty}^{\infty} \int_{-\infty}^{\infty} AI(x',y',t') W(x,y,z,x',y',v) U'(\vartheta,t,v)\, dx' dy' \tag{4.20}$$

where

$$U'(\vartheta,t,v) = \int_0^t U(x,y,z,t,x',y',t',v) dt' \tag{4.21}$$

The coordinates (x',y',z') represent the location of the point source relative to the coordinate system fixed to the laser beam, and should not be confused with the coordinate system of the work piece.

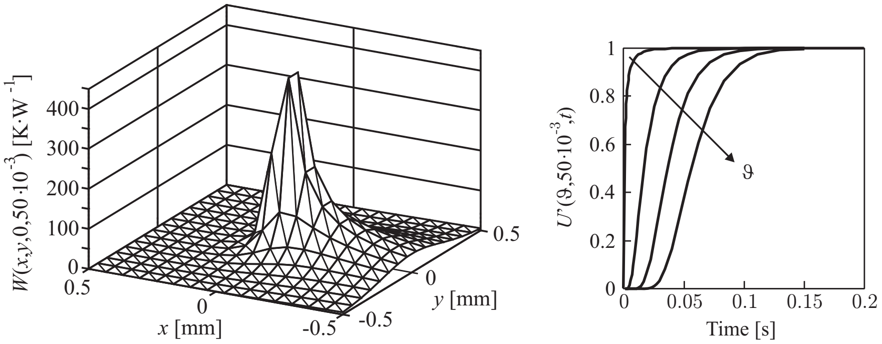

(a) Steady state term W evaluated at the surface for a point source in the origin.

(b) Time dependent term $U'(\vartheta,t,v)$ as a function of time for $\vartheta = 0.1, 1, 2, 3$mm.

Figure 4.3: Functions W and U' for Ti6Al4V and $v = 50\,mm{\cdot}s^{-1}$.

which can be rewritten, using $\xi = 1/\sqrt{\kappa(t-t')}$, as

$$\begin{aligned} U'(\vartheta,t,v) &= \frac{\vartheta}{\sqrt{\pi}} \int_{1/\sqrt{\kappa t}}^{\infty} \exp\left[-\frac{\left(\vartheta\xi^2 - v/\kappa\right)^2}{4\xi^2}\right] d\xi \\ &= \frac{1}{2}\left[1 - \operatorname{erf}\left(\frac{\vartheta - vt}{2\sqrt{\kappa t}}\right) + e^{\vartheta v/\kappa}\left(1 - \operatorname{erf}\left(\frac{\vartheta + vt}{2\sqrt{\kappa t}}\right)\right)\right] \end{aligned} \tag{4.22}$$

Figure 4.3 shows the functions W and U' for titanium and several values of ϑ. As can be observed from figure 4.3(a) the function W is asymmetric with respect to the yz-plane, but is symmetric with respect to the xz-plane. The asymmetry is introduced by the increased convective heat losses compared to the conductive heat losses, when the laser beam is moving. As can be observed from figure 4.3(b), $U' \to 1$ for $t \to \infty$. Hence, the product WU' describes the transient behavior of the temperature field, whereas W describes the steady state (or quasi stationary) behavior of the temperature. This discrimination will be used in section 4.4.1 to derive a dynamic model in the frequency domain.

4.2.2 The use of image heat sources

To analyze the effect of small dimensions of the work piece (geometrical disturbance) on the temperature distribution, the well known method of virtual heat sources (or image heat sources) will be applied (Zauderer, 1989).

In figure 4.4 the use of image sources is illustrated for a plate with thickness z_d [m]. An image source (♯ 1), with the same absorbed intensity profile $AI(x,y)$ as the laser beam is "located" at $z = -2z_d$. This source accounts for the boundary condition $\partial T/\partial z = 0$ at $z = z_d$ (see equation (4.5)). However, this image source will induce a heat flow at $z = 0$ which does not fulfill the boundary condition (4.5) at $z = 0$. This can be compensated

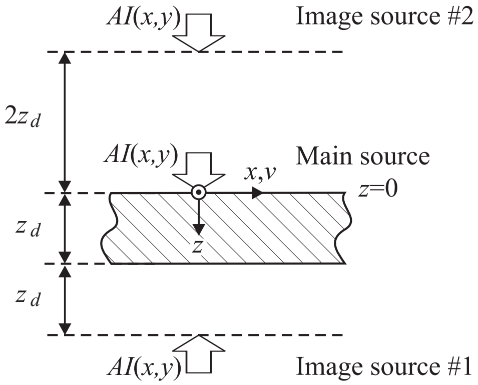

Figure 4.4: To calculate the temperature profile in a plate with thickness $z_d\,[m]$ *and of infinite dimensions in x and y direction, an infinite number of image sources are applied to account for the boundary condition* $\partial T/\partial z = 0$ *at* $z = 0$ *and* $z = z_d$*.*

for by an image source (♯ 2) at $z = 2z_d$. However, this last image source will induce heat flow at $z = z_d$ which does not fulfill the boundary condition $\partial T/\partial z = 0$. To account for this error, an additional image source at $z = 4z_d$ is required, etc. Hence, by denoting $T_{\text{si}}(x,y,z,t)$ as the temperature profile in a semi-infinite work piece (4.15), the temperature profile $T_{\text{is}}(x,y,z,t)$, $z \in [0,z_d]$ in the plate reads,

$$\begin{aligned} T_{\text{is}}(x,y,z,t) &= T_{\text{si}}(x,y,z,t) + \\ &\int_0^t \int_{-\infty}^{\infty} \int_{-\infty}^{\infty} AI(x',y') \sum_{n=1}^{\infty} G(x,y,2nz_d + z,t,x',y',0,t')dx'dy'dt' + \\ &\int_0^t \int_{-\infty}^{\infty} \int_{-\infty}^{\infty} AI(x',y') \sum_{n=1}^{\infty} G(x,y,2nz_d - z,t,x',y',0,t')dx'dy'dt' \end{aligned} \tag{4.23}$$

With increasing n, the contribution of an additional image source to $T_{\text{is}}(x,y,z,t)$ reduces exponentially. So the series in (4.23) rapidly converge. Hence, the temperature profile in the plate can be approximated by incorporating a finite number of sources. This method was used to generate figure 3.6 on page 25, and will be used in section 4.3.1 to analyze the effect of small dimensions of the work piece (geometrical disturbance) on the temperature distribution.

4.2.3 Numerical evaluation

Unfortunately, no explicit analytical solution of equation (4.15) for an arbitrary intensity profile $I(x,y)$ is known to the author. However, the equation can be solved in explicit form after introducing several approximations. To test the validity, these approximated analytic models will be compared to the numerical solution. Moreover, these methods can be used

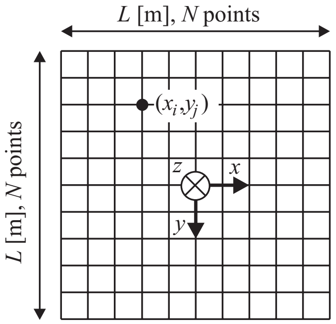

Figure 4.5: Square grid of $N \times N$ equidistant points in the xy-plane on which the intensity profile is considered as piece wise constant.

to analyze the response of the temperature distribution to the operating parameters and disturbances.

Three numerical methods are discussed: *(i) Multi-integration*, *(ii) Multi-grid multi-level integration* and *(iii)* the use of the Fast Fourier Transform (FFT) algorithm. Although the methods apply to the transient temperature field, for simplicity the steady state situation $U' = 1$ is considered only.

Multi-integration

The laser intensity profile $I(x,y)$ is approximated as piecewise constant with the value $I(x_i,y_j) = I(x,y)$ in the region

$$\left\{ (x_i,y_j) \in \mathbb{R}^2 \,\middle|\, x_i - \frac{L}{2N} \le x \le x_i + \frac{L}{2N} \wedge y_j - \frac{L}{2N} \le y \le y_j + \frac{L}{2N} \right\} \tag{4.24}$$

representing a square grid of $N \times N$ equidistant points in the *xy*-plane (figure 4.5),

$$(x,y) \in \left[-\frac{L}{2} \le x \le \frac{L}{2}, -\frac{L}{2} \le y \le \frac{L}{2} \right] \tag{4.25}$$

The temperature distribution (4.20) with $U' = 1$, can be numerically evaluated as

$$T(x,y,z,t) = T_0 + \frac{AL^2}{2\pi K N^2} \sum_{i=1}^{N} \sum_{j=1}^{N} \frac{I(x_i,y_j)}{\vartheta'} \exp\left[-\frac{v(x-x_i)+\vartheta'}{2\kappa} \right] \tag{4.26}$$

where $\vartheta' = \sqrt{(x-x_i)^2 + (y-y_j)^2 + z^2}$. This is a straightforward way of calculating the surface temperatures and is referred to as *multi-summation*. As ϑ' is a factor in the denominator of the function W it represents a singularity, which causes numerical problems if $\vartheta' \ll 1$. In that case the function W should be replaced by W_0, which is defined by

Li *et al.* (1996)

$$\begin{aligned}W_0(x,y,z,x_i,y_j,v) = \frac{1}{2\pi K\Delta x\Delta y}\exp\left(-\frac{vz}{2\kappa}\right)\times\\ \left[\Delta x\ln\left(\frac{w_1+\Delta x}{w_1-\Delta x}\right)+\Delta y\ln\left(\frac{w_2+\Delta y}{w_2-\Delta y}\right)\right.\\ \left.-4z\left(\tan^{-1}\left(\frac{w_1}{2z}\right)+\tan^{-1}\left(\frac{w_2}{2z}\right)\right)+2z\pi\right]\end{aligned} \tag{4.27}$$

where $\Delta x = \Delta y = L/N$ and

$$\begin{aligned}&w_1 = \sqrt{\frac{\Delta x^2+4z^2\cos^2\beta}{\sin^2\beta}},\ w_2 = \sqrt{\frac{\Delta y^2+4z^2\sin^2\beta}{\cos^2\beta}},\\ &\beta = \tan^{-1}\left(\frac{\Delta y}{\Delta x}\right)\end{aligned} \tag{4.28}$$

In the case $z = 0$ and $\vartheta' \ll 1$, function W should be replaced by $\lim_{z\to 0} W_0$. The number of operations, which are required to evaluate (4.26) for a xy-plane of $N\times N$ nodal points, is proportional to N^4. This is denoted by $O(N^4)$. For accuracy reasons, N must be large (typically $N > 250$).

Multi-grid Multi-level integration

Brandt and Lubrecht (1990) developed an algorithm referred to as *Multi-grid Multi-level integration*, which evaluates expression (4.26) in only $O(N^2 \log N^2)$ operations, provided the function W (4.18) meets some smoothness requirements. Basically the application of the algorithm consists of four steps:

(i) Equation (4.26) is restricted to a coarser grid of only $\sqrt{N}\times\sqrt{N}$ grid points by adjoint interpolation,

(ii) The summation (4.26) is evaluated on this course grid, which takes $O(N^2)$ operations,

(iii) The temperature field is interpolated from the coarse grid to the fine grid of $N\times N$ grid points, which again takes $O(N^2)$ operations,

(iv) If necessary, local corrections are performed, which requires $O(\log N^2)$ operations for each point if the smoothness properties of W, as stated by Brandt and Lubrecht (1990) are met.

Then, the total number of operations is reduced to $O(N^2 \log N^2)$. This method is applied in section 4.3.2 to calculate the maximum steady state surface temperature induced by several laser beam intensity profiles.

Two-dimensional Fast Fourier Transform

Even fewer operations are required when the two-dimensional Fast Fourier Transform (FFT) algorithm is applied to evaluate (4.20) numerically. For that purpose it is noted that

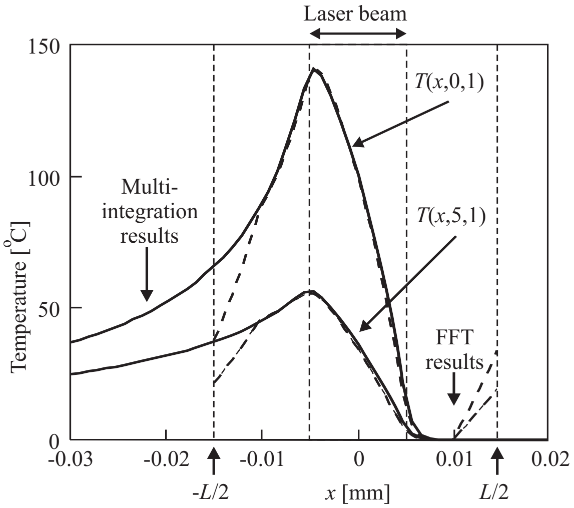

Figure 4.6: Comparison of the longitudinal-section of the temperature increase in C45 induced by a square uniform laser power intensity profile of $10\,mm \times 10\,mm$*, moving at* $v = 50\,mm{\cdot}s^{-1}$ *and* $AP_L = 300\,W$*,* $z = 1\,mm$ *as calculated by the multi-integration method (solid curve) and the FFT method (dashed curve). Dimensions in mm. Errors in the FFT results are caused by truncation of the intensity profile* I *and the function* W*. Near the center of the laser spot, where the temperatures are high, these errors can be neglected.*

the steady state version ($U' = 1$) of equation (4.20) can be rewritten as

$$T(x,y,z) = \int_{-\infty}^{\infty}\int_{-\infty}^{\infty} AI(x',y',t')W(x-x',y-y',z,v)\,dx'dy' \tag{4.29}$$

which is a convolution of the intensity profile AI and the function W, with respect to the coordinates x and y, — i.e. $T = AI * W$, where $*$ denotes the convolution operator. Hence, by applying the two-dimensional Fourier transform $F_2\{\cdot\}$ (Bracewell, 1986), equation (4.29) can be rewritten as

$$F_2\{T\} = F_2\{AI * W\} = AF_2\{I\}F_2\{W\} \tag{4.30}$$

where the well known equality $F_2\{f * g\} = F_2\{f\}F_2\{g\}$ has been applied. Finally, by applying the inverse Fourier transform to this expression yields,

$$T = AF_2^{-1}\{F_2\{I\}F_2\{W\}\} \tag{4.31}$$

By replacing the continuous convolution by discrete convolution, and using the two-dimensional FFT method, the temperature distribution (4.31) can be calculated numerically in only $O(N^2)$ operations. This method was used to calculate the temperature profile in an semi-infinite work piece and a plate, as shown in figure 3.6 on page 25. Moreover, this method will be used to analyze the effects of varying beam velocity and laser power on the temperature field in section 4.3.1.

A basic condition for the two-dimensional Fourier transformation is that the function to be transformed is periodic in the *xy*-plane. This is not the case for the intensity profile I and the function W, and will introduce errors in the evaluation of the temperature distribution, as is illustrated in figure 4.6. These errors are introduced by the truncation of I and W—i.e. if L (figure 4.5) is chosen too small, then for $|x| > L$ and $|y| > L$, $W(x,y) \neq 0$ and $I(x,y) \neq 0$. The errors are significant for low temperatures only, as is illustrated by figure 4.6. To reduce these errors, the region of calculation should be chosen sufficiently large. As a rule of thumb, one should choose $L > 3d$, where d is the diameter of the laser beam.

Solution of the inverse problem

Besides the calculation of the temperature distribution, given the intensity profile I and the function W, also the inverse problem can be solved by applying the FFT method. That is, given a desired temperature distribution T and the function W, the required intensity profile I inducing the desired temperature field can be determined (Li and Yuan, 1994), by rewriting equation (4.30) as

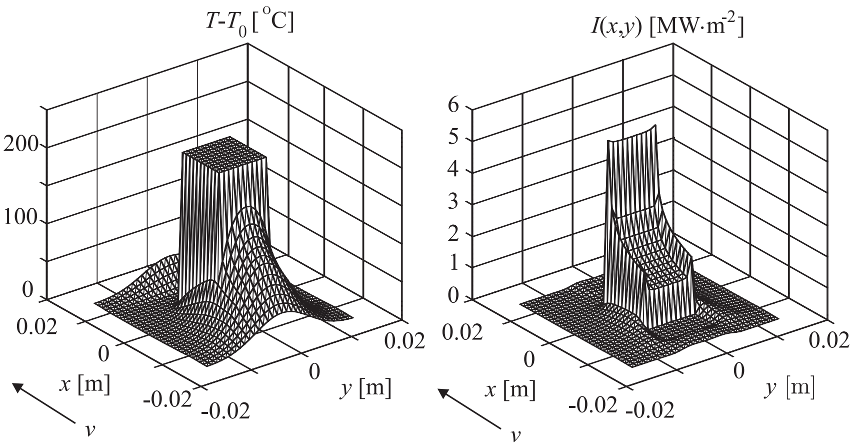

Figure 4.7: Fictitious temperature (left) of Ti6Al4V at $v = 50\,mm\cdot s^{-1}$. The corresponding laser beam intensity profile (right) was calculated by applying equation (4.33). Because, the desired temperature gradients are too high, this desired temperature is not physically feasible. Therefore, the calculation (4.33) returned some locations of negative intensity, which jointly represent 7% of the total power, and were set to zero in the right graph.

$$F_2\{I\} = \frac{1}{A} F_2\{T\} \left[F_2\{W\}\right]^{-1} \tag{4.32}$$

and by applying the inverse Fourier transform. Then, the intensity profile reads,

$$I = \frac{1}{A} {F_2}^{-1} \{ F_2\{T\} \left[F_2\{W\} \right]^{-1} \} \tag{4.33}$$

This is a very powerful method as it allows the calculation of the required intensity profile directly from any desired temperature distribution. Figure 4.7 shows a surface temperature distribution and the corresponding intensity profile, as calculated by applying (4.33). It is evident that this method will only yield a feasible intensity profile ($I(x,y) \geq 0 \; \forall \; (x,y) \in \mathbb{R}^2$), if the desired temperature field is physically feasible.

4.3 Steady state process models

In this section three steady state (i.e. $\partial T / \partial t = 0$) process models are presented. In subsection 4.3.1 the 3-dimensional temperature distribution in a solid, induced by a moving intensity profile, is analyzed numerically. The FFT method is applied for this purpose. In subsection 4.3.2 a pseudo-analytical model of the *maximum* surface temperature is derived. In the last subsection a model is derived which relates the melt pool depth to the operating parameters.

4.3.1 Steady state temperature field

In this subsection, the effects of the intensity profile, the beam velocity, the laser power, and work piece thickness on the 3-dimensional steady state temperature distribution in the semi-infinite work piece is analyzed numerically using the FFT method.

Figures 4.8 and 4.9 show the surface temperature increase $T(x,y,z)$ in titanium, induced in a semi-infinite work piece by four different intensity profiles. All intensity profiles are moving at $50\,\mathrm{mm \cdot s^{-1}}$ with constant laser power of $1000\,\mathrm{W}$. The absorptivity is assumed to be equal to $A = 3.5\%$. Hence, the absorbed laser power equals $AP_L = 35\,\mathrm{W}$. These operating parameters correspond to the experiments, which will be discussed in chapter 5. The influence of the laser beam profile on the temperature field is clearly visible. Comparing figures 4.8(a) and 4.9(b) shows that the temperature distribution in the *xz*-plane is nearly uniform, if the intensity profile is uniform.

The temperature distribution is asymmetric in the *x*-direction, but is symmetric with respect to the *xz*-plane. The asymmetry is introduced by the relative motion of the beam. For a stationary laser beam ($v = 0$) the temperature field would be symmetric with respect to the *z*-axis, and the maximum surface temperature is reached in the center of the laser beam.

Figures 4.10(a) and 4.10(b) show the longitudinal-section of the temperature distribution at two beam velocities, induced by a Top Hat (circular uniform, see equation (4.37)) intensity profile. As can be observed, the asymmetry of the temperature distribution in the *x*-direction increases with increasing beam velocity. Due to the higher beam velocity the maximum surface temperature as well as the heat penetration depth δ_h (4.4) decrease. Moreover, the shape of the temperature distribution changes significantly. The location of maximum surface temperature shifts from the center of the laser beam (at $v = 0$) to the negative *x*-direction (for $v > 0$) with increasing velocity.

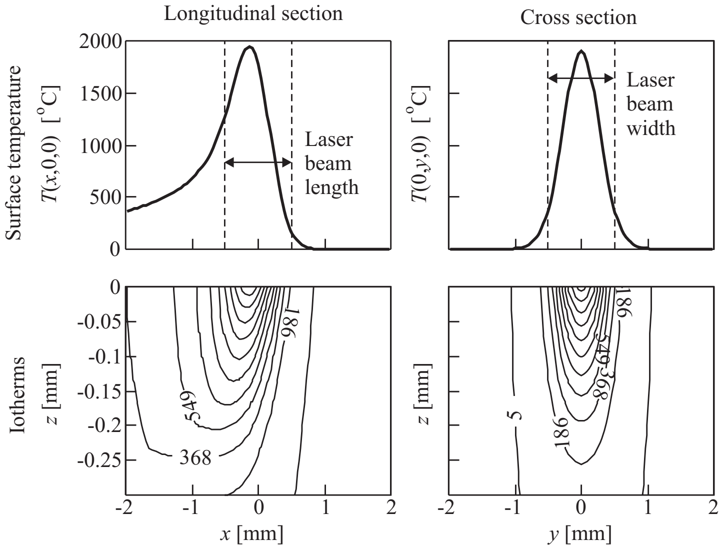

(a) Gaussian intensity profile, $d = 1\,\text{mm}$.

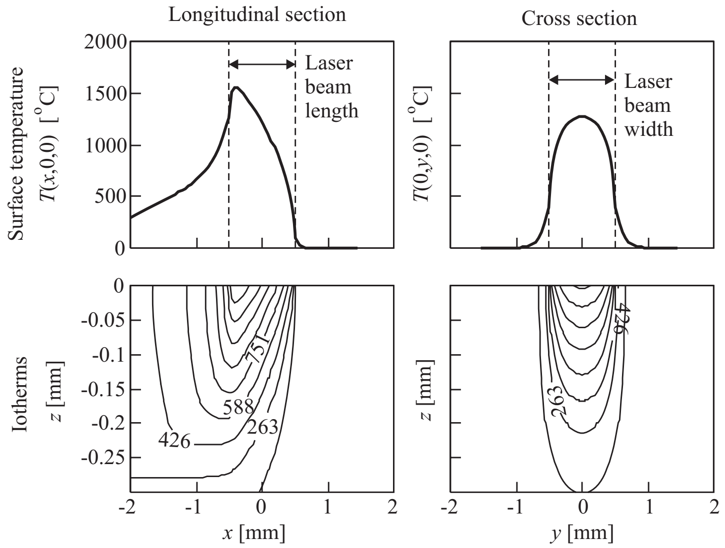

(b) Circular and uniform intensity profile (Top Hat), $d = 1\,\text{mm}$.

Figure 4.8: Longitudinal-section and cross sections of the temperature increase in Ti6Al4V induced by a Gaussian and Top Hat intensity profile, $AP_L = 35\,W$, $v = 50\,mm{\cdot}s^{-1}$.

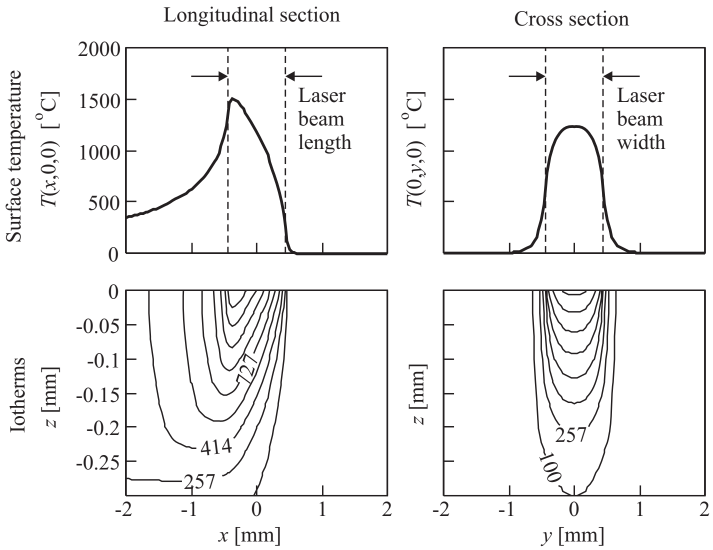

(a) Square and uniform intensity profile, $d_x = d_y = \frac{\sqrt{\pi}}{2}$ mm.

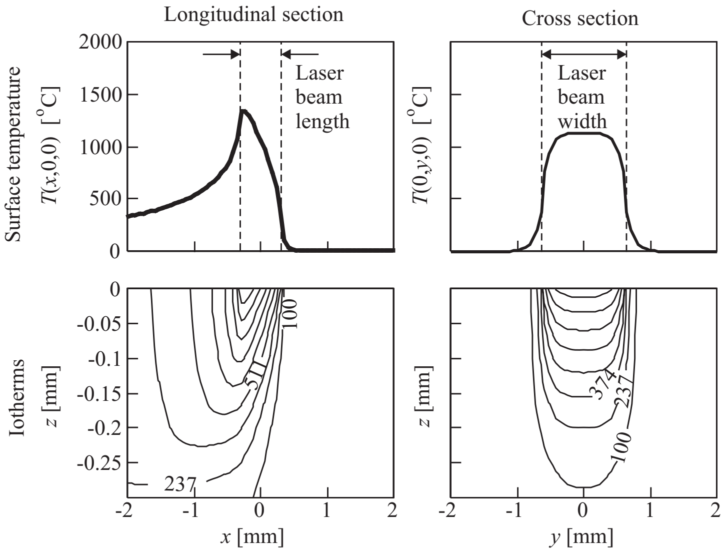

(b) Rectangle, $d_x = \frac{1}{4}\sqrt{2\pi}$ mm, $d_y = 2d_x$.

Figure 4.9: Longitudinal-section and cross sections of the temperature increase in Ti6Al4V induced by a square uniform and rectangular uniform intensity profile, $AP_L = 35\,W$, $v = 50\,mm{\cdot}s^{-1}$.

Varying the laser power only affects the amplitude of the temperature distribution and not its shape. This can be easily understood by expressing the steady state temperature distribution (4.20) in dimensionless variables. These dimensionless variables are defined as

$$\begin{aligned} &\chi = 2x/d_x,\ \eta = 2y/d_x,\ \zeta = 2z/d_x, \\ &\Phi(\chi,\eta) = \frac{d_x d_y}{4AP_L} I(\chi,\eta), \\ &\theta(\chi,\eta) = \frac{K\pi\sqrt{d_x d_y}}{2AP_L} T(\chi,\eta) \end{aligned} \tag{4.34}$$

where (χ,η,ζ) are the dimensionless coordinates (in the coordinate system fixed to the laser beam), Φ denotes the dimensionless intensity profile and θ denotes the dimensionless temperature. The length and width of the laser beam are denoted by d_x [m] and d_y [m] respectively. Finally, the *Peclet number* Pe is applied as the dimensionless beam velocity. The Peclet number is defined as the ratio of the heat flow due to conduction and the heat convective flow due to relative motion between the laser beam and the work piece (Bos and Moes, 1994),

$$\mathrm{Pe} = \frac{d_x v}{\kappa} \tag{4.35}$$

The steady state temperature distribution (4.20), expressed in these dimensionless variables equals

$$\begin{aligned} \theta(\chi,\eta,\zeta) &= \frac{2}{d_x^{3/2}\sqrt{d_y}} \int_{-\infty}^{\infty}\int_{-\infty}^{\infty} \frac{\Phi(\chi',\eta')}{\psi} \exp\left[-\frac{\mathrm{Pe}}{4}\left(\chi-\chi'+\psi\right)\right] d\chi' d\eta' \\ \psi &= \sqrt{(\chi-\chi')^2+(\eta-\eta')^2+\zeta^2} \end{aligned} \tag{4.36}$$

The dimensionless temperature field $\theta(\chi,\eta,\zeta)$ is independent of the absorbed laser power AP_L. Hence, only the amplitude of the temperature distribution depends on the laser power and not its shape. The same conclusion holds for the dependency on the absorptivity A. Hence, for the elimination of absorptivity disturbances, the laser power is the appropriate command signal. This will be verified experimentally in chapter 5 and 6.

Figure 4.10(c) shows the temperature distribution induced by the Top Hat intensity profile, but now moving with $v = 5\,\mathrm{mm{\cdot}s^{-1}}$, instead of $v = 50\,\mathrm{mm{\cdot}s^{-1}}$, over the surface of a plate with a thickness of $z_d = 0.4\,\mathrm{mm}$. This temperature distribution was calculated using the method of image sources (section 4.2.2). The influence of the finite dimensions of the work piece on the temperature is evident. In figure 4.11, the normalized equivalents of the three distributions of figure 4.10 are shown. As can be observed, the shape of the temperature distribution in the plate resembles that of the fast moving beam in the infinite work piece. If the beam velocity is increased, the heat penetration depth (4.4) decreases. This implies that for high velocities the plate may be considered as a semi-infinite work piece. From these two observations it may be concluded that for the elimination of a geometrical disturbance (work piece of reduced thickness) the beam velocity might be a better command signal than the laser power. This conclusion is verified in chapter 5 and 6.

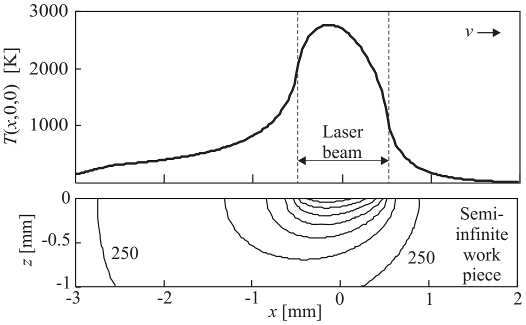

(a) Semi-infinite work piece $v = 5\,\mathrm{mm{\cdot}s^{-1}}$.

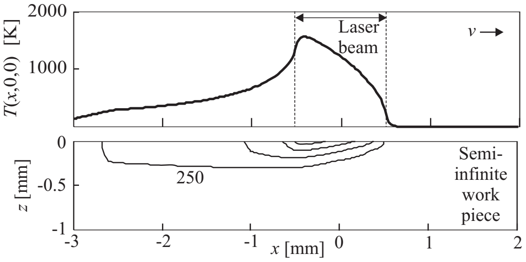

(b) Semi-infinite work piece $v = 50\,\mathrm{mm{\cdot}s^{-1}}$.

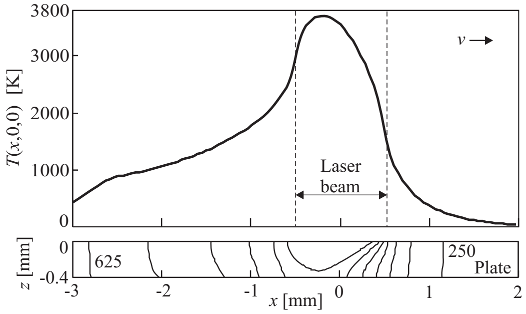

(c) Plate $z_d = 0.4\,\mathrm{mm}$, $v = 5\,\mathrm{mm{\cdot}s^{-1}}$.

Figure 4.10: Longitudinal section of the temperature increase $T(x,0,0)$ at the surface (top graph) of Ti6Al4V and the corresponding isotherms in the material for $y = 0$ (bottom graph), induced by a Top Hat intensity profile. $T(x,0,z) \in \{250, 625, \cdots, 2500\}$, $AP_L = 35\,W$, $d = 1\,mm$.

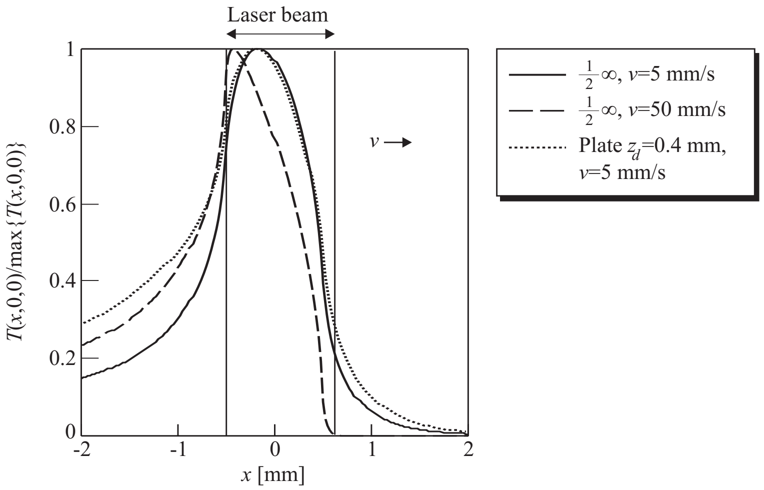

Figure 4.11: Normalized longitudinal surface temperature increase in Ti6Al4V, induced by a circular uniform intensity profile (top hat) with $AP_L = 35\,W$ and beam diameter $d = 1\,mm$, at two beam velocities and two work piece geometries.

4.3.2 Steady state maximum surface temperature

In laser transformation hardening the maximum surface temperature should never exceed the melting temperature. Hence, the maximum surface temperature should be controlled on-line during hardening. For this purpose an analytical model of the steady state maximum surface temperature for a moving beam is preferred. Unfortunately, only analytic models for stationary ($v = 0$) laser beams are available from the literature. In this section, pseudo-analytical models are derived for the steady state maximum surface temperature, which are induced by moving beams in a work piece of semi-infinite dimensions.

Maximum surface temperature induced by stationary beams

For stationary ($v = 0$) laser beams, analytical models for the maximum surface temperature are available from literature, but these can also be calculated from equation (4.15). For an intensity profile, which is symmetrical with respect to the xz-plane, the maximum steady state surface temperature is reached in the center of the beam $(x = 0, y = 0, z = 0)$.

Consider a circular laser beam with diameter d, having a uniform intensity distribution (Top Hat):

$$I_{TH}(x,y) = \begin{cases} 4P_L/\pi d^2, & \sqrt{x^2+y^2} \leq d/2, \\ 0, & \sqrt{x^2+y^2} > d/2, \end{cases} \tag{4.37}$$

Then the maximum surface temperature equals (Carslaw and Jaeger, 1959)

$$T_0^{TH}(0,0,0) = \frac{2AP_L}{\pi d K} \tag{4.38}$$

where the subscript ”0” indicates zero beam velocity. The maximum steady state surface temperature induced by a stationary Gaussian intensity profile (TEM$_{00}$), with diameter d, equals (Ready, 1971)

$$T_0^G(0,0,0) = \frac{AP_L}{dK}\sqrt{\frac{2}{\pi}} \tag{4.39}$$

And the maximum steady state surface temperature, induced by a rectangular uniform intensity profile, bounded by $-d_x/2 \leq x \leq d_x/2$ and $-d_y/2 \leq y \leq d_y/2$, equals (Bass, 1987)

$$T_0^{\Box}(0,0,0) = \frac{AP_L}{K\pi d_x d_y}\left[d_y \sinh^{-1}\left(\frac{d_x}{d_y}\right) + d_x \sinh^{-1}\left(\frac{d_y}{d_x}\right)\right] \tag{4.40}$$

Maximum surface temperature induced by fast moving beams

When the velocity of the laser beam approaches infinity, the heat flow in the solid can be approximated by a one-dimensional flow perpendicular to the surface of the work piece (Carslaw and Jaeger, 1959). Then the corresponding surface temperature distribution $T(x,y,v)$, induced by an arbitrary laser beam intensity profile $I(x,y)$, can be approximated by (Blok, 1937; Jaeger, 1943)

$$T(x,y,v) \approx \frac{1}{K}\sqrt{\frac{\kappa}{\pi v}} \int\limits_{\xi = x_L(y)}^{\min\{x, x_R(y)\}} \frac{I(\xi,y)}{\sqrt{x-\xi}} d\xi \tag{4.41}$$

where $x_L(y)$ and $x_R(y)$ represent the left and right boundaries of the intensity profile respectively. This approximation is valid when the effect of the heat conduction in the solid in the direction of v is small compared to the convective effects due to the motion—i.e. if $\mathrm{Pe} > 10$ (Pietro *et al.*, 1994).

The intensity profiles under consideration are symmetric with respect to the x-axis. Then the maximum surface temperature for high beam velocities is reached at $y = 0$. Hence, the maximum surface temperature induced by the Top Hat intensity profile (4.37) follows from equation (4.41) to give

$$T_\infty^{TH} = \frac{8}{K(\pi d)^{\frac{3}{2}}} AP_L \sqrt{\frac{\kappa}{v}} \tag{4.42}$$

where the subscript ”∞” indicates high beam velocity. Analogously, the maximum surface temperature induced by the Gaussian intensity profile, equals

$$T_\infty^G = \frac{4C\sqrt{2}}{K(\pi d)^{\frac{3}{2}}} AP_L \sqrt{\frac{\kappa}{v}},\ C = \max_{\chi \in \mathbb{R}} \left\{ \int\limits_{-\infty}^{\chi} \frac{\exp[-2\eta^2]}{\sqrt{\chi - \eta}} d\eta \right\} \approx 1.81 \tag{4.43}$$

and for the rectangular intensity profile, the maximum surface temperature equals

$$T_\infty^{\Box} = \frac{2}{K d_y \sqrt{\pi d_x}} AP_L \sqrt{\frac{\kappa}{v}} \tag{4.44}$$

Maximum surface temperature induced at intermediate velocities

The previous paragraph considered beams moving at velocities approaching infinity. By combining the solutions for the stationary T_0 and the fast moving beam T_∞, according to a rule adopted from the theory of sliding contacts (Greenwood, 1991)

$$T_v = \frac{T_0 T_\infty}{\sqrt{T_0^2 + T_\infty^2}} \tag{4.45}$$

a simple approximation of the maximum surface temperature T_v for intermediate beam velocities ($0 < v < \infty$) is obtained. It should be noted that this rule has no physical basis. Then, applying the rule for the Top Hat intensity profile yields

$$T_v^{TH} = \frac{8}{\pi d K} A P_L \sqrt{\frac{\kappa}{\pi d v + 2\kappa}} \tag{4.46}$$

For the Gaussian intensity profile the rule yields

$$T_v^{G} = \frac{4C\sqrt{2}}{dK\sqrt{\pi}} A P_L \sqrt{\frac{\kappa}{\pi^2 d v + (4C)^2 \kappa}} \tag{4.47}$$

And finally, for the rectangular uniform intensity profile the rule yields

$$T_v^{\square} = \frac{2\zeta A P_L}{d_y K \sqrt{\pi d_x}} \sqrt{\frac{\kappa}{\zeta^2 v + 4\kappa\pi d_x}} \tag{4.48}$$

with

$$\zeta = d_y \sinh^{-1}\left(\frac{d_x}{d_y}\right) + d_x \sinh^{-1}\left(\frac{d_y}{d_x}\right) \tag{4.49}$$

To evaluate the accuracy of these approximations, the expressions (4.46) to (4.48), are compared to the corresponding temperatures as obtained with the multi-grid multi-level integration method (section 4.2). To facilitate comparison of the results the dimensionless variables (4.34) are considered. Figure 4.12 shows the maximum dimensionless surface temperature $\max\{\theta(\chi,\eta)\}$, as a function of dimensionless velocity Pe (4.35), for several laser beam intensity profiles. As can be observed from figure 4.12, the maximum surface

Table 4.1: Relative errors

Intensity profile	Relative error [%]
Top Hat	2.56
Gauß	1.98
Square uniform	3.16
Rect. uniform 1:2	4.52
Rect. uniform 1:5	3.48
Rect. uniform 1:10	5.30
Rect. uniform 1:15	7.65

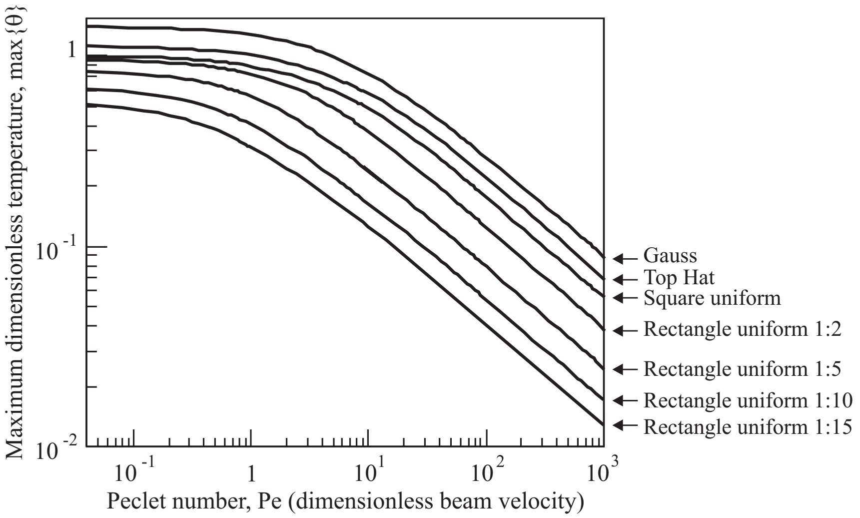

Figure 4.12: Maximum dimensionless surface temperature max$\{\theta(\chi,\eta)\}$ *as a function of dimensionless velocity Pe,* $d_x = 1/2$*, for several laser beam intensity profiles, as calculated by the multi-grid multi-level integration method (*$N = 129$*). For rectangular intensity profiles the aspect ratio* $d_x : d_y$ *is given.*

temperature decreases with increasing beam velocity. The Gaussian intensity profile induces the highest maximum surface temperature. The maximum surface temperature of the rectangular uniform profiles decreases with increasing aspect ratio $d_x : d_y$. For Pe $\rightarrow 0$, the curves converge to the dimensionless equivalents of the stationary intensity profiles (equations (4.38), (4.39) and (4.40)). For Pe $\rightarrow \infty$, the curves converge to the dimensionless equivalents of the intensity profiles moving at high velocity (equations (4.42), (4.43) and (4.44)). The maximum relative errors between approximations (4.46) to (4.48) and the corrsponding numerical results are listed in table 4.1. These errors are small.

4.3.3 Geometry of the melt pool

The melt pool depth during laser treatment determines the thickness of the resulting surface layer after solidification of the melt pool. Therefore, it is important to know the relations between the geometry (depth) of the melt pool and the operating parameters. Moreover, the microstructure, which forms upon solidification, depends not only on the temperature distribution in the melt pool, but also on its geometry. More specifically, the microstructure which forms depends on three quantities: the velocity v_s $[\mathrm{m{\cdot}s^{-1}}]$ of the solidification front $\partial\Omega_{sl}$, its local cooling rate $\partial T/\partial t|_{\partial\Omega_{sl}}$ $[\mathrm{K{\cdot}s^{-1}}]$, and its local temperature gradient $|\nabla T|$ $[\mathrm{K{\cdot}m^{-1}}]$, see figure 4.13. The velocity v_s of the solidification front follows from the geometry of the solidification front $\partial\Omega_{sl}$ and the relative beam velocity $\mathbf{v}$ (Kurz and Trivedi, 1988; Gilgien and Kurz, 1994). It can be calculated from the projection of the outward normal on the solidification front ($\mathbf{n} = (\nabla T/|\nabla T|)|_{\partial\Omega_{sl}}$) onto the beam velocity

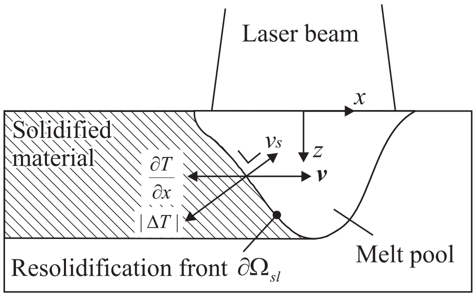

Figure 4.13: The microstructure formed depends on the local rate of solidification v_s, which is composed of the beam velocity **v** *and the geometry of the solidification front.*

v. Assuming that the beam moves in the x-direction, the velocity v_s of the solidification front equals

$$v_s = \frac{\mathbf{v} \bullet \frac{\partial T}{\partial x} \mathbf{e}_x}{|\nabla T|} \tag{4.50}$$

The local cooling rate on the solidification front reads

$$\left.\frac{\partial T}{\partial t}\right|_{\partial\Omega_{sl}} = \mathbf{v} \bullet \frac{\partial T}{\partial x} \mathbf{e}_x \tag{4.51}$$

Hence, the velocity of the solidification front v_s, its local cooling rate $\partial T/\partial t|_{\partial\Omega_{sl}}$ and its local temperature gradient $|\nabla T|$ are related as

$$\left.\frac{\partial T}{\partial t}\right|_{\partial\Omega_{sl}} = v_s\,|\nabla T| \tag{4.52}$$

The metallurgical structure formed during solidification depends on these three quantities and the material properties (Kurz and Trivedi, 1988; Gilgien and Kurz, 1994; Kreutz *et al.*, 1992; Rappaz *et al.*, 1987; Basu and Date, 1992a; Basu and Date, 1992b). This is illustrated on the basis of figure 4.14, which shows the metallurgical structure formed as a function of the velocity of the solidification front and the local cooling rate. The local cooling rate $\partial T/\partial t|_{\partial\Omega_{sl}}$ determines the refinement of the microstructure structure, whereas the ratio $|\nabla T|/v_s$ determines the morphology of the microstructure (planar, cellular or denditric). For example, when going in figure 4.14 from the lower left along a line ($|\nabla T|/v_s$ = constant) to the upper right, the refinement of the microstructure increases without a changing solidification morphology. However, at extremely high cooling rates, over $10^6\,\mathrm{K{\cdot}s^{-1}}$, the formation of a crystal structure is no longer possible, and an amorphous microstructure (metallic glass) is formed. When going in figure 4.14 from the upper left along a line ($\partial T/\partial t|_{\partial\Omega_{sl}}$=constant) to the lower right, the solidification morphology changes from planar over cellular to dendritic, without a change in the refinement of the structure.

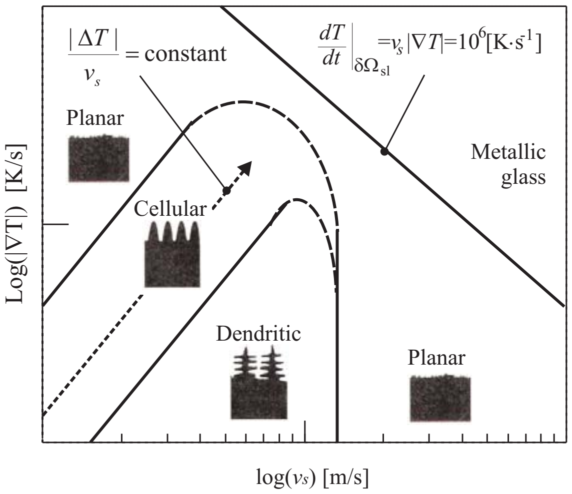

Figure 4.14: Metallurgical structure upon solidification as a function of local temperature gradient $|\nabla T|$ and rate of solidification v_s (Gasser, 1991).

This analysis shows that the microstructure upon solidification not only depends on the temperature distribution of the melt pool, but also on the geometry of the solidification front, and therefore on the geometry of the melt pool. Hence, the melt pool geometry is also an important quantity to be controlled. The geometry of the melt pool can be calculated from the numerical results discussed in the previous sections (e.g. figure 4.8 and figure 4.10), by determining the geometry of the isotherm corresponding to the melting temperature of the base material. However, in practice a simple explicit analytical model, relating the operating parameters to the dimensions of the melt pool (e.g. melt pool depth), is preferred, because such a model reduces the number of time-consuming trial and error experiments, which are required to find optimal operating parameters. Such a simple analytical model can be obtained by assuming that the shape of the solid-liquid interface is parabolic. This is a reasonable assumption (see e.g. figure 4.8 and 4.9), which is supported by experimental results (section 5.2.1). In the following, this simple analytical model is derived.

A quasi-stationary situation in an isotropic and homogeneous semi-infinite work piece with a parabolic melt pool geometry is assumed, see figure 4.15. The same simplifying assumptions, as discussed in section 4.1, are applied. However, the contribution of the reaction energy Q_R, resulting from a chemical reaction of the additional material with the liquid base material, to the energy balance of the sample is taken into account separately.

The energy balance within the sample consists of four terms: the absorbed laser energy Q_L, the reaction energy Q_R, the energy Q_C transported by heat conduction from the liquid-solid interface of the melt pool into the non-molten material, and the energy Q_F required to create a melt pool. Although this energy is small compared to the total energy required for processing, it is temporarily removed from the input energy and is not available for melting more material (Ashby and Easterling, 1984). Due to the relative

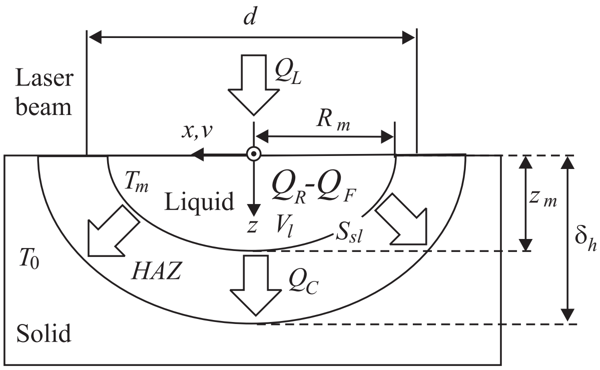

Figure 4.15: Melt pool geometry and energy flows in quasi-stationary situation.

velocity between the laser beam and the work piece, energy is virtually removed from the interaction zone (convective losses). The energy Q_F, required to create a melt pool, is accounted for in the energy balance to compensate for these convective losses. Then, the heat balance reads,

$$Q_L - Q_F + Q_R = Q_C \tag{4.53}$$

Laser energy

The laser energy Q_L absorbed by the work piece, can be approximated by

$$Q_L = AP_L t_i \tag{4.54}$$

where t_i [s] denotes the interaction time of the laser beam with a given point on the surface of the work piece. This interaction time is approximated by (Kuilboer *et al.*, 1994)

$$t_i = \frac{d}{v} \tag{4.55}$$

where d denotes the diameter of the laser beam, see figure 4.15.

Heat conduction

The energy Q_C, which flows from the melt pool into the solid material, can be calculated from the heat enclosed by the heat affected volume under consideration, and equals

$$Q_C = \rho c_p \int\limits_{V_s} T(x,y,z,t_i)dV_s \tag{4.56}$$

where V_s [m^{-3}] denotes the heat affected volume in the solid under the melt pool and where $T(x,y,z,t_i)$ denotes the corresponding temperature field at time $t = t_i$. It is assumed that the heat transfer under the melt pool may be considered as one-dimensional. Then the temperature $T(x,y,z,t_i)$ is equal to the solution of the problem in which a semi-infinite sample attains a surface temperature equal to the melting temperature T_m at time $t = 0$ (Incropera and Witt, 1981)

$$T(z,t_i) = (T_m - T_0)\,\mathrm{erfc}\left(\frac{z}{2\sqrt{\kappa t_i}}\right) + T_0 \tag{4.57}$$

The thickness of the heat affected volume V_s is assumed to be equal to the heat penetration depth (4.4)—i.e. $\delta_h = 2\sqrt{\kappa t_i}$. Then the integral (4.56) can be evaluated if the area S_{sl} [m^2] of the solid-liquid interface is known. The parabolic shape of the solid-liquid interface is described by the function,

$$z = z_m\left(\frac{x^2+y^2}{R_m^2} - 1\right) \text{ for } x^2+y^2 \le R_m^2 \tag{4.58}$$

where z_m [m] denotes the depth of the melt pool and R_m [m] the radius of the melt pool (see figure 4.15). The area S_{sl} of the solid-liquid interface is calculated from equation (4.58) to equal

$$\begin{aligned} S_{sl} =& 2\pi\int_0^{R_m} r\sqrt{1+\left(\frac{dz}{dr}\right)^2}\,dr \\ =& 2\pi\int_0^{R_m} r\sqrt{1+4\frac{z_m^2 r^2}{R_m^4}}dr = \frac{\pi R_m^4}{6z_m^2}\left[\left(\frac{R_m^2+4z_m^2}{R_m^2}\right)^{\frac{3}{2}} - 1\right] \approx \frac{4}{3}\pi R_m z_m \end{aligned} \tag{4.59}$$

where $x^2+y^2 = r^2$ has been used. Then, substitution of (4.55), (4.57) and (4.59) into equation (4.56) yields,

$$Q_C = \frac{4}{3} z_m \pi R_m \rho c_p (T_m - T_0) \int_0^{2\sqrt{\kappa d/v}} \left[\mathrm{erfc}\left(\frac{zv}{2\sqrt{\kappa dv}}\right) + T_0\right] dz \tag{4.60}$$

Latent heat of fusion

The energy Q_F, required to create a melt pool, follows from the latent heat of fusion L_f [J·kg^{-1}] per unit of mass of the material material and the volume V_l of the melt pool,

$$Q_F = L_f \rho V_l \tag{4.61}$$

in which the volume V_l of the melt pool can be calculated from (4.58) and $x^2+y^2 = r^2$ as

$$V_l = \int_{-z_m}^{0} \pi r^2\,dz = \int_{-z_m}^{0} \pi R_m^2\left(\frac{z}{z_m}+1\right)dz = \frac{\pi z_m R_m^2}{2} \tag{4.62}$$

Reaction energy

The reaction energy Q_R follows from the energy of formation $H_r\,[\mathrm{J}\cdot\mathrm{kg}^{-1}]$ per unit mass of reaction product and the volume of the melt pool. Assuming that a fraction $\beta \in \langle 0\,,\,1]$ of the melt pool volume V_l chemically reacts with the additional material, the reaction energy equals,

$$Q_R = \beta V_l \rho H_r = \frac{1}{2}\beta\pi z_m R_m^2 \rho H_r \tag{4.63}$$

In the case of laser-(re)melting and -dispersing $\beta = 0$.

Melt pool depth

Substitution of equations (4.54), (4.55) and (4.60) to (4.63) into the energy balance (4.53) and solving this equation for melt pool depth z_m yields

$$z_m = \frac{AP_L d}{c_p\sqrt{d\kappa v}R_m\rho\,(C_1T_0 + C_2T_m) - \frac{1}{2}\rho R_m^2 v\pi\,(\beta H_r - L_f)} \tag{4.64}$$

with the constants

$$\begin{aligned} C_1 &= \frac{8}{3}\left[\pi\operatorname{erf}(1) + \left(e^{-1} - 1\right)\sqrt{\pi}\right] \approx 4.07 \\ C_2 &= \frac{8}{3}\pi - C_1 \approx 4.31 \end{aligned} \tag{4.65}$$

Expression (4.64) will be verified experimentally in section 5.2.3, by comparing the model output to the measured depth of the solidified melt pool formed during laser nitriding of titanium

The model (4.64) can be simplified significantly by applying the following three considerations. First, the reaction energy Q_R can be considered as part of the absorbed laser energy, by setting $\beta = 0$. This results in a virtually increased or decreased absorptivity $\bar{A}$. Secondly, for many metals $Q_F \ll Q_L$ (see section 4.1). Finally, the initial work piece temperature T_0 may be neglected compared to the melting temperature, $T_m \gg T_0$. Then, assuming that the melt pool diameter is equal to the beam diameter, expression (4.64) simplifies to

$$z_m = \frac{2\bar{A}}{\rho c_p C_2 T_m\sqrt{\kappa}}\,\frac{P_L}{\sqrt{d}\sqrt{v}} \tag{4.66}$$

This expression shows a linear dependence of the melt pool depth on the ratio $P_L/(\sqrt{d}\sqrt{v})$, which is sometimes referred to as the *specific energy* (Schneider, 1998). The same dependence is frequently found from experimental analysis e.g. by Derouet *et al.* (1994), but was never shown theoretically before. Note, that similar relations hold for the maximum surface temperature during laser transformation hardening (section 4.3.2). In section 5.2.3, expression (4.66) will be verified experimentally.

4.4 Dynamic process models

In this section dynamic models (transfer functions) of the temperature in a solid are derived. That is, the accumulation term in the heat conduction equation (4.11) is not equal to zero, $\partial T/\partial t \neq 0$. These dynamic models are required for the design of feedback controllers.

Two transfer functions, relating the command signal (laser power or beam velocity) to the temperature distribution are distinguished. First, the transfer function $G(s)$ relating the laser power P_L to the temperature distribution $T(x,y,z,t)$, at constant beam velocity, which is defined as

$$G(s) = \left.\frac{T(x,y,z,s)}{P_L(s)}\right|_{v=\text{const.}} \tag{4.67}$$

where s denotes the Laplace or frequency variable and $T(x,y,z,s)$ and $P_L(s)$ the corresponding Laplace transforms with respect to time. The second transfer function $G_v(s)$, relates the beam velocity v to the temperature field $T(x,y,z,t)$, at constant laser power,

$$G_v(s) = \left.\frac{T(x,y,z,s)}{v(s)}\right|_{P_L=\text{const.}} \tag{4.68}$$

This latter transfer function is hard to calculate analytically, and will be determined experimentally in chapter 5.

An explicit analytic expression for the transfer function (4.67) requires an explicit analytic expression for the 3-dimensional temperature field $T(x,y,z,s)$, which cannot be calculated analytically for an arbitrary intensity profile. In appendix B a first approach to solve this 3-dimensional problem is presented—i.e. the appendix does not present a final solution, but must be read as a contribution to the scientific discussion in this field.

In the next two subsections simplified equations are considered, which can be solved explicitly. The resulting expressions provide insight in the transient behavior of the process, and are therefore valuable for the design of feedback controllers. First, the 3-dimensional temperature field, and the corresponding transfer function, induced by a *point source* is derived. Next, the one-dimensional temperature field induced by an infinite uniform intensity profile is derived.

4.4.1 Transient 3D temperature field induced by point source

In contrast to the temperature distribution caused by an arbitrary intensity profile, the temperature field induced by a point source can be calculated in explicit form. The temperature distribution caused by an arbitrary intensity profile is a superposition of the temperature distributions caused by point sources (Carslaw and Jaeger, 1959). Therefore, the transfer function corresponding to the point source is derived in this section. For this purpose, the intensity profile of a point source $I(x,y,t) = P_L H(t)\delta(x)\delta(y)$ is substituted in equation (4.20), which yields,

$$T(x,y,z,t) = P_L W U' \tag{4.69}$$

where W follows from equation (4.18)

$$W = \frac{1}{2\pi K\vartheta}\exp\left[-\frac{v}{2\kappa}(x+\vartheta)\right],\ \vartheta = \sqrt{x^2+y^2+z^2} \tag{4.70}$$

and where U' follows from equation (4.22)

$$\begin{aligned} U' &= \frac{1}{2}\left[1-\operatorname{erf}\left(\frac{\vartheta - vt}{2\sqrt{\kappa t}}\right) + e^{\vartheta v/\kappa}\left(1-\operatorname{erf}\left(\frac{\vartheta+vt}{2\sqrt{\kappa t}}\right)\right)\right] \\ &= \frac{1}{2}\left[\operatorname{erfc}\left(\frac{\vartheta - vt}{2\sqrt{\kappa t}}\right) + e^{\vartheta v/\kappa}\operatorname{erfc}\left(\frac{\vartheta+vt}{2\sqrt{\kappa t}}\right)\right] \end{aligned} \tag{4.71}$$

Then, by applying the Laplace transform pair (Oberhettinger and Badii, 1973)

$$L\left\{\operatorname{erfc}\left(\frac{at+b}{\sqrt{t}}\right)\right\} = \frac{\exp\left[-2b\left(a+\sqrt{s+a^2}\right)\right]}{\sqrt{s+a^2}\left(a+\sqrt{s+a^2}\right)},\quad \Re(s) > 0 \tag{4.72}$$

and some rewriting, it follows that the transfer function (4.67) of the temperature caused by the point source can be written as

$$G(s) = \frac{L\{T(x,y,z,t)\}}{P_L/s} = L\{WU'\}s = \frac{1}{2\pi K\vartheta}\exp\left[-\frac{vx+\vartheta\sqrt{4s\kappa+v^2}}{2\kappa}\right] \tag{4.73}$$

Compared to the complex expressions in the time domain, this transfer function is particularly simple.

The response of the temperature to the laser power at $s = 0\,\mathrm{rad}\cdot\mathrm{s}^{-1}$ is, conform the nomenclature of control theory, referred to as the *DC gain*, and is denoted by $G_0\,[\mathrm{K}\cdot\mathrm{W}^{-1}]$,

$$G_0 = G(0) = \frac{1}{2K\vartheta\pi}\exp\left[\frac{-v(x+\vartheta)}{\kappa}\right] \tag{4.74}$$

The bandwidth $\omega_{BW}\,[\mathrm{rad}\,s^{-1}]$ —i.e. the frequency at which the gain $|G(s)|$ of (4.73) is reduced by 3dB, compared to the gain at 0Hz, equals

$$\omega_{BW} = \frac{v\vartheta+\kappa C}{2\kappa\vartheta^2}\sqrt{(\kappa C)^2+2v\vartheta\kappa C},\ C = \ln(1000) \tag{4.75}$$

Figure 4.16 shows the Bode diagram of transfer function (4.73) for Ti6Al4V at several values of x and ϑ. From these diagrams and equations (4.73) to (4.75) the following observations can be made:

- The gain $|G(s)|$ decreases for increasing values of ϑ, which can be attributed to the fact that the temperature reached at a large distance ϑ from the point is less than the temperature near the point source,
- At finite velocities, the gain just behind ($x < 0$) the point source is larger than the gain just in front of ($x > 0$) the point source. This can be attributed to accumulated heat for $x < 0$. However, with increasing distance from the point source ($|x| \gg 1$) this asymmetry diminishes. For a stationary beam ($v = 0$) the gain is symmetric with respect to the z-axis, which can be attributed to the symmetry of the temperature field about the z-axis, for $v = 0$,

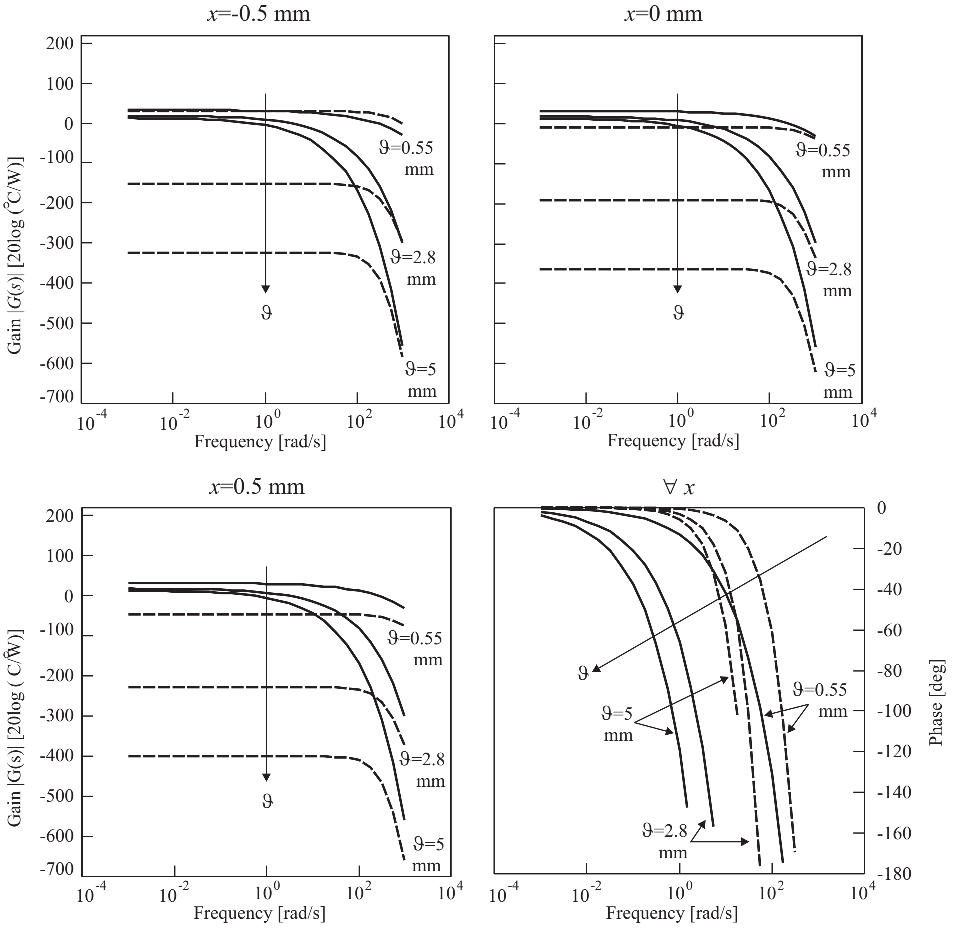

Figure 4.16: Gain and phase shift (lower right) of transfer function (4.16) evaluated for Ti6Al4V at three locations $x = -0.5\,mm$ (just behind the point source), $x = 0\,mm$ (in the center of point source), and $x = 0.5\,mm$ (just in front of the point source) and several values of ϑ, at two values of the beam velocity $v = 50\,mm{\cdot}s^{-1}$ (dashed) and $v = 0\,mm$ (solid curve).

- For increasing beam velocity v, at constant values of ϑ, the gain decreases, which can be attributed to the increasing convective losses due to the increasing beam velocity (see equation (4.13) and (4.14)),
- The bandwidth, for a given value of ϑ, increases with increasing beam velocity v. Due to the increased velocity the heat affected volume decreases. As a result the temperature field will respond faster to a laser power variation, than when the heat affected volume is large,
- For increasing frequency the gain of the source moving at a low beam velocity approaches that of the source moving at a high beam velocity,
- If the thermal material properties (K and κ) are large the bandwidth is large, but then the gain is small. This can be attributed to increased heat conduction, if K and κ are large.

It is evident from equation (4.73) and the above mentioned observations that the temporal response of the temperature field to laser power variations is non-linear.

Moreover, transfer function (4.73) is a function of $\sqrt{s}$, which is typical for an process which is described by a partial differential equation (heat conduction equation). Therefore, this process is also referred to a *distributed parameter process*, as are all processes which are described by partial differential equations. Apart from *one* partial differential equation, the dynamics of a distributed parameter process can be described by an infinite number of ordinary differential equation(s). This, in turn, implies that the dynamics are described by a linear parametric model of infinite order. Consequently, the terminology *infinite-dimensional process* is used (Curtain and Zwart, 1995; Levine, 1995).

Such a high order parametric model is too computationally demanding to be used in a control loop. However, from the time domain response (figure 4.3(b)) and Bode plot 4.16, it can be concluded that the low frequency behavior may be approximated by a low (possibly first) order rational transfer function. This statement will be verified analytically in the next subsection, and experimentally in chapter 5. It will be shown in chapter 6 that the accuracy of these low order models is sufficient for the design of effective feedback controllers.

4.4.2 Transient one-dimensional temperature field

When considering a uniform intensity profile, with infinite dimensions in the x and y-direction, the heat flow in the solid is one-dimensional (in z-direction). This implies that the temperature field is a function of z and t only. As was noted earlier, this assumption is valid if $\mathrm{Pe} > 10$ (high beam velocities) or near the center of the laser beam for $t \approx 0$. This simplified problem is used to show that the dynamics of the infinite-dimensional process can be approximated by a transfer function of low order, and to analyze its controllability and observability.

For a one-dimensional heat flow the heat conduction equation (4.11) and boundary condition (4.12) simplify to

$$\frac{\partial T}{\partial t} - \kappa \frac{\partial^2 T}{\partial z^2} = 0, \forall \mathrm{z} \in \mathbb{R}^+,\ t \geq 0 \tag{4.76}$$

$$-K \left.\frac{\partial T}{\partial z}\right|_{z=0} = AI_0 H(t) \tag{4.77}$$

where $I_0 = 4P_L/(\pi d^2)$, with boundary condition $T(\infty,t) < \infty$, $t < \infty$ and initial condition $T(z,0) = 0$. In the following the transfer functions corresponding to a semi-infinite work piece, and to a plate of finite thickness are derived.

Semi-infinite work piece

The set of equations (4.76) and (4.77) can be solved by applying the Laplace transform with respect to time, which reduces the partial differential equation (4.76) to an ordinary differential equation

$$s\widetilde{T} - \kappa \frac{d^2\widetilde{T}}{dz^2} = 0,\ \forall z \in \mathbb{R}^+ \tag{4.78}$$

where $\widetilde{T} = \widetilde{T}(z) = L\{T(z,t)\}$ denotes the Laplace transform of $T(z,t)$ with respect to time. Then the corresponding boundary and initial condition read,

$$-K \left.\frac{d\widetilde{T}}{dz}\right|_{z=0} = \frac{AI_0}{s} \Rightarrow \left.\frac{d\widetilde{T}}{dz}\right|_{z=0} = -\frac{AI_0}{Ks} \tag{4.79}$$

$$\widetilde{T}(\infty) = 0 \tag{4.80}$$

Solving differential equation (4.78) yields

$$\widetilde{T}(z) = C_1 e^{z\sqrt{s/\kappa}} + C_2 e^{-z\sqrt{s/\kappa}} \tag{4.81}$$

where C_1 and C_2 are constants to be determined from the boundary and initial conditions. From (4.81) and (4.80) it follows that $C_1 = 0$. Then C_2 follows from (4.79) and (4.81). Hence, the corresponding transfer function $G(s)$, according to (4.67), follows from (4.81) divided by I_0/s,

$$G(s) = \frac{A\sqrt{\kappa}}{K}\frac{1}{\sqrt{s}} e^{-z\sqrt{s/\kappa}} \tag{4.82}$$

Figure 4.17(a), shows the Bode diagram of this transfer function for Ti6Al4V. The nonlinearities of the transfer function are comparable to those of the transfer function of the point source (4.73). The gain of transfer function (4.82) decays with 10 dB per decade, instead of (a multiple of) 20 dB per decade, as would be the case for a finite-dimensional process. For increasing depth the gain decreases. The exponent has a strong effect on the phase shift. For a finite-dimensional process a term like $\exp[-zs/\sqrt{\kappa}]$ implies a depth dependent delay. However, the argument of the exponent in (4.82) is a function of $\sqrt{s}$ instead of s. This makes that the phase shift of (4.82) for $z > 0$ is increasing with an ever increasing rate as frequency increases.

The availability of transfer function (4.82) has the advantage that the temperature field $T(z,t)$ in time domain can be calculated for an arbitrary time function $g(t)$ of the

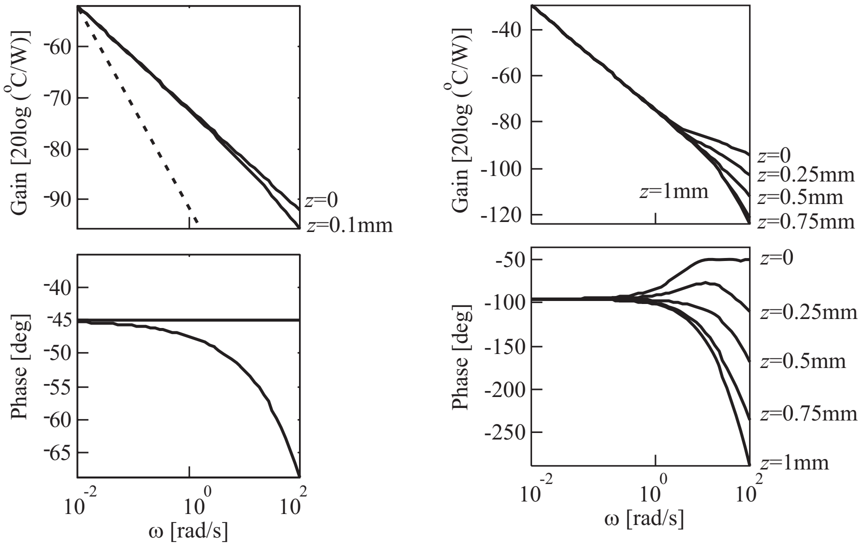

(a) Semi-infinite work piece. Equation (4.82). The dashed curve in the gain diagram decreases at 20 dB per decade.

(b) Plate of thickness $z_d = 1\,\text{mm}$. Equation (4.93).

Figure 4.17: Bode diagram of the transfer function of laser heating of Ti6Al4V at several depths.

absorbed laser energy input (i.e. $AI_0 g(t)$), without restarting the solution procedure all over again. E.g. the temperature field $T(z,t)$ for a step shaped time function $g(t) = H(t)$ is obtained by multiplying equation (4.82) with the Laplace transform of the absorbed power $\mathcal{L}\{AI_0 H(t)\} = AI_0/s$ and by subsequently calculating the inverse Laplace transformation of the product,

$$T(z,t) = \mathcal{L}^{-1}\left\{G(s)\frac{AI_0}{s}\right\} = \frac{2AI_0}{K}\sqrt{\kappa t}\,\text{ierfc}\left(\frac{z}{2\sqrt{\kappa t}}\right), t > 0 \tag{4.83}$$

where the inverse Laplace transform $\mathcal{L}^{-1}\{s^{-3/2}e^{-C\sqrt{s}}\} = 2\sqrt{t}\,\text{ierfc}\left[C/(2\sqrt{t})\right]$ from Erdelyi (1954) has been applied. Figure 4.18 shows the temperature according to equation (4.83) for Ti6Al4V at several depths (dashed curves). As can be observed from this figure, and the Bode diagram (figure 4.17(a)), the process of one-dimensional heat flow laser heating resembles that of a linear first order, delayed process, in which the delay increases for increasing depth, according to

$$G(s) = \frac{s\tau_1 + 1}{s(s\tau_2 + 1)}e^{-zs\tau_3} \tag{4.84}$$

in which the constants τ_i, $i = 1, 2, 3$ depend on material properties, the depth z, and the

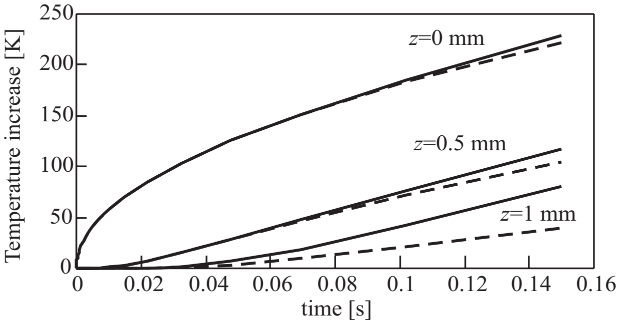

Figure 4.18: Temperature at three depths z in Ti6Al4V, for semi-infinite work piece (dashed curves) and plate of thickness $z_d = 1\,mm$ (solid curves), absorbed density $AI_0 = 50\,MWm^{-2}$.

frequency range of interest. Hence, the dynamics of the non-linear process can be approximated by a low order time-invariant parametric function.

Observability and controllability

Assume that the temperature at the surface $T_{\text{surf}}(t)$ is measured in real-time, then it follows from (4.83) that $t = \pi[KT_{\text{surf}}(t)/(AI_0)]^2/(4\kappa)$ and

$$T(z,t) = T_{\text{surf}}(t)\sqrt{\pi}\,\text{ierfc}\left(\frac{zAI_0}{K\sqrt{\pi}T_{\text{surf}}(t)}\right) \tag{4.85}$$

This implies that $T(z,t)$ directly follows from the measured $T_{\text{surf}}(t)$. This, in turn implies that the process, when approximated by a one-dimensional heat flow, is observable.

Substitution of the interaction time (4.55) $t = t_i = d/v$ in equation (4.83) gives

$$T(z,t_i) = \frac{2AI_0}{K}\sqrt{\frac{\kappa d}{v}}\,\text{ierfc}\left(\frac{zv}{2\sqrt{\kappa d v}}\right) \tag{4.86}$$

For $z \approx 0$ this temperature is close to the maximum temperature reached during the heating phase. For the surface ($z = 0$) this temperature equals

$$T(0,t_i) = \frac{2AI_0}{K}\sqrt{\frac{\kappa d}{v}}\,\text{ierfc}(0) = \frac{2AI_0}{K}\sqrt{\frac{\kappa d}{v\pi}} \tag{4.87}$$

Then, the ratio of the temperature $T(z,t_i)$ (4.86) and the surface temperature (4.87)

$$\frac{T(z,t_i)}{T(0,t_i)} = \frac{1}{\sqrt{\pi}}\,\text{ierfc}\left(\frac{zv}{2\sqrt{\kappa d v}}\right) \tag{4.88}$$

Observability is a characteristic of a dynamic process. A process is observable if the entire process state can be calculated from the (measured) process inputs and outputs (Åström and Wittenmark, 1997).

is independent of I_0. This implies that the temperature $T(z,t_i)$ is controllable through I_0 and v. Consider for instance, two pairs of operating parameters (I_1, v_1) and (I_2, v_2), which are to generate the same maximum surface temperature at $t = t_i$. This requires for I_2

$$T(0,t_i)|_{I_1,v_1} = T(0,t_i)|_{I_2,v_2} \Rightarrow \frac{2AI_1}{K}\sqrt{\frac{\kappa d}{v_1\pi}} = \frac{2AI_2}{K}\sqrt{\frac{\kappa d}{v_2\pi}} \Rightarrow I_2 = I_1\sqrt{\frac{v_2}{v_1}} \tag{4.89}$$

Then the temperature $T(z,t_i)$ reached at a depth z at time $t = t_i$, can be arbitrarily chosen such that

$$T(z,t_i)|_{I_1,v_1} \neq T(z,t_i)|_{I_2=I_1\sqrt{\frac{v_2}{v_1}},v_2}\,,\ z > 0 \tag{4.90}$$

by appropriate selection of v_1 and v_2. This allows the dimensions of the heat affected zone ($0 \leq z \leq \delta_h$) to be selected arbitrarily and simultaneously keeping the maximum surface temperature at a constant value.

Controllability and observability of infinite-dimensional processes

It should be noted that the conclusions of observability and controllability of the process are based on one-dimensional heat flow in the work piece. The 3-dimensional temperature distribution in the work piece is not controllable, nor observable, according to the definitions of the classical linear control theory. However, Curtain and Zwart (1995) showed that the 3-dimensional temperature distribution is *approximately controllable*. According to this definition an infinite-dimensional process with command signal $u(t)$, is approximately controllable if for any initial state x_1, and constant $\varepsilon > 0$, there exists a time t_0 such that through proper selection of $u(t)$, the state x_2 can be reached, within accuracy ε, from state x_1, in time range $[0, t_0]$. *Approximate observability* is defined analogously.

Plate of finite thickness

Consider a one-dimensional heat flow in a plate with thickness z_d [m]. Then the process is also described by partial differential equation (4.76) and initial condition $T(z,0) = 0$, except for the boundary condition (4.77), which is replaced by

$$\left.\frac{\partial T}{\partial z}\right|_{z=0} = \begin{cases} -AI_0H(t)/K, & z = 0 \\ 0, & z = z_d \end{cases} \tag{4.91}$$

The procedure to solve (4.76) with (4.91) is identical to the method discussed in the previous paragraph. In this case however, the constants C_1 and C_2 both follow from the Laplace transform of (4.91). This yields for the Laplace transform $\widetilde{T}(z) = L\{T(z,t)\}$

$$\widetilde{T}(z) = \frac{AI_0\sqrt{\kappa}}{Ks^{\frac{3}{2}}\left(1 - \exp\left[2z_d\sqrt{s/\kappa}\right]\right)}\left(\exp\left[-z\sqrt{\frac{s}{\kappa}}\right] + \exp\left[-2(z_d - z)\sqrt{\frac{s}{\kappa}}\right]\right) \tag{4.92}$$

for $0 \leq z \leq z_d$. Hence, the transfer function $G(s)$ of this process, according to (4.67) equals

$$G(s) = \frac{A\sqrt{\kappa}}{K\sqrt{s}\left(1 - \exp\left[2z_d\sqrt{s/\kappa}\right]\right)} \left(\exp\left[-z\sqrt{\frac{s}{\kappa}}\right] + \exp\left[-2(z_d - z)\sqrt{\frac{s}{\kappa}}\right]\right) \tag{4.93}$$

This transfer function approaches the transfer function of the semi-infinite work piece (4.82) if $z_d \rightarrow \infty$. This is also the case for high frequencies ($s \rightarrow \infty$). This implies that for $t \approx 0$ a work piece of finite thickness resembles that of semi-infinite dimensions.

Figure 4.17(b) shows the Bode diagram of this transfer function for Ti6Al4V with $z_d = 1\,\text{mm}$. The transfer function (4.93) is a function of $\sqrt{s}$, like was the case for the semi-infinite work piece. However, for low frequencies the gain decays with 20 dB/decade, which corresponds to that of a first order process. For low frequencies the phase shift equals -90°, which also corresponds to that of a first order process.

Similar as in the previous paragraph, the temperature field $T(z,t)$ in the time domain is obtained by inverse Laplace transformation with respect to s (Prudnikov *et al.*, 1992a), or by the use of the principle of image heat sources (see section 4.2.2), to yield

$$T(z,t) = \frac{AI_0\sqrt{4\kappa t}}{K}\left[\text{ierfc}\left(\frac{z}{\sqrt{4\kappa t}}\right) + \sum_{n=1}^{\infty}\left(\text{ierfc}\left(\frac{2nz_d - z}{\sqrt{4\kappa t}}\right) + \text{ierfc}\left(\frac{2nz_d + z}{\sqrt{4\kappa t}}\right)\right)\right] \tag{4.94}$$

Figure 4.18 shows this temperature (4.94) for Ti6Al4V, at several depths (solid curves). The influence of finite thickness is obvious.

It can be concluded from these observations that the process of one-dimensional heat flow in a plate resembles that of a linear first order, delayed process (4.84), in which the parameters τ_i, $i = 1,2,3$ also depend on the plate thickness z_d.

4.5 Conclusions

In this chapter, it was shown that the conservation law of energy (heat conduction equation) plays a central role in the physical modelling of the process of laser surface treatment. The models resulting from this equation were used to analyze the effects of the laser power, the beam velocity and the disturbances on the temperature distribution and the melt pool dimensions:

- Steady state properties like the maximum surface temperature (4.46)-(4.48) and the melt pool depth (4.66) depend on the ratio $P_L/(\sqrt{vd})$ of the operating parameters,
- It followed from the temperature distribution (4.36), expressed in the dimensionless variables, that the effects of an absorptivity disturbance can be best suppressed by applying the laser power as a command signal,
- To counteract the temperature increase due to a part of the work piece of reduced thickness (geometrical disturbance), the beam velocity can be best applied as a command signal (figure 4.11),

- The transfer function relating the laser power to the work piece temperature is a non-rational function of $\sqrt{s}$ (section 4.4.1 and 4.4.2), but its low frequency properties can be approximated by a delayed, (possibly) first order, rational transfer function.

These conclusions will be verified in the next chapter. It will be shown that these conclusions also hold for the melt pool surface area during laser alloying.

Chapter 5

EXPERIMENTAL SET-UP AND PROCESS IDENTIFICATION

In this chapter the experimental set-up is presented and some of the models of the previous chapter are verified. Guided by the conclusions from the models of the previous chapter, the static and dynamic response of the alloying process are analyzed experimentally.

5.1 Experimental set-up

The laser material processing system for laser alloying of titanium with nitrogen consists of: a laser source, focusing optics, an XY-table to manipulate the work piece and means of supplying additional material. Two pyrometers and a thermal camera are applied as sensors for feedback control.

Laser source and focusing optics

A ROFIN SINAR 1700RF, radio frequency excited, fast axial flow CO_2 laser source with a maximum output power of 1700 W is used in the experiments (see table 5.1). The response of the source to a step input was shown in figure 3.3 on page 21. The laser source is characterized by having a fast response on power command (rise time $t_r \approx 22\,\mu\mathrm{s}$), and is therefore well suited as an actuator for closed loop control. The laser beam is guided by mirrors to focusing optics, through which it impinges perpendicularly on the work piece mounted on a XY-table.

A plano-convex ZnSe lens, with focal length of $f = 154.5\,\mathrm{mm}$, is applied to converge the beam to a diameter of $d = 1.1\,\mathrm{mm}$ on the work piece surface. The measured intensity profile of the focused beam, is shown in figure 5.1. To protect the lens against contamination from the process, nitrogen gas (purity 3.0, flow rate $4\,\mathrm{l}\cdot\mathrm{min}^{-1}$) is supplied coaxially

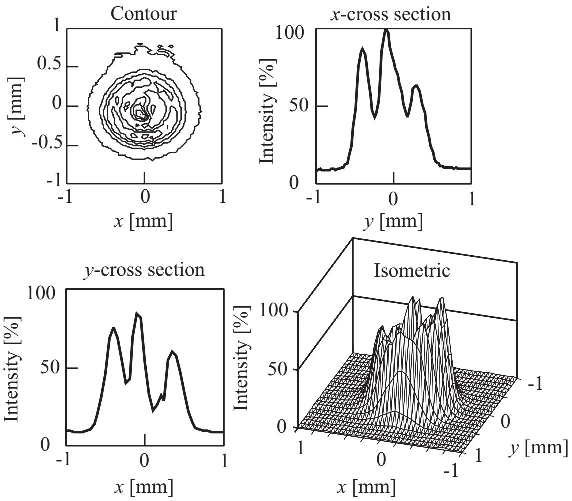

Figure 5.1: Laser beam intensity profile on the work piece (averaged over 5 measurements), as measured by a PROMETEC *UFF100 beam analyzer. Beam diameter $d = 1.1\,mm$.*

Table 5.1: Characteristics of the ROFIN SINAR *1700RF CO_2-laser.*

Wavelength [μm]	10.6
Polarization	circular
Maximum output power [W]	1700
TEM_{pl} mode†	TEM_{01^*}+TEM_{00}
Unfocussed diameter [mm]	17
Beam quality $M^2\,[-]$	1.72
Ellipticity $d_x/d_y\,[-]$	1.079
Bandwidth [kHz]	16

† See appendix A.1.

through a nozzle. The lens is heated prior to processing, by irradiating a dummy work piece. This suppresses varying beam diameter caused by thermal lensing (see figure 3.3).

The laser source is operated by means of a *Laser Controller* (LC), which in turn accepts commands from a *Work Station Controller* (WSC), see figure 5.2.

Product manipulation

The work piece is manipulated by a SCHAAD XY-table (Schippers, 1994). The two independent axes are servo-controlled by a GALIL DMC-630, three axis, digital PID motion controller, which is a PC-board hosted by the Work Station Controller (WSC). The acceleration is programmable up to $3\,\text{m}\cdot\text{s}^{-2}$. During the experiments the acceleration is set

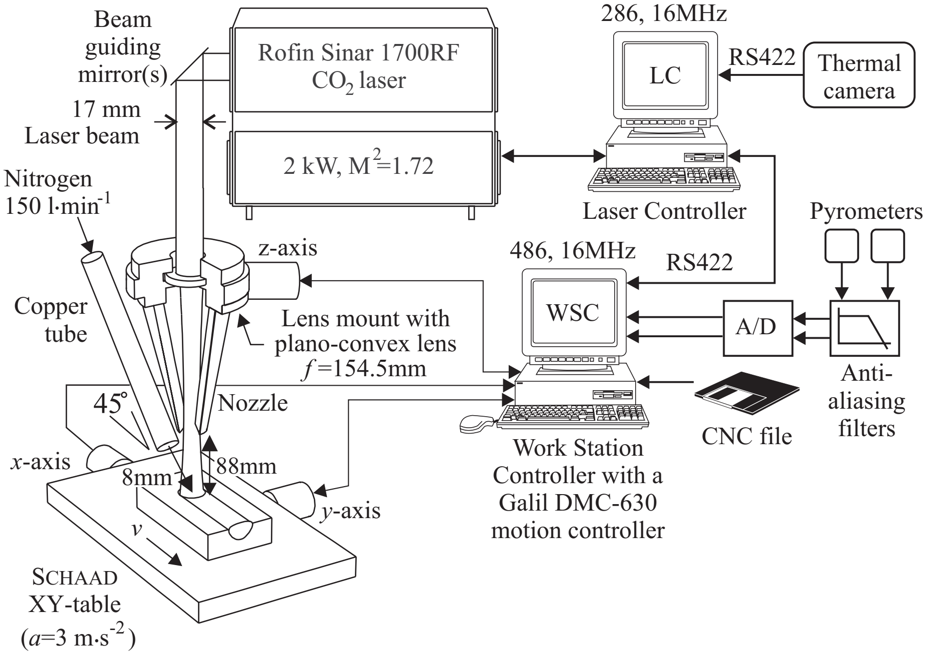

Figure 5.2: The experimental set-up.

to this maximum in all cases. The maximum velocity of both axis is 300 mm·s $^{-1}$. The actual velocity, as indicated by the motor encoders, has been measured during the experiments. The microprocessor of the Work Station Controller communicates with the GALIL motion controller through a First-In-First-Out (FIFO) buffer. This buffer introduces a considerable delay of 6.2 ms. The closed loop bandwidth of the XY-table is 50Hz, which is considerably smaller than the bandwidth of the laser source. The third axis of the motion controller drives the *z*-axis to which the focusing optics are mounted.

Supply of additional material & process shielding

Nitrogen is supplied to the melt pool by a copper tube with an inner diameter of 6 mm, at a standoff distance of 8 mm and under an angle of 45 °. The tube is directed in the positive *x*-direction, which provides protection against oxidation behind the melt pool. The applied gas flow rate of 150 l·min $^{-1}$ is relatively large to avoid plasma (Beyer, 1985; Seirsten, 1988).

The set-up is operated through ISO CNC files, loaded into the Work Station Controller. This computer takes also care of data logging. The Laser Controller and Work Station Controller are part of a multi-laser, multi-work-station configuration (Blonk, 1991).

Sensors

Two commercially available pyrometers and a thermal camera are applied as sensors for the control of laser surface alloying.

Pyrometers

The pyrometers are a KLEIBER 270A spectral pyrometer and an IMPAC ISQ-LO ratio pyrometer. Table 5.2 lists the properties of these pyrometers.

Table 5.2: Some characteristics of the applied pyrometers.

Characteristic	KLEIBER 270A	IMPAC ISQ-LO
Operating type	Spectral	Ratio
Spectral sensitivity [μm]	0.85 to 1.1	0.95 and 1.05
Temperature range [°C]	790 to 2300	1050 to 2600
Rise time t_r [ms]	0.3	10
Accuracy, in % of measured value	±1	±1
Diameter measurement spot	$\geq 1\,$mm	$\geq 0.45\,$mm
Measuring distance [mm]	380	87

The spectral pyrometer is calibrated for black body radiation. The emissivity can be corrected for between 0.1 and 1. Preliminary alloying experiments showed that the emissivity of the pyrometer should be set to $\varepsilon = 0.7$ to properly measure the temperature of liquid titanium (see also figure 2.3(b) on page 10). The advantage of this pyrometer is its small response time of $t_r = 0.3\,$ms. The pyrometer housing is attached to the lens mount and directed at the laser-material interaction zone, in the negative x-direction, at an angle of 30°, see figure 5.3.

The optics of the pyrometer are adjusted such that the diameter of the effective measurement spot on the work piece is larger than diameter of the melt pool, see figure 5.6. In this configuration, the signal variations of the pyrometer signal are determined by the melt pool temperature, as well as by the surface area of the melt pool. This can be understood by analyzing the voltage V (3.12) generated by the optical detector in the spectral pyrometer. This voltage is electronically processed by the pyrometer to obtain a signal T_s which is proportional to the temperature T,

$$T_s \propto \sqrt[n]{V} = \sqrt[n]{K_s' S_m S_d T^n} = T \sqrt[n]{K_s' S_m S_d} \tag{5.1}$$

in which the area S_b of the emitting body was replaced by the melt pool area S_m. Because the effective measurement spot of the pyrometer on the work piece is larger than the melt pool surface diameter ($S_d > S_m$), the relative sensitivity of the pyrometer signal T_s to a change in temperature follows from (5.1) as

$$\frac{dT_s}{T_s} \Big/ \frac{dT}{T} = 1 \tag{5.2}$$

and the relative sensitivity of the pyrometer signal T_s to a change in melt pool surface area

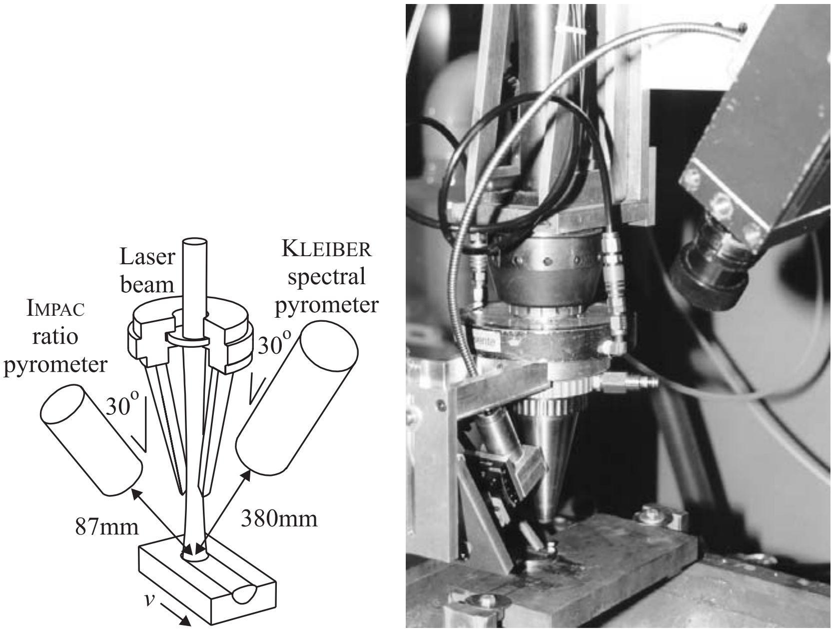

(a) Configuration of the pyrometers with respect to the laser beam and the work piece.

(b) Optical head of ratio pyrometer (lower left), lens mount and nozzle (center), work piece (center bottom) and spectral pyrometer (upper right).

Figure 5.3: Arrangement of the pyrometers in the experimental set-up.

equals

$$\frac{dT_s}{T_s}\bigg/\frac{dS_m}{S_m}=\frac{1}{n} \tag{5.3}$$

with $n \geq 1$. For laser alloying of titanium with nitrogen the average melt pool temperature is about 2400 °C (see section 5.3.1). For this temperature, the maximum spectral radiance occurs at $\lambda_m \approx 1.07\mu$m, see equation (3.7). The center of spectral sensitivity of the KLEIBER pyrometer is $\lambda_d = 0.975\mu$m (table 5.2). Then it follows from equation (3.8) that $n \approx 5.48$. This means that the spectral pyrometer is more sensitive to a change in temperature, than to a change in melt pool area. However, it will be shown in section 5.3.1 that for laser nitriding of titanium the relative variation of the melt pool area, due to a variation of the operating parameters, is much larger than the relative increase of the melt pool temperature. As a result, variations of the pyrometer signal are mainly determined by the melt pool area, and to a lesser extent by the melt pool temperature.

The ratio pyrometer consists of three parts: (*i*) an optical head with an achromatic lens, (*ii*) a 2.5 m long fiber optic (core 0.2 mm) guiding the radiation from the optical head to a signal converter, and (*iii*) a signal converter, which converts the radiation into an electrical signal. The optical head is attached to the lens mount and directed to the laser-material interaction zone, at an angle of 30°, see figure 5.3. The main advantage of this pyrometer is the small diameter of the measurement spot (0.45 mm). This pyrometer will be used to measure the temperature in, or directly behind the melt pool.

Both pyrometers are connected, through anti-aliasing filters, to two 14 bit, 42 μs, A/D-converters, hosted by the Work Station Controller, see figure 5.2. The anti-aliasing filters are second order low-pass Butterworth filters with adjustable cut-off frequency. The total set-up allows a maximum sample rate of the pyrometer signals of 1100 Hz.

Thermal camera

A high speed DALSA digital CCD camera is used to monitor the temperature distribution of the laser-material interaction zone. The DALSA CA-D1-128A area scan camera is equipped with a silicon Charge Coupled Device (CCD), with an active area of 2.048 mm × 2.048 mm consisting of 128 × 128 photogate photoelements of 16μm × 16μm with a pitch of 16μm (100% fill factor). Due to the high fill factor, aliasing in spatial domain is prevented. The exposure time of the chip is almost equal to the inverse of the frame rate of the camera. Hence, aliasing in temporal domain is also prevented. The camera can generate up to 419 frames per second, which implies an exposure time of approximately 2.4 ms. Introductory tests proved that this exposure time is sufficiently short in order to detect variations in the shape of the melt pool during processing. The camera is equipped with an A/D-converter, which converts the analog pixel signals to a digital RS422, 8 bit output (each pixel can represent 256 gray levels (*GL*)). The spectral sensitivity of the silicon chip ranges from 400 to 1100 nm, which was narrowed by SCHOTT optical filters (KG1 and RG1000) to obtain a high temperature resolution during the nitriding of titanium. This is discussed in more detail in appendix C.1.

The camera is attached to the lens mount and directed at the laser-material interaction zone, parallel to the direction of processing, under an angle of 35°, see figure 5.4. To ensure sharp images despite this angle, the camera, its optics and the work piece are configured to satisfy *Scheimpflug's condition* (Zhang and Prasad, 1997), see figure 5.4(a).

The camera and its optics were placed at a distance of 160 mm from the laser-material interaction zone, to protect it against high temperatures and drops of molten metal from the melt pool. The camera optics are composed of an achromatic lens ($f = 160$ mm, $\varnothing$40 mm) and a commercially available AUTO UNIVERSAR tele-lens with a focal length of $f = 200$ mm (1:3.5), see figure 5.4(b). Spectral filters were placed between the achromatic lens and the telelens. In this configuration, an area of 1.55 mm × 1.55 mm of the work piece is projected on to the CCD chip. Prior to each experiment the camera was (re)adjusted carefully to guarantee sharp and well aligned images.

The images generated by the camera are uploaded, via a RS422 link, to a DIPIX XPG-1000 frame grabber PC-board, which is equipped with a Digital Signal Processor (DSP). This frame grabber allows simultaneous image acquisition and processing, resulting in a high image processing rate. The frame grabber is hosted by an IBM compatible PC (486, 66MHz), which is referred to as the *Camera Computer* (CC). It is connected via an RS422 link to the Laser Controller for on-line control purposes.

Figure 5.5(a) shows a typical image, which was recorded during laser alloying of titanium. Figure 5.5(b) and 5.5(c) show a contour plot (isotherms) and a three dimensional

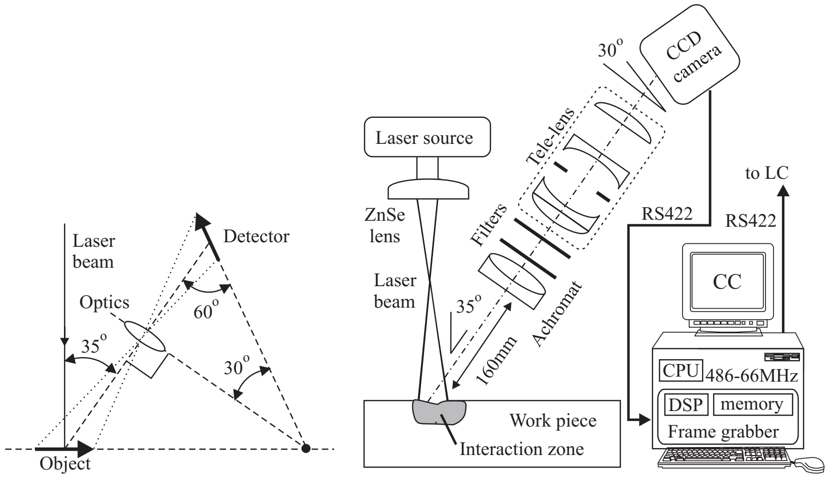

(a) Alignment of work piece, optics and detector, according to Scheimpflug's condition.

(b) The camera, its optics, the filters and the frame grabber in the experimental set-up.

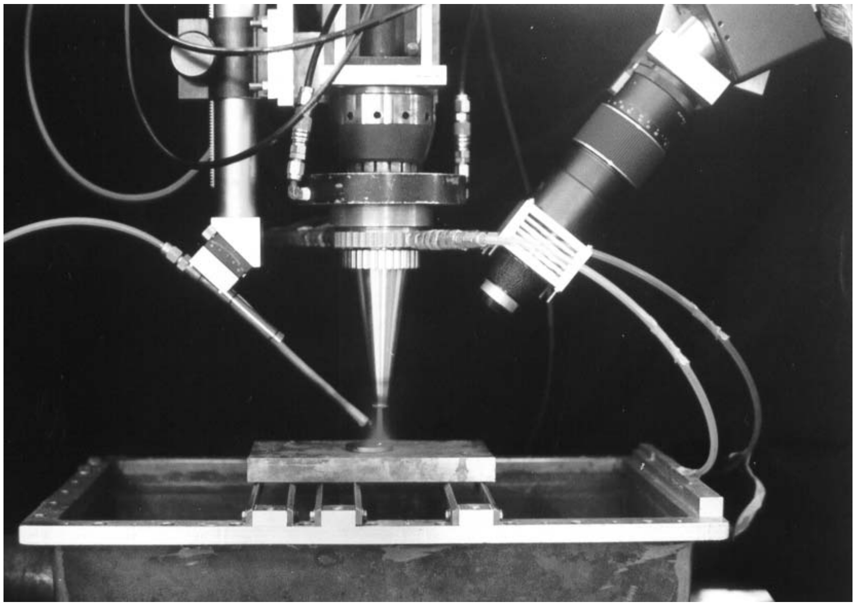

(c) The tube supplying nitrogen (left), the lens mount and nozzle (center), work piece on the XY-table (center bottom) and the thermal camera (right).

Figure 5.4: Arrangement of the thermal camera in the experimental set-up.

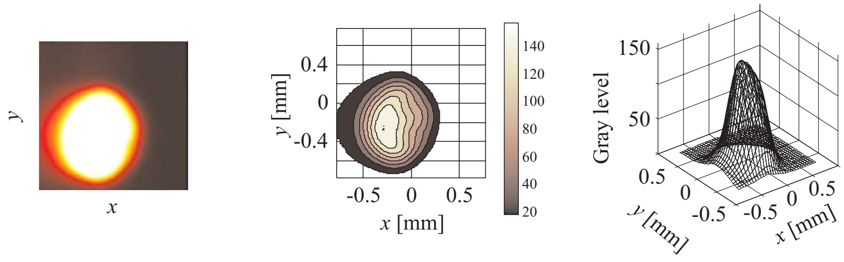

(a) Thermal image.

(b) Contour plot.

(c) Isometric gray levels.

Figure 5.5: Some representations of an image of the melt pool during laser alloying of titanium obtained by the thermal camera. Laser power 500 W*, beam velocity* 50 mm·s^{-1}*, beam diameter* 1.1 mm*. The laser beam moves from left to right (positive x-direction).*

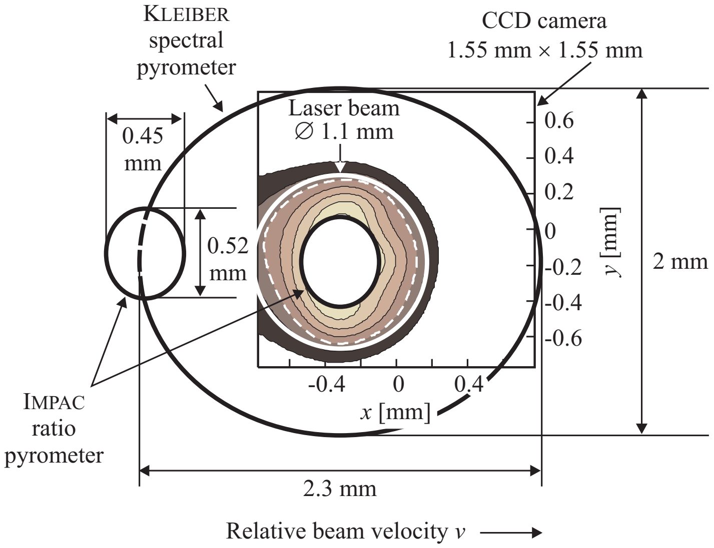

Figure 5.6: The alignment of the field of view of the three optical sensors with respect to the laser beam, the melt pool (white, dashed) and gray level contour (as measured by the thermal camera). The ratio pyrometer is applied in two configurations. Either to measure the temperature in or behind the melt pool.

(isometric) representation of the same data. The gray level of each pixel on the CCD chip is determined by the temperature and the exposure time or *integration time*. Hence, each gray level corresponds to a temperature. It was found by calibration (appendix C.2) that the gray level (GL_m), corresponding to the temperature of the solid-liquid interface during laser nitriding of titanium, equals $GL_m = 60.9 \pm 5.3$. With this gray level, the shape and dimensions of the melt pool can be determined from the recorded images. The melt pool surface area can be determined by summing all pixels with a gray level over 61. Then, for this set-up, the melt pool area in mm^2, can be calculated by multiplying the sum by the factor $(1.55)^2/(128)^2$.

Figure 5.6 shows the alignment of the field of view of the three optical sensors with respect to the laser beam and the melt pool. The ratio pyrometer is applied in two ways: (*i*) to measure the temperature in the melt pool and (*ii*) to measure the temperature behind the melt pool (section 5.3.1 and 5.3.3 respectively). Due to the limited space it was not possible to apply the pyrometers and the thermal camera simultaneously.

5.2 Analysis of steady state characteristics

In this section, the steady state properties of laser alloying of titanium with nitrogen are analyzed. These properties include the microstructure after solidification, the melt pool depth and the absorptivity. In addition, the output of the model describing the melt pool, which was derived in section 4.3.3, is verified experimentally.

5.2.1 Laser alloying of titanium with nitrogen

Laser nitriding of titanium improves its wear and friction properties (Dobbs and Robertson, 1983). Titanium-nitride (TiN) is formed by melting the surface in a nitrogen atmosphere, according to the exothermic chemical reaction

$$Ti + \frac{1}{2}N_2 \leftrightharpoons TiN \tag{5.4}$$

Titanium-nitride shows extreme hardness (Vickers hardness HV=2000-3000), high melting temperature (2950 °C) and the aesthetic qualities of a golden color (Savvides and Window, 1988; Zambon *et al.*, 1994). After solidification the layer thickness is of the order of 250 μm, which is large compared to nitriding by solid state diffusion (Laurens *et al.*, 1996; L'Enfant, 1996). The physical properties of titanium and titanium-nitride are listed in appendix D.

The titanium used in the experiments is a commercial grade Ti6Al4V ($6\%Al, 4\%V$). The samples were in the form of discs (∅ 40 mm), with a thickness of 4 mm. The surface of each sample was blasted with glass balls to obtain an equal and uniform surface. The discs were subsequently degreased in alcohol, and mounted on a heat sink to simulate a thermally semi-infinite sample. The samples were submitted to single parallel scannings (no overlap) and always in the same direction. The beam velocity was varied from 20 to 90 mm·s^{-1} and the laser power was varied from 500 to 1500 W. The layer thickness and its microstructure were studied with a microscope from cross sections, obtained by a *saw-polish-etch* method.

Microstructure

Figures 5.7 and 5.8 show the cross sections of samples produced with beam velocities at two laser power levels. For $P_L = 1000$ W, the gray level contour plots as measured by the

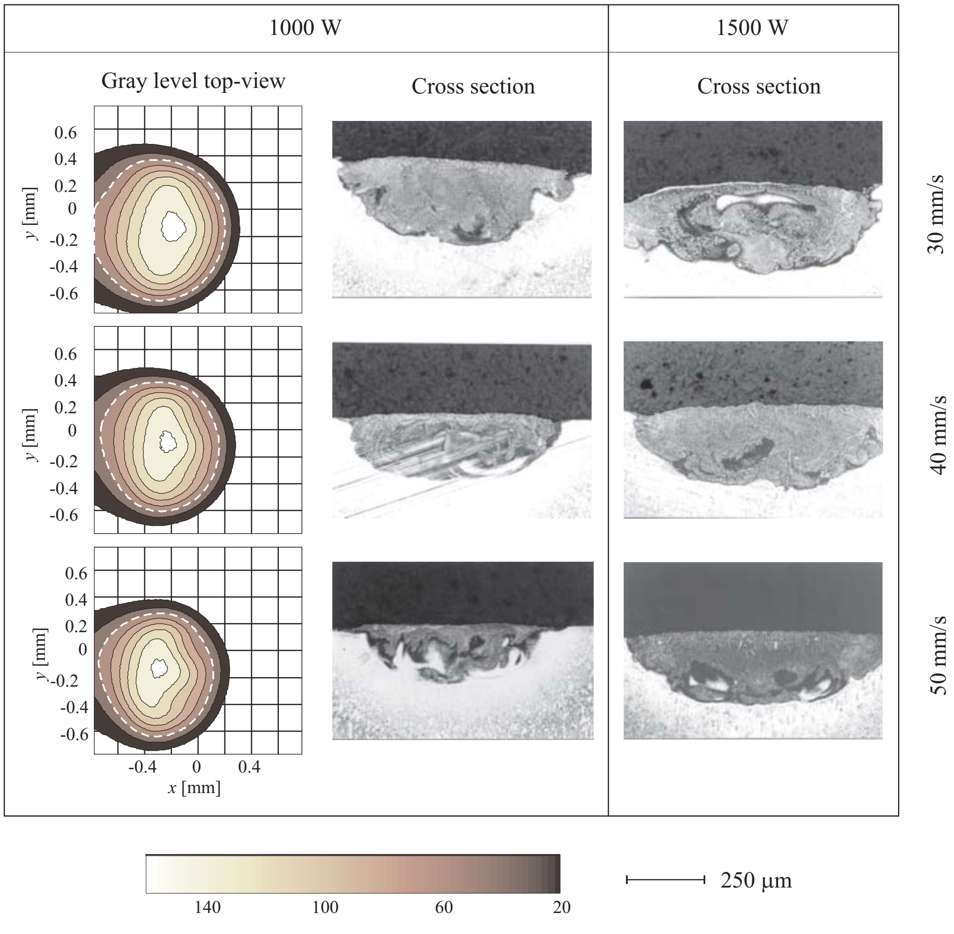

Figure 5.7: Cross-sections of Ti6Al4V alloyed with nitrogen at two power levels and at different beam velocities. For $P_L = 1000\,W$, also the gray level contour plots of the melt pool are shown. The dashed white contour represents the gray level $GL_m = 61$ corresponding to the temperature of the solid-liquid interface. Continued in figure 5.8.

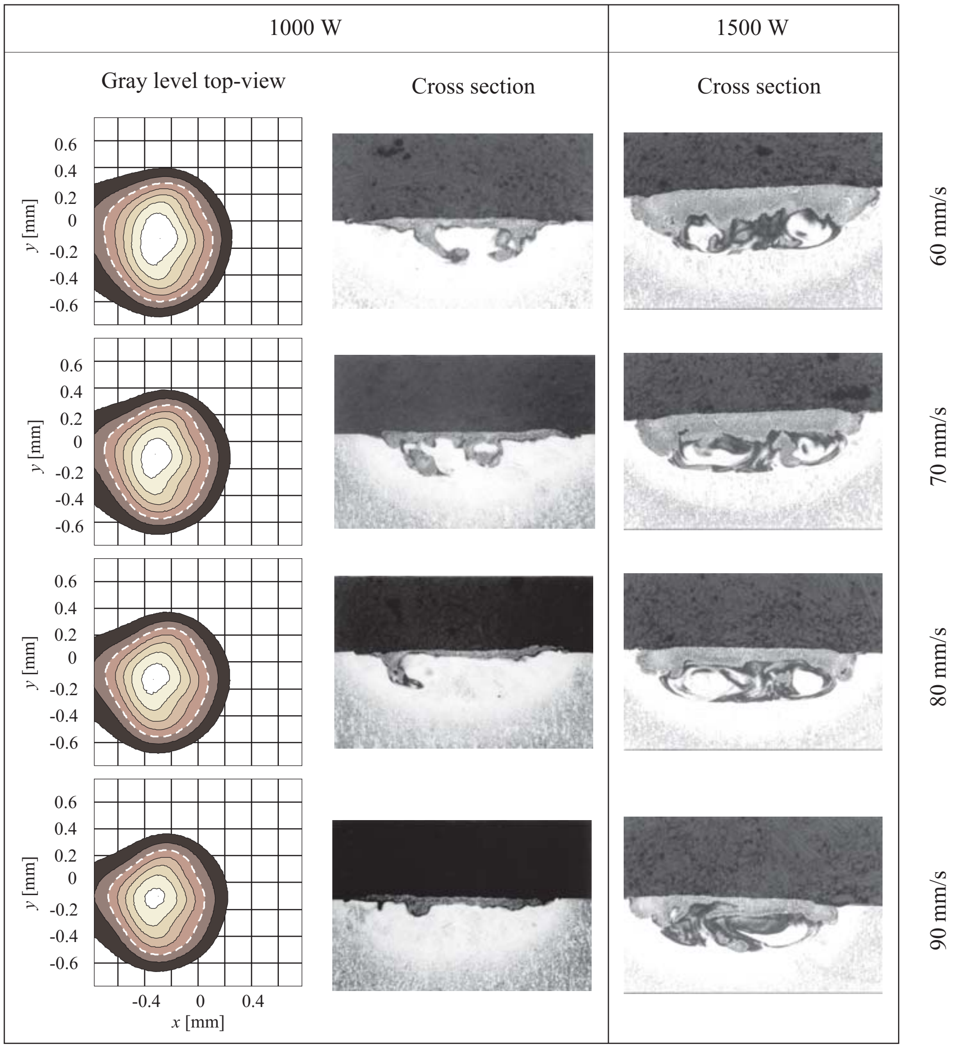

Figure 5.8: Continued from figure 5.7.

thermal camera are also shown. As can be observed from these contour plots, the shape of the melt pool changes, with increasing beam velocity.

The cross sections clearly show the solidified melt pool, the ”frozen” thermocapillary flow within, the Heat Affected Zone (HAZ) beneath it, and the untreated base material. Figure 5.9 shows these regions schematically. With decreasing beam velocity and increasing laser power, the microstructure of the solidified melt pool becomes more homogeneous. For beam velocities over $70\,\mathrm{mm \cdot s^{-1}}$ at a laser power of 1000 W, the supplied energy is insufficient for complete development of the melt pool. Therefore, these operating conditions are not considered in the following.

The microstructure of the solidified melt pool consists primarily of TiN dendrites within a nitrogen enriched $\alpha - \mathrm{Ti}$ matrix (Robinson *et al.*, 1994). The top region consists of a layer (zone 1) of columnar TiN dendrites, oriented perpendicularly to the surface. The solidification temperature of this zone ranges between 2950 °C and 3290 °C. On the basis of the orientation of these dendrites, it can be concluded that the solidification starts at the surface and not at the solid-liquid interface (Zambon *et al.*, 1994). Under the columnar layer, a dark colored layer (zone 2), with randomly oriented dendrites is observed, involving a peritectic reaction (at 2350 °C) between $\alpha - \mathrm{Ti}$ and $\delta - \mathrm{TiN}$, see the phase diagram of the titanium-nitrogen system in appendix D. Finally, a light colored region (zone 3) is observed. The nitrogen amount in this region is low (Kloosterman, 1998). Careful analysis with a SEM microscope suggested that this region was not melted during laser radiation.

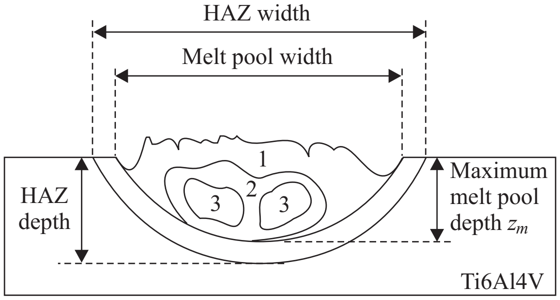

Figure 5.9: Dimensions of the solidified melt pool, the zones within, the heat affected zone beneath it, and the untreated base material.

It should be noted that, the duration (here 12 to 36 ms) of the thermal cycle is so small that the microstructures are not formed under conditions of thermal equilibrium. Kloosterman (1998) analyzed the microstructure of TiN in Ti6Al4V, as a result of laser radiation, in more detail.

At the edges of the melt pool, ”arms” of TiN dendrites lead deeper into the melt pool. For high beam velocities these arms are more developed on the left side of the interaction zone than on the right side. This asymmetry can be attributed to the asymmetry of the laser beam intensity profile (figure 5.1). The edges of the melt pool solidify below the untreated titanium surface, appearing dark colored when observed from the top (figure 5.10(a)).

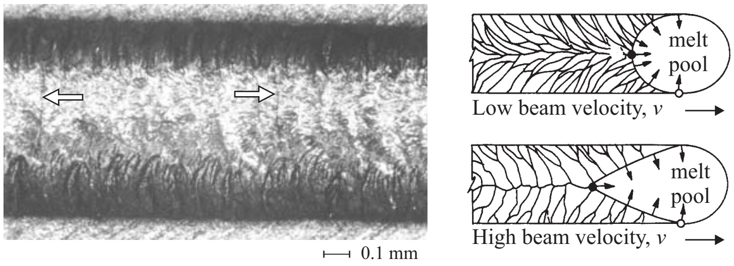

(a) Surface morphology of Ti6Al4V alloyed with nitrogen. The arrows point out cracks. Laser power $P_L = 1000\,\mathrm{W}$, beam velocity $v = 40\,\mathrm{mm{\cdot}s^{-1}}$, $d = 1.1\,\mathrm{mm}$.

(b) The shape of the melt pool, the solidification fronts and the resulting surface morphology depend on the beam velocity (Kloosterman, 1998).

Figure 5.10: Surface morphology of Ti6Al4V alloyed with nitrogen.

Surface morphology

The surface is characterized by typical fish bone shaped ripples, which indicate the contours of the solidification fronts. During solidification, the crystals grow perpendicularly to the solidification front, which corresponds to the direction of the maximum temperature gradient. Because this temperature gradient depends on the beam velocity (see section 4.3.3), the solidification pattern depends also on the beam velocity, see figure 5.10(b).

At small laser powers the surface is characterized by rough and yellow/gray colored ripples. With decreasing laser power the temperature of the melt pool drops and TiN-dendrites form instantaneously. These dendrites impede the thermocapillary flow and as a result a rough surface morphology is obtained (Gasser, 1991; Gasser *et al.*, 1988). Moreover, with decreasing melt pool temperature the amount of TiN-dendrites which are formed reduces, see phase diagram in appendix D. This results in a yellow/gray color of the surface (Robinson *et al.*, 1994). With increasing laser power, the melt pool temperature increases and more TiN will be present in the liquid phase. Moreover, the thermocapillary flow is not impeded in that case. This results in a smooth surface with a shiny golden color (Burchards and Weisheit, 1988).

As can be observed from figure 5.10(a) some cracks are present in the track, perpendicular to the direction of processing. The presence of cracks in the surface layer does not necessarily imply inferior tribological behavior (Kloosterman, 1998; Robinson *et al.*, 1994; Brenner *et al.*, 1996). The detailed analysis of the mechanisms causing these cracks and the methods to minimize crack formation falls outside the scope of this thesis.

At beam velocities less than $20\,\mathrm{mm{\cdot}s^{-1}}$ at power levels over $1500\,\mathrm{W}$, plasma occurred over the laser-material interaction zone, in spite of the carefully aligned nitrogen gas supply. Therefore, these operating parameters will not be applied in the following.

Dimensions of the solidified melt pool

Figure 5.11 shows the dimensions (depth and width) of the different zones in the cross section, as measured from the cross sections. Only laser powers over 1000 W and beam velocities less than 70 mm · s^{-1} are considered, because at these operating parameters, the supplied laser energy is sufficient for complete development of the melt pool. The dimensions increase with increasing laser power and decreasing beam velocity. In section 5.2.3 the measured melt pool depth is discussed in more detail and is compared to the predicted depth, according to the models (4.64) and (4.66).

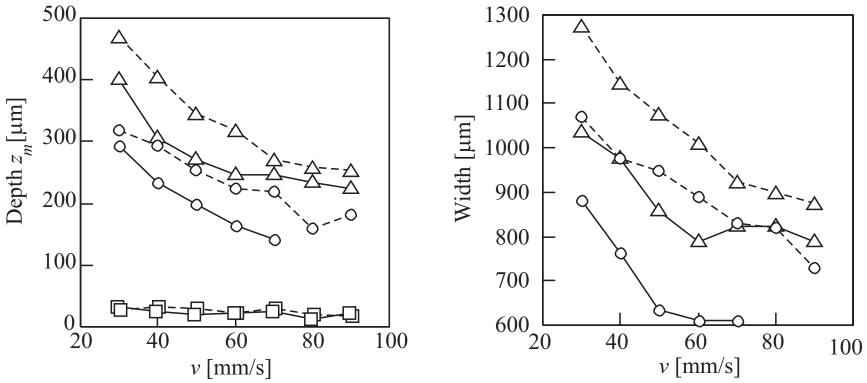

(a) Measured depth of several regions of the alloyed tracks: △ heat affected zone, ○ melt pool, □ zone 1.

(b) Measured width of several regions of the alloyed tracks: △ heat affected zone, ○ melt pool.

Figure 5.11: Measured dimensions of laser processed tracks as a function of beam velocity, at two laser power levels: 1500W (dashed) and 1000W (solid).

Melt pool surface area and thickness of alloyed layer

In figure 5.12 the measured depth of the solidified melt pool and the melt pool surface area S_m as measured by the thermal camera, are depicted in one graph. As can be observed from this figure, the melt pool depth and area show the same dependency on beam velocity—i.e. the melt pool depth is proportional to the melt pool area: $z_m \approx C{\cdot}S_m$, $C = 620\,\mathrm{m}^{-1}$. From this analysis it can be concluded that the melt pool surface area is a measure for the depth of the solidified melt pool, which in turn determines the thickness of the alloyed surface layer. This implies that controlling the thickness of the surface layer is achieved by controlling the melt pool area.

Figure 5.13 shows the dependency of the melt pool area on the beam velocity and laser power. As can be observed, the melt pool area increases not linearly, but at least monotonously with increasing laser power and decreasing beam velocity. This is sufficient for feedback control.

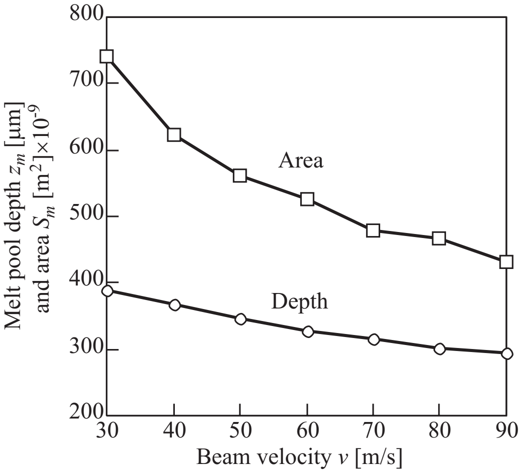

Figure 5.12: Depth of the solidified melt pool (layer thickness) and the melt pool area S_m, as measured by the thermal camera, as functions of beam velocity at constant laser power $P_L = 1000\,W$.

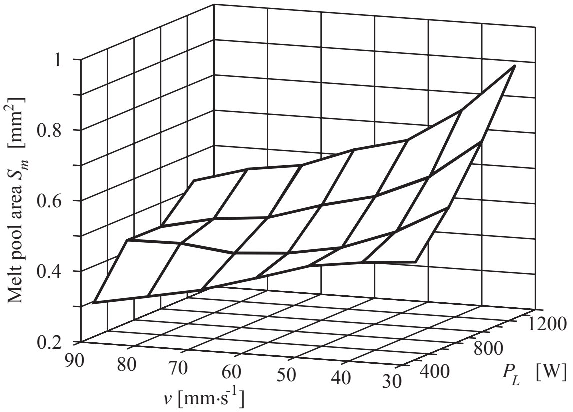

Figure 5.13: Steady state melt pool area S_m as a function of beam velocity and laser power.

5.2.2 Absorptivity of Ti6Al4V in Ar and N_2 atmospheres

To apply the model of the melt pool depth, as derived in section 4.3.3, the absorptivity of liquid Ti6Al4V in an nitrogen atmosphere is required. The absorptivity was measured experimentally. Two methods can be applied:

(*i*) Direct measurement of A by calorimetric methods (Bamberger and Geler, 1997; Frenk *et al.*, 1991; Dekumbis and Frenk, 1988; Hügel *et al.*, 1994),
(*ii*) Indirect determination of A, by measuring the reflectivity R (Ramanathan and Modest, 1994; Prokhorov *et al.*, 1990; Willerscheid, 1990).

The indirect method suffers from some practical difficulties. First, in general the reflected power consists of a direct component and a diffuse (or scattered) component, requiring signal collection over the half space of the irradiated surface. Secondly, for metals the reflectivity is large (typically $R > 0.7$). Consequently a small relative measurement error in R results in a large relative error in $A = 1 - R$. Therefore, the calorimetric method is applied. This method determines the absorptivity using the equation

$$A = \frac{P_A}{P_L} = \frac{mc_p \Delta T}{P_L \Delta t} \tag{5.5}$$

where P_A denotes the absorbed laser energy, P_L the incident laser energy, $m\,[\mathrm{kg}]$ the mass of the work piece, $\Delta t\,[\mathrm{s}]$ the period of irradiation, and $\Delta T\,[^\circ\mathrm{C}]$ the maximum temperature rise of the entire work piece immediately after the irradiation. This maximum temperature rise is derived from the initial temperature T_0 and two temperatures T_1 and T_2 at time t_1 and t_2 ($t_2 > t_1$), measured during the cooling phase, according to (Schneider, 1998)

$$\Delta T = \exp\left[\frac{t_1 \ln(T_2 - T_0) - t_2 \ln(T_1 - T_0)}{t_1 - t_2}\right] \tag{5.6}$$

The temperature of the work piece was measured by a thermocouple. The net laser power impinging on the sample was measured by means of a PROMETEC power meter (accuracy ±1%). Table 5.3 lists the absorptivity at two power levels, during laser alloying of Ti6Al4V with nitrogen (Römer, 1996). For comparison also the absorptivity of Ti6Al4V during melting in an inert atmosphere (argon) was measured. As can be observed from this table, the absorptivity during melting in an argon atmosphere increases with increasing laser power. This can be attributed to increased temperature of the laser-material interaction zone (see figure 3.5 on page 24).

Table 5.3: Measured ($\bar{A}$) and corrected (A) absorptivity of CO_2-laser radiation of liquid Ti6Al4V in Ar and N_2 atmosphere.

Condition	Gas	Beam velocity $v\,[\mathrm{mm\cdot s^{-1}}]$	Laser power $P_L\,[\mathrm{W}]$	$\bar{A}$ [%]	A [%]
Melting	Ar	45	965	9.2 ± 0.3	-
Melting	Ar	45	1420	18.2 ± 1.2	-
Alloying	N_2	60	965	17.4 ± 0.9	3.5
Alloying	N_2	60	1420	17.3 ± 0.8	3.9

The reaction of titanium with nitrogen is exothermic ($H_r = 5.4{\cdot}10^6\,\mathrm{J{\cdot}kg^{-1}}$), and will contribute to the maximum temperature rise $\Delta\underline{T}$ of the work piece. This leads to an overestimation of the absorptivity, denoted by $\underline{A}$, in table 5.3. The energy released per unit of time due to the reaction was estimated from the volume of formed TiN, and was used to correct the measured absorptivity (Römer, 1996), and is denoted by A in table 5.3.

5.2.3 Comparison of measured and calculated melt pool depth

In this section the model of the melt pool depth, as derived in section 4.3.3, is compared to the experimentally measured depth, as found in section 5.2.1. The relevant thermophysical properties of Ti6Al4V and titanium-nitride for the evaluation of equation (4.64) are listed in appendix D. The fraction of the melt pool volume which chemically reacts with nitrogen was estimated to equal $\beta = 0.1$ (Römer, 1996). For the absorptivity A the value determined in the previous section is applied.

Figure 5.14(a) shows the measured depths (from figure 5.11(a)) as well as the calculated depths, as a function of the ratio $P_L/\sqrt{v}$. For a laser power of 1500W, the predicted melt pool depth corresponds well with the experimental values. For a laser power of 1000 W the model and the experimental values match only for $P_L/\sqrt{v} > 150\,\mathrm{W{\cdot}m^{-\frac{1}{2}}{\cdot}s^{-\frac{1}{2}}}$. The poor correspondence at small values of $P_L/\sqrt{v}$ can be attributed to the shape of the melt pool, which is not parabolic at these operating parameters, whereas the model assumes a parabolically shaped melt pool.

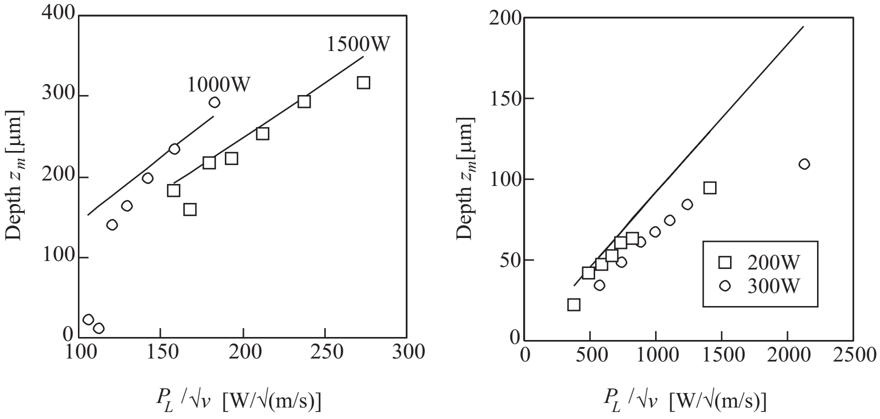

(a) Measured (tick marks) and calculated (curves) melt pool depth for Ti6Al4V alloyed with N_2.

(b) Measured (tick marks) and calculated (curve) melt pool depth for ASI304 alloyed with preplaced Cr.

Figure 5.14: Comparison of model of melt pool depth as function of $P_L/\sqrt{v}$ with experiments.

To evaluate the simplified model (4.66) of the melt pool depth, an experiment was carried out in which no energy is produced due to a chemical reaction of the additional material with the base material—i.e. $Q_R = 0$ and $\beta = 0$. For this purpose, AISI304 samples were alloyed with pre-placed chromium. The surface of each AISI304 sample ($30\,\mathrm{mm} \times 20\,\mathrm{mm} \times 2\,\mathrm{mm}$) was galvanically coated with a $10\,\mu$m Cr layer and subsequently melted by the laser beam. The beam diameter was $d = 0.22\,\mathrm{mm}$. Laser powers of 200 and 300 W were applied. The samples were mounted on a heat sink to simulate a thermally semi-infinite sample. The beam velocity was varied between 20 and $285\,\mathrm{mm{\cdot}s^{-1}}$. The melt pool was shielded by argon. Multiple, overlapping tracks were produced, with an overlap of 0.1 mm. The absorptivity of chromium ($A = 0.04$, (Boyer and Gall, 1985)) was substituted in the model, whereas the thermo-physical properties of AISI304 are listed in table 5.4. After processing, the depth of the solidified melt pool of each track was measured optically from cross sections. As can be observed from figure 5.14(b), the predicted melt pool depth corresponds well with the experimental values up to $P_L/\sqrt{v} = 1500\,\mathrm{W{\cdot}m^{-\frac{1}{2}}{\cdot}s^{-\frac{1}{2}}}$. The measured values are all close to a straight line. This confirms that equation (4.66) is a fair approximation of the melt pool depth.

Table 5.4: Thermo-physical properties of AISI304 at 20 °C.

Property	Value
Density ρ $[\mathrm{kg{\cdot}m^{-3}}]$	8000
Melt trajectory T_m [K]	1673 to 1723
Thermal conductivity K $[\mathrm{W{\cdot}m^{-1}{\cdot}K^{-1}}]$	16.2
Thermal capacity c_p $[\mathrm{J{\cdot}kg^{-1}{\cdot}K^{-1}}]$	500
Latent heat of fusion L_f $[\mathrm{J{\cdot}kg^{-1}}]$	$276 \cdot 10^3$

Source: Boyer and Gall (1985)

It can be concluded that, for relevant operating parameters, there is relatively good correspondence between the predicted melt pool depth and the experimental values, in spite of the simplifications introduced during modeling.

5.3 Analysis of process dynamics

As was noted in section 3.5.3, a prerequisite for the design of a controller is a dynamic process model, which accurately describes the temporal relation between the command input(s) and the measured signal(s). In this section, these models are determined by process identification. The conclusions and insights obtained from the theoretical analysis of the process (chapter 4) are used to estimate the structure and the number of parameters of the models to be obtained by process identification.

In the following subsections, two linear time-invariant parametric models are identified: (*i*) a transfer function relating the laser power (input) to the melt pool area (output), and (*ii*) a transfer function relating the beam velocity (input) to the melt pool area (output). Next, the process response to an absorptivity and a geometric disturbance is analyzed. Finally, a MIMO process model is identified, which relates the laser power as well as the beam velocity (inputs) to the melt pool area and temperature behind the melt pool (outputs).

5.3.1 Laser power as input

In this section the process response to varying laser power, at constant beam velocity, is analyzed.

The laser power was varied in steps of 250 W, from 500 W to 1250 W at constant beam velocity of $v = 50\,\mathrm{mm{\cdot}s^{-1}}$. Figure 5.15 shows the melt pool temperature in the center of the melt pool, the melt pool surface area S_m and some temperature contour plots of the melt pool. In this figure the communication delay between the Work Station Controller and the laser source, as well as the processing delay of the thermal camera (in total 16.5 ms), have been eliminated.

The melt pool temperature reacts slightly faster to an increase of the laser power than

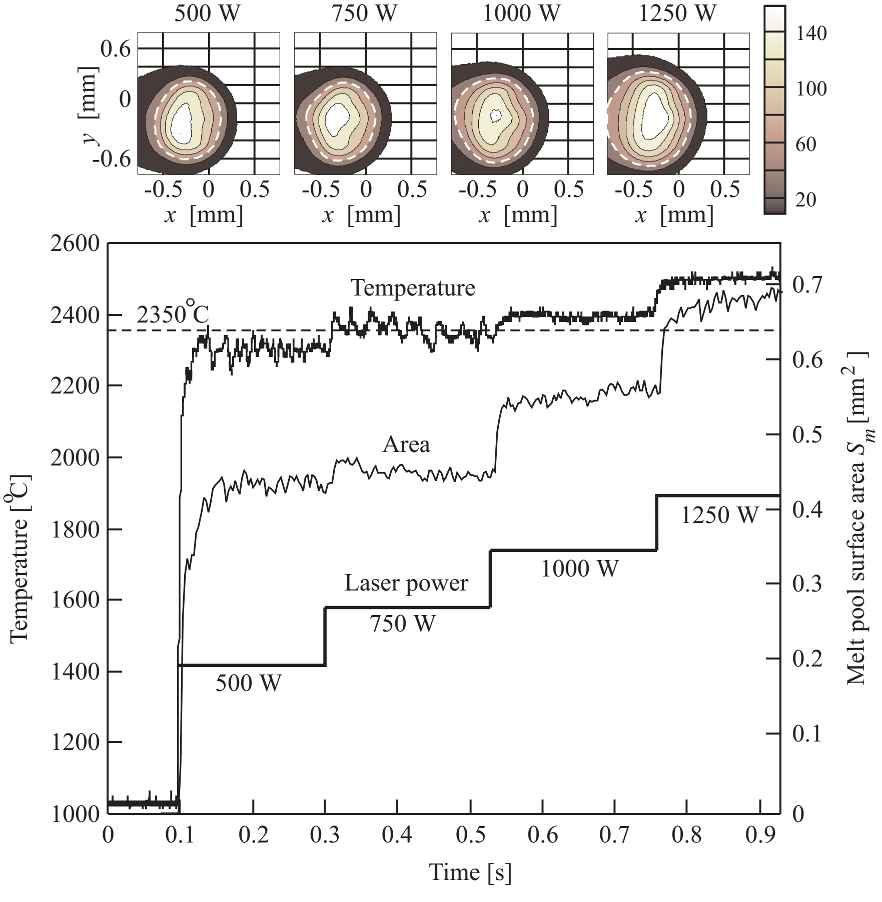

Figure 5.15: Melt pool temperature (as measured by the ratio pyrometer), the melt pool surface area (as measured by the thermal camera) as functions of time, due to a step wise variation of the laser power. Additionally, the gray level contour plots of the melt pool at four power levels is shown. $v = 50\,mm{\cdot}s^{-1}$.

the melt pool area (average rise time $t_r = 3.5\,\mathrm{ms}$ and $t_r = 4\,\mathrm{ms}$ respectively). The relative increase of the melt pool area, due to an increase in laser power, is much larger than the relative increase of the melt pool temperature (table 5.5). This is confirmed by the gray level contour plots, which show an increase of the gray level distribution, and to a lesser extent an increase of maximum gray level value. This result supports the statement that the melt pool surface area is a relevant quality parameter for feedback control, as was claimed on the basis of figure 5.12.

Table 5.5: Relative increase of melt pool temperature and melt pool area due to step in laser power.

Laser power step [W]	$\Delta T/T$	$\Delta S_m/S_m$
500→750	0.024	0.029
750→1000	0.017	0.229
1000→1250	0.046	0.220

The melt pool temperature, as well as the melt pool area do not vary linearly with laser power, which confirms the non-linearity of the process, as predicted in section 4.1. However, for a laser power over 750 W the melt pool area varies nearly linear with laser power. For a laser power of 500 W and less, the absorbed laser energy is insufficient for the development of a melt pool with thermocapillary flows. Hence, only laser powers over 750 W are of interest.

The melt pool temperature and area show fluctuations during a period of constant laser power. This can be attributed to the thermocapillary flows and the presence of solidified titanium-nitride in the melt pool. At power levels less than 750 W, the melt pool temperature is below the peritectic temperature of 2350 °C, see figure 5.15. As a result the TiN almost immediately nucleates and grows to form dendrites. This causes the fluctuation of the melt pool temperature and melt pool area. At laser powers over 750 W, more liquid TiN is contained in the melt pool, and the thermocapillary flow can fully develop. The thermocapillary flow smoothens the melt pool temperature distribution (Gasser *et al.*, 1988; Gasser, 1991). As these fluctuations are no disturbances, but part of the nitriding process, they should not be suppressed by feedback control. Therefore, the fluctuations will be considered as ”noise” during process identification.

Identification of transfer function

In the following the transfer function G from the laser power P_L to the melt pool area S_m is determined by process identification, see figure 5.16. This transfer function will not only include the process, but also the dynamics of the laser source and the thermal camera. However, the dynamics of the laser source and the sensor are faster than the dynamics of the process. Hence, the dynamics of the laser source and the thermal camera can be considered as a static gain in the identified process.

To obtain the transfer function, first the delay was removed from the data. This process (communication) delay will be taken into account in the control loop (see chapter 6).

Because the process is non-linear, it is essential to select an operating point and to

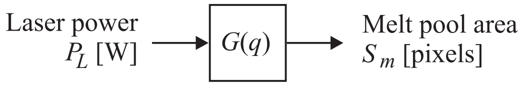

Figure 5.16: Input-output configuration for process identification with laser power as input signal and melt pool area, as measured by the thermal camera, as output signal.

consider only small variations of the signals around this operating point,

$$\begin{aligned} P_L &= P_{L0} + \Delta P_L \\ S_m &= S_{m0} + \Delta S_m \end{aligned} \tag{5.7}$$

where ΔP_L [W] and ΔS_m [pixels] denote the small deviations of the laser power and the melt pool area around the laser power P_{L0} [W] and melt pool area S_{m0} [pixels] respectively. The applied model relating $\Delta P_L\,[W]$ to ΔS_m is an ARX model. The AR in the acronym ARX arises from an *Auto Regressive* part $A(q)\Delta S_m(k)$, whereas the X refers to an *eXogenous* term $B(q)\Delta P_L(k)$, and is mathematically described by

$$G(q) = \frac{\Delta S_m}{\Delta P_L} = q^{-n_k}\frac{B(q)}{A(q)} + \frac{w(k)}{A(q)} \tag{5.8}$$

or equivalently

$$A(q)\Delta S_m(k) = B(q)\Delta P_L(k - n_k) + w(k) \tag{5.9}$$

where $A(q) = 1 + a_1 q^{-1} + \cdots + a_{n_a} q^{-n_a}$ and $B(q) = b_0 + b_1 q^{-1} + \cdots + b_{n_b} q^{-n_b}$ are polynomials in the backward shift (or delay) operator q^{-1}, and where $w(k)$ represents white noise. The numbers n_a and n_b are the orders of the respective polynomials. The process delay, expressed in number of sample periods is denoted by n_k. As the delay is eliminated from the data, n_k is set to zero.

It was also shown in chapter 4 that the dynamics of the process can be approximated by a low (possibly first) order parametric model. The temporal response of the melt pool area, as depicted in figure 5.15, resembles the response of a simple first order process. Therefore, in the following, the parameters of this first order model are obtained by process identification, on the basis of the data shown in figure 5.15. The first order model is a special case of (5.8) and is defined as

$$G(q) = \frac{b}{1 + aq^{-1}} \tag{5.10}$$

in which a and b are the model parameters, and where the noise term $w(k)$ has been omitted for convenience. The process identification consists of adjusting the parameters a and b such that the output of the model coincides well with the measured melt pool area S_m. For this purpose MATLAB is applied, which is a software package for scientific and engineering numeric computation. MATLAB's *system identification toolbox* (Ljung, 1995) contains the necessary mathematical tools and algorithms for process identification.

In the system identification toolbox of MATLAB, n_b denotes the number of zeros plus 1.

The identification toolbox applies the *Least-Squares* algorithm, which minimizes the least square prediction error of the model, to calculate the model parameters (Ljung, 1995). The *Mean Square Fit* (MSF) is the corresponding measure for the error between the model output and the measured data and is defined as (Ljung, 1995),

$$MSF = \frac{\sqrt{\sum_{k} |\hat{z}(k) - z(k)|^2}}{N_k} \tag{5.11}$$

where $z(k)$ denotes the measured data at sample period k, $\hat{z}(k)$ the corresponding output of the model, and N_k the number of data points. The smaller the MSF, the better the model output coincides with the measured data. Analysis showed that the output generated by the first order model (5.10) coincides well (small MSF) with the measured melt pool area, whereas higher order models did not yield more accurate models.

To obtain a dynamic process model which is independent of the sample frequency (419Hz in this case) the discrete time transfer function was transformed to a continuous time transfer function (assuming zero-order hold sampling of the inputs). This model is described by

$$G(s) = \frac{\Delta S_m}{\Delta P_L} = \frac{K_{DC}}{s\tau + 1} \tag{5.12}$$

where $K_{DC}\,[\mathrm{pixels}\cdot\mathrm{W}^{-1}]$ denotes the (low frequency or DC) gain of the process, and $\tau\,[\mathrm{s}]$ the time constant. To analyze the dependence of the gain and the time constant on laser power and beam velocity, the model parameters were identified from the measured melt pool area at several operating points—i.e. at laser power steps from 500 → 750 W, from 750 → 1000 W and from 1000 → 1250 W, at seven beam velocities (30, 40, 50 … 90 $\mathrm{mm}\cdot\mathrm{s}^{-1}$), see figure 5.17. It should be noted that the values of the time constants at high beam velocity are close to half the sample period $(1/(2f_s) \approx 1\,\mathrm{ms})$. This implies that the uncertainty in these values is large compared to the uncertainty of the time constants at low beam velocity. Nevertheless, it can be concluded from figure 5.17(b) that in general the time constant reduces with increasing beam velocity. This implies that the melt pool area responds faster to a change in laser power if the beam velocity is high, than when the beam velocity is small. This can be attributed to the fact that at a high beam velocity the melt pool volume is small and a variation of laser power results in a rapid volume variation. This in turn, implies that the bandwidth of the process is larger at high beam velocity. The same conclusion was drawn, with respect to the heat affected volume, in section 4.4.1.

For laser powers between 750 and 1250 W, the gain K_{DC} decreases with increasing beam velocity, see figure 5.17(a). This can be attributed to the increasing convective losses with increasing velocities. The same conclusion was drawn with respect to the temperature in a solid work piece, in section 4.4.1. The negative gain for $P_L = 1000\,\mathrm{W}$ to 1250 W and $v = 90\,\mathrm{mm}\cdot\mathrm{s}^{-1}$ is the result of erroneous process identification in the face

---

The term Mean Square Fit for the prediction error of the model is misleading. Other terms like *Least Square Prediction Error* (LSPE) or *Model Residuals* (MR) when compared to the measured data, would be better. However, to comply with the internationally accepted nomenclature of process identification, as suggested by Ljung (1987), the term Mean Square Fit (MSF) will be applied in the following.

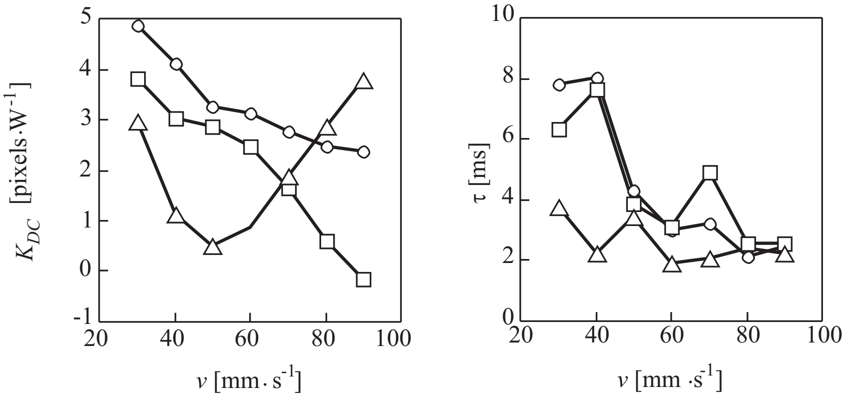

(a) Gain.

(b) Time constant.

Figure 5.17: Dependency on operating point P_{L0} and beam velocity of the gain and time constant of the transfer function relating the laser power ΔP_L to the melt pool area ΔS_m as measured by the thermal camera: △ $500 \rightarrow 750\,W$, □ $750 \rightarrow 1000\,W$, ○ $1000 \rightarrow 1250\,W$.

of strong fluctuations of the measured melt pool area, which is caused by a low melt pool temperature ($T < 2350\,^\circ$C). The irregular behavior of the gain for laser powers between 500 and 750 W can be attributed to the irregular processing results (rough surface area and small layer thickness) obtained at these low laser powers (see section 5.2.1).

The best surface quality is obtained for velocities around $50\,\text{mm}\cdot\text{s}^{-1}$ and laser powers ranging from 750 to 1250 W. For this range of laser powers the model parameters were determined by process identification, from the data of figure 5.15,

$$\begin{aligned} &G(s) = \frac{\Delta S_m}{\Delta P_L} = \frac{K_{DC}}{s\tau + 1},\ K_{DC} = 3.12\,\text{pixels}\cdot\text{W}^{-1},\ \tau = 4.5\,\text{ms}, \\ &P_{L0} = 997\,\text{W},\ S_{m0} = 3840\,\text{pixels},\ v = 50\,\text{mm}\,\text{s}^{-1} \end{aligned} \tag{5.13}$$

A similar model will be applied in section 6.3.1 for the design of a controller. In figure 5.18 the model output is compared to the measured melt pool area. As can be observed from this figure, the dynamics of the melt pool area are fairly accurately predicted for laser powers near the chosen operating point. Due to the non-linear behavior of the process, the prediction is poor for laser powers less than 750 W. For the data $t \in [0.2, 0.6]$ s given in figure 5.18, it was found that the mean square fit of the discrete equivalent of (5.13) equals MSF=75.3 pixels. This error is only 2% of the operating point $S_{m0} = 3840$ [pixels].

Figure 5.19 shows the Bode plot of the discrete equivalent of model (5.13) as well as the Bode plot obtained by spectral analysis of the measured melt pool area. Spectral analysis is a non-parametric identification method to estimate the frequency response of the process without the use of a parametric model (Ljung, 1987). It can be concluded from figure 5.19 that the low frequency dynamics of the process are reasonably well

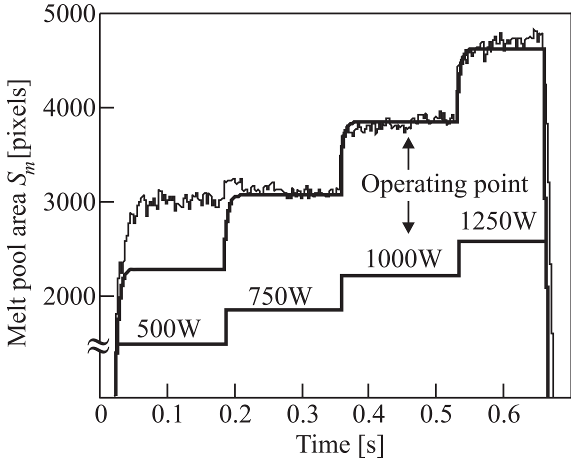

Figure 5.18: Comparison of the discrete equivalent of model (5.13) and the measured melt pool area S_m due to a step wise increase of the laser power. MSF=75.3 pixels.

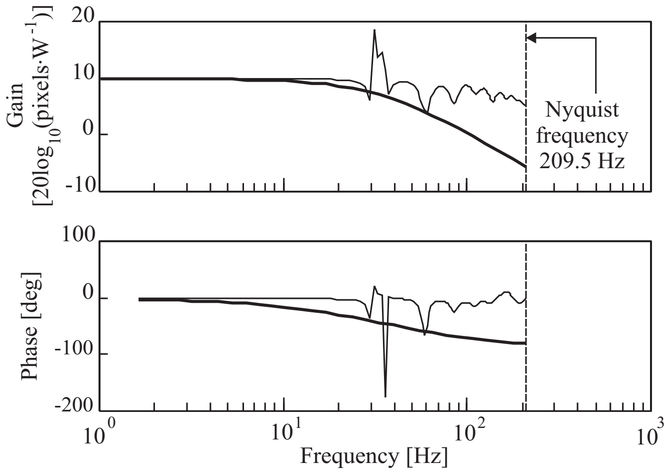

Figure 5.19: Bode plot (thin curve) of melt pool area S_m as obtain by spectral analysis of the measured melt pool area and of the discrete equivalent (bold curve) of model (5.13).

approximated by the first order model, as was predicted in section 4.4.1.

Spectral pyrometer as melt pool area sensor

By comparing the relative variation of the melt pool area and the melt pool temperature (figure 5.15) due to a variation in the laser power, it is found that the change of melt pool surface area is up to 9.1 times as large as the change of the melt pool temperature, see table 5.5. This, combined with equations (5.2) and (5.3), with $n \approx 5.48$, shows that signal variations of a spectral pyrometer, are caused mainly (65%) by a change of the melt pool surface area and only partly (35%) by a change of the melt pool temperature. Hence, the spectral pyrometer can be considered as a melt pool area sensor. To indicate that the pyrometer signal is partly (65%) determined by the melt pool area, the signal will be noted as ”area” $S_{m,T}$ $[^\circ\mathrm{C}]$. Experiments showed that when the diameter of the measurement spot is twice the melt pool diameter, the measurement results are insensitive to small alignment errors of the measurement spot (figure 5.6). An advantage of the experimental set-up including the KLEIBER spectral pyrometer is that it allows a sample frequency (1100 Hz), which is higher than the sample frequency of the thermal camera (419 Hz).

Figure 5.20 shows the melt pool area as measured by the thermal camera as well as the ”area” measured by the spectral pyrometer. Both signals, show the same dependency on laser power (except for the absolute values). Therefore, the spectral pyrometer can be used as a melt pool area sensor for feedback control. Figure 5.21 shows the dependency of the melt pool area $S_{m,T}$ on the beam velocity and laser power. Comparing figure 5.21 with figure 5.13 shows that the melt pool area S_m, as measured by the thermal camera, and the ”area” $S_{m,T}$, as measured by the spectral pyrometer show the same trend, for the laser powers of interest—i.e. $P_L > 750\,\mathrm{W}$.

Identification of transfer function

Also, for the configuration, in which the spectral pyrometer is used as a melt pool area sensor, a first order model (5.12), relating the laser power ΔP_L (input) to the melt pool ”area” $\Delta S_{m,T}$ (output) was derived, see figure 5.22. This configuration is afflicted with a communication delay (1.8 ms), which was eliminated from the data set prior to process identification. To obtain a dynamic process model which is independent of the sample frequency (1100Hz) the discrete time transfer function was transformed to a continuous time transfer function. For the design of a digital controller the a discrete transfer function will be applied (section 6.3.2).

To analyze the dependence of the continuous time model parameters (DC gain and the time constant) on laser power and beam velocity, the model parameters were identified from measured melt pool ”area” as induced by four, step-wise increases of the laser power P_{L0}, at five constant beam velocities (30, 40, 50, 60, and $70\,\mathrm{mm}\cdot s^{-1}$), see figure 5.23. These values of these model parameters are different from the model parameters corresponding to the which the thermal camera was used. However, the dependence of the model parameters on the operating parameters (laser power and beam velocity) show the same trend as the model parameters corresponding to the configuration with the thermal camera. For example, the time constant decreases with increasing beam velocity, and the irregularity of the gain for laser powers less than 750 W.

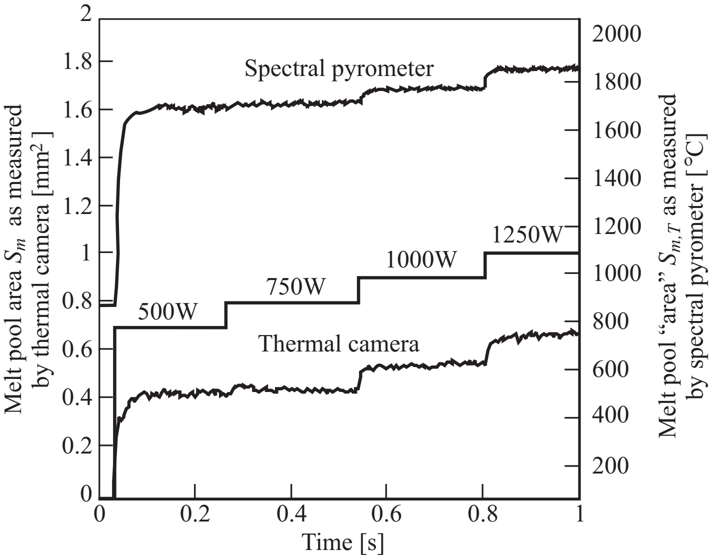

Figure 5.20: Comparison of melt pool area as measured by thermal camera and spectral pyrometer, at constant beam velocity $v = 50\, mm \cdot s^{-1}$ and step wise increase of laser power.

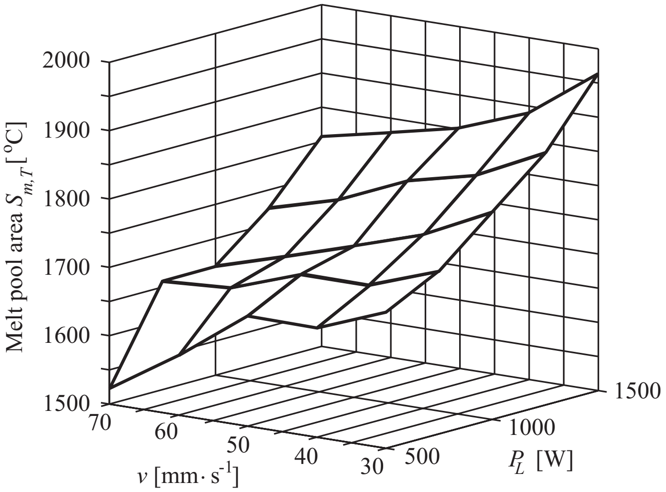

Figure 5.21: Steady state melt pool "area" $S_{m,T}$ as measured by the spectral pyrometer as a function of beam velocity and laser power.

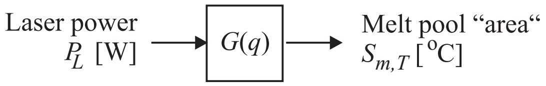

Figure 5.22: Input-output configuration for process identification with laser power as input signal and melt pool "area", as measured by the spectral pyrometer, as output signal.

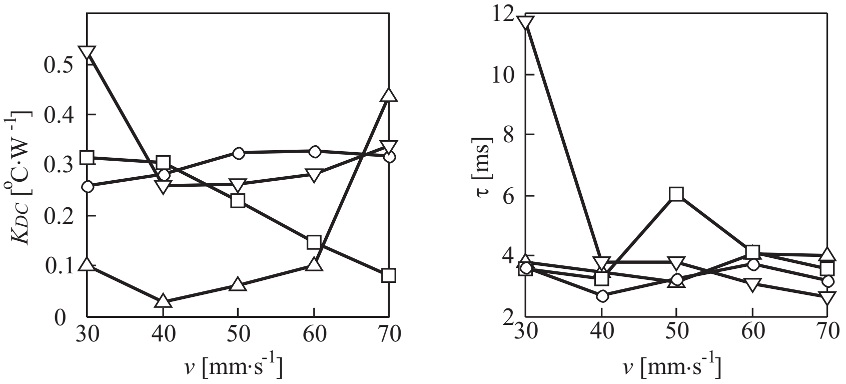

(a) Gain.

(b) Time constant.

Figure 5.23: Dependency on operating point P_{L0} and beam velocity of the gain and time constant of the transfer function relating the laser power ΔP_L to the melt pool "area" $\Delta S_{m,T}$ as measured by the spectral pyrometer: $\triangle$ 500 $\rightarrow$ 750 W, $\square$ 750 $\rightarrow$ 1000 W, $\circ$ 1000 $\rightarrow$ 1250 W, $\triangledown$ 1250 $\rightarrow$ 1500 W.

Increasing versus decreasing laser power

In the preceding the gain and time constant were determined by process identification of the melt pool area induced by a step wise *increase* of laser power. Figure 5.24 shows the models parameters as identified as a function of laser power operating point P_{L0} from a step wise *decrease* as well as *increase* of laser power. As can be observed from this figure the gain and time constants differs for the two cases. This may be attributed to the fact that the heating and cooling mechanisms are different and therefore have different time constants (see equation (4.13) and (4.14)). These non-linearities do not necessarily imply that no efficient controller can be designed. For stability reasons, the model with the largest gain should be used for the design of a controller. Therefore, the model parameters were calculated from a step wise *increase* of laser power from 750 to 1250 W, at constant

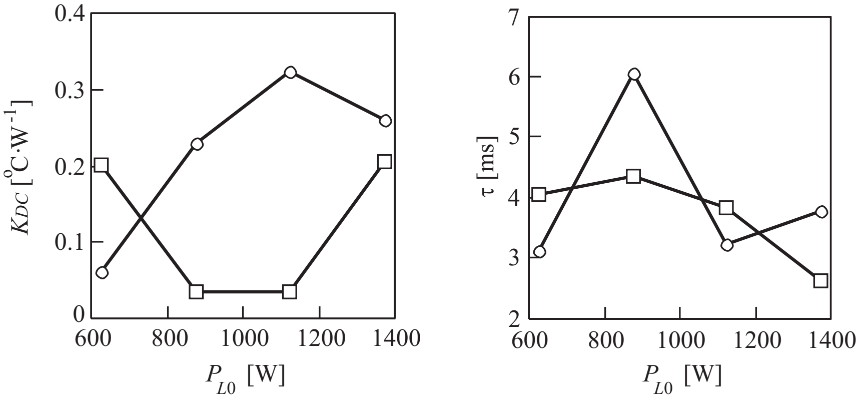

(a) Gain.

(b) Time constant.

Figure 5.24: Dependency of the gain and time constant of the transfer function relating the laser power ΔP_L to the melt pool "area" $\Delta S_{m,T}$ on the operating point P_{L0}, as calculated from a step wise decrease (□ tick marks) and increase (○ tick marks) of laser power at constant beam velocity $v = 50\,mm{\cdot}s^{-1}$.

beam velocity of $40\,\mathrm{mm{\cdot}s^{-1}}$, to give

$$\begin{aligned} &G(s) = \frac{\Delta S_{m,T}}{\Delta P_L} = \frac{K_{DC}}{s\tau + 1},\ K_{DC} = 0.295\,^{\circ}\mathrm{C{\cdot}W^{-1}},\ \tau = 3.14\,\mathrm{ms}, \\ &P_{L0} = 1033.8\,\mathrm{W},\ S_{m,T0} = 1754.7\,^{\circ}\mathrm{C},\ v = 40\,\mathrm{mm{\cdot}s^{-1}} \end{aligned} \tag{5.14}$$

On the basis of transfer function (5.14) a controller will be designed in section 6.3.2.

In figure 5.25 the model output is compared to the measured melt pool "area". As can be observed from this figure, the dynamics of melt pool "area" are fairly accurately predicted for a laser power near the operating point. As could be expected, the prediction is poor for laser powers smaller than 750W. The mean square fit of the model for $P_L > 750\,\mathrm{W}$ is MSF $= 6.87$°C. This error is only 0.4% of the operating point $S_{m,T0} = 1033$°C.

Figure 5.26 shows the Bode plot of model (5.14), as well as the Bode plot obtained by spectral analysis of the measured melt pool "area". The process dynamics are well approximated up to a frequency of approximately 100Hz. Hence, also in the frequency domain the process dynamics are reasonably well approximated by a first order model, as was predicted in section 4.4.1.

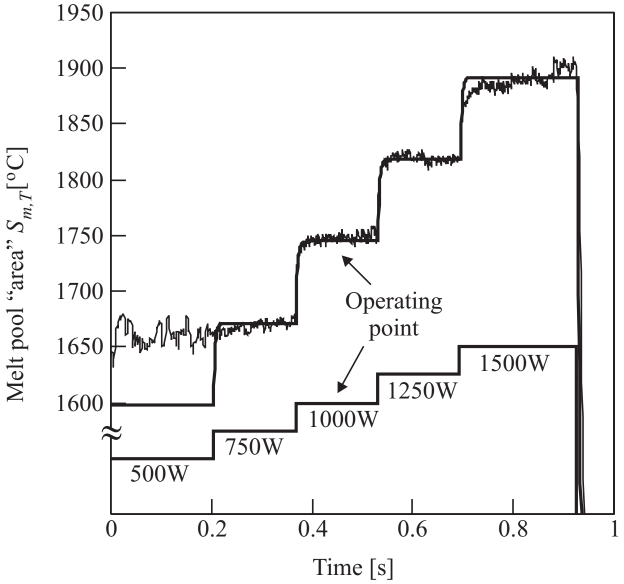

Figure 5.25: Comparison of the model output (5.14) and the measured melt pool "area" $S_{m,T}$ due to a step wise increase of the laser power, $v = 40\,mm\cdot s^{-1}$. MSF=6.87 °C.

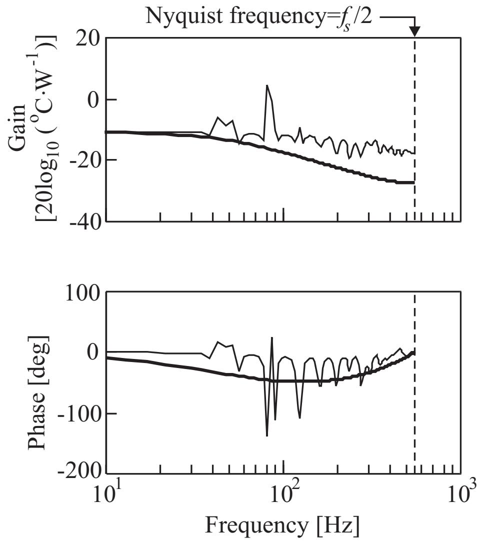

Figure 5.26: Bode plot (thin curve) of melt pool area $S_{m,T}$ as obtained by spectral analysis of the measured melt pool "area" and of the model (bold curve) according to equation (5.14).

5.3.2 Beam velocity as input

In this section the temporal response of the process to varying beam velocity, at constant laser power, is analyzed.

Figure 5.27 shows the response of the melt pool ”area” $S_{m,T}$ to a step-wise increase of the beam velocity at constant laser power of 1250 W. As can be observed from this figure the melt pool ”area” decreases when the beam velocity increases, which implies a negative DC gain. Moreover, the melt pool ”area” shows some overshoot. This overshoot is induced by overshoot in the beam velocity, which is a characteristic of the XY-table. Differences between the desired and measured velocity are caused by poor tuning of the motion controller. Hence, the measured melt pool ”area” of figure 5.27 includes the dynamics of the XY-table. Therefore, the *measured* beam velocity $v^*\,[\mathrm{mm\cdot s^{-1}}]$ must be considered as the input signal during process identification, to obtain a transfer function, which describes the dynamics of the alloying process only, see figure 5.28(a). However, for the design of a controller which applies the beam velocity as a command signal, a combined transfer function of the XY-table and the process is more convenient. The latter is obtained by considering the *commanded* beam velocity (dashed in figure 5.27) as the input signal during process identification, see figure 5.28(b). Both approaches are discussed in the following.

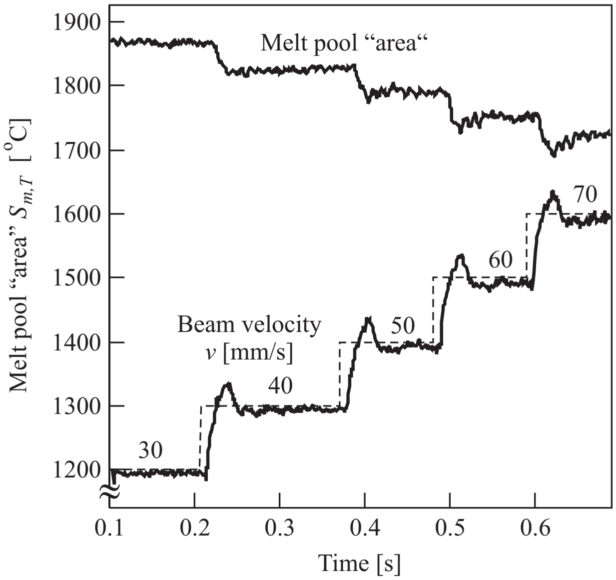

Figure 5.27: Melt pool ”area” $S_{m,T}$, as measured by the spectral pyrometer, the commanded (dashed) and measured (solid curve) step wise velocity increase the measured beam velocity (solid curve) as a function of a commanded (dashed) step wise velocity increase. $P_L = 1250\,W$, $f_s = 1100\,Hz$.

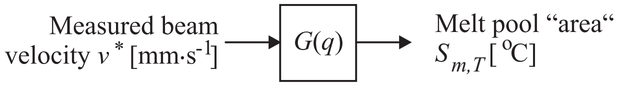

(a) *Measured* beam velocity v^* as input signal.

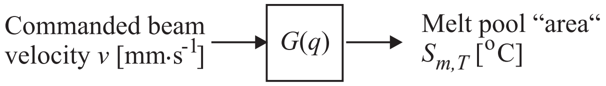

(b) *Commanded* beam velocity v as input signal.

Figure 5.28: Two input-output configurations for process identification with melt pool ”area” as output signal.

Measured beam velocity as input

The Bode plot (figure 5.29) of the transfer function, which relates the measured beam velocity to the melt pool area, was obtained by spectral analysis of the data from figure 5.27. As the bandwidth of the XY-stage is only 50Hz, this experiment does not reveal the high frequency response of the melt pool to varying beam velocity. Only frequencies up to approximately 200 Hz may be considered in process identification. The 180 ° phase shift for low frequencies indicates an decrease of the melt pool ”area” when the beam velocity is increased.

For low frequencies, the process dynamics are estimated by a first order model (5.10). This was confirmed by process identification, in which the model output generated by a the first order model was compared with the measured melt pool ”area”. Higher order models did not yield more accurate models. Next, process identification was carried out to obtain the low frequency gain and time constant, corresponding to the first order ARX model. The discrete time transfer function was transformed to a continuous time transfer function, described by

$$\begin{aligned} G(s) &= \frac{\Delta S_{m,T}}{\Delta v^*} = \frac{K_{DC}}{s\tau + 1} \\ v^* &= v_0^* + \Delta v^*, \quad S_{m,T} = S_{m,T0} + \Delta S_{m,T} \end{aligned} \tag{5.15}$$

where K_{DC} $[^\circ\mathrm{C}\cdot\mathrm{s}\cdot\mathrm{mm}^{-1}]$ denotes the DC gain.

The dependence of the gain and the time constant on laser power and beam velocity v_0^* (operating point) was analyzed by process identification of the model parameters, by varying the beam velocity in steps of 10 mm·s^{-1} at four levels of constant laser power, see figure 5.30. The time constant varies considerably with laser power and operating point v_0^*. However, in general the time constant reduces with increasing beam velocity, which implies that the melt pool area responds faster to a change in beam velocity at higher beam velocity. At high beam velocity the melt pool volume is small and a variation of the beam velocity results in a rapid volume variation. The absolute value of the K_{DC}

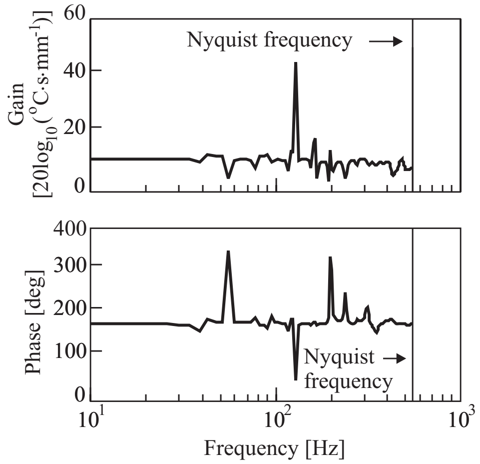

Figure 5.29: Bode plot of melt pool "area" $S_{m,T}$ as obtain by spectral analysis of the measured melt pool "area" and the measured beam velocity v^* at constant laser power $P_L = 1000\,W$, $f_s = 1100\,Hz$. As the bandwidth of the XY-stage is 50Hz, only frequencies up to approximately $200\,Hz$ are of interest for process identification.

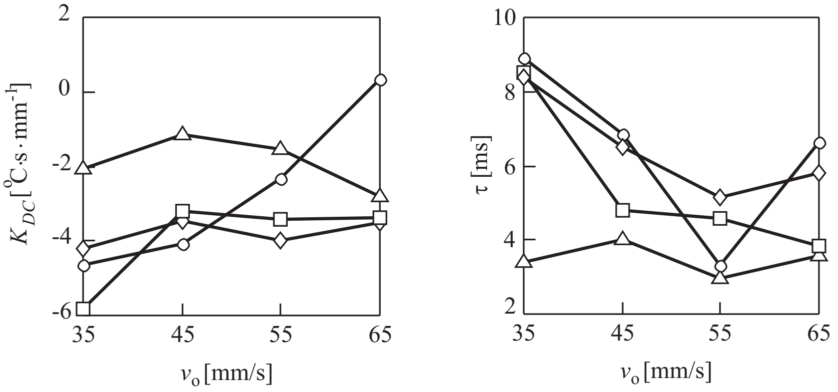

(a) Gain.

(b) Time constant.

Figure 5.30: The gain and time constant of transfer function (5.15), relating the measured beam velocity Δv^* to the melt pool "area" $\Delta S_{m,T}$ as a function of the operating point v_0, at constant laser power: △ $750\,W$, ○ $1000\,W$, ◇ $1250\,W$, □ $1500\,W$.

gain decreases slightly with increasing beam velocity. The positive gain for $P_L = 1000\,\mathrm{W}$ and $v = 60 \rightarrow 70\,\mathrm{mm{\cdot}s^{-1}}$ is the result of erroneous process identification, caused by high frequency noise in the input signal.

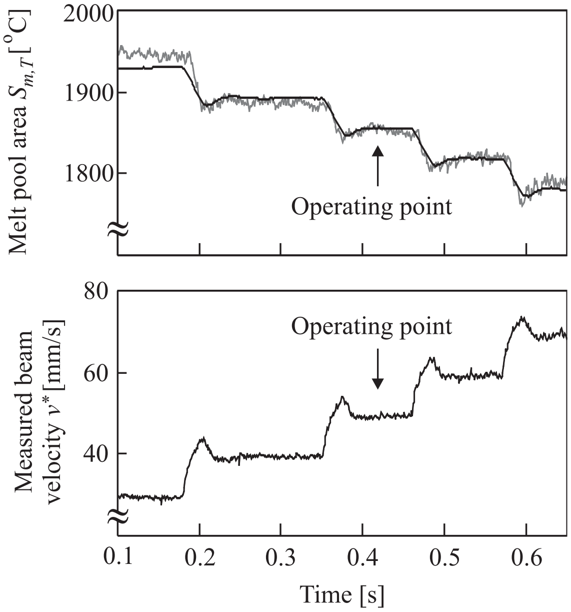

Figure 5.31: Comparison of the model output (solid black curve) of equation (5.16) and the measured melt pool "area" $S_{m,T}$ (gray) induced by the (measured) beam velocity v^*, at constant laser power $P_L = 1250\,W$, MSF=7.98 °C.

From the microstructural analysis (section 5.2.1) it followed that a smooth and shiny titanium-nitride surface layer is obtained for beam velocities around 30 to $50\,\mathrm{mm{\cdot}s^{-1}}$ and laser power ranging from 1000 to 1500 W. For this range of beam velocities and a laser power of 1250 W, the model parameters were determined by process identification,

$$\begin{aligned} G(s) &= \frac{\Delta S_{m,T}}{\Delta v^*} = \frac{K_{DC}}{s\tau+1},\ K_{DC} = -3.75\,^\circ\mathrm{C{\cdot}s{\cdot}mm^{-1}},\ \tau = 8.4\,\mathrm{ms} \\ v_0^* &= 41.0\,\mathrm{mm{\cdot}s^{-1}},\ S_{m,T0} = 1824.3\,^\circ\mathrm{C},\ P_L = 1250\,\mathrm{W} \end{aligned} \tag{5.16}$$

In figure 5.31 this model is compared to the measured melt pool area. The mean square fit is MSF = 7.98°C. This error is only 0.4% of the operating point $S_{m,T0}$. Hence, this first order model describes the low frequency response of the process fairly accurate.

In the following the combined transfer function of the XY-table and the process is identified. This transfer function relates the *commanded* beam velocity to the melt pool "area".

Commanded beam velocity as input

In section 5.1, a time delay of 6.2 ms was found for the XY-table, which is introduced by a FIFO buffer. This limits the control frequency to maximally 157Hz. The spectral pyrometer however, allows a sample frequency up to 1100Hz. Therefore, during control (section 6.4), the mean value of 7 samples of the melt pool ”area” is calculated and supplied to the controller which actuates the XY-table. This averaging constitutes a low pass filtering of the data. This averaging results in an control frequency of 157Hz. For the design of this controller a discrete transfer function $G(q)$, relating the commanded beam velocity v to the melt pool ”area”, at 157Hz is required. For this purpose the data of figure 5.27 was averaged over sets of 7 samples, prior to process identification.

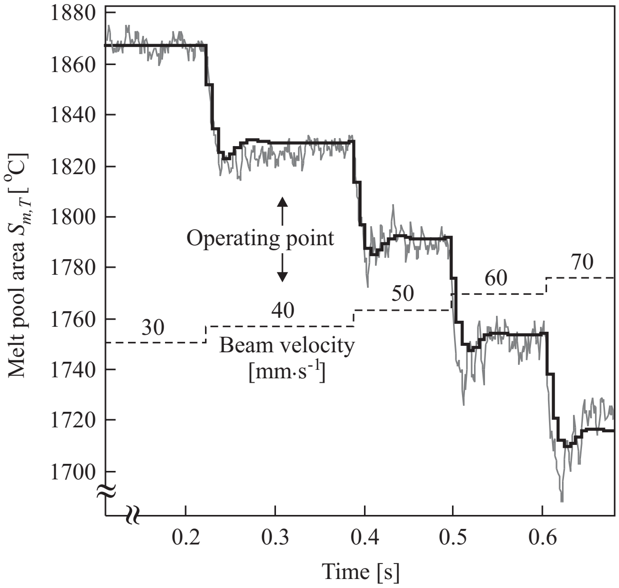

Figure 5.32: Comparison of the model output (black) according to equation (5.17) with $f_s = 157\,Hz$ and the measured melt pool ”area” $S_{m,T}$ (gray, at 1100Hz) due to a step wise increase of the beam velocity, MSF $= 7.61\,^{\circ}C$.

The positioning dynamics of the XY-table are accurately described by a fourth order ($n_a = 4$) parametric model (Schippers, 1994). Hence, the transfer function relating the commanded beam velocity to the actual velocity of the XY-table is of third order ($n_a = 3$). The transfer function of melt pool ”area”, actuated by the measured beam velocity is of first order ($n_a = 1$), see previous paragraph. So the joint transfer function of the XY-table and the melt pool, relating the commanded beam velocity v to the melt pool ”area” is of fourth order ($n_a = 4$). Similar to the previous paragraph, the transfer function was determined from the data of figure 5.27, at beam velocity around 30 to 50 mm·s^{-1} and a laser power of $P_L = 1250\,\mathrm{W}$. It was found that the following model gives the best results,

$$\begin{aligned} G(q) = \frac{\Delta S_{m,T}}{\Delta v} &= \frac{0.039q^4 - 1.6123q^3 - 0.814q^2}{q^4 - 0.5623q^3 + 0.0368q^2 + 0.01289q + 0.0277} \\ v_0 = 40.2\,\mathrm{mm{\cdot}s^{-1}},\ S_{m,T0} &= 1828.5\,^\circ\mathrm{C},\ P_L = 1250\,\mathrm{W},\ f_s = 157\,\mathrm{Hz} \end{aligned} \tag{5.17}$$

As the bandwidth of the XY-stage is small compared to the bandwidth of the process, the dynamics of the XY-stage are dominant in this model. The model will be used in section 6.4 for the design of a digital controller.

In figure 5.32 the model output (5.17) is compared to the measured melt pool ”area”. The low frequency dynamics of the process are accurately predicted over a wide range of beam velocities.

5.3.3 Process response to intrinsic disturbances

In this section, the response of the process to an absorptivity disturbance and a geometrical disturbance is analyzed experimentally.

It was stated in chapter 4, that for the suppression of an absorptivity disturbance the laser power should be used as a command signal. Whereas, for the suppression of the negative effects of a work piece with an area of reduced thickness (geometrical disturbance), the beam velocity should be applied. These statements will be verified in this section.

Geometrical disturbance

The response of the process to a geometrical disturbance was analyzed experimentally. For this purpose, a groove of 6.5 mm wide and 3.6 mm deep was milled into the bottom of a Ti6Al4V disc, representing a well defined geometrical disturbance, see figure 5.33. The remaining ”bridge” of material has a thickness of only 0.4 mm, which is of the order of the heat penetration depth (4.4). Because the beam velocity is relatively high (40 to $50\,\mathrm{mm{\cdot}s^{-1}}$), the groove is a relatively severe geometrical disturbance.

Figure 5.33 shows a longitudinal-section of the work piece, which was processed at constant laser power $P_L = 1000\,\mathrm{W}$ and constant beam velocity $v = 50\,\mathrm{mm{\cdot}s^{-1}}$. Due to the small dimensions of the bridge, the temperature and the volume of the melt pool increase significantly. The increase of the alloyed layer thickness, due to the reduced work piece thickness, is evident. At the elevated temperatures, oxides are formed on the back side of the bridge, because this side is exposed to oxygen. This results in a brittle bridge, which easily breaks into pieces.

Figure 5.34 shows the response of the sensor signals during the processing of the work piece. The size of the melt pool area S_m, as measured by the thermal camera (figure 5.34(a)), increases from about 3850 pixels at the 4 mm region up to 7600 pixels over the 0.4 mm region. Analysis of the contour plots in figure 5.34(a), and their time sequence in figure 5.35, shows that the length of the melt pool increases significantly, whereas the width increases only slightly, when the laser passes the bridge. The same conclusion was drawn in section 4.3.1 with respect to the temperature distribution in a plate.

Figure 5.34(b) shows the melt pool ”area” $S_{m,T}$ and the temperature T_i [°C] just behind the center of the melt pool, during a similar experiment at slightly different operating parameters. The temperature just behind the melt pool increases significantly (about 40%),

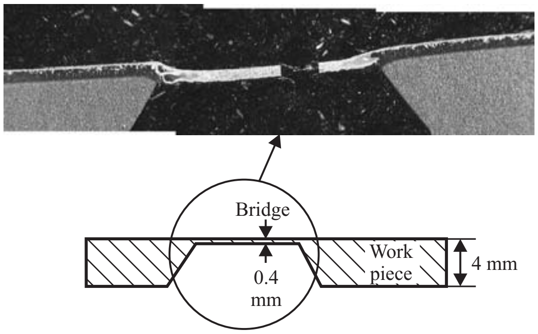

Figure 5.33: Longitudinal-section of a work piece with an region of reduced thickness, which was processed at constant laser power $P_L = 1000\,W$ and constant beam velocity $v = 50\,mm{\cdot}s^{-1}$. Due to the high content of titanium-nitride and oxides formed on the back of the bridge, it is brittle and easily breaks into pieces.

from just under 1400 °C at the 4 mm region up to 1985 °C at the 0.4 mm region, which is higher than the melting temperature of titanium (1650 °C). Hence, when the laser beam irradiates the 4 mm region, the ratio pyrometer measures the temperature of the solidified TiN, whereas it measures the temperature of molten pool when the laser beam passes the area of reduced thickness. This again confirms that the length of the melt pool increases when the laser beam passes the area of reduced thickness.

The signal of the ratio pyrometer is delayed compared to the signal of the spectral pyrometer, which can be mainly attributed to the fact that its measurement spot is aligned behind the melt pool (figure 5.6). This delay will be accounted for in the control loop.

Recursive process identification

If the laser beam irradiates the region of reduced thickness, the process is no longer correctly described by model (5.13). This becomes clear when analyzing the recursively identified model parameters. For this purpose the laser power was varied as a block wave, see figure 5.36. The top graph of this figure shows the response of the melt pool area S_m, as measured by the thermal camera. The bottom graph of the figure, shows the model parameters a and b, as a function of sample number k, of the first order discrete transfer function (5.10). As these model parameters depend on the sample number, this transfer function is rewritten as

$$\begin{aligned} &G(q) = \frac{\Delta S_m}{\Delta P_L} = \frac{b(k)}{1 + a(k) q^{-1}} \\ &P_{L0} = 1000\,\mathrm{W},\ S_{m0} = 3928.8\,\mathrm{pixels},\ v = 50\,\mathrm{mm{\cdot}s^{-1}},\ f_s = 105\,\mathrm{Hz} \end{aligned} \tag{5.18}$$

The parameters $a(k)$ and $b(k)$ were obtained by recursive process identification of the data up to sample k. In this approach, data which is n samples old carries a weight λ^n of the weight of the most recent measurement. The factor $\lambda \leq 1$ is referred to as the

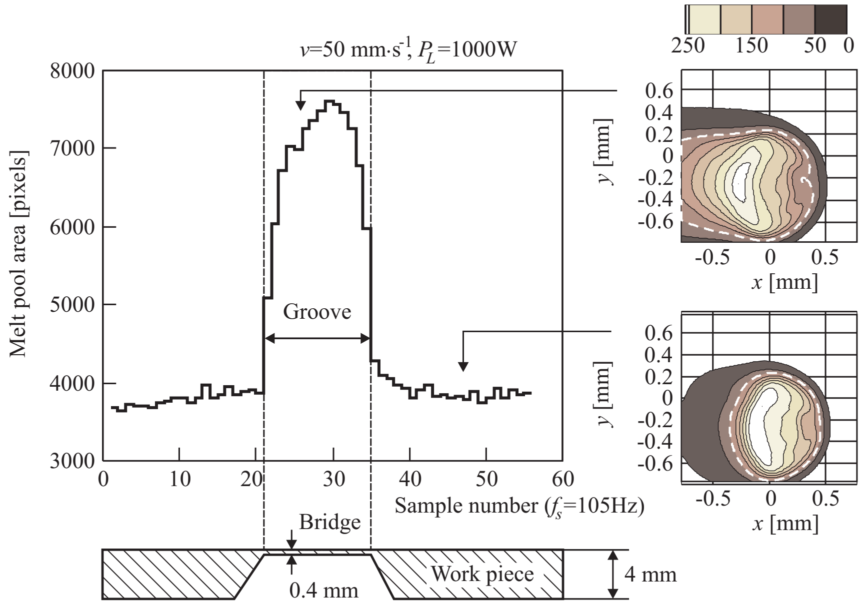

(a) The melt pool area S_m and gray level contour plots, as measured by the thermal camera.

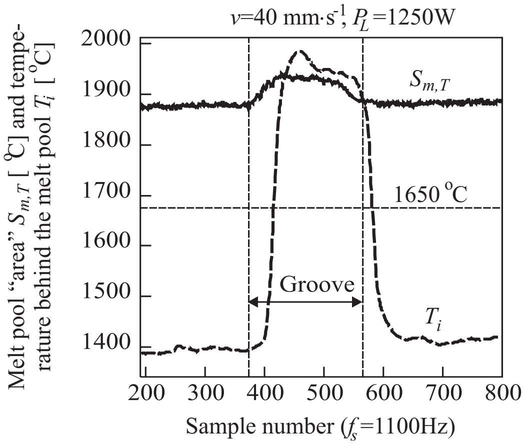

(b) The melt pool "area" $S_{m,T}$ (solid) as measured by the spectral pyrometer and the temperature T_i (dashed) behind the melt pool as measured by the ratio pyrometer.

Figure 5.34: Response of the sensors during the processing of a work piece with an reduced thickness, at constant beam velocity and constant laser power.

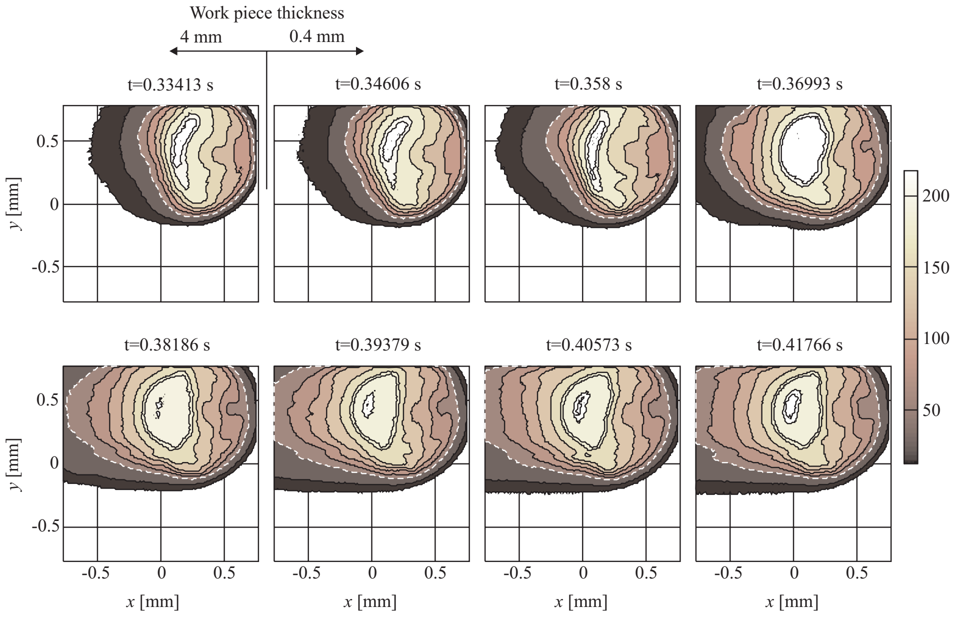

Figure 5.35: Time sequence of gray level contour plots and melt pool (white, dashed) during which the laser beam reaches the region of reduced thickness (geometrical disturbance), at constant beam velocity $v = 50\,mm{\cdot}s^{-1}$ and constant laser power $P_L = 1000\,W$, $f_s = 419\,Hz$. When the laser passes the bridge, the length of the melt pool increases significantly, whereas the width increases only slightly.

forgetting factor, and was set to $\lambda = 0.8$ (Ljung, 1995). Then, the factor $n = 1/(1-\lambda) = 5$ can be considered as the *memory horizon* of the recursive identification. As can be observed from the graph, the model parameters are different for an increase and decrease of the laser power. Model parameter *b* increases significantly when the laser beam passes the region of reduced thickness.

Hence, the performance of feedback controller, which is based on a model describing the dynamics of a work piece with semi-infinite dimensions, may be poor when applied to a work piece of reduced thickness. However, when the beam velocity increases the heat penetration depth decreases. Hence, when the beam velocity is increased, the model describing the dynamics of a work piece with reduced thickness, will more and more resemble the model, which describes the dynamics of a semi-infinite work piece.

It can be concluded from these results that the negative effects of a work piece, with an area of reduced thickness, should be suppressed by applying the beam velocity as a command signal.

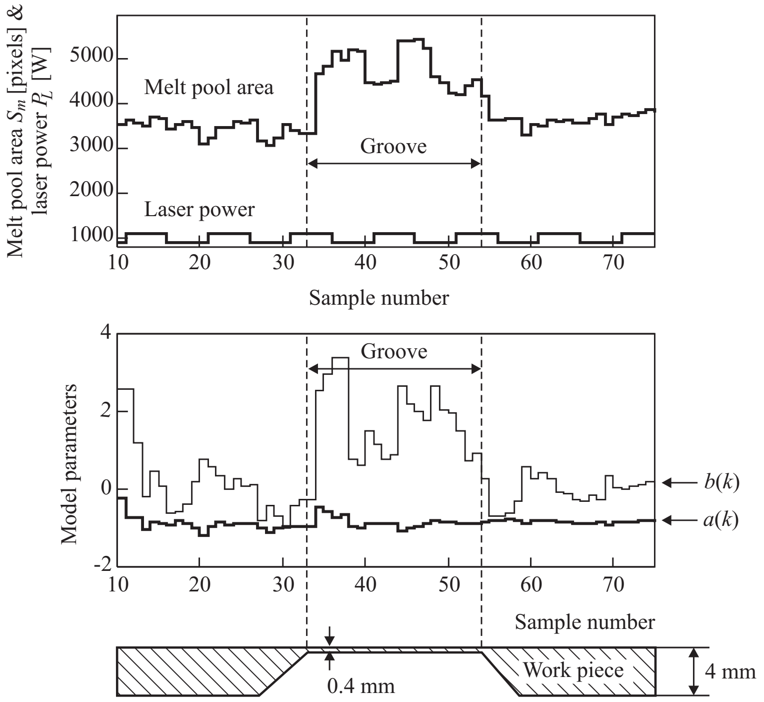

Figure 5.36: Recursive process identification during a track at constant beam velocity $v = 50\,mm{\cdot}s^{-1}$, in which the laser beam passes the region of reduced thickness. Top graph: measured melt pool area S_m, as measured by the thermal camera, induced by a block-wave variation of laser power, as a function sample number. Bottom graph: parameters a and b of model (5.18) as function of sample number. $f_s = 105\,Hz$, memory horizon n=5 samples.

Absorptivity disturbance

The response of the process to an absorptivity disturbance was analyzed experimentally. For this purpose, the surface of the work piece was coated with a $3\,\mu$m graphite layer over a width of 15.5 mm, which represents a well defined absorptivity disturbance. Figure 5.37 shows a longitudinal-section of the work piece, which was processed at constant laser power and constant beam velocity. Due to the increased absorptivity, the temperature and the volume of the melt pool increase. As a result, a stronger thermocapillary flow develops and the titanium-nitride is transported deeper into the melt pool. The increase of the thickness of the alloyed layer, due to the increased absorptivity, is evident.

Figure 5.38 shows the response of the sensor signals during the processing of the work piece. The size of the melt pool area S_m, as measured by the thermal camera, increases approximately 30%, as a result of the increased absorptivity (figure 5.38(a)). Also the melt pool ”area” $S_{m,T}$, as measured by the spectral pyrometer, and the temperature behind the melt pool T_i increase due to the absorptivity disturbance (figure 5.38(b)).

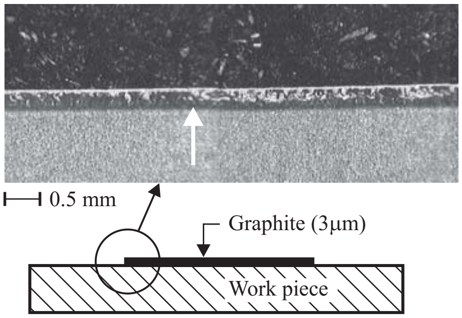

Figure 5.37: Longitudinal-section of a work piece with an region of increased absorptivity, which was processed at constant laser power $P_L = 1000\,W$ and constant beam velocity $v = 50\,mm{\cdot}s^{-1}$. The white arrow indicates the start of the graphite coating.

Analysis of the contour plots, and their time sequence in figure 5.39, shows that the increase of the melt pool length is of the same order as the increase of its width. Hence, mainly the size of the melt pool varies with AP_L and not its shape. The same conclusion was drawn in section 4.3.1 with respect to the shape of the temperature distribution. This result supports the conclusion that for the suppression of an absorptivity disturbance the laser power should be used as a command signal.

It was found that the model parameters during an absorptivity disturbance do not differ significantly from the parameters of the unperturbed process. Hence, the dynamics of the melt pool area are accurately described by transfer functions (5.13) and (5.14), during an absorptivity disturbance.

Model of the temperature behind the melt pool

It is possible to discriminate between a geometrical and an absorptivity disturbance, by analyzing the response of the two pyrometer signals. In the case of an absorptivity disturbance the relative increase of the melt pool ”area” and the temperature behind the melt pool are approximately equal. Whereas, in the case of a geometrical disturbance, the relative increase of the temperature behind the melt pool is much larger than the relative increase of the melt pool area. This phenomenon will be used in section 6.5.2 for the design of a controller. For this purpose, a transfer function relating the commanded beam velocity to the temperature T_i is required, see figure 5.40. The identification procedure to obtain this transfer function is analogous to the procedure described in section 5.3.2. Therefore, only brief results will be presented here.

Figure 5.41 shows the response of the temperature behind the melt pool to a step wise increase of the beam velocity at constant laser power. The delay (19 ms) between the commanded velocity and the pyrometer signal was removed, prior to process identification. This delay will be accounted for in the controller (section 6.5.2). The data from $t = 0.12$ to $t = 0.58\,s$ was averaged over sets of 7 samples, to comply with the maximum control frequency of the XY-stage. It was found that the process can be best approximated

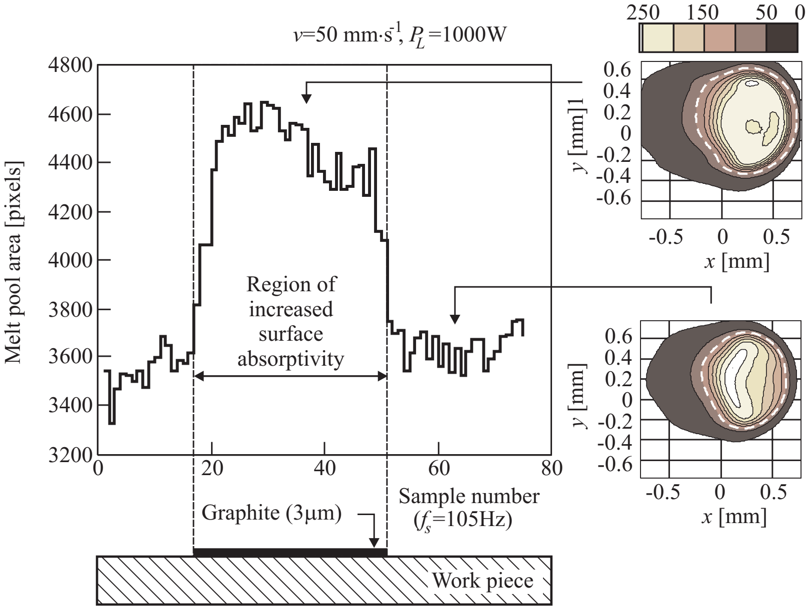

(a) The melt pool area S_m and gray level contour plots, as measured by the thermal camera.

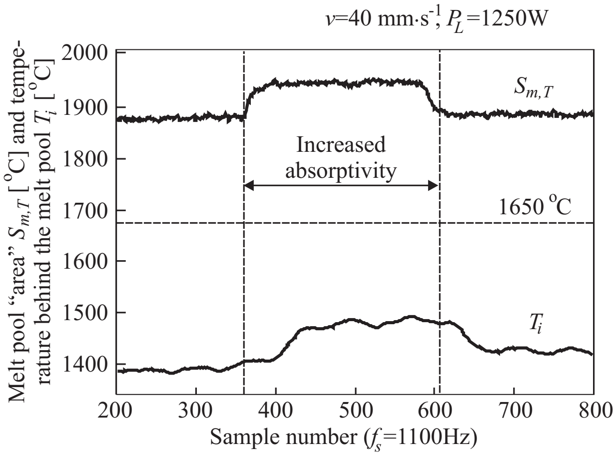

(b) The melt pool "area" $S_{m,T}$ as measured by the spectral pyrometer and the temperature T_i behind the melt pool as measured by the ratio pyrometer.

Figure 5.38: Response of the sensors during the processing of a work piece with increased absorptivity, at constant beam velocity and constant laser power.

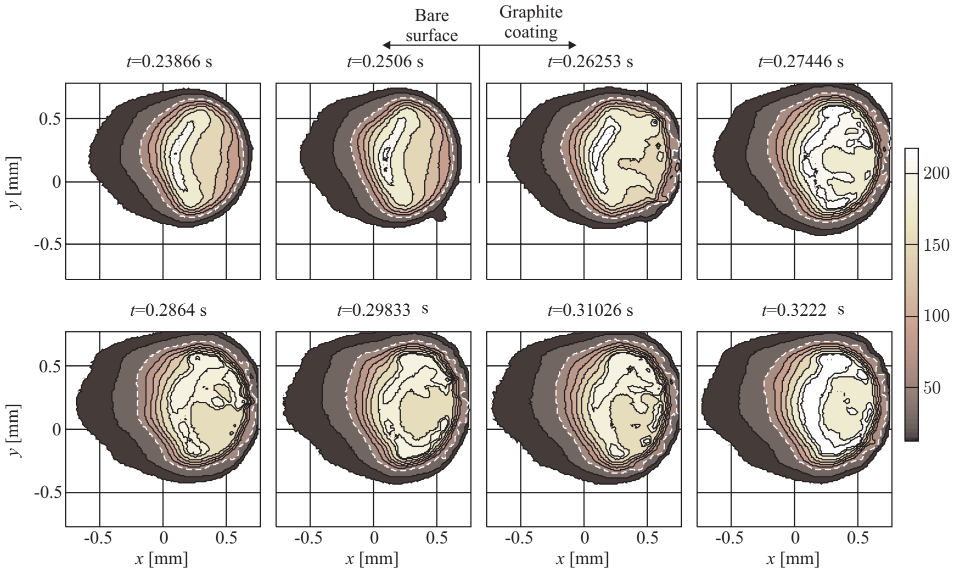

Figure 5.39: Time sequence of gray level contour plots and melt pool (white, dashed) during which the laser beam reaches the surface of increased absorptivity (absorptivity disturbance), at constant beam velocity $v = 50\,mm{\cdot}s^{-1}$ and constant laser power $P_L = 1000\,W$, $f_s = 419\,Hz$.

by the ARX model,

$$\begin{aligned} G(q) &= \frac{\Delta T_i}{\Delta v} = \frac{0.037184q^4 + 1.777q^3 + 1.473q^2 + 2.383q - 2.855}{q^4 - 1.611q^3 + 1.331q^2 + 0.6778q + 0.2089} \\ v_0 &= 50.6\,\mathrm{mm{\cdot}s^{-1}},\ T_{i0} = 1644\,^{\circ}\mathrm{C},\ P_L = 1250\,\mathrm{W},\ f_s = 157\,\mathrm{Hz} \end{aligned} \tag{5.19}$$

In figure 5.42 the model output is compared to the measured melt pool area. The mean square fit is $\mathrm{MSF} = 52.1\,^{\circ}\mathrm{C}$. This error is only 3% of the operating point T_{i0}.

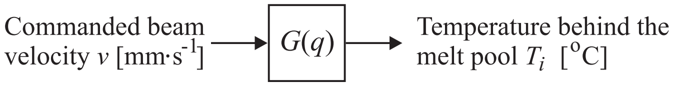

Figure 5.40: Input-output configuration for process identification with commanded beam velocity v as input signal and the temperature behind the melt pool, as output signal.

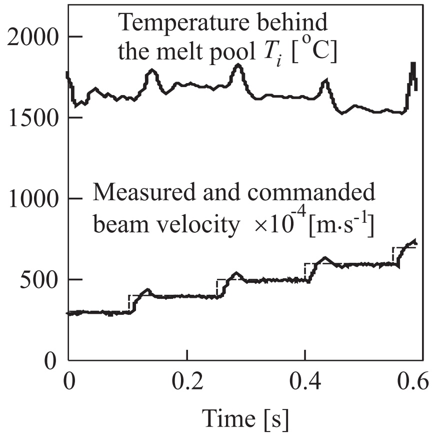

Figure 5.41: Response of the temperature behind the melt pool T_i, at constant laser power $P_L = 1250\,W$, induced by a step wise increase of the commanded (dashed) and measured (bold curve) beam velocity, $f_s = 1100\,Hz$.

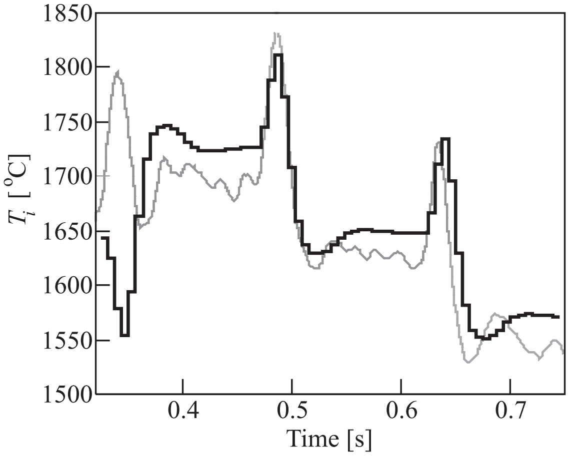

Figure 5.42: Comparison of the model output (5.19) and the measured (gray) temperature behind the melt pool, induced by a step wise increase of the beam velocity. $MSF = 52.1\,°C$.

5.3.4 Laser power and beam velocity as input

Simultaneous actuation of the laser power and the beam velocity may proof to be a more efficient method to control the process than separate actuation of laser power or beam velocity. For the design of a corresponding multivariable controller a MIMO model is required.

Therefore, the parameters of a model were calculated, in which the melt pool ”area” $S_{m,T}$ and the temperature T_i behind the melt pool were considered as inputs. The laser power and beam velocity were considered as outputs, see figure 5.43.

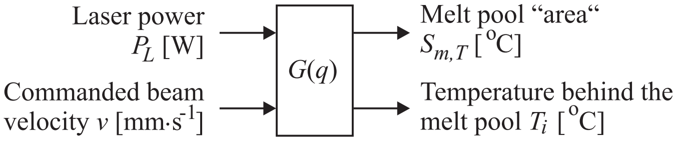

Figure 5.43: Input-output configuration for process identification of MIMO process.

Then, the MIMO model is described by the matrix transfer function $G(q)$, which is defined by

$$\begin{bmatrix}\Delta S_{m,T}\\ \Delta T_i\end{bmatrix} = G(q)\begin{bmatrix}\Delta P_L\\ \Delta v\end{bmatrix} = \begin{bmatrix}G_{11}(q) & G_{12}(q)\\ G_{21}(q) & G_{22}(q)\end{bmatrix}\begin{bmatrix}\Delta P_L\\ \Delta v\end{bmatrix} \tag{5.20}$$

in which G_{ij} represents an ARX model (5.8), relating the j-th input to the i-th output. An experiment was carried out in which a *Pseudo Random Binary Signal* (PRBS) was applied as input signal. Figure 5.44 shows the response of the pyrometers to this signal.

Preliminary experiments showed that the maximum sample frequency of a multivariable controller, which is based on this model (section 6.5.1), is limited to $f_s = 100\,\text{Hz}$. This low sample frequency can be attributed to the limited processor speed of the Work Station Controller in combination with the involved controller calculations for a MIMO model. Therefore, the measured data was resampled at 100Hz, after appropriate low pass filtering, prior to process identification. The optimal four-stage instrumental variable algorithm (IV4) of MATLAB’s identification toolbox was applied to calculate a model parameters (Ljung, 1995). This algorithm is especially useful for process identification of multivariable models.

As the transfer function, relating the beam velocity to each output, is of fourth order, the order of each transfer function G_{ij} was set to four. The use of a Smith predictor (section 6.2), to cope with process delays in the control loop, is computationally demanding for multivariable systems. Therefore, the delay will be included in the model by allowing higher oder degrees of the B polynomial, see equation (5.8). It was found that the

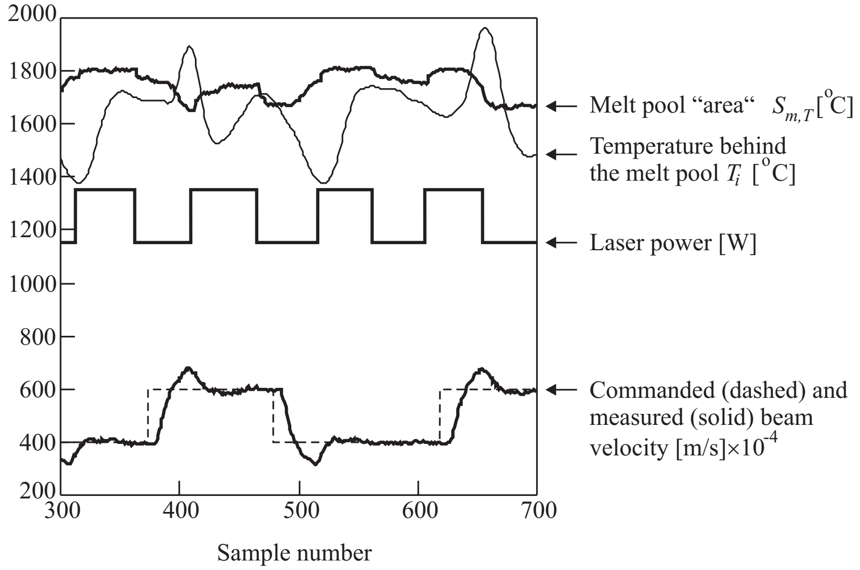

Figure 5.44: Response of the melt pool "area" and temperature behind the melt pool to a pseudo random binary input signal, with the laser power varying between 1150 *and* 1350 *W and the commanded beam velocity varying between* 40 *and* 60 *mm*·*s*$^{-1}$, $f_s = 1100$ *Hz.*

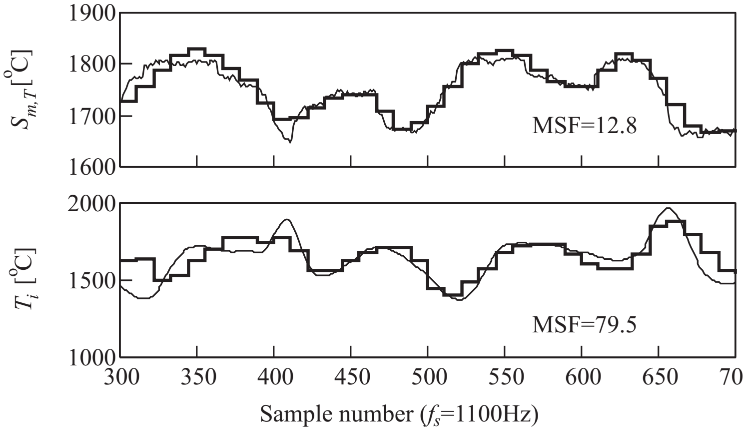

Figure 5.45: Comparison of the MIMO model output (5.20) with (5.21), at 100Hz (solid curves) and the measured data at 1100Hz (thin curves) as a function of sample number (at 1100Hz).

following model predicts the process output with satisfactory accuracy,

$$\begin{aligned}
G_{11}(q) &= \frac{0.15q^3 - 0.017q^2 + 0.034q + 0.0049}{q^4 - 0.76q^3 + 0.20q^2 + 0.23q - 0.13} \\
G_{12}(q) &= \frac{-0.045q^3 - 0.1908q^2 + 0.4935q - 0.020}{q^4 - 0.76q^3 + 0.20q^2 + 0.23q - 0.13} \\
G_{21}(q) &= \frac{0.67q^3 - 2.62q^2 + 0.37q - 0.78}{q^4 - 0.76q^3 + 0.20q^2 + 0.23q - 0.13} \\
G_{22}(q) &= \frac{2.11q^3 - 1.52q^2 + 8.31q - 9.49}{q^4 - 0.76q^3 + 0.20q^2 + 0.23q - 0.13} \\
P_{L0} &= 1246.8\,\mathrm{W},\ v_0 = 49.2\,\mathrm{mm{\cdot}s^{-1}}, \\
S_{m,T0} &= 1749.6\,^\circ\mathrm{C},\ T_{i0} = 1640.0\,^\circ\mathrm{C},\ f_s = 100\,\mathrm{Hz}
\end{aligned} \tag{5.21}$$

In figure 5.45 the model outputs are compared to the measured outputs. There is reasonable correspondence between the measured data and the model outputs. Better models may be obtained at higher sample frequencies, but these models are too computationally demanding for the Work Station Controller. Model (5.20) with (5.21) will be used in section 6.5.1 for the design of a Linear Quadratic Gaussian controller.

5.4 Conclusions

In this chapter the experimental set-up was presented. The model from chapter 4, which relates the operating parameters to the melt pool depth, was verified. There is relatively good correspondence between the model and the experimental values, despite the model's simplifications. In addition, the process dynamics of laser alloying of Ti6Al4V were analyzed:

- A smooth and shiny titanium-nitride surface layer is obtained at a beam velocity around 40 and 50 $\mathrm{mm{\cdot}s^{-1}}$ and a laser power around 1000 and 1250 W
- The melt pool surface area and the depth of the melt pool are correlated,
- The melt pool surface area appears to be a better quality parameter for feedback control, than the melt pool temperature,
- By adapting the measurement spot of a spectral pyrometer, such that it is larger than the melt pool, the signal variations generated by the pyrometer are mainly determined by the variations in the size of the melt pool,
- The low frequency dynamics of the melt pool area, when actuated by the laser power, can be acceptably approximated by a first order ARX model,
- The low frequency dynamics of the melt pool area, when actuated by the beam velocity, can be acceptably approximated by a first order ARX model,
- During a geometrical disturbance, the length of the melt pool increases significantly, whereas the width increases only slightly. Therefore, the beam velocity should be used to counteract this type of disturbances,
- Due to an absorptivity disturbance, the increase of the melt pool length is of the same order as the increase of its width. Therefore, the laser power should be used to suppress this type of disturbances,

- By analyzing the response of both the melt pool ”area” and the temperature behind the melt pool, it is possible to discriminate between a geometrical and an absorptivity disturbance.

On the basis of the identified models, obtained in this chapter, several controllers will be designed and tested in the next chapter.

Chapter 6

CONTROLLER DESIGN AND TESTING

In this chapter several controllers are designed and implemented. The performance of these controllers are tested by analyzing their response to absorptivity and geometrical disturbances, during laser alloying of titanium.

6.1 Control strategy and performance criteria

It was stated in chapter 4 and chapter 5 that for the suppression of the effects of an absorptivity disturbance, it is better to apply the laser power as a command signal. Whereas, the beam velocity should be used as a command signal to counteract the negative effects of a geometrical disturbance. In this chapter, these statements will be verified by evaluating the performance of three SISO controllers and two MIMO controllers. The SISO controllers consider either the laser power or beam velocity as the command signal. Then, the melt pool area measured by the CCD camera, or the ”area” measured by the spectral pyrometer are applied as the quantity to be controlled. The two MIMO controllers consider both the laser power and the beam velocity as command signals. Then, the melt pool ”area” measured by the spectral pyrometer, and the temperature behind the melt pool, are the quantities to be controlled. One of the MIMO controllers is a multivariable *Linear-Quadratic-Gaussian* (LQG) controller, whereas the other is a *mode-switch* controller.

The aim of the controller is to obtain a constant melt pool area despite (intrinsic) disturbances. More specifically, no steady state error(s) for a step-wise disturbances are permitted. The maximum allowable deviation of the controlled melt pool area from its reference value (*allowable error*), may follow from metallurgical and tribological considerations. Unfortunately this data is not available. Therefore, the maximum allowable error is arbitrarily chosen as half the error, which would occur in the case the process is not controlled (see section 5.3.3).

Another performance criterion is the speed at which disturbances are eliminated. Rapid disturbance rejection requires an accurate process model. Unfortunately, an accurate process model is available near the operating point only. Furthermore, the experimental set-up is afflicted with a communication delay, which can not be influenced by the controller. Therefore, the transient behavior of the process is not improved. This yields a reasonable compromise between (steady state) error reduction and stability robustness.

As the laser power is restricted to the range $P_L \in [0, 2000]\,\mathrm{W}$, the admissible control actions for the laser source are limited to this range. The velocity of the axes of the XY-table are limited to $v \in [-0.3, 0.3]\,\mathrm{m{\cdot}s^{-1}}$. It is clear that for laser alloying reversing the velocities is pointless. Therefore, the admissible beam velocity is limited to $v \in \langle 0, 0.3]\,\mathrm{m{\cdot}s^{-1}}$.

The controller parameters are tuned and validated by simulation of the controller and the identified process model using SIMULINK. SIMULINK is toolbox of MATLAB for simulation of dynamical systems. It provides a graphical user interface (GUI) for building block diagrams. Moreover, SIMULINK provides access to the features of MATLAB for analysis and visualization of the simulation results.

Sample frequency

For accurate signal reconstruction, the number of sample periods per *rise time* t_r of the uncontrolled process should be of the order of 4 to 10 (Åström and Wittenmark, 1997). For efficient disturbance rejection, the sample frequency should be 10 to 20 times the desired closed-loop bandwidth. Table 6.1 lists the rise time and bandwidth of the models, which were determined in the previous chapter.

Table 6.1: Rise time and bandwidth of the alloying process and control frequency.

Input	Output	Equation model	t_r [ms]	Bandwidth [Hz]	Control f_s [Hz]
P_L	S_m	5.13	9.9	35.4	105
P_L	$S_{m,T}$	5.14	6.9	50.7	550
v^*	$S_{m,T}$	5.16	18.5	18.9	(†)
v	$S_{m,T}$	5.17	17.2	20.2	157
v	T_i	5.19	34.4	14.2	157

(†) No controller was based on this model.

The frame rate of the CCD camera is 419Hz (section 5.1). Unfortunately, the computational power of the Camera Computer, which is used to determine the melt pool area S_m from a recorded image in real-time, limits the maximum sample rate to $f_s = 105\,\mathrm{Hz}$ (Hoeksma, 1998). This lower sample rate will be applied during on-line control (see table 6.1). This sample frequency is relatively small compared to the bandwidth and the rise time of the process. However, this sample frequency is larger than the frequencies reported in publications in which also area scan camera's are applied for on-line control, e.g. Derouet *et al.* (1997, 12.5Hz), Meriaude *et al.* (1995, 50Hz), Auric *et al.* (1987, 6.25Hz), Rosenthal (1990, 60Hz).

The maximum control frequencies of the configurations, in which the pyrometers are applied, are limited by the computational power of the Work Station Controller (550Hz) as well as by the FIFO buffer of the Galil motion controller (157Hz). However, these sample frequencies are reasonable, when compared to the bandwidth and rise time of the corresponding process models, see table 6.1. The cut-off frequency of the anti-aliasing filters (figure 5.2) were adjusted such that the sampled pyrometer signals do not contain frequencies above the Nyquist frequency ($f_s/2$).

6.2 Smith-predictor

To cope with process delay, the parameters of a conventional controller need to be chosen quite conservative to prevent instability of the controlled process. This results in a controlled process which eliminates a disturbance relatively slow. The *Smith-predictor* (Smith, 1959) is a particular control law that has been proposed to cope with this problem. To apply Smith's control scheme, the transfer function G of the process to be controlled is written as the product of a delay free transfer function G_0 and the delay term

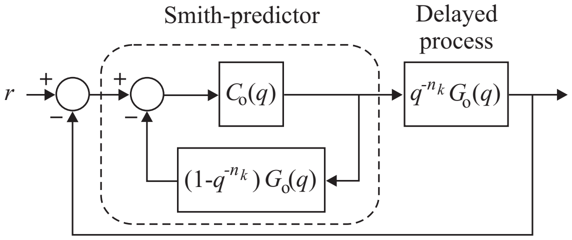

Figure 6.1: Controller augmented with a Smith-predictor to control a process with delay.

$$G(q) = q^{-n_k} G_0(q) \tag{6.1}$$

where n_k represents the delay of the system expressed in number of sample periods. Next, a control law C_0 is designed for the process as if there was no delay—i.e. for the transfer function G_0. Then the control law C, suggested by Smith (1959) for the delayed process, equals

$$C(q) = \frac{C_0(q)}{1 + (1 - q^{-n_k})\, G_0(q) C_0(q)} \tag{6.2}$$

Figure 6.1 shows the corresponding block diagram. As a result, the closed loop transfer function G_{cl} of the controlled delayed process equals

$$G_{\mathrm{cl}}(q) = q^{-n_k} \frac{G_0(q) C_0(q)}{1 + G_0(q) C_0(q)} \tag{6.3}$$

Hence, this method results in a controlled process with time delay n_k, but otherwise showing the same response as the closed-loop design based on the process without delay. Moreover, it can be shown that when the control law C_0 stabilizes the delay free process G_0, the Smith-predictor C will stabilize the delayed process G (Zwart and Bontsema, 1997).

6.3 The laser power as command signal

In this section, control of the melt pool area by actuation of the laser power is discussed. First, the performance of a SISO controller, which applies the CCD camera to measure the melt pool area, is evaluated. In the subsequent section, a SISO controller is designed and tested, which applies the spectral pyrometer for this purpose.

6.3.1 Thermal camera as melt pool area sensor

Figure 6.2 shows a block diagram of the controlled process, in which the thermal camera is applied as melt pool area sensor, and the laser source as actuator. In this configuration, the beam velocity is constant, $v = 50\,\text{mm}\cdot\text{s}^{-1}$. The maximum control frequency is limited to 105Hz by the Camera Computer. For the design of a controller a process model at this sample frequency is required. Therefore, the measured melt pool area S_m (figure 5.18 on page 104) was resampled at 105Hz and the subsequent calculation of the model parameters gave

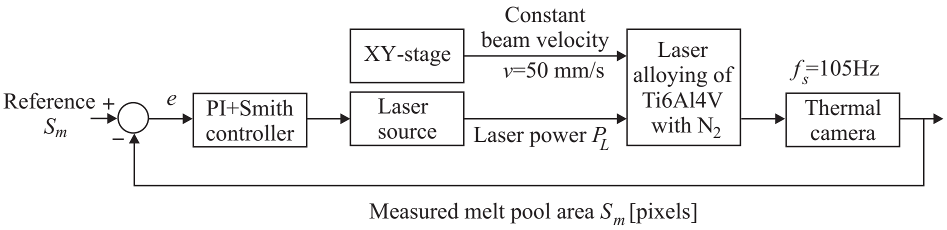

Figure 6.2: Block diagram of the control loop, in which the thermal camera is applied as the melt area sensor and the laser power is applied as the command signal.

$$G(q) = \frac{\Delta S_m}{\Delta P_L} = \frac{1.919}{1 - 0.4076q^{-1}}$$
$$n_k = 2, P_{L0} = 1026\,\text{W}, S_{m0} = 3879\,\text{pixels}, \; f_s = 105\,\text{Hz}, v = 50\,\text{mm}\cdot\text{s}^{-1} \tag{6.4}$$

The model does not include an integrator. The disturbances enter the controlled system at the process input (e.g. absorptivity variations) as well as the process output (geometrical disturbance). Therefore the controller should include an integrator to guarantee a zero steady state error for step like disturbances. Hence, a simple PI-controller suffices to control the process.

Rather than tuning a continuous PI-controller (3.16) and subsequent translation of the design into the discrete domain, the discrete equivalent of the PI-controller was tuned. The transfer function of a discrete PI-controller reads (Åström and Wittenmark, 1997),

$$C_{PI}(q) = K_P\left(1 + \frac{K_I}{q-1}\right) = \frac{K_P q + K_P(K_I - 1)}{q-1} \tag{6.5}$$

where K_P denotes the proportional gain, $\tau_i = (K_I f_s)^{-1}$ [s] the integration time of the integrator, and K_I the integrator gain. Figure 6.3 shows the corresponding block diagram. The discrete PI-controller was tuned by the use of SIMULINK, see figure 6.4. As an initial value for the integrator gain K_I, the value given by the Ziegler-Nichols tuning rules was applied (Åström and Wittenmark, 1997),

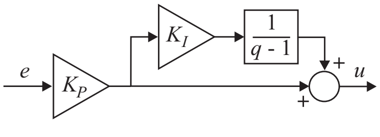

Figure 6.3: Block diagram of discrete PI-controller.

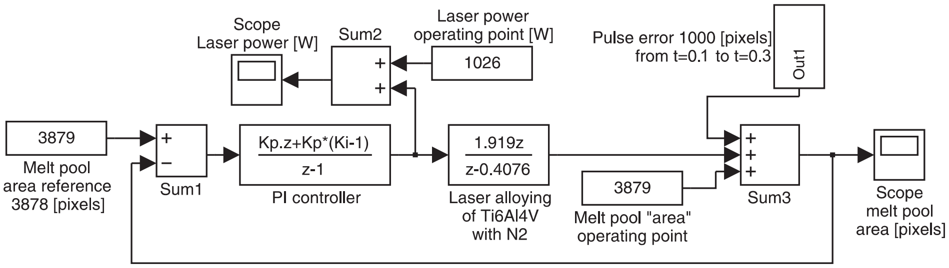

Figure 6.4: The SIMULINK *model of the PI-controlled process, which was applied to tune the PI-controller. The laser power is applied as actuator and the melt pool area, as measured by the thermal camera, as output signal.*

$$K_I = \frac{1}{f_s \tau_i} \approx 0.1 \text{ to } 0.3 \tag{6.6}$$

The closed loop response was tuned by adjusting the controller parameters such that a typical absorptivity disturbance (1000 pixels, see figure 5.34(a) on page 117) is eliminated with reasonable speed without overshoot. This was achieved by $K_P = 4.125$ and $K_I = 0.272$. In theory these values imply infinite gain and phase margins of the controlled process, but as model (6.4) is only valid near its operating point, these margins have limited validity. Figure 6.5 shows the simulation results of the corresponding controlled process (solid curves). The disturbance is eliminated in approximately 0.12 seconds. Moreover, the controller output u (laser power) is well confined within the admissible range of 0 to 2 kW. Hence, no precautions need to be taken in order to avoid integrator windup (Åström and Wittenmark, 1997). As can be observed from the simulation results the laser power drops below 750 W, to eliminate the disturbance, which is well outside the region in which the process reacts linearly to the laser power (see figure 5.18 on page 104). Hence, large disturbances may cause a poor performance of the controlled system.

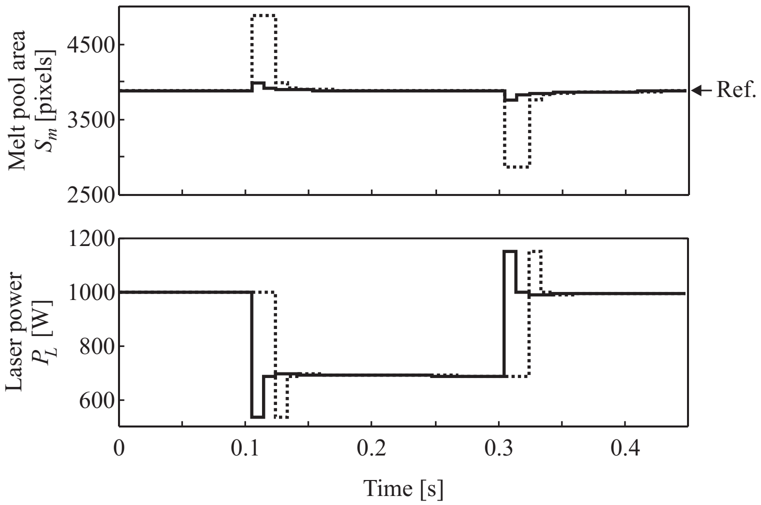

Figure 6.5: Simulation results of the SIMULINK *model which was used to tune the PI-controller. Controller parameters: $K_P = 4.125, K_I = 0.272$, $f_s = 105\,Hz$. From $t = 0.1$ to $t = 0.3\,s$ a pulse shaped increase of the melt pool area of 1000 pixels was introduced. Solid curves: PI-controller without Smith-predictor, dotted curve: PI-controller augmented with Smith-predictor.*

To verify the behavior of the Smith-predictor, additional simulations were carried out in which the PI-controller was augmented with the corresponding Smith-predictor ($n_k = 2$). The dotted curves in figure 6.5 illustrate the results of these simulations.

Because model (6.4) is valid near the operating point only, it is a poor description of the process dynamics during the start-up of laser processing. As a result the controlled process may become unstable during the start-up phase. Therefore, the following procedure was implemented to ensure that the process reaches its operating point as fast as possible:

(i) The work piece is accelerated prior to irradiation. Hence, the processing velocity is reached prior to the instant at which laser irradiation starts,
(ii) The melt pool area is measured from the start, but the controller is not yet activated. Up to the instant at which the controller becomes active, the controller states are constant: $e(k) = 0, u(k) = P_{L0}$, in which k denotes the sample number,
(iii) The initial laser power is chosen larger than the operating point P_{L0}, which results in a rapidly increasing melt pool area,
(iv) As soon as the measured melt pool area reaches a value larger than 100 pixels ($\approx 0.1\,\text{mm}^2$) the controller is activated.

To relieve the Work Station Controller from the corresponding computational load, the PI-controller, the Smith-predictor, and the start-up procedure were implemented on the Camera Computer (figure 5.4(b) on page 87), which is connected to the Laser Computer (figure 5.2 on page 83).

Figure 6.6 shows the results of an experiment in which the surface of the work piece was coated with a 3 μm graphite layer over a width of 15 mm. As can be observed from this figure, the laser power is decreased as soon as the melt pool area increases due to increased the absorptivity. It takes about 16 samples before the melt pool area returns to its reference value. The corresponding laser power is 500 W. At sample number $k = 50$ the absorptivity disturbance ends and the melt pool area drops below its reference. As a result the laser power is increased again. The maximum deviation of the melt pool area from its reference value during the disturbance is 1212 pixels. Unfortunately, this error is of the same magnitude as the maximum error during the uncontrolled situation (figure 5.38 on page 121).

Except for the maximum error, it might be concluded from the measured signals that the absorptivity disturbance is successfully eliminated. However, analysis of the longitudinal-section of the work piece in figure 6.6, shows that the surface roughness of the track is high. This indicates that the absorbed laser power, during the disturbance, is too low (see section 5.2.1). This, in turn implies that the melt pool temperature dropped below peritectic temperature of 2350 °C. Below this temperature, the titanium-nitride solidifies instantaneously and the thermocapillary is impeded. This induces surface rippling (see section 5.2.1). From these observations it can be concluded that, although the melt pool area S_m is an important quantity to be controlled, the temperature of the melt pool apparently can not be ignored entirely. Because the melt pool "area" $S_{m,T}$ as measured by the spectral pyrometer is partly (35%) determined by the melt pool temperature, the melt pool "area" may proof to be a better quantity to be controlled than the melt pool area S_m, as measured by the thermal camera. This statement will be verified in the next subsection.

Figure 6.7 shows the results of an experiment in which the laser beam passes a region of reduced thickness. As can be observed from this figure, the controlled process is nearly unstable, during the period in which the laser beam passes the region of reduced thickness. This unstable behavior can be attributed to the poor description of the process dynamics by model (6.4) during the disturbance (figure 5.36 on page 119). This conclusion is supported by the fact that the melt pool area is steered correctly to its reference value just before and after the disturbance.

As can be observed from the longitudinal-section of the work piece in figure 6.7, the layer thickness reflects the unstable behavior of the controller. With increasing surface area the layer thickness increases, and vise versa. Moreover, the bridge sags due to the self weight effect at the elevated temperatures.

It can be concluded from these experiments that the performance of the controlled system is poor. This can be attributed to a combination of several reasons:

- Although the melt pool area S_m is an important quantity to be controlled, the temperature of the melt pool can not be ignored entirely (see figure 6.6),
- The sample frequency of 105Hz is too low compared to the rise time of the process. Due to the relatively long sample period it takes a long time before a disturbance is detected. As a result the melt pool area may have deviated strongly from its reference value. Then the process state is no longer near its operating point and the linear model (6.4) does not accurately describe the non-linear process dynamics at this state. This conclusion is supported by the results of an experiment in which the reference signal is changed from 4000 to 3200 pixels, see figure 6.8. The

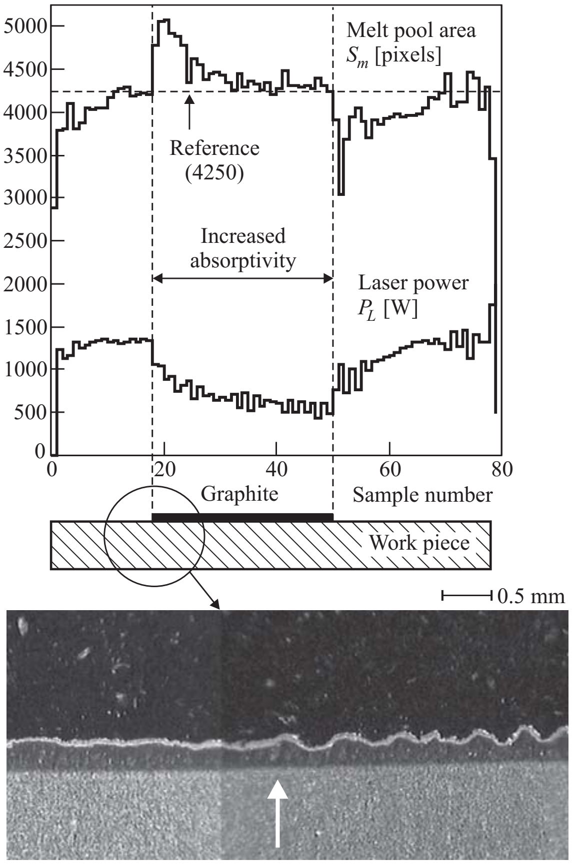

Figure 6.6: Performance of the PI/Smith-controlled process, in which the melt pool area S_m is controlled by actuating the laser power at constant beam velocity $v = 50\,mm\cdot s^{-1}$, during an experiment including an absorptivity disturbance. Melt pool area S_m and laser power P_L as a function of time (top). Controller parameters: $K_P = 4.125, K_I = 0.272$, $n_k = 2$, $f_s = 105\,Hz$. Longitudinal-section of the work piece (bottom). The white arrow indicates the start of the graphite coating.

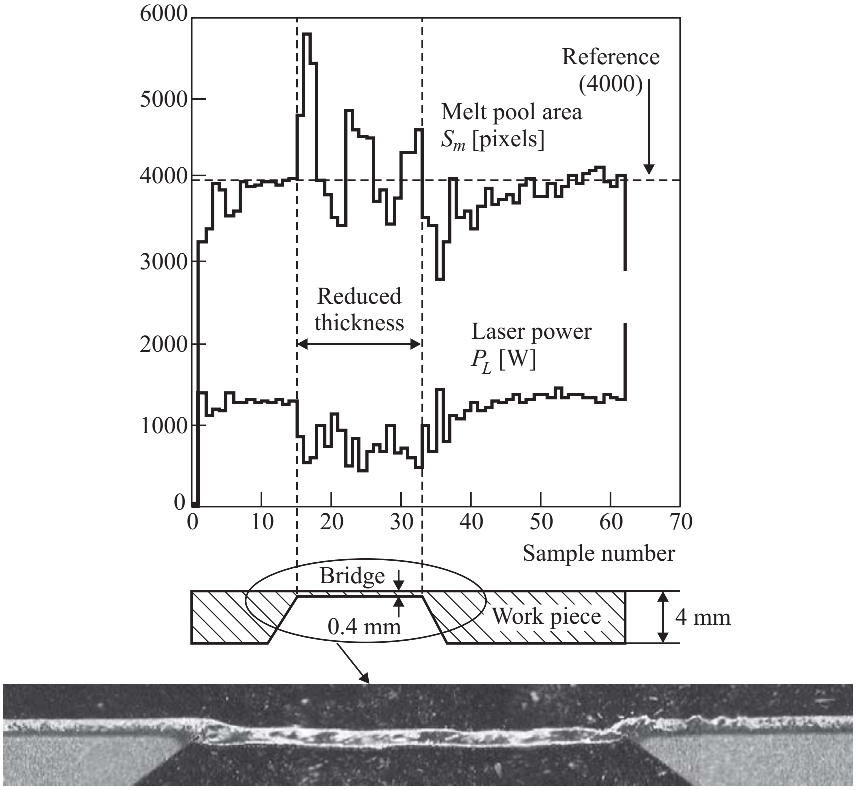

Figure 6.7: Performance of the PI/Smith-controlled process, in which the melt pool area S_m is controlled by actuating the laser power at constant beam velocity $v = 50\,mm \cdot s^{-1}$, during an experiment including a geometrical disturbance. Melt pool area S_m and laser power P_L as a function of time (top). Controller parameters: $K_P = 4.125, K_I = 0.272$, $n_k = 2$, $f_s = 105\,Hz$. Longitudinal-section of the work piece (bottom).

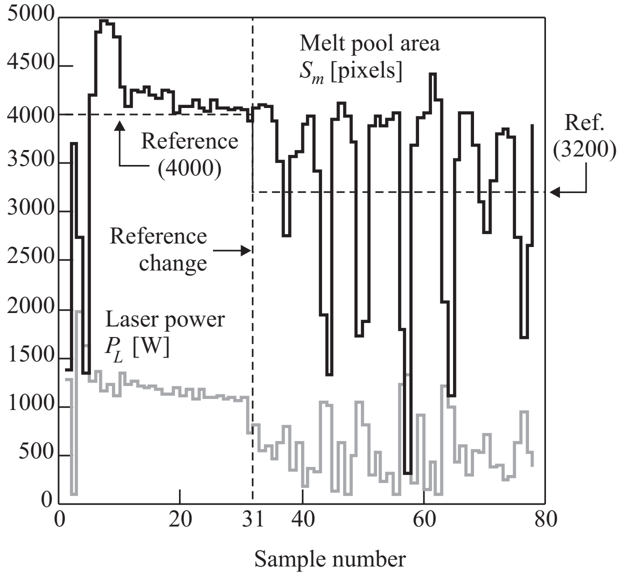

Figure 6.8: Response of the PI/Smith-controlled melt pool surface area S_m to a reference change (at sample number 31, from 4000 to 3200) at constant beam velocity $50\,mm \cdot s^{-1}$, with the laser power as the command signal. Controller parameters: $K_P = 4.125$, $K_I = 0.272$, $n_k = 2$, $f_s = 105\,Hz$. The process dynamics corresponding to a reference value of 3200 is not properly described by model (6.4), which causes instability.

laser power is reduced in an attempt to steer the melt pool area to its new reference value. However, the reference of 3200 pixels corresponds to a laser power of approximately 800 W. At this low laser power, the process dynamics are not accurately described by model (6.4), and the controlled process becomes unstable,

- Conceptually the Smith-predictor is feeding back a simulated process output to cancel the true process output and then adds a simulated process output without the delay (see figure 6.1). Hence, the Smith-predictor highly depends on the process model, and a small error in the model leads to a poor performance of the controlled process (Franklin *et al.*, 1994). This model sensitivity increases with decreasing sample frequency,
- Model (6.4) is a poor description of the process dynamics, when the laser beam passes an area of reduced thickness.

6.3.2 Spectral pyrometer as melt pool area sensor

Figure 6.9 shows a block diagram of the controlled process, in which the spectral pyrometer is applied as melt pool area sensor, and the laser source as actuator. As was mentioned before, this configuration allows the pyrometer signal to be sampled up to a fre-

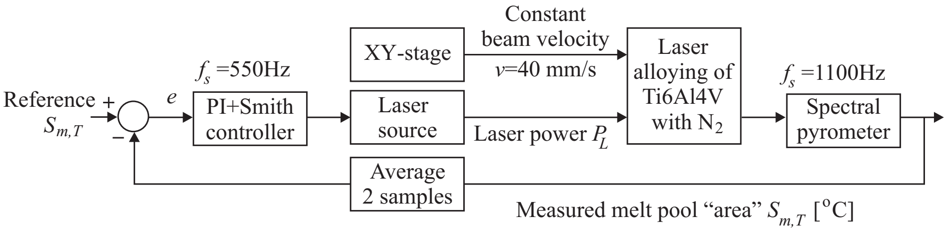

Figure 6.9: Block diagram of the control loop, in which the spectral pyrometer is applied as the melt area sensor and the laser power is applied as the command signal. The beam velocity is constant.

quency of 1100Hz, but the computational power of the Work Station Controller limits the control frequency to 550 Hz. Therefore, the average value of two samples, which are acquired at 1100Hz, will be calculated and supplied to the controller, resulting in an control frequency of 550Hz. Process identification of the model parameters for power levels from 750 to 1500 W gave the transfer function

$$G(q) = \frac{\Delta S_{m,T}}{\Delta P_L} = \frac{0.07034}{1-0.743q^{-1}}$$
$$P_{L0} = 1285\,\mathrm{W},\ S_{m,T0} = 1827\,^{\circ}\mathrm{C},\ f_s = 550\,\mathrm{Hz},\ v = 40\,\mathrm{mm}\cdot\mathrm{s}^{-1} \quad (6.7)$$

The communication delay, expressed in number of sample periods, was found to equal $n_k = 1$. Again the model does not include any integrator. Therefore the controller should include an integrator to guarantee a zero steady state error for step like disturbances. For this purpose again a discrete PI-controller (6.5) suffices.

The discrete PI-controller was tuned by the use of an analogous SIMULINK model as depicted in figure 6.4. The closed loop response was tuned by adjusting the controller parameters such that a typical absorptivity disturbance of 63 °C is eliminated with reasonable speed, with almost no overshoot. This was achieved by $K_P = 7.5$ and $K_I = 0.4$. These parameters imply an infinite gain margin and a phase margin of approximately 90 °.

Figure 6.10 shows the simulation results of the corresponding controlled process. As can be observed from this figure, the disturbance is eliminated in approximately 35 ms, which is 3.5 times as fast as in the case were the thermal camera was used as a sensor. Moreover, the laser power not only is confined within the admissible range of 0 to 2000 W, but also is close to its operating point P_{L0}. To verify the behavior of the Smith-predictor, additional simulations were carried out in which the PI-controller was augmented with the corresponding Smith-predictor ($n_k = 2$). The simulation results were as could be expected and are therefore not presented here.

The PI-controller, augmented with the Smith-predictor, was implemented on the Work Station Controller. A slightly different start-up procedure, as described in the previous section, was implemented:

(*i*) The irradiation and the acceleration of the work piece start simultaneously, introducing some overshoot of the melt pool area during the start-up phase. This tran-

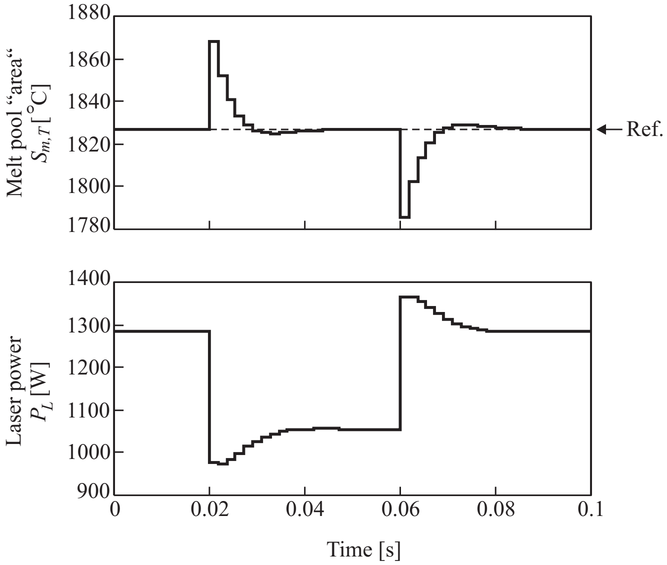

Figure 6.10: Simulation results of the SIMULINK *model which was used to tune the PI-controller. Controller parameters:* $K_P = 7.5$, $K_I = 0.4$, $f_s = 550\,Hz$. *From* $t = 0.02$ *to* $t = 0.06\,s$ *a pulse shaped increase of the melt pool "area" of* $63\,°C$ *was introduced.*

sient behavior ends after a short period of time, typically 75 ms, and the melt pool "area" stabilizes to a value corresponding to the applied laser power,

(ii) The controller is not yet activated. Up to the instant at which the controller becomes active, the controller states are constant: $e(k) = 0$, $u(k) = P_{L0}$,

(iii) After 110 samples (at 1100 Hz) the controller is activated.

Figure 6.11 shows the results of an experiment in which the surface of the work piece was coated with a 3 μm graphite layer over a width of 15 mm. The laser power is decreased to about 900 W, which is near the operating point, to counteract the disturbance. It takes about 34 ms before the melt pool "area" returns to its reference value, which is almost equal to the time found during simulation (figure 6.10). At sample number $k = 480$ (1100Hz) the absorptivity disturbance ends and the melt pool "area" drops below its reference value. As a results the laser power is increased to 1250 W. The maximum deviation of the melt pool "area" from its reference value during the disturbance occurs at sample number 487 (1100Hz). This error is less than half the maximum error during the uncontrolled situation (figure 5.38(b) on page 121).

As can be observed from the longitudinal-section in figure 6.11, the layer thickness is nearly constant despite the absorptivity disturbance. During the absorptivity disturbance the melt pool depth is slightly smaller than the depth in the unperturbed region. The cause of this slight over-control is not clear. Nevertheless, it can be concluded from these observations that the absorptivity disturbance is successfully eliminated.

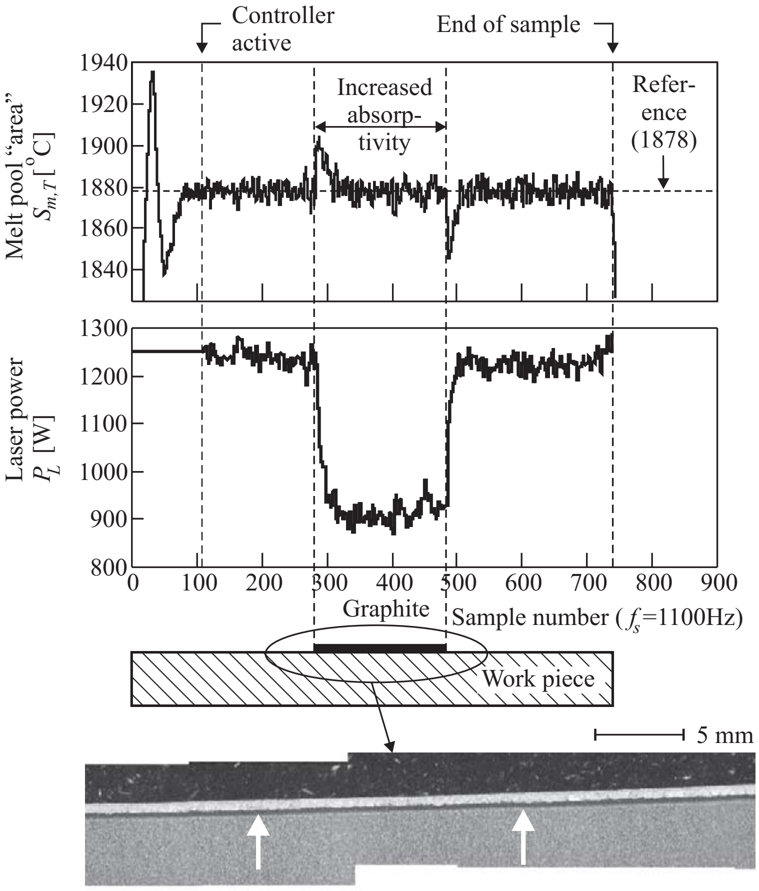

Figure 6.11: Performance of the PI/Smith-controlled process, in which the melt pool "area" $S_{m,T}$ is controlled by actuating the laser power at constant beam velocity $v = 40\,mm \cdot s^{-1}$, during an experiment including an absorptivity disturbance. Melt pool "area" $S_{m,T}$ and laser power P_L as a function of time (top). Controller parameters: $K_P = 7.5, K_I = 0.4$, $n_k = 1$, control frequency $f_s = 550\,Hz$. Longitudinal-section of the work piece (bottom). The white arrows indicate the start and end of the surface of increased absorptivity.

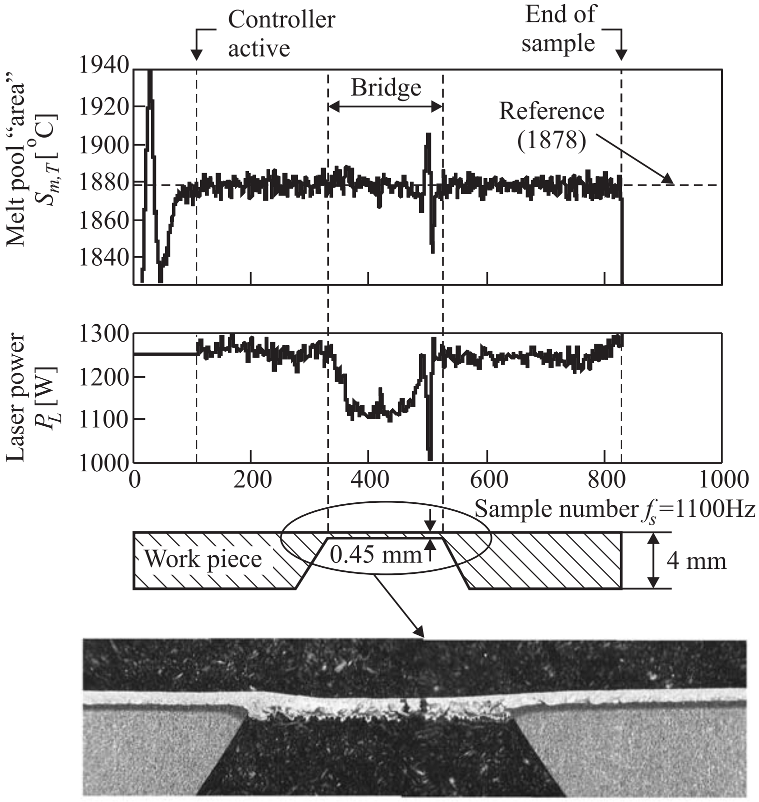

Figure 6.12: *Performance of the PI/Smith-controlled process, in which the melt pool "area" $S_{m,T}$ is controlled by actuating the laser power at constant beam velocity $v = 40\,mm{\cdot}s^{-1}$, during an experiment including a geometrical disturbance. Melt pool "area" $S_{m,T}$ and laser power P_L as a function of time (top). Controller parameters: $K_P = 7.5, K_I = 0.4$, $n_k = 1$, control frequency $f_s = 550\,Hz$. Longitudinal-section of the work piece (bottom).*

Figure 6.12 shows the results of an experiment in which the laser beam passes a region of reduced thickness. The laser power is decreased to about 1100 W, as soon as the laser beam irradiates the region of reduced thickness. As a result, there is almost no increase of the melt pool area due to the disturbance. Near sample number $k = 500$ (1100Hz) a short and unexpected increase of the melt pool ”area” occurs. The controller responds to this spike by briefly reducing the laser power. The maximum deviation of the melt pool ”area” from its reference value during the disturbance occurs at sample number 511 (1100Hz). This error is error is half the maximum error during the uncontrolled situation (figure 5.34(b) on page 117).

It can be observed from the longitudinal-section of the work piece that the layer thickness is not constant over the total width of the bridge. This can be partly attributed to the strong oxidation of the back side of the bridge. Nevertheless, it can be concluded from these observations that the geometrical disturbance considerably suppressed, compared to the uncontrolled situation (figure 5.33 on page 116). Hence, the melt pool ”area” $S_{m,T}$, as measured by the spectral pyrometer, is a better quantity to be controlled than the melt pool area S_m as measured by the CCD camera. This can be attributed to the fact that the melt pool ”area” $S_{m,T}$ is not only determined by the melt pool area, but also by its temperature.

6.4 The beam velocity as command signal

In this section the control of the melt pool ”area”, by actuation of the beam velocity, is discussed. Figure 6.13 shows a block diagram of the corresponding controlled process. In this configuration, the spectral pyrometer is applied to monitor the melt pool, and the laser power is constant $P_L = 1250$ W.

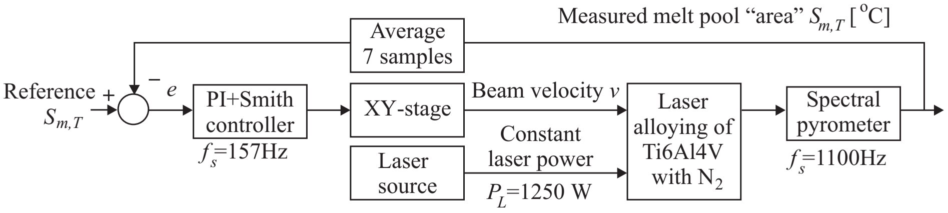

Figure 6.13: Block diagram of the control loop, in which the spectral pyrometer is applied as the melt ”area” sensor and the beam velocity is applied as the command signal. The laser power is constant.

The process model (5.17), which includes the dynamics of the XY-table, was determined in section 5.3.2. Also this model does not include an integrator. Hence, the controller should add an integrator to guarantee a zero steady state error in the face of disturbances. For this purpose again the discrete PI-controller (6.5) suffices. The controller parameters where determined by simulation of the closed loop, such that a typical absorptivity disturbance of 63°C is eliminated with reasonable speed without overshoot. Figure 6.14 shows the root locus of the controlled process, when the integrator gain is chosen as

$K_I = \frac{3}{5}$. Then, the controlled process is stable for $-1.09 < K_P < 0$. Figure 6.15 shows the

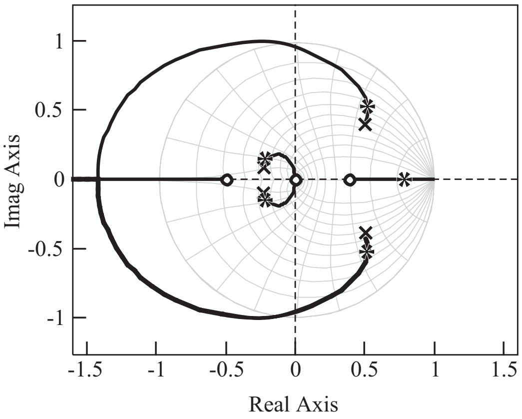

*Figure 6.14: Root locus of the controlled process with $K_I = \frac{3}{5}$ and $K_P \in [0, -\infty\rangle$. The zero at 41.42 is not shown. The pole locations marked with * correspond to $K_P = -\frac{1}{8}$.*

simulation results of the corresponding controlled process, when the proportional gain is chosen as $K_P = -\frac{1}{8}$. These controller parameters imply a gain margin of 18.8 dB and a phase margin of about 83°. As can be observed from figure 6.15, the step-wise disturbance is eliminated in about 0.13 seconds. This period is relatively long, compared to the configuration in which the laser power was applied as the command signal. This can be attributed to the fact that the bandwidth of the XY-table is small compared to that of the laser source. The commanded beam velocity is not only confined within the admissible range $v \in \langle 0, 0.3]\,\mathrm{m{\cdot}s^{-1}}$, but is also close to the operating point ($v_0 = 40.2\,\mathrm{mm{\cdot}s^{-1}}$). To verify the behavior of the Smith-predictor, additional simulations were carried out in which the PI-controller was augmented with the corresponding Smith-predictor ($n_k = 2$).

The PI-controller, augmented with the Smith-predictor , were implemented on the Work Station Controller. A slightly different start-up procedure, as described in the previous section, was implemented:

(i) The irradiation and the acceleration of the work piece start simultaneously. This causes some overshoot of the melt pool area during the start-up phase. The melt pool ”area” stabilizes after a short period of time (typically 75 ms),
(ii) The controller is not yet activated. Up to the instant at which the controller becomes active, the controller states are constant: $e(k) = 0$, $u(k) = v_0$,
(iii) After 16 samples (at $f_s = 157\,\mathrm{Hz}$) the controller is activated.

Figure 6.16 shows the results of an experiment in which the surface of the work piece was coated with a $3\,\mu$m graphite layer over a width of ±10 mm. The beam velocity is increased to approximately $66\,\mathrm{mm{\cdot}s^{-1}}$, as soon as the melt pool ”area” increases due to the increased absorptivity. There is good correspondence between these measurements and the simulation (figure 6.15). For example, it takes about 0.15 seconds before the melt

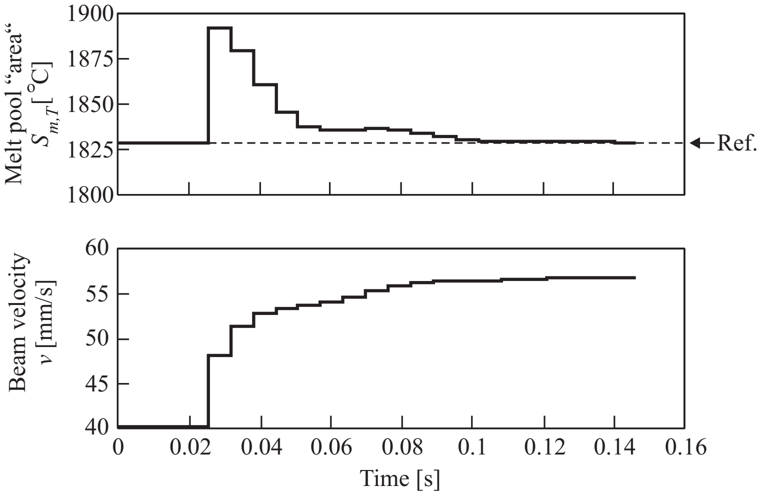

Figure 6.15: Simulation results of the SIMULINK *model which was used to tune the PI-controller. Controller parameters:* $K_P = -\frac{1}{8}, K_I = \frac{3}{5}, f_s = 157\,Hz$*. At* $t = 0.02\,s$ *a step-wise increase of the melt pool "area" of* 63°C *was introduced (disturbance).*

pool "area" returns to its reference value, which is almost equal to the time found during simulation.

The maximum deviation of the melt pool "area" from its reference value, due to the disturbance, is 72°C and occurs at sample number 58 (157Hz). Unfortunately, this error is of the same magnitude as the maximum error during the uncontrolled situation (figure 5.38(b) on page 121). This can be attributed to the long sample period and the small bandwidth of the XY-table. Nevertheless, it can be concluded from the measured signals that the absorptivity disturbance is successfully eliminated.

It can be observed from the longitudinal-section of the work piece that the thickness of the alloyed layer, during the absorptivity disturbance, is smaller than in the unperturbed situation. This over-control supports the statement that the beam velocity should not be used to compensate for absorptivity disturbances.

Figure 6.17 shows the results of an experiment in which the laser beam passes a region of reduced thickness. The beam velocity is increased to about $50\,\mathrm{mm} \cdot \mathrm{s}^{-1}$, as soon as the laser beam irradiates the region of reduced thickness. During the disturbance the melt pool "area" shows fluctuations, but the deviation of the melt pool "area" from its reference value is always less than 43°C. This error is about 30% smaller than the maximum error during the uncontrolled situation (figure 5.34(b) on page 117). The longitudinal-section of the work piece shows some considerable oxidation of the back side of the bridge. Nevertheless, when analyzing the thickness of the alloyed layer, it can be stated that the disturbance is better suppressed compared to the configuration in which the laser power was applied as a command signal (figure 6.12).

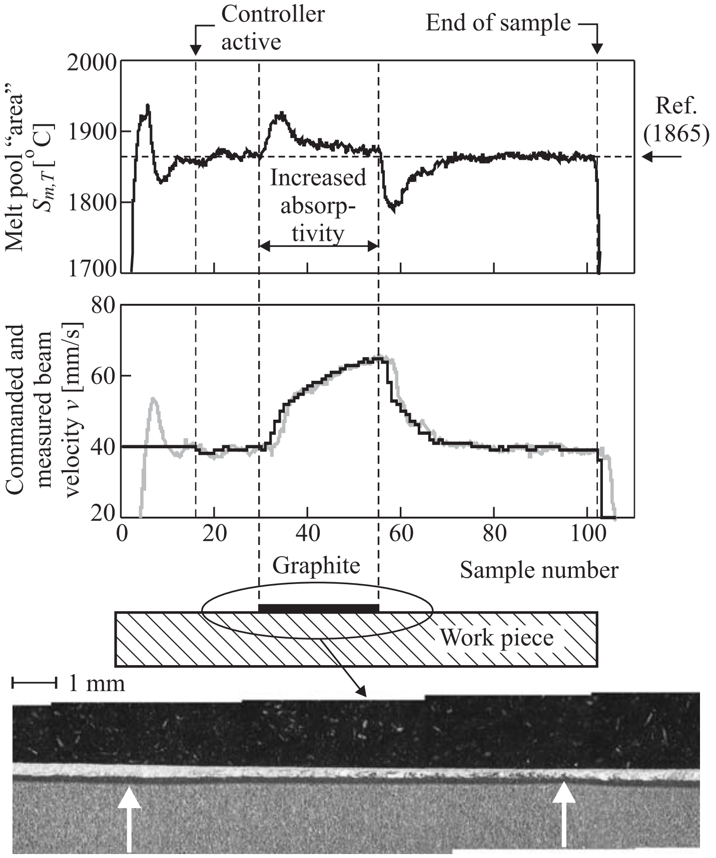

Figure 6.16: Performance of the PI/Smith-controlled process, in which the melt pool "area" $S_{m,T}$ is controlled by actuating the beam velocity at constant laser power $P_L = 1250\,W$, during an experiment including an absorptivity disturbance. Melt pool "area" $S_{m,T}$, commanded (solid) and measured (gray) beam velocity as a function of time (top). Controller parameters: $K_P = -\frac{1}{8}$, $K_I = \frac{3}{4}$, $n_k = 2$, control frequency $f_s = 157\,Hz$. Longitudinal-section of the work piece (bottom). The white arrows indicate the start and end of the surface of increased absorptivity.

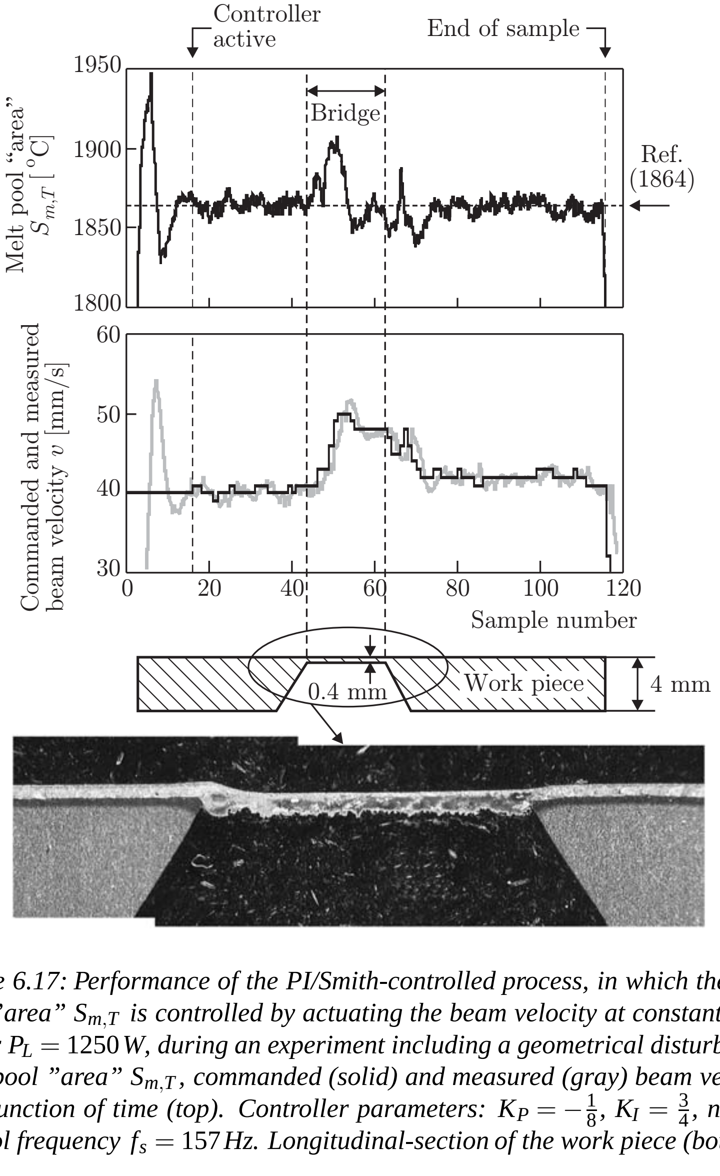

Figure 6.17: Performance of the PI/Smith-controlled process, in which the melt pool "area" $S_{m,T}$ is controlled by actuating the beam velocity at constant laser power $P_L = 1250\,W$, during an experiment including a geometrical disturbance. Melt pool "area" $S_{m,T}$, commanded (solid) and measured (gray) beam velocity as a function of time (top). Controller parameters: $K_P = -\frac{1}{8}$, $K_I = \frac{3}{4}$, $n_k = 2$, control frequency $f_s = 157\,Hz$. Longitudinal-section of the work piece (bottom).

6.5 Multivariable control

In this section two MIMO controllers are discussed, which apply the laser power as well as the beam velocity as a command signal. First a *Linear-Quadratic-Gaussian control* controller is discussed, which *simultaneously* actuates the laser power and the beam velocity. Next, a *mode-switch* controller is discussed. This controller either actuates the laser power or the beam velocity, depending on the type of disturbance.

6.5.1 Linear-Quadratic-Gaussian control

The simultaneous actuation of the laser power and the beam velocity may proof to be a more efficient method to control the laser alloying process than separate actuation of the laser power or the beam velocity. For this purpose, a multivariable *Linear-Quadratic-Gaussian* (LQG) controller is discussed in this section. Figure 6.18 shows the corresponding block diagram. The LQG controller synthesis is formulated as an optimal control problem, and is known for its robustness properties.

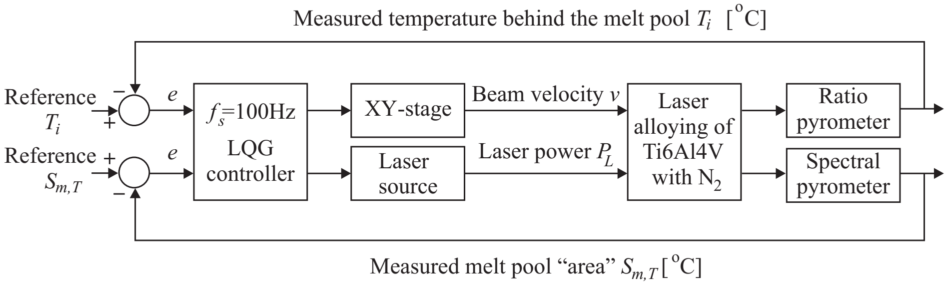

Figure 6.18: Block diagram of the control loop in which the laser alloying process is controlled by an LQG-controller.

LQG controller synthesis

The name Linear-Quadratic-Gaussian arises from the use of a linear model, an quadratic cost function and Gaussian white noise processes to model disturbance signals and noise. In LQG control, it is assumed that the process dynamics are linear and known. The measurement noise and disturbance signals (process noise) are assumed to be stochastic with known statistical properties. The process model, when expressed in state space representation, is defined as

$$\begin{aligned} \dot{\mathbf{x}} &= A\mathbf{x} + B\mathbf{u} + \mathbf{w}_d \\ \mathbf{y} &= C\mathbf{x} + \mathbf{w}_n \end{aligned} \tag{6.8}$$

where $\mathbf{x} = \mathbf{x}(t) \in \mathbb{R}^n$ represents the process state vector with n the order of the process, $\mathbf{y} = \mathbf{y}(t) \in \mathbb{R}^m$ the output vector with m the number of outputs, $\mathbf{u} = \mathbf{u}(t) \in \mathbb{R}^p$ the input vector with p the number of inputs, $A \in \mathbb{R}^n \times \mathbb{R}^n$, $B \in \mathbb{R}^n \times \mathbb{R}^p$, and $C \in \mathbb{R}^m \times \mathbb{R}^n$ the state space matrices. The disturbances (process noise) $\mathbf{w}_d \in \mathbb{R}^n$ and the measurement noise $\mathbf{w}_n \in \mathbb{R}^m$ are assumed to be uncorrelated zero-mean Gaussian stochastic signals with constant power spectral densities W and V respectively—i.e. $\mathbf{w}_d$ and $\mathbf{w}_n$ are *white noise* signals with (auto)covariances

$$\begin{array}{ll} E\left\{\mathbf{w}_d(t)\mathbf{w}_d(\tau)^T\right\} = W\delta(t-\tau), & E\left\{\mathbf{w}_n(t)\mathbf{w}_n(\tau)^T\right\} = V\delta(t-\tau), \\ E\left\{\mathbf{w}_d(t)\mathbf{w}_n(\tau)^T\right\} = 0 & E\left\{\mathbf{w}_n(t)\mathbf{w}_d(\tau)^T\right\} = 0 \end{array} \tag{6.9}$$

where $E\{\cdot\}$ denotes the expectation operator. The LQG control problem is defined as finding the optimal control command $\mathbf{u}(t)$ which minimizes the cost function

$$J = E\left\{ \lim_{\tau\to\infty} \frac{1}{\tau} \int_0^\tau \mathbf{x}^T Q\mathbf{x} + \mathbf{u}^T R\mathbf{u}\, dt \right\} \tag{6.10}$$

where $Q \in \mathbb{R}^n \times \mathbb{R}^n$ and $R \in \mathbb{R}^p \times \mathbb{R}^p$ are symmetric and positive definite weighting matrices (design parameters). Increasing Q relative to R results in a LQG controller which penalizes large deviations of the states (small output errors) at the expense of large command signals.

Solving the LQG problem consists of two steps. First the optimal control command $\mathbf{u}(t)$, minimizing the cost function (6.10) for the deterministic process—i.e. without w_d and w_n—is determined. This control command happens to be a simple state feedback law (Anderson and Moore, 1989)

$$\mathbf{u}(t) = -Lx(t) = -R^{-1}B^T X x(t) \tag{6.11}$$

where $L = R^{-1}B^T X$ is a constant matrix, which is independent of the statistical properties of $\mathbf{w}_d$ and $\mathbf{w}_n$. The matrix X is the unique positive-semidefinite solution to the algebraic Riccati equation

$$A^T X + XA - XBR^{-1}B^T X + Q = 0 \tag{6.12}$$

The next step is to find an estimate $\hat{\mathbf{x}}$ of the state $\mathbf{x}$. An optimal estimator, which minimizes $E\{(\mathbf{x}-\hat{\mathbf{x}})^T(\mathbf{x}-\hat{\mathbf{x}})\}$, is known as the *Kalman filter*. This estimator is independent of the weighting matrices Q and R and has the structure

$$\dot{\hat{x}} = A\hat{x} + Bu + K(y - C\hat{x}) \tag{6.13}$$

where K is the Kalman matrix given by

$$K = YC^T V^{-1} \tag{6.14}$$

in which Y is the positive-semidefinite solution of the algebraic Riccati equation

$$YA^T + AY - YC^T V^{-1} CY + W = 0 \tag{6.15}$$

The required solution to the stochastic LQG problem is then found by replacing $\mathbf{x}$ by $\hat{\mathbf{x}}$ to give $\mathbf{u}(t) = -L\hat{\mathbf{x}}(t)$, see figure 6.19. Note that the calculation of L and K are independent,

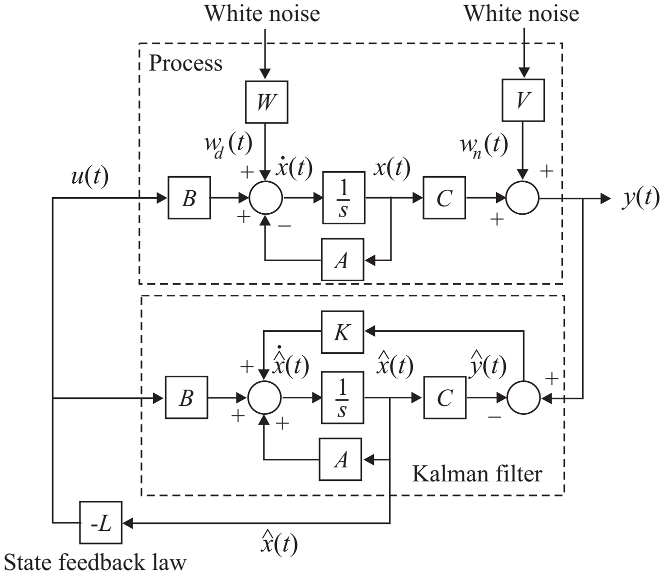

Figure 6.19: The LQG controller and the noisy process.

which is known as the *separation theorem* or *certainty equivalence principle*.

Stability can not be guaranteed for an LQG controller. However, it can be shown that when the weight matrix R is chosen diagonal and the process is noise free (i.e. no stochastic inputs and all states are available), the state feedback (6.11) results in a controlled system with gain margin in the range of 0.5 to infinity and a phase margin over 60° (Skogestad and Postlethwaite, 1996).

Because the LQG controller will be implemented on the Work Station Controller the discrete equivalent of the above-mentioned design method must be applied. In that case the cost function (6.10) is replaced by

$$J = \sum_{i=0}^{\infty} \mathbf{x}^T Q \mathbf{x} + \mathbf{u}^T R \mathbf{u} \tag{6.16}$$

The corresponding feedback control law is identical to the continuous version (6.11), but the matrix X is replaced by the unique positive-semidefinite solution X of the *discrete-time* algebraic Riccati equation (Houpis and Lamont, 1992)

$$A^T XA - X - [A^T XB][R + B^T XB]^{-1}[B^T XA] + Q = 0 \tag{6.17}$$

The discrete version the Kalman matrix K is given by equation (6.14) in which Y is the unique positive-semidefinite solution to the *discrete-time* algebraic Riccati equation (Houpis and Lamont, 1992)

$$AYA^T - Y - [AYC^T][V + CYC^T]^{-1}[CYA^T] + W = 0 \tag{6.18}$$

Design of an LQG controller for the laser alloying process

For the design of the discrete LQG controller, the identified process model (5.20) with (5.21), from section 5.3.4, was converted into the corresponding state space representation.

None of the transfer functions G_{ij} of the matrix transfer function (5.20) contains an integrator. Hence, the controller should add an integrator to guarantee a zero steady state error despite disturbances. The standard LQG design procedure does not yield a controller with an integration. Therefore, the process model is augmented with an integrator before the LQG design procedure is started. Then, after calculation of the LQG controller for the augmented process, this integrator is incorporated as part of the final controller on the Work Station Controller.

As only the ratio between Q and R is of importance, the R matrix was chosen equal to the unit matrix, $R = I$. The weighting matrix Q was chosen as $Q = q_0 C^T C$, where q_0 is a scalar. This implies that the output $y = [\Delta S_{m,T}\ \Delta T_i]^T$ is weighted rather than the states $\mathbf{x}$. The Kalman weighting matrices where chosen as $W = I$ and $V = I$ (pure white noise). The remaining controller parameter q_0 was tuned by applying SIMULINK, see figure 6.20. The parameter q_0 was tuned such that a typical disturbance is eliminated with admissible command signals. Figure 6.21 shows simulation results for $q_0 = 10^3$.

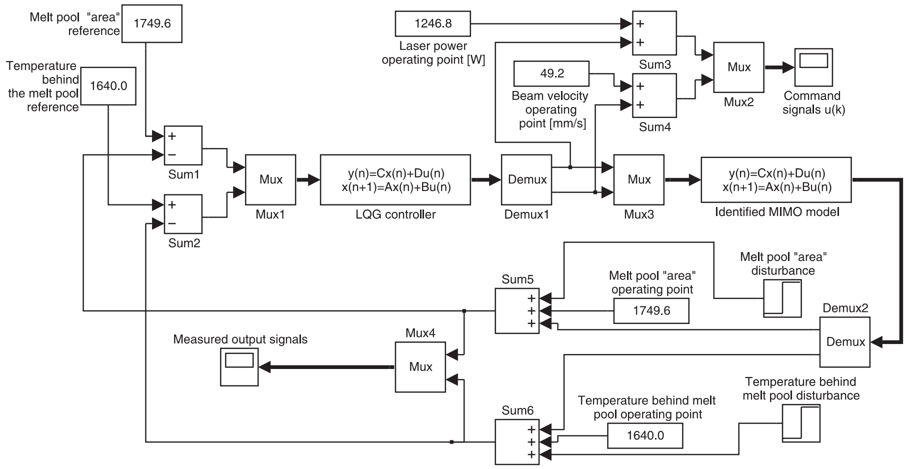

Figure 6.20: The SIMULINK *model of the LQG controlled multivariable process, which was applied to tune the LQG controller. The bold arrows indicate multiple signals.*

The response to typical absorptivity disturbance is shown in figure 6.21(a). Both the laser power and the beam velocity are applied by the controller to counteract the disturbance. The relative variation of the laser power (11%) is of the same magnitude as the relative variation of the beam velocity (9%), whereas it followed from the previous sections that the laser power is preferred over the beam velocity to suppress the absorptivity disturbance.

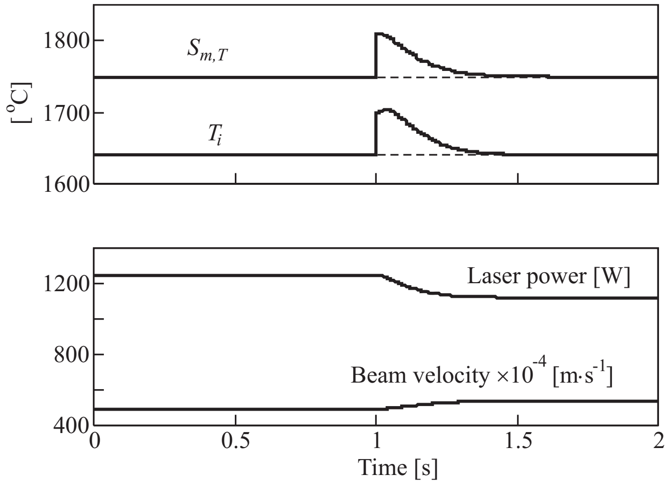

(a) Absorptivity disturbance. At $t = 1$s a step-wise increase of the melt pool "area" of 60°C, as well as a step-wise increase of the temperature behind the melt pool of also 60°C was introduced.

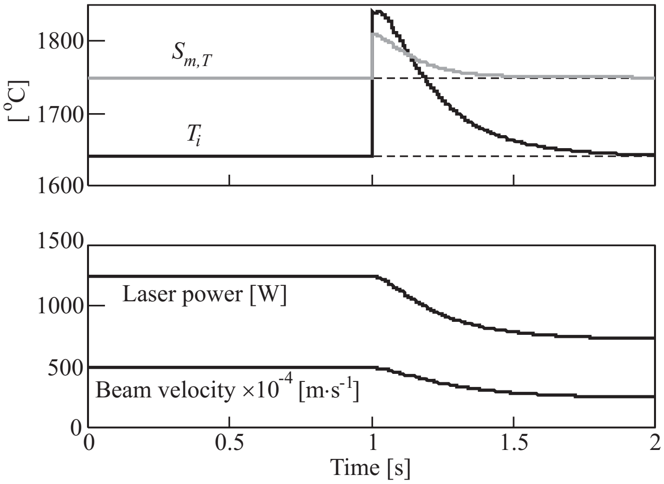

(b) Geometrical disturbance. At $t = 1$s a step-wise increase of the melt pool "area" of 60°C, as well as a step-wise increase of the temperature behind the melt pool of 200°C was introduced.

Figure 6.21: Simulation results of the SIMULINK *model (figure 6.20), which was used to tune the LQG-controller,* $q_0 = 1000$, $f_s = 100\,Hz$.

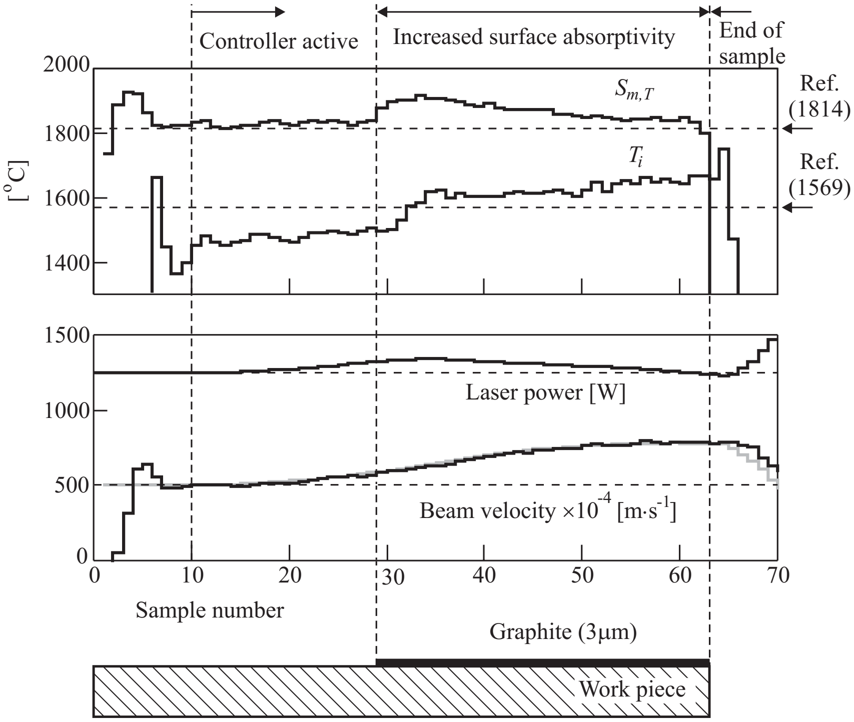

Figure 6.22: Performance of the LQG-controlled process, during an experiment including an absorptivity disturbance. Input and output signals (top) as well as the measured beam velocity (gray) as a function of time. Controller parameters: $Q = 10^3 C^T C$, $R = W = V = I$, *control frequency* $f_s = 100\,Hz$.

The response to typical geometrical disturbance is shown in figure 6.21(b). Again, both the laser power and the beam velocity are applied to counteract the disturbance. However, mainly the laser power is applied to suppress the disturbance, whereas it followed from the previous sections that the beam velocity is preferred to counteract the geometrical disturbance. Moreover, the beam velocity is decreased instead of increased.

It can be concluded from these simulations that the LQG-controller mainly applies the laser power to suppress a geometrical disturbance. To counteract absorptivity disturbances also beam velocity actuation is applied, whereas the reverse actuation is preferable. Unfortunately, this response of the controller can not be reversed by adjusting the elements of the weighting matrices Q and R, or by reversing the input and output pairing of the model (5.20).

The time required to eliminate the disturbances is too long. This can be attributed to the integrator, which was added to the controller to guarantee a zero steady state error. Then, the derivative of the command signals du/dt is penalized by the weight R. This makes it difficult for the controller to respond quickly to the error signals. This behavior is difficult to improve by adjusting the weight Q, without risking the command signals u

to exceed their admissible ranges (Skogestad and Postlethwaite, 1996).

Two experiments were carried out to verify the simulations. Figure 6.22 shows the results of an experiment in which the laser beam passes an absorptivity disturbance. Figure 6.22 shows the results of an experiment in which the laser beam passes region of reduced thickness. The results corresponds to the conclusions drawn from the simulations.

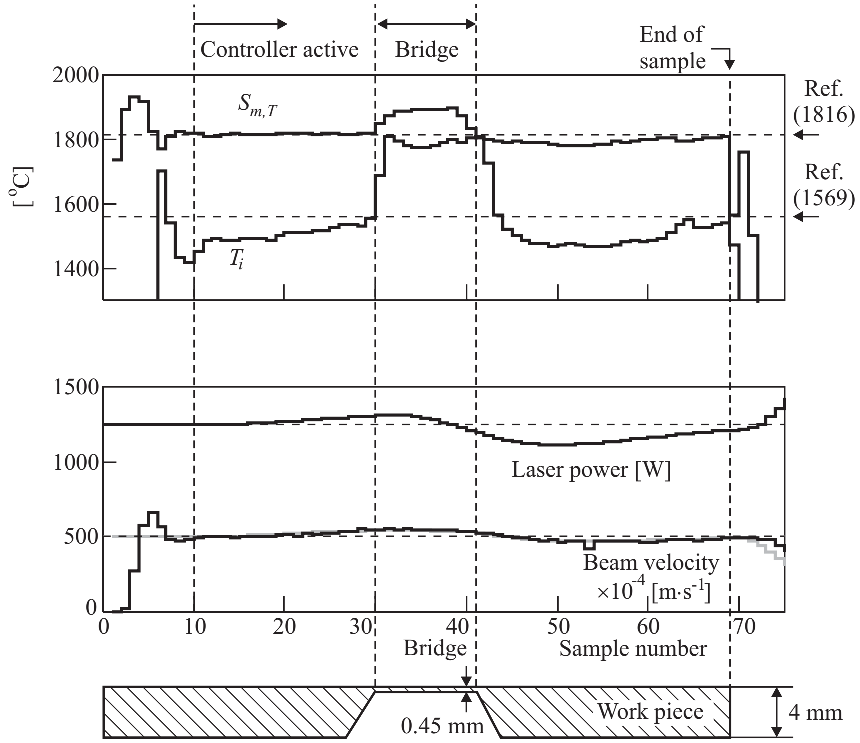

Figure 6.23: Performance of the LQG-controlled process, during an experiment including a geometrical disturbance. Input and output signals (top) as well as the measured beam velocity (gray) as a function of time. Controller parameters: $Q = 10^3 C^T C$, $R = W = V = I$, *control frequency* $f_s = 100\,Hz$.

6.5.2 Mode-switch control

It can be concluded from the previous sections, that the process cannot be controlled by a fixed controller. This can be attributed the dissimilar *modes* in which the process operates. That is, the dynamics of a work piece with large dimensions differ significantly from the dynamics of a thin plate. Moreover, as was shown, an absorptivity disturbance can be best suppressed by actuation the laser power, and a geometrical disturbance by the beam velocity. Such a process, which frequently ”switches” between a limited number of modes is referred to as a *switch-mode process* (Hilhorst, 1992). A limited number of distinct, but fixed, controllers suffices to control these distinct modes. These controllers may differ in structure, in the number of parameters, and even may operate at distinct sample rates.

In the case under consideration, two modes (or types of disturbances) can be distinguished: (*i*) a work piece of reduced thickness, in which the beam velocity can be best applied to actuate the process, and (*ii*) all other situations, in which the laser power can be best applied to actuate the process. These two modes can be discriminated by analyzing the relative response of the two pyrometers (see section 5.3.3). That is, in the case of an absorptivity disturbance the relative variation of the melt pool ”area” and the temperature behind the melt pool are approximately equal. Whereas in the case of a geometrical disturbance, the relative increase of the temperature behind the melt pool is much larger than the relative increase of the melt pool ”area”. Based on these two modes a mode-switch controller was implemented. Figure 6.24 shows the corresponding block diagram. Depending on the state of the *switch* either the upper or lower control loop is active. The upper loop consists of the spectral pyrometer, the PI/Smith-controller, the laser source and the process, as discussed in section 6.3.2. The lower loop consists of the ratio pyrometer, a PI/Smith-controller, the XY-table and the process. The latter controller will be designed and tuned in the following.

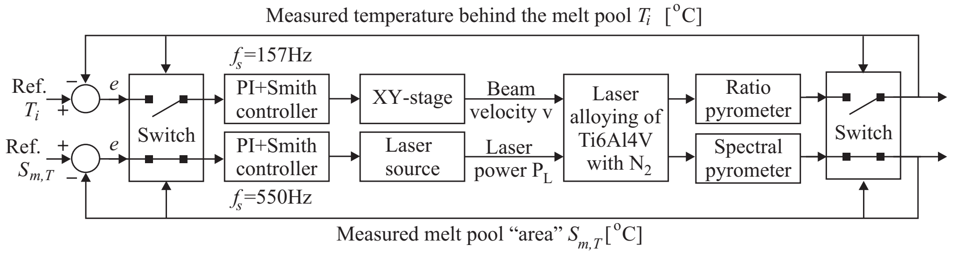

Figure 6.24: Block diagram of the laser alloying process controlled by the mode-switch controller. In the situation shown, the lower control loop is active, whereas the upper loop is inactive.

The transfer function (5.19), relating the commanded beam velocity v to the temperature behind the melt pool T_i was derived in section 5.3.3. The communication delay, expressed in number of sample periods (157Hz), was found to equal $n_k = 3$. The model does not include an integrator, and a PI-controller (6.5) suffices to obtain a zero steady state error. The controller parameters where determined by simulation of the closed loop, such that a typical disturbance of 200 °C is eliminated with reasonable speed with almost no overshoot. Figure 6.25 shows the root locus of the controlled process, if the integrator gain is chosen as $K_I = 0.35$. Then the controlled system is stable for $-0.047 < K_P < 0$. Figure 6.26 shows the simulation results of the corresponding controlled process, when the proportional gain is chosen as $K_P = -0.03$. These controller parameters imply a gain margin of 4.1 dB and a phase margin of about 63°. As can be observed from figure 6.26, the step-wise disturbance is eliminated in about 0.18 seconds. This period is relatively long, which can be attributed to the fact that the bandwidth of the XY-table is small. Due

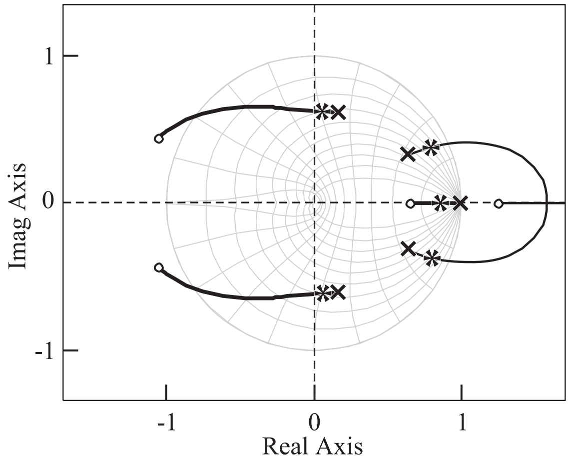

Figure 6.25: Root locus of the controlled process with $K_I = 0.35$ *and* $K_P \in [0, -\infty\rangle$*. The zero at -46.9 is not shown. The pole locations marked with * correspond to* $K_P = -0.03$*.*

to the long sample period the disturbance is detected later than $t = 0.02\,\mathrm{s}$. As can be observed, the beam velocity is confined to its admissible range $v \in \langle 0, 0.3]\,\mathrm{m{\cdot}s}^{-1}$.

Both controllers (figure 6.24) were augmented with a Smith-predictor and were implemented on the Work Station Controller. The computational load imposed on the Work Station Controller by the mode-switch controller is significantly lower than the load imposed by the LQG-controller, because only one controller is active during the control of the process.

The switch, determining which of the two control loops is active, was defined as

$$\text{Switch}: \begin{cases} \text{Control of } S_{m,T} & \text{by actuation of } P_L & \text{if } \Psi > 1 \\ \text{Control of } T_i & \text{by actuation of } v & \text{if } \Psi \leq 1 \end{cases} \tag{6.19}$$

in which Ψ denotes the *mode-indicator*, which was defined as

$$\Psi = 1.15 \left| \frac{S_{m,T}}{S^r_{m,T}} \right| / \left| \frac{T_i}{T^r_i} \right| \tag{6.20}$$

where $S^r_{m,T}$ [°C] and T^r_i [°C] denote the reference values of the melt pool ”area” and the temperature behind the melt pool, respectively. The number 1.15 compensates for the difference between the two reference values.

When a mode-switch is detected, one of the controllers is activated and the other controller is de-activated. As a result, an undesirable switching transient (bump) in the command signal may be introduced (Hilhorst, 1992). Therefore, when the controller switches from laser power actuation ($\Psi > 1$) to beam velocity actuation ($\Psi \leq 1$), a constant laser power level is applied. This power is set to the level, which was applied just before the switch. In addition, the error signal corresponding to the melt pool ”area” is set to zero:

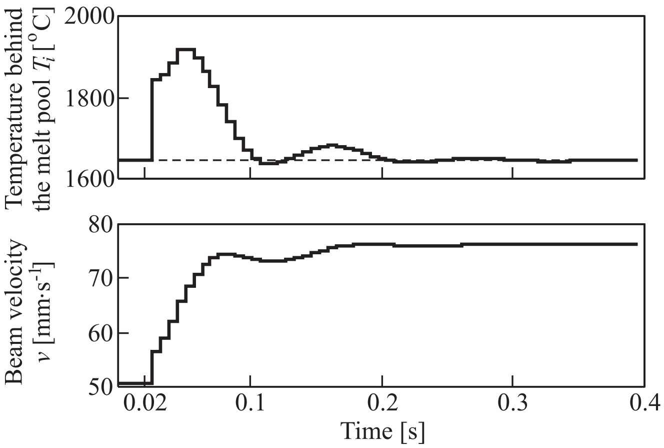

Figure 6.26: Simulation results of the SIMULINK *model which was used to tune the PI-controller. Controller parameters:* $K_P = -0.03, K_I = 0.35,\ f_s = 157\,Hz$*. At* $t = 0.02\,s$ *a step-wise increase of the melt pool area of* $200\,°C$ *was introduced (disturbance).*

$e(k) = S^r_{m,T} - S_{m,T} = 0$. However, this does not guarantee a bumpless transfer from laser power actuation to beam velocity actuation ($\Psi > 1$).

A slightly different start-up procedure, as described in the previous sections, was implemented:

(i) The irradiation and the acceleration of the work piece start simultaneously, causing some overshoot of the melt pool area. The melt pool ”area” and the temperature behind the melt pool stabilize after a short period of time,

(ii) The controller is not yet activated. Up to the instant at which the controller becomes active, the controller states are constant: $e(k) = T^r_i - T_i = 0$, $u(k) = v_0$ and $e(k) = S^r_{m,T} - T_{m,T} = 0$, $u(k) = P_{L0}$. Moreover, the mode-indicator is set to $\Psi > 1$,

(iii) After 0.1 seconds the controller is activated.

The performance of the mode-switch controller was evaluated by an experiment in which the surface of the work piece was coated with a graphite layer. During the whole experiment the mode-indicator Ψ was larger than one. Hence, only the laser power was actuated during the whole experiment. The experimental results were identical to the results as described in section 6.3.2. Therefore, these results are not presented here.

Figure 6.27 shows the results of an experiment in which the laser beam passes a region of reduced thickness. As can be observed from this figure, the process is controlled by actuation of the laser power ($\Psi > 1$) up to $t = 0.33$s. At $t = 0.3$s a disturbance was detected, but not yet identified as the geometrical disturbance. As a result the laser power was reduced from 1050 W to about 800 W. From $t = 0.33$s, the beam velocity is actuated ($\Psi \leq 1$). Then, the temperature behind the melt pool is the quantity to be controlled. As a result, the beam velocity is increased from 40 to 60 mm·s^{-1}. At $t \approx 0.36$s the geometrical disturbance is no longer encountered. As a result, the controller switches back to control

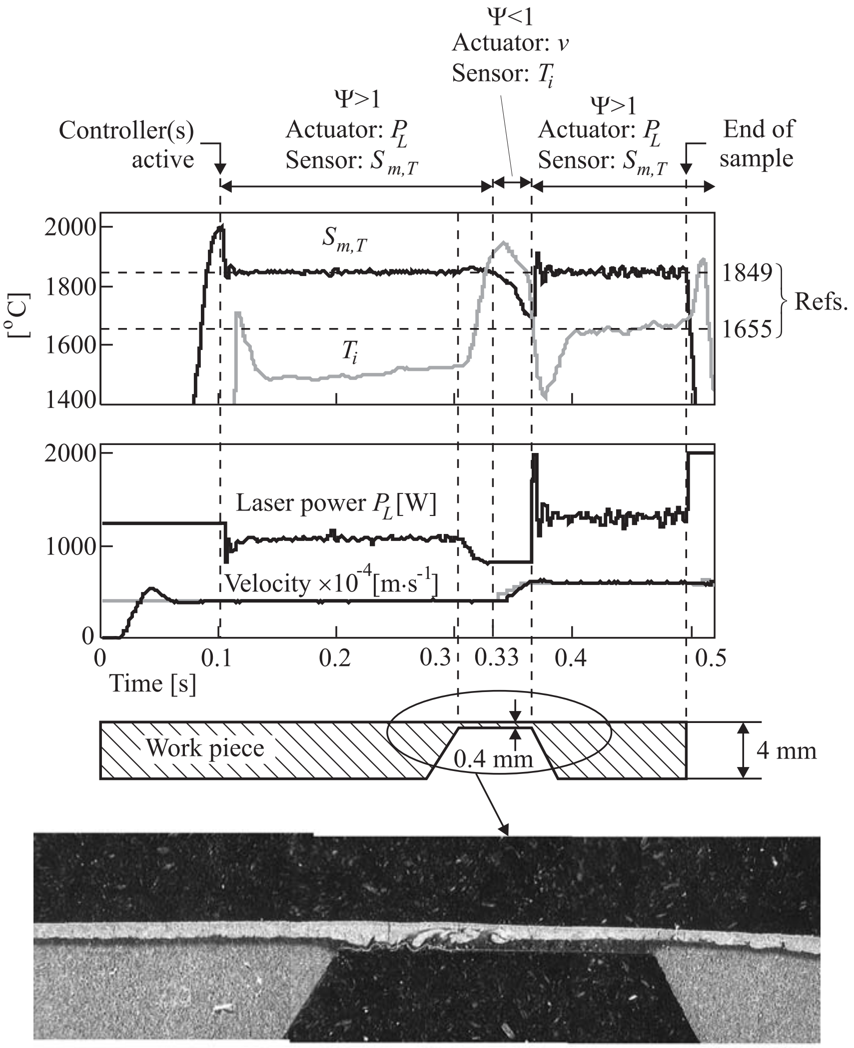

Figure 6.27: Performance of the mode-switch controller process during a geometrical disturbance. Measured input and output signals (top). For the controller parameters for $\Psi > 1$ *see section 6.3.2. Controller parameters for* $\Psi \leq 1$*:* $K_P = -0.03, K_I = 0.35$, $f_s = 157$*Hz. Longitudinal-section of the work piece (bottom).*

of the ”area” by laser power actuation ($\Psi > 1$). This is induces a bump in the laser power and some overshoot of the melt pool ”area”. The beam velocity applied is equal to the beam velocity just before the switch (i.e. $v = 60\,\mathrm{mm\,s^{-1}}$). This beam velocity is larger than the beam velocity before the geometrical disturbance. As a result, the applied laser power is larger ($P_L = 1250\,\mathrm{W}$) than before the disturbance.

The maximum deviation of the melt pool ”area” from its reference due to the disturbance occurs just before the mode-switch at $t = 0.36\,\mathrm{s}$ and equals $-157\,^{\circ}\mathrm{C}$. This error is large, compared to the uncontrolled situation (figure 5.34(b) on page 117). However, the error is negative, whereas the error during the uncontrolled situation was positive. The maximum deviation of the temperature behind the melt pool T_i, from its reference due to the disturbance occurs at $t = 0.34\,\mathrm{s}$. This error is less than half the error, which would occur if no control was applied.

As can be observed from longitudinal-section of the work piece, the alloyed layer thickness increases first, but it then reduces to a thickness which is somewhat smaller than the depth in the uncontrolled situation. No oxidation of the back side of the bridge occurs. Based on these results it can be concluded that for the suppression of an absorptivity disturbance, it is better to apply the laser power as the command signal. Whereas, for the suppression of the negative effects of a work piece with an area of reduced thickness (geometrical disturbance), the beam velocity should be used as the command signal.

6.6 Conclusions

In this chapter the feedback controllers for laser nitriding of titanium were designed and their performance during absorptivity and geometrical disturbances were analyzed. From the performance of the controllers during disturbances the following can be concluded:

- The aim of the controllers was to guarantee zero steady state error in the face of step-wise disturbances, which are to be eliminated with reasonable speed without overshoot,
- A Smith-predictor was successfully applied to cope with the (communication) delay of the identified processes,
- The sample frequency ($f_s = 105\,\mathrm{Hz}$) of the control loop, in which the thermal camera was used as melt pool area sensor and the laser power as the command signal, is too low compared to the bandwidth of the process,
- Although the melt pool area is an important quantity to be controlled, the temperature of the melt pool can not be ignored entirely. Because the melt pool ”area” $S_{m,T}$, as measured by the spectral pyrometer is partly determined by the melt pool temperature, the melt pool ”area” is a better quantity to be controlled than the melt pool area S_m,
- To counteract the negative effects of an absorptivity disturbance, it is better to apply the laser power as the command signal. Whereas, for the suppression of the negative effects of a work piece with an area of reduced thickness (geometrical disturbance), the beam velocity should be used as the command signal,
- The performance of the controllers, which apply the beam velocity as the command signal, can be improved by applying an XY-table with an increased bandwidth,

- The LQG-controller mainly applies the laser power to counteract a geometrical disturbance. To suppress the absorptivity disturbance also the beam velocity is applied, whereas the reverse actuation is preferable. Moreover, the response of the LQG controller to disturbances is too slow,
- The mode-switch controller successfully eliminates both intrinsic disturbances by appropriate actuation of the laser power and the beam velocity,
- When, the laser beam passes the area of reduced thickness the dynamics of the process change. Better performance may be obtained when the design of the controller includes a model of the dynamics of the disturbance. Alternatively, adaptive control (section 3.5.4) may be considered to cope with variations of the process dynamics.

Chapter 7

REVIEW, CONCLUSIONS AND SUGGESTIONS

This chapter reviews the results and conclusions from the previous chapters and presents suggestions for future research.

7.1 Review and conclusions

The work discussed in this thesis was addressed to the development of process models and control strategies for laser surface treatment. As a test case laser alloying of titanium (Ti6Al4V) with nitrogen was considered.

The processing results of laser surface treatment, such as hardness and layer dimensions, are sensitive to small variations of the operating parameters (extrinsic disturbances, e.g. laser power), as well as to disturbances originating from the work piece itself (intrinsic disturbances). The varying surface absorptivity and the small dimensions of the work piece, were found to be important intrinsic disturbances.

The goal of the control system is to obtain constant processing results (e.g. thickness of the alloyed layer) in the face of the disturbances. The desired results can not be measured on-line, or can only be measured after laser-material interaction (i.e. after cooling of the surface), whereas the manipulation of the process output can only take place at the laser-material interaction zone. The quantities, which can be measured are temperature related, such as the (melt pool) temperature distribution and its dimensions. Models were derived, which relate the measurable quantities to the desired properties of the laser treatment. Operating parameters, which can be readily commanded on-line, are the laser power and the beam velocity.

To be able to design an appropriate controller, the technology of laser surface treatment was discussed in the view of control theory. It was found that laser surface treatment is non-linear. However, the process response to command inputs, around an operating point, can be described with acceptable accuracy by a linear model of first order.

The current status of sensors, actuators and models for control of laser surface processing was discussed. It was found that for the observation of the temperature distribution or the melt pool dimensions, optical sensors which measure thermal radiation (pyrometers, thermal camera's) can be best applied.

Several models were developed, which provide insight in the steady-state behavior, as well as dynamics of the temperature distribution and the melt pool. It was found that the ratio $P_L/\sqrt{v}$ of the laser power and beam velocity is a quantity determining the maximum surface temperature during hardening and the melt pool depth during processing with a liquid phase.

For the design of an controller a transfer function, which relates the command inputs to the outputs of the process, is required. It was found mathematically and experimentally that, the gain of these transfer functions decreases with increasing beam velocity, whereas the bandwidth increases. In addition, it was found that variations in laser power only affect the amplitude and not the shape of the temperature distribution. Moreover, the shape of the temperature distribution induced in a plate, resembles the temperature distribution in a semi-infinite work piece, induced by a fast moving beam. Therefore, it was concluded that for the suppression of an absorptivity disturbance the laser power can be best applied as the command signal. Whereas, the beam velocity can be best applied to counteract the negative effects of a geometrical disturbance.

The conclusions derived from the models were verified experimentally by process identification. For this purpose a fast thermal camera was developed to measure the melt pool area. It was shown that a spectral pyrometer can be modified such that its signal variations are mainly (65%) determined by the melt pool area and partly (35%) by the melt pool temperature. The relative variation of the melt pool area, due to variations of the input commands, are much larger than variations of the melt pool temperature. The low frequency dynamics of the melt pool area were shown to be described, with an acceptably accuracy, by first order transfer functions. Typical time constants of the melt pool area, if actuated by the laser power or beam velocity, are of the order of 3 to 10 ms. There was relative good correspondence between the experimental results and the models. Moreover, the conclusions drawn from the models were proven to be correct. Smooth and shiny titanium-nitride layers were obtained at beam velocities ranging from 40 to $50\,\mathrm{mm \cdot s^{-1}}$, and at laser power levels ranging from 1000 to 1250 W. For these operating points, the parameters of transfer functions, which relate the melt pool area to the input commands, were calculated.

On the basis of these models controllers were designed and tuned. It was shown that a simple PI-controller suffices to guarantee zero steady state errors. It was found that the sample rate of the thermal camera is too small, compared to the dynamics of the melt pool area. Improved performance was achieved by a control system in which the modified spectral pyrometer was applied as an area sensor. This can be partly attributed the fact that the pyrometer signal is determined by the melt pool area, as well as by the melt pool temperature. The performance of a multivariable LQG controller was poor, because it mainly applied the laser power to eliminate both types of intrinsic disturbances. The performance of a mode-switch controller was better, because it commanded the laser power in the case of an absorptivity disturbance and the beam velocity in the case of a geometrical disturbance.

7.2 Suggestions for future research

As an alternative to the mode-switch controller, a (new) multivariable control algorithm should be designed and tuned. This controller should simultaneously apply the laser power and the beam velocity to counteract disturbances. It should mainly actuate the laser power in the case of an absorptivity disturbance, and mainly the beam velocity in the case of a geometrical disturbance. Moreover, when a disturbance is detected the controller should gradually change from one actuator to the other. This will guarantee a bumpless transfer.

To cope with the varying process dynamics an adaptive controller may be considered. Alternatively, the dynamics of the geometrical disturbance may be modelled and be used, with the process model, for the design of a controller.

The time required to design, tune and test controllers for laser material processing should be reduced. This can be achieved by automating:

- The acquisition of input and output data, and storing the data in a database,
- The process identification,
- The generation and implementation of controller code,

This requires a laser material processing system, in which all devices are designed according to an open architecture model.

REFERENCES

J.H. Abboud, D.R.F West, and R.D. Rawlings, 1994. Functionally gradient coating layers produced by laser alloying/cladding. In *Proceedings of the NATO advanced study institute on laser processing, Sesimbra, Portugal, july 3-16*, p. 237–254.

M. Alavi, M. Lorinez, and S. Buttgenbach, 1989. Lichtemission wärhend des Laserschweissprozesses. *Laser und Optoelectronik*, 21-3 (1989), 69–72.

B.D.O. Anderson and J.B. Moore, 1989. *Optimal control, linear quadratic methods*. Prentice-Hall, Englewood Cliffs, U.S.A.

A.G. Arlt and R. Müller, 1994. Technology for wear resistant inside diameter cladding of tubes. In *Proceedings of the ECLAT'94*, p. 203–211.

M.F. Ashby and K.E. Easterling, 1984. The transformation hardening of steel surfaces by laser beams -I. Hypo eutectoid steels. *Acta metallurgica*, 32 (1984), 1935–1948.

K.J. Åström and B. Wittenmark, 1995. *Adaptive control*. Addison-Wesley, Reading, U.S.A.

K. J. Åström and B. Wittenmark, 1997. *Computer controlled systems, theory and design*. Prentince-Hall, Englewood Cliffs, U.S.A.

D. Auric, E. Hanonge, E. Kerrand, J.C. de Miscault, and J. Cornillault, 1987. Thermal imaging system for material processing. In *High power lasers, SPIE 801*.

G. Backes, A. Gasser, K. Wissenbach, and E. Beyer, 1994. *Materialbearbeitung mit CO_2 Laserstrahlung höchster Leistung*, Chapter: Prozesskontrolle und Regelung beim Beschichten, p. 89–93. DVI.

M. Bamberger and M. Geler, 1997. Energy coupling between CO_2-laser irradiation and metallic substrates. *Lasers in Engineering*, 6 (1997), 213–234.

M. Bamberger, W.D. Kaplan, B. Medres, and L. Shepeleva, 1998. Calculation of process parameters for laser alloying and cladding. *Journal of laser applications*, 10-1 (1998), 29–33.

M. Bass, 1987. *Laser-materials interactions*. San Diego, U.S.A., Academic Press.

B. Basu and A.W. Date, 1990a. Numerical study of steady state and transient laser melting problems I. Characterisation of flow field and heat transfer. *International journal of heat and mass transfer*, 33-6 (1990), 1149–1163.

B. Basu and A.W. Date, 1990b. Numerical study of steady state and transient laser melting problems - II. Effect of the process parameters. *International journal of heat and mass transfer*, 33-6 (1990), 1165–1175.

B. Basu and A.W. Date, 1992a. Rapid solidification following laser melting of pure metals -I. Study of flow field and role of convection. *International journal of heat and mass transfer*, 35-5 (1992), 1049–1058.

B. Basu and A.W. Date, 1992b. Rapid solidification following laser melting of pure metals -II. Study of pool and solidification characteristics. *International journal of heat and mass transfer*, 35-5 (1992), 1059–1067.

F. Bataille, J.M. Cerez, and D. Kechemair, 1992. A systematic method for the design of a multi-variable controller actuating power and speed during a CO_2 laser surface treatment. *Journal of laser applications*, 4 (1992), 43–47.

F. Bataille, D. Kechemair, and R. Houdjal, 1991. Real time actuation of laser power and scanning velocity for thermal regulation during laser hardening. In *Industrial and scientific uses of high-power lasers, SPIE 1502*, p. 135–139.

F. Bataille, D. Kechemair, C. Pawlovski, and R. Houdjal, 1990. Thermal regulation applied to CO_2 laser self quenching of complex geometry workpieces. In *Gas flow and chemical lasers, SPIE 1397*, p. 839–842.

F. Bataille, C. Pawlowski, and D. Kechemair, 1992. Thermal regulation applied to CO_2 laser surface treatments. *Measurement science & technology*, 3 (1992), 50–57.

M. Bea, S. Borik, A. Giesen, and U. Zoske, 1990. Transient behavior of optical components and their correction by adaptive optical elements. In *Proceedings of ICALEO'90*.

L.H.J.F. Beckmann and D. Ehrlichmann, 1995. Optical systems for high-power laser applications: principles and design aspects. *Optical and Quantum Electronics*, 27 (1995), 1407–1425.

H.W. Bergman and E. Geissler, 1990. Laser hardening of steel. In *Proceedings of the ELCAT'90*, p. 321–331.

H.W. Bergmann, J. Breme, and S.Z. Lee, 1988. Laser hardfacing by melt reactions. In *Proceedings of the ECLAT'88*, p. 70–73.

H.W. Bergmann and E. Geissler, 1988. On-line computer controlled laser hardening. In *Proceedings of the ECLAT'88*, p. 109–113.

E. Beyer, 1985. *Einfluss des Laserinduzierten Plasmas beim Schweissen mit CO_2-Lasern*. Ph.D. thesis, Technische Hochschule Darmstadt, Germany.

E. Beyer, 1995. Systeme zur Prozessüberwachung und Regelung in der Laserfertigungstechnik. In *Aachener Kolloqium für Lasertechnik '95*.

E. Beyer and P. Abels, 1992. Process monitoring in laser materials processing. In *Proceedings of the LAMP'92*, p. 433–435.

H.W. Bieler, A. Gasser, G. Herziger, E.W. Kreutz, J. Seelhorst, W. Sokolowski, and K. Wissenbach, 1988. Methods of adaptive control in surface processing with laser radiation. In *Proceedings of the ECLAT'88*, p. 46–53.

S. Biermann and M. Geiger, 1991. Integration of diagnostics in high power laser systems for optimization of laser material processing. In *Proceedings of the conference on Modeling and simulation of laser systems II, 23-24 January, Los Angeles, U.S.A., SPIE 1415*, p. 330–341.

W. Bloehs, B. Grünenwald, F. Dausinger, and H. Hügel, 1996a. Recent progress in laser surface treatment: II. Adopted processing for high efficiency and quality. *Journal of laser applications*, 8 (1996), 65–77.

W. Bloehs, D. Grünenwald, F. Dausinger, and H. Hügel, 1996b. Recent progress in laser surface treatment: I. Implications of laser wavelength. *Journal of laser applications*, 8 (1996), 15–23.

H. Blok, 1937. Theoretical study of temperature rise at surface of actual contact under oiliness lubricating conditions. In *Proceedings of the general discussion on lubrication and lubricants, Instn. Mech. Engrs.*, p. 222–235.

P. Blonk, 1991. *On the design of cell and workstation controllers for automated production systems*. Ph.D. thesis, University of Twente, Enschede, the Netherlands.

J. Bos and H. Moes, 1994. Frictional heating of elliptic contacts, flash temperatures, dissipative processes and tribology. In *Proceedings of the 20th Leeds-Lyon symposium on tribology*, p. 491–500.

O.H. Bosgra and H. Kwakernaak, 1995. *Design methods for control systems, Lecture notes*. Dutch Institute for Systems and Control (DISC), Enschede, the Netherlands.

H.E. Boyer and T.L. Gall, 1985. *Metals handbook*. ASM international, Ohio, U.S.A.

R. Boyer, G. Welsch, and E.W. Collings, 1994. *Materials properties handbook: titanium alloys*. ASM International, U.S.A.

R.N. Bracewell, 1986. *The Fourier transformation and its applications*. McGraw-Hill, New York, U.S.A.

A. Brandt and A.A. Lubrecht, 1990. Multilevel matrix multiplication and fast solution of integral equations. *Journal of computational physics*, 90 (1990), 348–370.

B. Brenner, S. Bonßand R. Franke, I. Haase, and H.J. Scheibe, 1996. Mechanical and tiribological properties of laser gas alloyed Ti6Al4V. In *Proceedings of the ECLAT'96*, p. 477–484.

D.J. Brookfield and S.J. Sharkey, 1992. Modelling and control of laser transformation hardening. In *Proceedings of the 11th IASTED international conference in modelling, instrumentation and control, feb., Insbruck, Austria*, p. 514–517.

J. E. Bullema, 1994. Constante laskwaliteit met vaag geregelde laser. *Polytechnisch tijdschrift*, 3 (1994), 12–15.

H.D. Burchards and A. Weisheit, 1988. Gasnitriren von Titanlegierungen mit Laserstrahl. In *Proceedings of the ECLAT'88*, p. 64–65.

H.S. Carslaw and J.C. Jaeger, 1959. *Conduction of heat in solids*. Clarendon Press, Oxford, U.K.

T. Chande and J. Mazumder, 1983a. Composition control in laser surface alloying. *Metallurgical transactions B*, 14B (1983), 181–190.

T. Chande and J. Mazumder, 1983b. Dimensionless parameters for process control in laser surface alloying. *Optical engineering*, 22-3 (1983), 362–365.

D.U. Chang, 1995. Feasibility of sound-based laser weld quality monitoring device. In *Proceedings of the ICALEO'95*, p. 613–622.

S.S. Charschan, 1972. *Lasers in industry*. Laser institute of America, Toledo, U.S.A.

M.W. Chase, C.A. Davies, J.R. Downey, D.J. Frurip, R.A. McDonald, and A.N. Syverud, 1985. JANAF thermochemical tables, part II, Cr-Zr. *Journal of physical and chemical reference data*, 14-1 (1985), 1542–1544.

H.B. Chen, L. Li, D.J. Brookfield, K. Williams, and W.M. Steen, 1991. Laser process monitoring with dual wavelength optical sensors. In *Proceedings of the ICALEO'91*, p. 113–122.

M.M. Chen, 1994. Scoping analysis and limitations of transport phenomena modeling for laser surface modifiaction. In *Proceedings of the NATO advanced study institute on laser processing, Sesimbra, Portugal, july 3-16*, p. 157–175.

P. Cielo, G. Vaudreuil, B. Arsenault, C. Gelinas, and W. Jamroz, 1992. Infrared temperature sensors for control of the surface melting process on super conduction materials. In *Proceedings of the LAMP'92*, p. 421–426.

H.E. Cline and T.R. Anthony, 1977. Heat treating and melting material wit a scanning laser or electron beam. *Journal of applied physics*, 48-9 (1977), 3895–3900.

J.F. Coutouly and J. Merlin, 1993. Determination of changes in absorptivity and emissivity during laser transformation hardening. Deduction of actual temperature. *Lasers in engineering*, 2 (1993), 227–238.

R. F. Curtain and H. Zwart, 1995. *An introduction to infinite-dimensional linear systems theory*. Springer, Heidelberg, Germany.

F. Dausinger, M. Beck, J.H. Lee, E. Meiners, T. Rudlaff, and J. Shen, 1990. Energy coupling in surface treatment processes. *Journal of laser applications*, summer/fall (1990), 17–21.

R. Deimann, G. Habenicht, and W. Stark, 1988. Use of acoustic emission analysis (AEA) in quality assurance of laser beam spot welding. In *Proceedings of the ECLAT'88*, p. 54–58.

G. Deinzer, A. Otto, P. Hoffmann, and M. Geiger, 1994. Optimizing systems for laser beam welding. In *Proceedings of the LANE'94*, p. 193–206.

R. Dekumbis and A. Frenk, 1988. Absorption of CO_2 laser light during laser surface melting. In *Proceedings of the ECLAT'88*, p. 134–137.

H. Derouet, 1996. *Instrumentation et contrôle en temps réel de traitements de surface par laser avec passage à l'état liquide*. Ph.D. thesis, Université Pierre et Marie Curie, Paris VI, France.

H. Derouet, G. Caillibotte, and D. Kechemair, 1994. Towards real time control of surface treatments with liquid phase: molten depth on line estimation. In *Laser materials processing: industrial and microelectronics applications, SPIE 2207*, p. 321–329.

H. Derouet, L. Sabatier, F. Coste, and R. Fabbro, 1997. Process control applied to laser surface remelting. In *Proceedings of the ICALEO'97*, p. 85–92.

H.S. Dobbs and J.L.M. Robertson, 1983. Tensile strength, fatigue life and corrosion behavior of Ti-318 and Ti-550. In *Proceedings of the symposium on titanium alloys in surgical implants, Phoenix, U.S.A., 11-12 may 1981*, p. 227–237.

C.W. Draper and C.A. Ewing, 1984. Review: Laser surface alloying: a bibliography. *Journal of material science*, 19 (1984), 3815–3825.

C.W. Draper and J.M. Poate, 1985. Laser surface alloying. *International metal reviews*, 30-2 (1985), 85–107.

A. Drenker, E. Böggering Beyer, R. L. Kramer, and K. Wissenbach, 1990. Adaptive temperature control in laser transformation hardening. In *Proceedings of the ECLAT'90*, p. 283–290.

A. Drenker, L. Boeggering, K. Wissenbach, and E. Beyer, 1991. Adaptive temperature control during transformation hardening with CO_2-laser. *Laser und Optoelektronik*, 23-5 (1991), 48–53.

M.G. Dreyfus, 1963. Spectral variation of blackbody radiation. *Applied optics*, 2-11 (1963), 1113–1115.

T. Duverneix, T. Puig, and F. Bataille, 1990. Laser nitriding of titanium by solid state diffusion of nitrogen at constant temperature. In *Proceedings of the ICALEO'90*, p. 525–538.

M.K. El-Adawi, M.A. Abd El-Naby, and S.A. Shalaby, 1994. Laser heating of a slab having temperature dependent surface absorptance. *Vacuum*, 45-1 (1994), 65–70.

M.K. El-Adawi, M.A. Abd El-Naby, and S.A. Shalaby, 1996. Laser heating of a slab with temperature dependent absorptance in relation to the cooling conditions. *Vacuum*, 47-10 (1996), 1167–1173.

M. Ellis, D.C. Xiao, W.M. Steen, C. Lee, K.G. Watkins, and W.P. Brown, 1994. Laser cladding of low melting point alloys. In *Proceedings of the NATO advanced study institute on laser processing, Sesimbra, Portugal, july 3-16*, p. 379–394.

A. Erdelyi, 1954. *Tables of integral transforms*, volume 2. McGraw-Hill, New York, U.S.A.

D.F. Farson, K.S. Fang, and J. Kern, 1991. Intelligent laser welding control. In *Proceedings of the ICALEO'91*, p. 104–112.

D. Farson, K. Hillsley, J. Sames, and R. Young, 1996. Frequency-time characteristics of air-borne signals from laser welds. *Journal of laser applications*, 8 (1996), 33–42.

D. Farson and J. Kern, 1995. Analysis of laser weld quality by classification of structure-born acoustic emissions. *Lasers in engineering*, 4 (1995), 13–23.

A. Fischer and G. Lensch, 1996. Technical application of laser surface treatment - Hardening, Alloying, Cladding. In *Proceedings of the ECLAT'96*, p. 399–405.

J.A. Folkes and K. Shibata, 1994. Laser cladding of Ti-6Al-4V with various carbide powders. *Journal of laser applications*, 6 (1994), 88–94.

G.F. Franklin, J.D. Powell, and A. Emami-Naeini, 1994. *Feedback control of dynamic systems*. Addison-Wesley, Reading, U.S.A.

A. Frenk, A.F.A. Hoadley, and J.D. Wagniere, 1991. In-situ technique for measuring the absorption during laser surface melting. *Metallurgical transactions B*, 22B (1991), 139–141.

G. Funk and W. Müller, 1990. Temperaturgeregeltes Laserhärten in der Präzisionsmegenfertigung. In *Proceedings of the ECLAT'90*, p. 227–236.

A. Gasser, 1991. *Oberflächenbehandlung metallischer Wersktoffe mit CO_2-Laserstrahlung in der flüssigen Phase*. Ph.D. thesis, Technische Hochschule Aachen, Germany.

A. Gasser, E.W. Kreutz, M. Schwarz, and K. Wissenbach, 1988. Gaslegieren von TiAl6V4 mit CO_2-laserstrahlung. In *Proceedings of the ECLAT'88*, p. 147–150.

A. Gasser, K. Wissenbach, E. Hoffmann, G. Schulte, and E. Beyer, 1996. Oberflächenbehandlung mit Zusatzwerkstoffen. In *Proceedings of the ECLAT'96*, p. 287–298.

E. Geissler and H.W. Bergmann, 1990. Temperature controlled laser transformation hardening. *Key engineering materials*, 46 and 47 (1990), 121–132.

C. Gerdes, A. Karimi, and H.W. Bieler, 1995. Water droplet erosion and microstructure of laser-nitrides Ti-6Al-4V. *Wear*, 186-187 (1995), 368–374.

P. Gilgien and W. Kurz, 1994. Microstructure and phase selection in rapid laser processing. In *Proceedings of the NATO advanced study institute on laser processing, Sesimbra, Portugal, july 3-16*, p. 77–92.

L. Grad and J. Monžina, 1995. Optodynamic monitoring of excimer laser drilling of ceramics. *Lasers in engineering*, 4 (1995), 255–262.

J.A. Greenwood, 1991. An interpolation formula for flash temperatures. *Wear*, 150 (1991), 153–158.

J. Griebsch, H. Hügel, F. Dausinger, and M. Jurca, 1995. Qualtiy assurance in pulsed laser welding. In *Proceedings of the ICALEO'95*, p. 603–612.

J. Griebsch, L. Schlichtermann, M. Jurca, S. Heissler, and D. Funk, 1996. Selbstlernendes Mehrdetektorensystem für die on-line Prozeßkontrolle und Qualitätsicherung beim Laserschweißen von Automobilkarosserien. In *Proceedings of the ECLAT'96*, p. 89–96.

B. Grünenwald, J. Shen, F. Dausinger, and H. Hügel, 1993. Laser cladding with composite powders using pyrometric temperature control and beam combining. In *Proceedings ISATA'93*, p. 287–294.

A.F. Hassan, M.M. El-Nicklawy, M.K. El-Adawi, and A.A. Hemida, 1993. A general problem of pulse laser heating of a slab. *Optics and laser technology*, 25-3 (1993), 155–162.

A.F. Hassan, M.M. El-Nicklawy, M.K. El-Adawi, E.M. Nasr, A.A. Hemida, and O.A. Abd El-Ghaffar, 1997. Heating a slab of finite thickness with a pulsed laser in the view of the theory of linear systems. *Pure and Applied optics*, 6 (1997), 67–84.

X. He, 1994. *Simulation und experimenteller Nachweis von Legierungsprozessen beim Laseroverflächenlegieren*. Ph.D. thesis, Technischen Universität Clausthal, Germany.

X. He, B.L. Mordike, N. Pirch, and E.W. Kreutz, 1995. Laser surface alloying of metallic materials. *Lasers in engineering*, 4 (1995), 291–316.

G. Herziger and P. Loosen, 1993. *Werkstoffbearbeitung mit Laserstrahlung*. München, Carl Hanser Verlag.

C.J. Heuvelman, W. König, H.K. Tönshoff, J. Meijer, P.K Kirner, M. Rund, M.F. Schneider, and I. van Sprang, 1992. Surface treatment techniques by laser beam machining. In *Annals of the CIRP, 41(2)*, p. 657–666.

R.A. Hilhorst, 1992. *Supervisory control of mode-switch processes*. Ph.D. thesis, University of Twente, Enschede, the Netherlands.

A.F.A. Hoadley, M. Rappaz, and M. Zimmermann, 1991. Heat-flow simulation of laser remelting with experimental validation. *Metallurgical transactions B*, 22B (1991), 101–109.

M. Hoeksma, 1998. *Control of laser surface alloying using the melt pool surface area as quality parameter*. M.Sc. thesis, Internal report WA-594, University of Twente, Dept. Mechanical Engineering, Enschede, the Netherlands.

P. Hoffmann and M. Geiger, 1995. Recent developments in laser system technology for welding applications. *Annals of the CIRP*, 44-1 (1995), 151–156.

P. Hoffmann, S. Schuberth, and M. Zuber, 1996. Quality control loops for precision laser beam welding. In *Proceedings of the ECLAT'96*, p. 159–168.

H. Holleck, 1986. Material selection for hard coatings. *Journal of vacuum science and technology, A*, 4-6 (1986), 2661–2669.

C. H. Houpis and G.B. Lamont, 1992. *Digital control systems: theory, hardware, software*. McGraw-Hill, New York, U.S.A.

H. Hügel, F. Dausinger, W. Bloehs, and B. Grünenwald, 1994. Basic coupling mechanisms in laser surface treatment. In *Proceedings of the NATO advanced study institute on laser processing, Sesimbra, Portugal, july 3-16*, p. 21–.

B. Hüttner, 1996. Optical properties of metals in the solid and liquid state: aluminium, indium, lead. In *Proceedings of ECLAT'96*, p. 637–643.

F. P. Incropera and D.P. De Witt, 1981. *Fundamentals of heat and mass transfer*. Wiley, Chichester, U.K.

ISO, 1994. *ISO 11 146 Optics and optical instruments: Test methods for laser beam parameters: beam widths, divergence angle, and beam propagation factor, ISO/TC172/SC 9/WG 1*. International Organization for Standardization.

J.C. Jaeger, 1943. Moving sources of heat and the temperature at sliding contacts. *Journal and proceedings of the Royal Society of New South Wales*, (1943), 203–224.

L. Jianglong, 1990. The study on relationship between composition of laser alloying and convection in the molten pool. *Key egineering materials*, 46 & 47 (1990), 487–496.

M.C. Jon, 1985. Noncontact acoustic emission monitoring of laser beam welding. *Welding journal*, 64-4 (1985), 43–48.

H. Jørgensen, 1990. *Investigations of on-line process monitoring and control in CO_2 laser cutting*. Ph.D. thesis, Technical University of Denmark, Lyngby, Denmark.

S.V. Kanstad and P.E. Nordal, 1986. Experimental aspects of photothermal radiometry. *Canadian Journal of Physics*, 64 (1986), 1155–1164.

A. Kaplan, B. Weinberger, and D. Schuöcker, 1997. Theoretical analysis of laser cladding and alloying. In *Proceedings of the conference on laser in material processing EUROPTO/SPIE, vol. 3097*.

D. Kechemair, F. Bataille, and H. Jørgensen, 1993. Some strategies for laser-materials process control. *Lasers in engineering*, 1 (1993), 233–250.

D. Kechemair, G. Caillibotte, and F. Bataille, 1990. *The industrial laser annual handbook, 1990 edition, SPIE 1241*, Chapter: Real-time control of high power laser material processing, p. 94–101.

R. Kern, R. Meyer, W.A. Theiner, and B. Valeske, 1995. Process integrated non-destructive testing of laser hardened components. In *Proceedings of the 7^{th} International syposium on nondestructive characterisation of materials*.

R. Kern and W. Theiner, 1986. Non-destructive magnetic testing of laser hardening parameters. In *Proceedings of the conference on laser treatment of materials*, p. 427–434.

R. Kern and W. Theiner, 1987. Auf der Spur de Lasers. *Maschinenmarkt, Würzburg*, 93-39 (1987), 76–82.

F. Klocke, L. Rozsnoki, and T. Celiker, 1996. New developments in surface technology: laser alloying using Mo/VC and Mn. In *Annals of the CIRP, 45(1)*, p. 179–182.

A.B. Kloosterman, 1998. *Surface modification of titanium with lasers*. Ph.D. thesis, University of Groningen, Groningen, the Netherlands.

W. Koechner, 1988. *Solid-state laser engineering*. Springer, Heidelberg, Germany.

E.W. Kreutz, B. Ollier, and N. Pirch, 1992. Melt dynamics and solification in surface processing with laser radiation. In *Proceedings of the LAMP'92*, p. 353–359.

E.W. Kreutz and N. Pirch, 1990. Melt dynamics in surface processing with laser radiation: calculations and applications. In *Proceedings of the european congress on optics (ECO3), CO_2 lasers and applications II, SPIE 1276*.

R.B. Kuilboer, P.K. Kirner, J. Meijer, M. Rund, and M.F. Schneider, 1994. Laser beam transformation hardening: transferability of machining parameters. In *Annals of the CIRP 43(2)*, p. 585–592.

W. Kurz and R. Trivedi, 1988. Microstructure selection in laser treatment of materials. In *Proceedings of the ECLAT'88*, p. 92–94.

K. Kußmaul, H. Britsch, M.J. Geitmann, H. Fink, and G. Pilsinger, 1996. Oberflächenveredelung von metallischen Oberflächen durch Einbringen von Zusatzwerkstoffen in Pulverform. In *Proceedings of the ECLAT'96*, p. 415–422.

C. Lampa, 1997. An analytical thermodynamic model of laser welding. *Journal of physics, Section D, Applied physics*, 30 (1997), 1293–1299.

P. Laurens, H. L'Enfant, M.C. Sainte Catherine, J.J. Bléchet, and J. Amouroux, 1996. Nitriding of titanium under CW laser radiation. *Thin Solid Films*, 293 (1996), 220–226.

H. L'Enfant, 1996. *Application du laser CO_2 continu á la nitruration en phase solide du titane sous atmosphére réactive*. Ph.D. thesis, Universite Pierre et Marie Curie, Paris VI, France.

D. Lepski, A. Wetzig, B. Brenner, and E. Beyer, 1999. FEM simulation of temperature fields, phase transformations, and stress states in the induction assisted laser remelting of grey cast iron. In *Proceedings of the 14th Meeting on Mathematical Modelling of Materials Processing with Lasers, Igls/Innsbruck, 20-22 January*, p. 2–7.

W.S. Levine, redactie, 1995. *The control handbook*. CRC press, Boca Raton, U.S.A.

J. Li, Q.H. Chen, and J. Merlin, 1996. Évaluation rapide du champ de température et de la forme de lase zone traitée lors d'un traitement superficiel de materiaux métalliques avec un faisceau laser de puissance. *Journal de physique III France*, 6 (1996), 1293–1306.

J. Li, J. Merlin, J. Chen, and Z. Fan, 1997. Quick approximate calculation on the transient temperature field of laser heat treatment. *Chinese journal of lasers*, B6-3 (1997), 280–288.

J.C. Li and L. Yuan, 1994. Mathematical method for optimizing the process of heat treatment with powerful lasers. *Lasers in engineering*, 2 (1994), 239–245.

L. Li, 1989. *Intelligent laser cladding control system design and construction*. Ph.D. thesis, Imperial college of science & technology, London, U.K.

L. Li, R.H. Hibberd, and W.M. Steen, 1987. In-process laser power monitoring and feedback control. In *Proceedings of the 4th conference on lasers in manufacturing*, p. 165–175.

L. Li, W.M. Steen, and R.D. Hibberd, 1990a. Computer aided laser cladding. In *Proceedings of the ELCAT'90*.

L. Li, W.M. Steen, R.D. Hibberd, and D.J. Brookfield, 1990b. In-process clad quality monitoring using optical method. In *Laser assisted processing II, SPIE 1279*, p. 89–100.

L Li, W.M. Steen, R.D. Hibberd, and V.M. Weerasinghe, 1987. Real-time expert system for supervisory control of laser cladding. In *Proceedings of the ICALEO'87*, p. 7.1–7.7.

S.Y. Lim and C.R. Chatwin, 1994. Intelligent digital control of a laser cutting process. *Lasers in engineering*, 3 (1994), 99–112.

L. Ljung, 1987. *System identification, theory for the user*. Prentice-Hall, Englewood Cliffs, U.S.A.

L. Ljung, 1995. *User's guide system identification toolbox for use with* MATLAB. The Mathworks Inc., Natick, U.S.A.

G.W. Lubbers, 1994. *Lasercladden op inlaatkleppen en nokkenstoters*. M.Sc. thesis, Internal report WA-371, University of Twente, Dept. Mechanical Engineering, Enschede, the Netherlands.

C.Z. Meijer and E.P.M. Bakker, 1997. Process parameters for high quality on-contour starting of laser cutting of steel. In *Proceedings of the conference on laser in material processing EUROPTO/SPIE 3097*, p. 58–69.

J. Meijer, 1988. *Laserbewerkingen*. Vereniging FME, Zoetermeer, the Netherlands.

J. Meijer, I. van Sprang, and I. Sarady, 1987. Shockhardening experiments on austentic Hadfield steels by high intensity TEA CO_2 laser pulses. In *Proceedings of the ICALEO'87*, p. 253–259.

F. Meriaude, E. Renier, and F. Truchetet, 1995. Visualisation de temperature proche infrarouge a l'aide d'une camera CCD. In *Proceedings of 7ème congrès international métrologie*, p. 189–194.

F Meriaudeau and F. Truchetet, 1996. Control and optimization of the laser cladding process using matrix cameras and image processing. *Journal of laser applications*, 8 (1996), 317–324.

F. Meyer, J.F. Mathieu, D. Cesario, and J.M. Pelletier, 1995. Production of Ti/TiC dispersoid coatings on titanium base alloys by laser treatment. *Lasers in engineering*, 4 (1995), 263–271.

E.K. Molchanova, 1965. *Phase diagrams of titanium alloys*. Ann Arbor-Humphrey, London, U.K.

M. Müller, F. Dausinger, and J. Griebsch, 1996. On-line Prozeßsicherung beim Laserschweißen. In *Proceedings of the ECLAT'96*, p. 243–250.

E. Nava-Rüdiger and M. Houlot, 1997. Integration of real-time quality control systems in a welding process. *Journal of laser applications*, 9 (1997), 95–102.

P.J. Oakley, 1981. Laser heat treatments and surface techniques - a review. *The Welding institute research bulletin*, january (1981), 4–11.

F. Oberhettinger and L. Badii, 1973. *Tables of Laplace transforms*. Springer, Heidelberg, Germany.

B. Ollier, N. Pirch, and E.W. Kreutz, 1995. A numerical model of the one-step laser cladding process. *Laser und optoelektronik*, 27-1 (1995), 63–70.

F.O. Olsen, H. Jørgensen, C. Bagger, T. Kristensen, and O. Gregersen, 1992. Recent Investigations in sensorics for adaptive control of laser cutting and welding. In *Proceedings of the LAMP'92*, p. 405–413.

S. Parthasarathia, P.A.A. Khan, and A.J. Paul, 1991. Intelligent laser processing of materials. In *Proceedings of the ICALEO'91*, p. 708–718.

D. Peidao, J.L. Liu, and S. Gongqi, 1993. Analysis of driving forces for convection in the laser melted pool. *Lasers in engineering*, 2 (1993), 75–79.

A. Penz, D. Leidinger, and D. Schuöcker, 1994. Modelling of a closed loop controlled laser machining process with different control strategies. In *Laser materials processing: industrial and microelectronics applications, SPIE 2204*, p. 270–281.

M. Picasso, C.F. Marsden, J.D Wagniere, A. Frenk, and M. Rappaz, 1994. A simple but realistic model for laser cladding. *Metallurgical and materials transactions B*, 25B (1994), 281–291.

M. Pietro, C. Rivela, and B. Marco, 1994. Mathematical modelling of laser treatment processes. In *Laser materials processing: industrial and microelectronics applications, SPIE 2204*, p. 256–268.

N. Pirch, E.W. Kreutz, L. Möller, A. Gasser, and K. Wissenbach, 1990. Melt dynamics in surface processing with laser radiation. In *Proceedings of the ECLAT'90*, p. 65–80.

M. Pöhler, 1998. Reflektorische Strahlung stört den Laserresonator. *Lasermarkt*, (1998), 50–52.

A.M. Prokhorov, V.I. Konov, I. Ursu, and I.N. Mihailescu, 1990. *Laser heating of metals*. Bristol, Adam Hilger.

A.P. Prudnikov, Yu.A. Brychkov, and O.I. Marichev, 1992a. *Integrals and series, Inverse Laplace transforms*, volume 5. Gordon and Breach, Reading, Berkshire, U.K.

A.P. Prudnikov, Yu.A. Brychkov, and O.I. Marichev, 1992b. *Integrals and series, Direct Laplace transforms*, volume 4. Gordon and Breach, Reading, Berkshire, U.K.

S. Ramanathan and M.F. Modest, 1994. Measurement of temperature and absorptance for laser processing applications. *Journal of laser applications*, 6 (1994), 23–31.

M. Rappaz, B. Carrupt, M. Zimmermann, and W. Kurz, 1987. Numerical simulation of eutectic solidification in the laser treatment of materials. *Helvetica Physica Acta*, 60 (1987), 924–936.

J.F. Ready, 1971. *Effects of high-power laser radiation*. Academic press, New York, U.S.A.

E. Renier, F. Meriaudeau, and F. Truchetet, 1996. CCD Technology applied to industrial welding applications. In *Proceedings of the 8th mediterranean electrotechnical conference*, p. 1335–1338.

G.E. Roberts and H. Kaufman, 1966. *Table of Laplace transforms*. Saunders, Philadelphia, U.S.A.

J.M. Robinson and R.C. Reed, 1995. Water droplet erosion of laser surface treated Ti-6Al-4V. *Wear*, 186-187 (1995), 360–367.

J.M. Robinson, R.C. Reed, and D.R.F. West, 1994. Laser surface melting and gas-alloying of Ti6Al4V. In *Proceedings of the NATO advanced study institute on laser processing, Sesimbra, Portugal, july 3-16*, p. 575–585.

G.R.B.E. Römer, 1996. Measurement of the absorptivity of CO_2 laser energy of Ti6Al4V and of Ti6Al4V alloyed with N_2. Technical report, WA-476, University of Twente, Dept. of Mechanical Engineering, Enschede, the Netherlands.

G.R.B.E. Römer, 1998. Final report IOP-Metals laser alloying, part University of Twente (in Dutch). Technical report, WA-597, University of Twente, Dept. Mechanical Engineering, Enschede, the Netherlands.

A.R. Rosenthal, 1990. On-line Diagnose bei der Laseroberflächenbearbeitung durch thermografische Systeme. *Laser und Optoelektronik*, 22-5 (1990), 44–49.

D. Rosenthal, 1941. Mathematical theory of heat distribution during welding and cutting. *Welding journal*, 20 (1941), 220–234.

D. Rosenthal, 1946. The theory of moving sources of heat and its application to metal treatments. *Transactions of the American Society of Mechanical Engineers (ASME)*, 67 (1946), 849–866.

V. Rubruck, E. Geissler, and H.W. Bergmann, 1990. Case depth control for laser treated materials. In *Proceedings of the ECLAT'90*, p. 207–216.

T. Rudlaff and F. Dausinger, 1990. Increasing the efficiency of laser beam hardening. In *Proceedings of the ICALEO'90*, p. 451–459.

N. Savvides and B. Window, 1988. Electrical transport, optical properties, and structure of TiN films synthesized by low-energy ion assisted deposition. *Journal of applied physics*, 64-1 (1988), 225–234.

D. Scheller, 1995. *Proceßüberwachung bei der Laseroberflächenbehandlung durch Reflexions- und Temperaturmessung*. Ph.D. thesis, Rheinisch-Westfälischen Technischen Hochschule, Aachen, Germany.

R.H. Schippers, 1994. Servo motion control for an XY-stage. Technical report, University of Twente, Dept. of Mechanical Engineering, Enschede, the Netherlands.

M.F. Schneider, 1994. Oppervlaktebehandelingen met lasers: legeren dispergeren en cladden. *MB magazine*, 11/12 (1994), 326–332.

M.F. Schneider, 1998. *Laser cladding with powder*. Ph.D. thesis, University of Twente, Enschede, the Netherlands.

D. Schuöcker and A. Kaplan, 1994. Overview over modelling for laser applications. In *Laser materials processing: industrial and microelectronics applications, SPIE 2207*, p. 236–247.

B. Seidel, J. Beersiek, K. Behler, and E. Beyer, 1994. Quality assurance and advanced use of process gas by means of process monitoring and control for laser beam welding. In *Proceedings of the ECLAT'94*, p. 163–245.

M. Seirsten, 1988. Surface nitriding of titanium by laser beams. In *Proceedings of the ECLAT'88*, p. 66–69.

H.R. Shercliff and M.F. Ashby, 1991. The prediction of case depth in laser transformation hardening. *Metallurgical transactions A*, 22A (1991), 2459–2466.

S.Z. Shuja, B.S. Yilbaş, and M.O. Budair, 1998. Modeling of laser heating of solid substance including assisting gas impingment. *Numerical heat transfer, Part A*, 33 (1998), 315–339.

A.E. Siegman, 1990. New developments in laser resonators. In *Optical resonators, SPIE 1224*, p. 2–13.

S. Skogestad and I. Postlethwaite, 1996. *Multivariable feedback control*. Wiley, Chichester, U.K.

O.J.M. Smith, 1959. A controller to overcome dead time. *ISA journal*, 6 (1959), 28–33.

W.J. Smith, 1990. *Modern optical engineering*. McGraw-Hill.

I. Smurov and M. Ignatiev, 1994. Innovative intermetallic compounds by laser alloying. In *Proceedings of the NATO advanced study institute on laser processing, Sesimbra, Portugal, july 3-16*, p. 267–326.

I. Smurov and M. Ignatiev, 1996. Real-time pyrometry in laser surface treatment. In *Proceedings of the NATO advanced study institute on laser processing, Sesimbra, Portugal, july 3-16*, p. 529–564.

I. van Sprang, 1992. *The use of models for the determination of the machining parameters of laser hardening and laser cladding*. Ph.D. thesis, University of Twente, Enschede, the Netherlands.

M. van der Staay, 1994. *Laser alloying with powder injection*. M.Sc. thesis, Internal report WA-385, University of Twente, Dept. of Mechanical Engineering, Enschede, the Netherlands, the Netherlands.

W.M. Steen, 1988. Surface treatment of materials by laser beam - a review. In *Proceedings of the ECLAT'88*, p. 60–64.

W.M. Steen, June 1992. Adaptive control of laser material processing. In *Proceedings of the LAMP'92*, p. 439–444, Nagoaka, Japan.

W.M. Steen, 1993. Laser process automation. In *Proceedings of the NATO Advanced Study Institute on laser applications for mechanical industry, Erice, Trapiani, Italy, 4-16 April*, p. 31–43.

W.M. Steen, 1994. Laser surface treatment: an overview. In *Proceedings of the NATO advanced study institute on laser processing, Sesimbra, Portugal, july 3-16*, p. 1–19.

G. Stern, 1990. Absorptivity of cw CO_2, CO and YAG-laser beams by different metallic alloys. In *Proceedings of the ECLAT'90*, p. 25–35.

Y. Tal, E. Lenz, and A. Shachrai, 1982. Temperature controlled laser cutting. In *Proceedings of ICALEO'82*, p. 149–161.

R.J. Tangelder, L.H.J.F. Beckmann, and J. Meijer, 1992. Influence of temperature gradients on the performance of ZnSe-lenses. In *Proceedings of the EOS/SPIE conference on lens and optical system design, Berlin, september 14-18, SPIE 1780*.

M. Tomie, N. Abe, S. Noguchi, Y. Kitahara, and Y. Satoh, 1991. Laser surface modification of stainless steel - alloying with molybdenum. *Transactions of JWRI*, 20-2 (1991), 43–47.

H.K. Tönshoff and L. Overmeyer, 1995. Process control systems in laser materials processing. *Optical and Quantum electronics*, 27 (1995), 1439–1447.

S. Tosto, 1993. Laser surface melting in the presence of beam translation: an analytical approach to calculate heat and mass flows in the liquid phase. *Lasers in engineering*, 2 (1993), 201–226.

S. Tosto, 1994. Laser surface treatments: a review of models. *Lasers in engineering*, 3 (1994), 157–186.

T. Ueda, M. Sato, T. Sugita, and K. Nakayama, 1995. Thermal behaviour of cutting grain in grinding. In *Annals of the CIRP 44(1)*, p. 325–328.

V.Y. Vasilev, V.S. Kraposhin, A.G. Densienko, and I.Ch. Kopetskaya, 1990. Relationship between passivation parameters of carbon steel and conditions of laser alloying with chromium. *Fizika I Khimiya Obrabotki Materialov*, 24 (1990), 70–74.

P.A. Vetter, Th. Engel, and J. Fontaine, 1994. Laser cladding: the relevant parameters for process control. In *SPIE 2207*, p. 452–462.

H. Willerscheid, 1990. *Prozeßüberwachung und Konzepte zur Prozeßoptimierung des Laserstrahlhärtens*. Ph.D. thesis, Rheinisch-Westfälischen Technischen Hochschule, Aachen, Germany.

B.S. Yilbaş, 1997. Theoretical and experimental investigation into laser melting of steel samples. *Optics and laser in engineering*, 27 (1997), 297–307.

B.S. Yilbaş and A.Z. Şahin, 1994. Laser heating mechanism including evaporation process. *International communications in heat and mass transfer*, 21-4 (1994), 509–518.

B.S. Yilbaş and M. Sami, 1997. Heat transfer analysis of a semi-infinite solid heated by a laser beam. *Heat and mass transfer*, 32 (1997), 245–253.

A. Zambon, E. Ramous, M. Magrini, M Bianco, and C. Rivela, 1994. Gas surface alloying of Ti6Al4V alloy by laser. In *Proceedings of the NATO advanced study institute on laser processing, Sesimbra, Portugal, july 3-16*, p. 327–335.

E. Zauderer, 1989. *Partial differential equations of applied mathematics*. Wiley, Chichester, U.K.

W. Zhang and A.K. Prasad, 1997. Performance evaluation of a Scheimpflug stereocamera for partical image velocimetry. *Applied optics*, 36-33 (1997), 8738–8744.

H. Zwart and J. Bontsema, 1997. An application driven guide through infinite-dimensional systems theory. In *Proceedings of the European Control Conference (ECC97), Brussels, Belgium*.

C. Zwikker, 1968. *Fysische materiaalkunde*, volume 3. Wetenschappelijke uitgeverij, Amsterdam, the Netherlands.

Appendix A

TEM MODES AND ISO 11146 STANDARD

A.1 Transverse electromagnetic modes

In an optical resonator electromagnetic fields can exist whose distribution of amplitudes and phases reproduce themselves upon repeated reflections between the mirrors (Koechner, 1988). These particular field configurations comprise the Transverse Electromagnetic Modes (TEM) of a passive resonator.

Transverse modes in polar coordinates (r, φ) are designated by TEM $_{pl}$ and referred to as *Gauß-Laguerre* modes. The integers p and l represent the number of locations (nodes) of zero intensity transverse to the beam axis in radial and tangential directions respectively. The intensity distribution $I_{pl}(r,\varphi)\,[\mathrm{W{\cdot}m^{-2}}]$ of a TEM$_{pl}$ mode is given by

$$I_{pl}(r,\varphi) = I_0 \left(\frac{8r^2M^2}{d^2}\right)^l \left[L_l^p\left(\frac{8r^2M^2}{d^2}\right)\right]^2 \cos^2(l\varphi)\exp\left(-\frac{8r^2M^2}{d^2}\right) \tag{A.1}$$

where $I_0\,[\mathrm{W{\cdot}m^{-2}}]$ denotes the intensity scale factor, d the diameter of the profile and $M^2 \geq 1$ the *times-diffraction-limited-factor*, or short beam quality number. The beam diameter and the beam quality number are defined according to the ISO 11 146 standard, see appendix A.2. Finally, $L_l^p(\cdot)$ denotes the generalized Laguerre polynomial of order p and index l. The intensity scale factor I_0, expressed in the modes numbers and the total laser power P_L, reads

$$I_0 = \begin{cases} \dfrac{8M^2}{\pi d^2} P_L\,, & l = 0 \\[2ex] \dfrac{16M^2 p!}{\pi d^2 (p+l)!} P_L\,, & l = 1,2,3,\ldots \end{cases} \tag{A.2}$$

For Gauß-Laguerre modes the times-diffraction-limited-factor equals $M^2 = 2p + l + 1$ (Siegman, 1990). A mode designation accompanied by an asterisk (*) indicates a mode which is a linear superposition of two identical modes, one rotated 90° about the optical axis relative to the other. For example, the mode TEM$_{01^*}$ is made up of two TEM$_{01}$ modes.

Transverse modes in cartesian coordinates are designated by TEM$_{mn}$ and referred to as *Gauß-Hermite* modes. The intensity distribution $I_{mn}(x,y)$ of a TEM$_{mn}$ mode is given by

$$I_{mn}(x,y) = I_0 \left[H^m \left(\frac{2x\sqrt{2}\sqrt{2m+1}}{d_x} \right) \exp\left(\frac{-4x^2(2m+1)}{d_x^2} \right) \right]^2 \times \\ \left[H^n \left(\frac{2y\sqrt{2}\sqrt{2n+1}}{d_y} \right) \exp\left(\frac{-4y^2(2n+1)}{d_y^2} \right) \right]^2$$

where $H^m(\cdot)$ denotes the m^{th} order Hermite polynomial, d_x [m] and d_y [m] the beam length and width respectively. The width and length are defined according to the ISO standard (appendix A.2). The intensity scale factor I_0, expressed in the modes numbers and the total laser power P_L, reads

$$I_0 = \frac{2^{3-m-n}\sqrt{(2m+1)(2n+1)}}{n!m!\pi d_x d_y} P_L \tag{A.3}$$

The times-diffraction-limited-factor for Gauß-Hermite modes equals $M^2 = m + n + 1$ (Siegman, 1990).

The intensity profile of a practical laser source is a combination of several TEM modes.

A.2 The ISO 11 146 standard

The ISO 11 146 standard (ISO, 1994), deals with test methods for laser beam parameters, such as beam diameters, beam propagation and the *times-diffraction-limit* factor, or beam propagation factor.

The beam diameter d [m] of an (arbitrary) laser intensity profile $I(r,\varphi)$, expressed in polar coordinates, is defined as

$$d = 2\sqrt{2\sigma_r^2} \tag{A.4}$$

where σ_r^2 [m^2] denotes the variance, or *second moment* of the intensity profile

$$\sigma_r^2 = \frac{\int\limits_{r=0}^{\infty}\int\limits_{\varphi=0}^{2\pi} I(r,\varphi)(r-\overline{r})^2\, r\,dr\,d\varphi}{\int\limits_{r=0}^{\infty}\int\limits_{\varphi=0}^{2\pi} I(r,\varphi)\, r\,dr\,d\varphi} = \frac{\int\limits_{r=0}^{\infty}\int\limits_{\varphi=0}^{2\pi} I(r,\varphi)(r-\overline{r})^2\, r\,dr\,d\varphi}{P_L} \tag{A.5}$$

in which $\bar{r}\,[\mathrm{m}]$ denotes the centeroid, or *first moment* of the intensity profile

$$\bar{r} = \frac{\int\limits_{r=0}^{\infty}\int\limits_{\varphi=0}^{2\pi} I(r,\varphi)\, r\, r\,dr\,d\varphi}{\int\limits_{r=0}^{\infty}\int\limits_{\varphi=0}^{2\pi} I(r,\varphi)\, r\,dr\,d\varphi} = \frac{\int\limits_{r=0}^{\infty}\int\limits_{\varphi=0}^{2\pi} I(r,\varphi)\, r\, r\,dr\,d\varphi}{P_L} \tag{A.6}$$

For example, figure A.1 shows the intensity profile of an Gaussian (TEM_{00}) intensity profile, which according to (A.1) reads,

$$I_{00}(r,\varphi) = I_0 \exp\left[-\left(\frac{2\sqrt{2}}{d}\right)^2 r^2\right],\; I_0 = \frac{8}{\pi d^2} P_L \tag{A.7}$$

Then, the first moment (A.6) equals $\bar{r} = 0$, and the second moment (A.5) equals

$$\sigma_r^2 = \frac{I_0}{P_L} 2\pi \int\limits_0^{\infty} \exp\left[-\left(\frac{2\sqrt{2}}{d}\right)^2 r^2\right] r^3\,dr = \left(\frac{d}{2\sqrt{2}}\right)^2 \tag{A.8}$$

Hence, with (A.4) the beam diameter equals d.

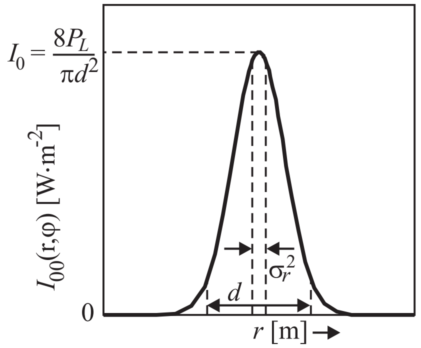

Figure A.1: Gaussian (TEM_{00}) intensity profile, its diameter and second moment.

The beam length $d_x\,[\mathrm{m}]$ and width $d_y\,[\mathrm{m}]$ for an arbitrary laser intensity profile $I(x,y)$ expressed cartesian coordinates is defined as,

$$d_x = 4\sqrt{\sigma_x^2}, \quad d_y = 4\sqrt{\sigma_y^2} \tag{A.9}$$

in which the x-component σ_x^2 of the variance is defined as

$$\sigma_x^2 = \frac{\int\limits_{-\infty}^{\infty}\int\limits_{-\infty}^{\infty} I(x,y)(x-\bar{x})^2\,dx\,dy}{\int\limits_{-\infty}^{\infty}\int\limits_{\infty}^{\infty} I(x,y)\,dx\,dy} = \frac{\int\limits_{\infty}^{\infty}\int\limits_{\infty}^{\infty} I(x,y)(x-\bar{x})^2\,dx\,dy}{P_L} \tag{A.10}$$

where $\overline{x}$ follows from

$$\overline{x} = \frac{\int\limits_{-\infty}^{\infty}\int\limits_{-\infty}^{\infty} I(x,y)x\,dx\,dy}{\int\limits_{-\infty}^{\infty}\int\limits_{\infty}^{\infty} I(x,y)\,dx\,dy} = \frac{\int\limits_{-\infty}^{\infty}\int\limits_{-\infty}^{\infty} I(x,y)\,dx\,dy}{P_L} \tag{A.11}$$

The variance σ_y^2 and first moment $\overline{y}$, in the y-direction, are defined analogously.

Beam propagation

The beam diameter of a radially symmetric laser beam, varies along the propagation axis, $d = d(z)$, and is described by

$$d(z)^2 = d_0^2 + \theta^2\,(z - z_0)^2 \tag{A.12}$$

where d_0 [m] denotes the beam diameter of the waist, z_0 [m] the waist location, and θ [rad] the far-field divergence, see figure A.2.

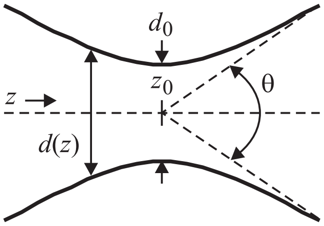

Figure A.2: The diameter $d(z)$ of a radially symmetric laser beam, along its propagation axis z, is completely described by three parameters: the waist diameter d_0, its location z_0 and the far-field divergence θ.

The propagation can also be described by the beam propagation factor Q [−], or the times-diffraction-limited-factor M^2 [−], which are related as

$$M^2 = \frac{1}{Q} = \frac{n\pi d_0\theta}{4\lambda_0} = \frac{\pi d_0\theta}{4\lambda} \tag{A.13}$$

where λ_0 [m] denotes the wavelength of the laser radiation in vacuum, λ [m] the wavelength in the medium under consideration, and n the index of refraction. Then the product

$$n d_0\theta = \frac{4\lambda_0}{\pi}M^2 = \frac{4\lambda_0}{\pi Q} \tag{A.14}$$

describes the beam propagation and is invariant through-out the propagation of the beam when aberration-free and non-aperturing optical systems are used. It can be shown that $M^2 \in [1, \infty\rangle$ and $Q \in \langle 0, 1]$ for an arbitrary laser beam, and $M^2 = Q = 1$ for the TEM$_{00}$ mode (Siegman, 1990).

Appendix B

TRANSFER FUNCTION OF LASER POWER TO TEMPERATURE

In this appendix the derivation of the transfer function from laser power to temperature, induced by an arbitrary laser beam intensity profile, is discussed. No explicit solution of this problem is known to the author. Therefore, the following will not present a final solution but must be read as a contribution to the scientific discussion in this field.

The methods discussed apply to the geometrically three dimensions, but for reasons of simplicity two dimensions are considered here. Because the beam velocity is an important operating parameter, the computations include the x and z coordinate, and the y coordinate is omitted. Then, assuming an uniform laser beam intensity profile with diameter d, equations (4.11) and (4.12) for a semi-infinite solid, simplify to

$$\frac{\partial T}{\partial t} - \kappa \left(\frac{\partial^2 T}{\partial x^2} - \frac{\partial^2 T}{\partial z^2} \right) - v \frac{\partial T}{\partial x} = 0,\ (x,y) \in \Omega,\ t \geq 0 \tag{B.1}$$

$$T(x,y,t=0) = 0, \tag{B.2}$$

$$-K \left. \frac{\partial T}{\partial z} \right|_{z=0} = AI(x,t) = AI_0 H(t) \left[H\left(x + \frac{d}{2} \right) - H\left(x - \frac{d}{2} \right) \right] \tag{B.3}$$

where $I_0 = 4P_L/(\pi d^2)$.

First, an approach is presented to derive the transfer function (4.67), based on integral transforms. Next, an approach is presented to derive the transfer function based on Green's functions.

Solution method based on integral transforms

Partial differential equation (B.1) can be reduced to an ordinary differential equation (ODE) and subsequently be solved, by successive application of integral transforms, i.e.

Laplace transforms and/or Fourier transforms. Applying the Laplace transform to equation (B.1) with respect to time yields

$$s\widetilde{T}(x,z) - T(x,z,0) - \kappa\left(\frac{\partial^2\widetilde{T}(x,z)}{\partial x^2} + \frac{\partial^2\widetilde{T}(x,z)}{\partial z^2}\right) - v\frac{\partial\widetilde{T}(x,z)}{\partial x} = 0 \tag{B.4}$$

were $\widetilde{T}(x,z) = L\{T(x,z,t)\}$ denotes the Laplace transform of the temperature with respect to time. Then, substitution of initial condition (B.2) eliminates the second term on the left hand side of (B.4). An ODE is obtained when an integral transform is applied to (B.4) once more. This integral transform can be a Laplace transform (with respect to x or z) or alternatively a Fourier transform (with respect to x or z). A transformation with respect to x seems to be sensible, as the resulting ODE will be a function of z only, and a boundary condition on z is available. Laplace transformation of equation (B.4) with respect to x yields

$$\begin{aligned} s\widetilde{\widetilde{T}}(z) - \kappa&\left[\xi^2\widetilde{\widetilde{T}}(z) - \xi\widetilde{T}(0,z) - \left.\frac{\partial\widetilde{T}(x,z)}{\partial x}\right|_{x=0} + \frac{\mathrm{d}^2\widetilde{\widetilde{T}}(z)}{\mathrm{d}z^2}\right] \\ &- v\left[\xi\widetilde{\widetilde{T}}(z) + \widetilde{T}(0,z)\right] = 0 \end{aligned} \tag{B.5}$$

where $\widetilde{\widetilde{T}}(z)$ denotes the Laplace transform of $\widetilde{T}(x,z)$ with respect to x and where ξ denotes the corresponding Laplace variable. Unfortunately the terms $\widetilde{T}(0,z)$ and $(\partial\widetilde{T}(x,z)/\partial x)|_{x=0}$ in this expression are unknown. Therefore, a Fourier transform of (B.4) with respect to x is applied instead, which yields the ODE

$$s\widetilde{\widetilde{T}}(z) - \kappa\left[-\xi^2\widetilde{\widetilde{T}}(z) + \frac{\partial\widetilde{\widetilde{T}}(z)}{\partial z^2}\right] - jv\xi\widetilde{\widetilde{T}}(z) = 0 \tag{B.6}$$

where $\widetilde{\widetilde{T}}(z)$ denotes the Fourier transform of $\widetilde{T}(x,z)$ with respect to x and where ξ denotes the corresponding Fourier variable. The general solution to (B.6) equals,

$$\widetilde{\widetilde{T}}(z) = C_1\exp\left[z\sqrt{\frac{s}{\kappa} + \xi^2 + j\xi\frac{v}{\kappa}}\right] + C_2\exp\left[-z\sqrt{\frac{s}{\kappa} + \xi^2 + j\xi\frac{v}{\kappa}}\right] \tag{B.7}$$

where C_1 and C_2 are constants to be determined from the initial and boundary conditions. Applying successive Laplace transform (with respect to t) and Fourier transform (with respect to x) to boundary condition (B.3) and solving the resulting equality with (B.7) for C_2 yields after some rewriting

$$\begin{aligned} \widetilde{\widetilde{T}}(z) =& 2C_1\cosh\left(z\sqrt{\frac{s}{\kappa} + \xi^2 + j\xi\frac{v}{\kappa}}\right) + \frac{2AI_0}{s\xi K\sqrt{\frac{s}{\kappa} + \xi^2 + j\xi\frac{v}{\kappa}}} \times \\ &\sin\left(\frac{\xi d}{2}\right)[j - \pi\delta(\xi)\xi]\exp\left[-z\sqrt{\frac{s}{\kappa} + \xi^2 + j\xi\frac{v}{\kappa}}\right] \end{aligned} \tag{B.8}$$

where $\delta(\cdot)$ denotes the Dirac delta function. Applying successive Laplace transform (with respect to t) and Fourier transform (with respect to x) to the initial condition (B.2), and recalling that $s\overset{\approx}{T}(z)$ must equal zero for $s \rightarrow \infty$, shows that the remaining constant must satisfy $C_1 = 0$. Then, the transfer function (4.67) is obtained when the inverse Fourier (with respect to x) of equation (B.8) can be calculated. After simplifications this comes down to

$$\widetilde{T}(x,z) = -\frac{AI_0}{Ks}\mathcal{F}^{-1}\left\{ \frac{\exp\left[-z\sqrt{\frac{s}{\kappa}+\xi^2+j\xi\frac{v}{\kappa}}\right]}{\xi\sqrt{\frac{s}{\kappa}+\xi^2+j\xi\frac{v}{\kappa}}}\left(\exp\left[-j\frac{d\xi}{2}\right]-\exp\left[j\frac{d\xi}{2}\right]\right)\right\} \tag{B.9}$$

where $\mathcal{F}^{-1}\{\cdot\}$ denotes the inverse Fourier operator with respect to ξ. Unfortunately, this inverse could not be calculated in explicit form.

Solution method based on Greens function

Another approach to obtain the transfer function from laser power to temperature is by applying the Laplace transform to the integral of the Green's function (4.15). For the two-dimensional problem under consideration this integral equals

$$\begin{aligned} T(x,z,t) &= \int\limits_0^t \int\limits_{-\infty}^{\infty} AI(x',t')G(x,z,x',t')dx'dt' \\ &= \int\limits_0^t \int\limits_{-d/2}^{d/2} AI_0 H(t')\left[H\left(x'+\frac{d}{2}\right)-H\left(x'-\frac{d}{2}\right)\right]\frac{\exp\left[\frac{(x-x'+v(t-t'))^2+z^2}{-4\kappa(t-t')}\right]}{2K\pi(t-t')}dx'dt' \end{aligned} \tag{B.10}$$

where the uniform intensity profile (B.3) has been substituted. Then, integration over x' yields,

$$\begin{aligned} T(x,z,t) =& \frac{AI_0}{2K}\sqrt{\frac{\kappa}{\pi}}\int_0^t H(t')\frac{\exp\left[\frac{-z^2}{4\kappa(t-t')}\right]}{\sqrt{t-t'}}\times \\ & \left[\operatorname{erf}\left(\frac{-v(t-t')+\frac{d}{2}-x}{\sqrt{4\kappa(t-t')}}\right)-\operatorname{erf}\left(\frac{-v(t-t')-\frac{d}{2}-x}{\sqrt{4\kappa(t-t')}}\right)\right]dt' \end{aligned} \tag{B.11}$$

Unfortunately, the integration over time cannot be calculated explicitly. However, taking the Laplace transform of (B.11), and dividing by Io/s yields the transfer function

$$G(s) = \frac{A\sqrt{\kappa}}{2K\sqrt{\pi}}\mathcal{L}\left\{\frac{\exp\left[\frac{-z^2}{4\kappa t}\right]}{\sqrt{t}}\left[\operatorname{erf}\left(\frac{vt+x+\frac{d}{2}}{\sqrt{4\kappa t}}\right)-\operatorname{erf}\left(\frac{vt+x-\frac{d}{2}}{\sqrt{4\kappa t}}\right)\right]\right\} \tag{B.12}$$

where the well known (convolution) equality $\mathcal{L}\{\int_0^t f(t-\tau)g(\tau)d\tau\} = \mathcal{L}\{f(t)\}\mathcal{L}\{g(t)\}$ and the symmetry relation erf($-x$)=$-$erf(x) have been applied. Several, well known tables of Laplace transforms (Prudnikov *et al.*, 1992b; Erdelyi, 1954; Roberts and Kaufman, 1966) have been checked, but unfortunately no Laplace transform of (B.12) is known to the author.

Appendix C
THERMAL CAMERA

C.1 Modification of spectral sensitivity

The spectral sensitivity of the silicon chip of the DALSA CA-D1-128A area scan camera ranges from 400 to 1100nm (see figure C.1(a)). This appendix discusses the modification of this range to increase the temperature resolution of the camera, during the alloying of titanium. The temperature range, as measured by the ratio pyrometer, during laser alloying of titanium with nitrogen roughly ranges from 1650 °C (melting temperature of titanium) to 2500 °C (the temperature of the melt pool containing TiN). Hence, the wavelength λ_m (3.7) at which the maximum radiance occurs is approximately 1 μm. The temperature resolution (sensitivity n) of the DALSA chip increases if its spectral range is modified such that it includes wavelengths smaller than and including λ_m (see section 3.5.1). For this purpose, spectral filters were placed in front of the chip. The filter (combination) yielding the best thermal resolution is difficult to determine theoretically (Coutouly and Merlin, 1993). Therefore, three spectral regions were evaluated experimentally:

(*i*) A region ranging from 400nm to 550nm, as transmitted by a combination of a 3 mm, ∅ 25 mm ANDOVER 550FL short wave pass edge filter and a 3 mm, 50 mm × 50 mm SCHOTT KG1 band pass filter; see figure C.1(b) and C.1(c),

(*ii*) A region ranging from 400nm to 700nm, as transmitted by a combination of a 3 mm, ∅ 25 mm ANDOVER 700FL short wave pass edge filter and a 3 mm, 50 mm × 50 mm SCHOTT KG1 band pass filter; see figure C.1(b) and C.1(c),

(*iii*) A region ranging from 800nm to 1100nm, as transmitted by a combination of a 3 mm, 50 mm × 50 mm SCHOTT KG1 and a 3 mm, 50 mm × 50 mm SCHOTT RG1000 filter; see figure C.1(c).

To prevent saturation of the CCD chip, several neutral density filters (SCHOTT NG4 and NG5) were applied, which have flat spectral transmittance and therefore do not affect the

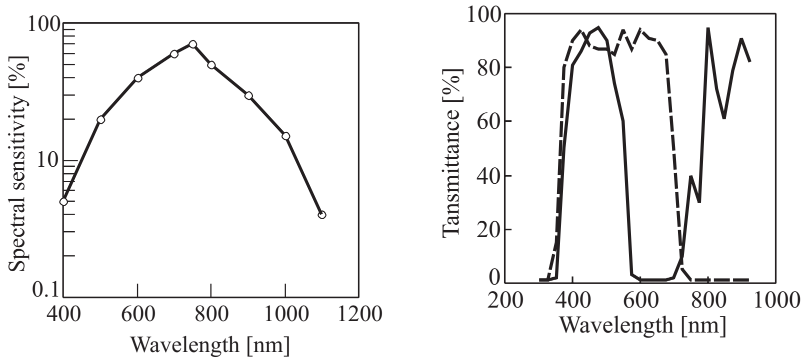

(a) Spectral sensitivity DALSA CA-D1-128A CDD camera.

(b) Spectral transmittance of (3 mm) Andover short wave pass edge filters: 550FL (solid curve) and 700FL (dashed).

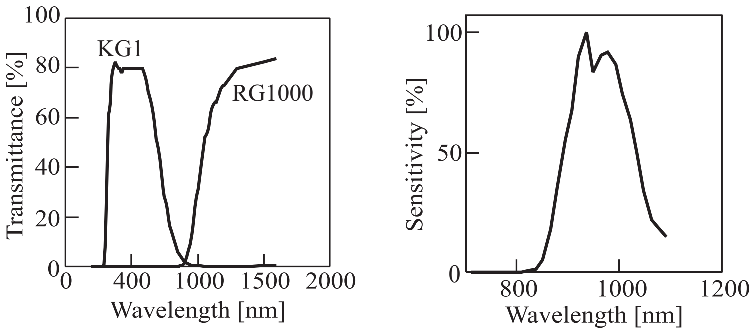

(c) Spectral transmittance of (3 mm) SCHOTT optical filters: KG1 and RG1000.

(d) Combined relative spectral sensitivity of CCD chip and KG1 and RG1000 filters. The maximum sensitivity was scaled to 100%.

Figure C.1: Spectral sensitivity of DALSA *camera and transmittance of optical filters.*

studied spectral region. The wavelength of the CO_2-laser radiation ($\lambda = 10.6\,\mu$m) falls far outside these spectral regions.

With each filter combination, the melt pool was recorded (at 419 frames/s) at a beam velocity of $50\,\mathrm{mm \cdot s^{-1}}$ and varying laser beam power. From each recorded image the maximum gray level (*GL*) was determined. Figure C.2 shows these (normalized) maximum gray levels as a function of time. As can be observed from this figure, the maximum gray level does not vary linearly with laser power. The gray level for the spectral region composed by filter combination (*iii*) varies strongly around a laser power of 1000 W, and only slightly around 500 W. Whereas, for the spectral region composed by filter combination (*i*), the gray level varies strongly around a laser power of 500 W, and only slightly around 1000 W. Preliminary experiments (see section 5.2.1) showed that a smooth and shiny titanium-nitride surface layer is obtained at a beam velocity around $40\,\mathrm{mm \cdot s^{-1}}$ and a laser power around 1000 W. For this operating point the filter combination (*iii*) yields the highest resolution (black curve in figure C.2). It follows from equations (3.8) and (3.9) that for this spectral region, the detected radiance is proportional to the sixth power of temperature (T^6). Then, errors introduced by varying emissivity are negligible (see section 3.5.1). Therefore, this filter combination was applied for the implementation of the CCD camera as a thermal camera. Figure C.1(d) shows the resultant spectral sensitivity of the camera, consisting of the product of the spectral sensitivity of the chip (figure C.1(a)) and the SCHOTT filters KG1 and RG1000 (figure C.1(c)). This spectral range is the same as the region in which the pyrometers operate (table 5.2).

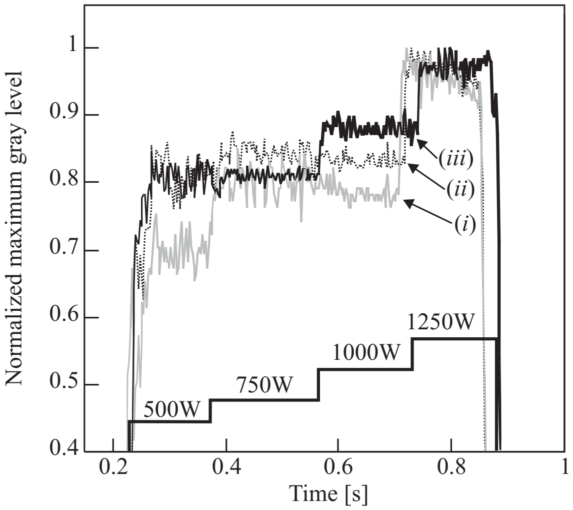

Figure C.2: Normalized maximum gray level as a function of time during laser alloying of titanium with nitrogen with varying laser power P_L (500, 750, 1000 and 1250 *W), as measured by the CCD camera with different optical filter combinations: (i) 550FL and KG1 (dotted), (ii) 700FL and KG1 (light gray), (iii) KG1 and RG1000 (black). Laser beam velocity* $50\,mm \cdot s^{-1}$*, beam diameter* 1.1 *mm.*

C.2 Calibration

To be able to determine the shape and dimensions of the melt pool, from images recorded by the thermal camera, the gray level (GL_m) corresponding to the temperature of the solid-liquid interface must be known. For this purpose, the envelope of the gray level profile in the y-direction (cross-section) was compared to the measured melt pool width obtained from cross-sections (figures 5.7 and 5.8), see figure C.3(a). Then, fitting the measured melt pool width in the measured gray level envelope yields the gray level corresponding to the temperature of the liquid-solid interface, see figure C.3(b). This gray level GL_m was found to equal 60.9 ± 5.3, for laser nitriding of titanium, at beam velocities varying between $20\,\mathrm{mm \cdot s^{-1}}$ and $90\,\mathrm{mm \cdot s^{-1}}$ and at laser power varying between 500 W and 1250 W.

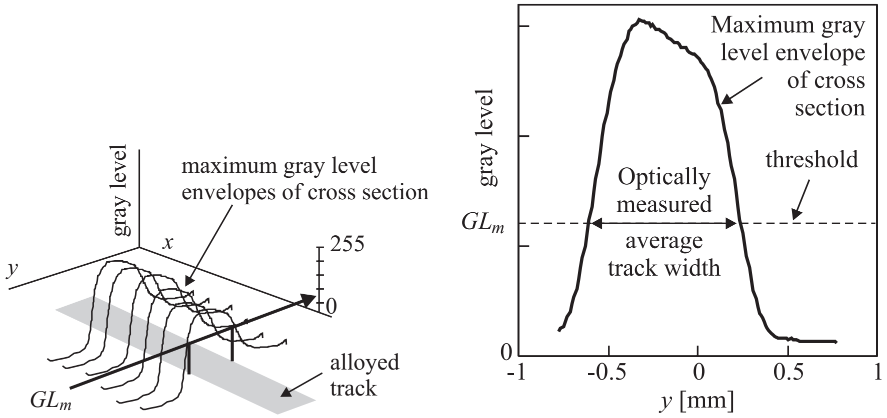

(a) Isometric representation of the maximum gray level envelopes over the cross-section along the alloyed track.

(b) Two dimension representation of a maximum gray level envelope over the cross-section along the alloyed track and the optically measured track width. $P_L = 1000\,\mathrm{W}$, $v = 50\,\mathrm{mm \cdot s^{-1}}$.

Figure C.3: Calibration of the thermal camera.

Appendix D

PROPERTIES OF TITANIUM AND ITS ALLOYS

D.1 Titanium and Ti6Al4V

Titanium is an important material in aeronautics, medicine and chemical industry because of its excellent mechanical and chemical properties, such as high specific strength, good bio-compatibility, and high corrosion resistance (Dobbs and Robertson, 1983). The commercial grade Ti6Al4V (6% Al, 4% V) is the most frequently applied grade in industry. Table D.1 lists the physical properties, which are relevant for this thesis.

Table D.1: Thermo-physical properties of titanium, Ti6Al4V and TiN at 20° C.

Property	Titanium	Ti6Al4V	TiN
Density, ρ [$\mathrm{kg \cdot m^{-3}}$]	4507	4428	5222
Melting temperature, T_m [°C]	1650	1650	2950
Thermal conductivity, K [$\mathrm{W \cdot m^{-1} \cdot K^{-1}}$]	17	6.8	n/a
Thermal capacity, c_p [$J\,kg^{-1}\,K^{-1}$]	523	564	602
Latent heat of fusion, L_f [$\mathrm{k}J\cdot\mathrm{kg}^{-1}$]	292	292	1078
Reaction energy, H_r [$\mathrm{k}J\cdot\mathrm{kg}^{-1}$]	-	-	5400

Sources: Boyer *et al.* (1994) and Chase *et al.* (1985).

D.2 Titanium-nitride

Titanium-nitride is of theoretical and practical interest due to the unique combination of properties including extreme hardness, high melting temperature, high temperature stability, low electrical sensitivity, the aesthetic qualities of the golden color, its application as a diffusion barrier in semi-conductor technology (Savvides and Window, 1988). Table D.1 list some physical properties of titanium-nitride. Figure D.1 shows the phase diagram of the titanium-nitrogen system.

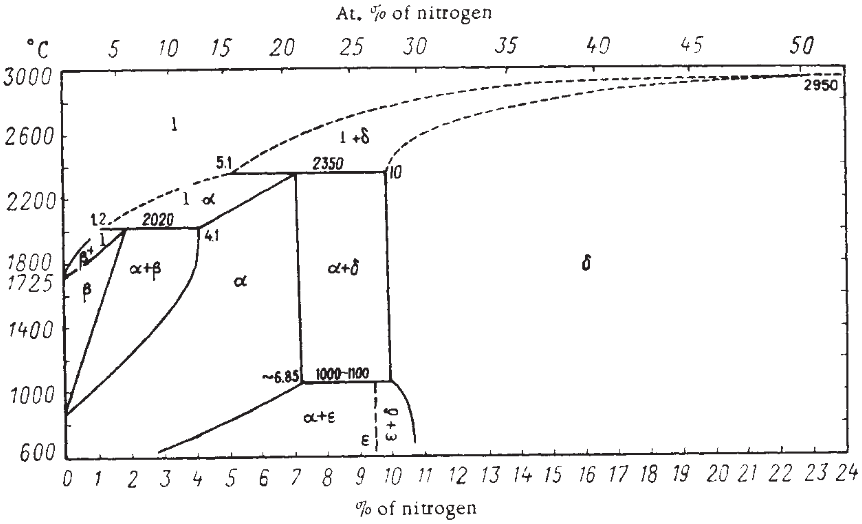

Figure D.1: Phase diagram of the titanium-nitrogen system (Molchanova, 1965).

SUMMARY

The results of laser surface treatment may vary significantly during laser surface processing. These variations arise from the sensitivity of the process to disturbances, such as varying absorptivity and the small dimensions of the work piece. To increase the reproducibility of the process, a real-time feedback control system was designed and tested. Process models were developed to gain insight in the process behavior. As a test case, laser alloying of titanium (Ti6Al4V) with nitrogen was considered.

Unfortunately, not all the desired processing results, such as the thickness of the alloyed layer, can be measured during processing. The quantities, which can be measured, are temperature related, e.g. the melt pool temperature and the melt pool surface area. Dynamic and steady-state models were developed, which relate the processing results to the measured quantities.

A thermographic CCD camera was developed to measure the melt pool surface area in real-time. Pyrometers were applied to measure its temperature. The effects of the laser power, the beam velocity and the disturbances (absorptivity, thin work piece) on the temperature distribution and melt pool surface area, were analyzed theoretically, as well as experimentally. The width and length of the temperature distribution and the melt pool vary due to the disturbances. In the case of a thin work piece, the length varies more than the width. In the case of an absorptivity disturbance, the variation of the length and width are of the same order. In addition, it was found that the laser power can be best applied to counteract an absorptivity disturbance. The beam velocity can be best applied to suppress the negative effects introduced by small dimensions of the work piece.

Based on these results, several controller algorithms, including multivariable algorithms, were implemented and tested. A mode-switch controller was able to produce a constant melt pool depth despite disturbances. This controller applied the laser power to suppress an absorptivity disturbance, and the beam velocity to counteract a geometrical disturbance.

Hence, although it is not possible to measure the thickness of the alloyed layer directly, it is possible to control it by measuring and controlling temperature related quantities (temperature, melt pool area) at the surface.

SAMENVATTING

De resultaten van laser-oppervlaktebewerkingen zijn gevoelig voor verstoringen, zoals het niet constant zijn van het laservermogen en de bundelsnelheid, of variaties in de absorptie en de dikte van het te bewerken produkt. Om de reproduceerbaarheid van de bewerking te vergroten is een regelsysteem ontworpen en getest. Er zijn procesmodellen ontwikkeld, die inzicht verschaffen in de procesdynamica. Het laserlegeren van titaan (Ti6Al4V) met stikstof is onderzocht als een test-case.

Helaas zijn niet alle bewerkingsresultaten, zoals de dikte van de gelegeerde laag, tijdens de bewerking te meten. Grootheden die wel gemeten kunnen worden zijn temperatuurgerelateerd, zoals de smeltbadtemperatuur en de grootte van het smeltbadoppervlak. Daarom zijn er dynamische en stationaire modellen ontwikkeld, die de meetbare signalen relateren aan de bewerkingsresultaten.

Een infrarood CCD camera is ontwikkeld om het smeltbadoppervlak te kunnen meten. En pyrometers zijn gebruikt om de temperatuur te meten. De effecten van het laservermogen, de bundelsnelheid en de verstoringen (absorptie, dun produkt) van de temperatuursverdeling en het smeltbadoppervlak zijn theoretisch en experimenteel onderzocht. De breedte en lengte van de temperatuursverdeling en het smeltbadoppervlak variëren t.g.v. de verstoringen. In het geval van een geometrieverstoring (dun produkt) is de variatie van de lengte groter dan de variatie van de breedte. In het geval van een absorptieverstoring zijn de lengte-, en breedtevariatie van gelijke orde. Ook bleek dat het laservermogen gebruikt moet worden om een absorptieverstoring te elimineren. Terwijl de bundelsneheid moet worden gebruikt om de negatieve effecten van variaties in produktdikte te reduceren.

Verschillende regelalgoritmen, waaronder multivariable algoritmen, zijn gerealiseerd en getest. Een z.g. mode-switch regelaar bleek het best in staat om, ondanks verstoringen, de dikte van de gelegeerde laag in de hand te houden. Deze regelaar past het laservermogen toe om een absorptieverstoring te onderdrukken en gebruikt de bundelsnelheid om geometrieverstoringen te onderdrukken.

Door het meten en regelen van temperatuurgerelateerde grootheden aan het oppervlak (temperatuur, smeltbadoppervlak) is het dus mogelijk om the dikte van de gelegeerde laag te regelen, ondanks het feit dat die dikte niet direct meetbaar is.

ABOUT THE AUTHOR

Gert-Willem Römer was born on October 11th, 1969 in ’s-Heerenberg, a small city in the east of the Netherlands. After successful completion of his VWO exam at the Ludger College in Doetinchem, he started his study in Electrical Engineering at the University of Twente in September 1988. During his M.Sc. project, performed at the Control Laboratory of the Department of Electrical Engineering, he investigated the combination of cautious and robust control for uncertain processes with bounded parameter and disturbance distributions. In March 1994 he received his M.Sc. degree, cum laude, in Electrical Engineering. In April 1994 he started his Ph.D. work as described in this thesis.

Page intended for notes.

Page intended for notes.

Page intended for notes.